Engineered Design of Efficient Nanostructured Photocatalysts for Energy Storage and Conversion Applications

(ナノ構造を有する高効率光触媒の工学的設計とエネルギー貯蔵・変換への応用)

July, 2023

Doctor of Philosophy (Engineering)

MOHAMED HAMADA MOHAMED ABDELKODOUS

モハメド ハマダ モハメド アブドエルコドス

Toyohashi University of Technology (TUT)

別紙４－１（課程博士（英文））

Date of Submission（month, day， year）: July 7th, 2023

Department of Electrical and Electronic Information Engineering	Student ID Number	D209203	Supervisors	Atsunori Matsuda Go Kawamura
Applicant's name	MOHAMED HAMADA MOHAMED ABDELKODOUS			

Abstract（Doctor）

Title of Thesis	Engineered Design of Efficient Nanostructured Photocatalysts for Energy Storage and Conversion Applications.

Approx. 800 words

The need for sustainable energy conversion and storage technologies has become increasingly vital in addressing the global energy crisis and environmental challenges. In this context, the development of efficient and versatile photocatalysts holds great promise. This doctoral thesis focuses on the design, synthesis, and characterization of novel nanostructured photocatalysts for energy storage and conversion applications, specifically water treatment (dye degradation - microbial disinfection) , photocatalytic water splitting and hydrogen (H_2) production and energy storage applications such as supercapacitors.

The first part of the research investigates the application of nanostructured photocatalysts in water treatment processes, with a particular emphasis on dye degradation and inactivation of waterborne pathogens. Traditional water treatment methods often fall short in eliminating organic, inorganic dyes and heavy metals, which pose a significant threat to water resources. Through the utilization of nanostructured photocatalysts, enhanced photocatalytic degradation of dyes can be achieved. In addition, microbial elimination of the pathogenic microorganisms causing serious health issues to humans and the aquatic environment can become accessible. This study explores the optimization of catalyst composition, morphology, and surface properties to enhance dye degradation efficiency, thereby providing a viable solution for water purification.

The second part of the research focuses on the utilization of nanostructured photocatalysts for photocatalytic water splitting and (H_2) production. The photocatalytic conversion of water into hydrogen fuel offers a promising route for clean and sustainable energy production. The thesis investigates the synthesis and characterization of novel nanostructured materials with enhanced light absorption properties, efficient charge separation, and improved catalytic activity for water splitting. The aim is to develop highly efficient and stable photocatalysts capable of harnessing solar energy to generate hydrogen as a clean energy source.

Lastly, this thesis explores the application of nanostructured photocatalysts in energy storage devices, particularly supercapacitors. Supercapacitors have garnered considerable attention as energy storage systems due to their high-power density, rapid charge-discharge rates, and long cycle life. The research investigates the design and fabrication of nanostructured electrode materials with enhanced surface area and electrical conductivity, aiming to improve the energy storage capacity and cycling stability of supercapacitors. The incorporation of nanostructured photocatalysts into supercapacitors offers the possibility of simultaneously harvesting solar energy and storing it as electrical energy.

Overall, this doctoral thesis contributes to the field of energy conversion and storage by presenting the development of novel nanostructured photocatalysts for addressing global environmental and energy challenges. The research findings provide insights into the design principles of efficient and stable photocatalysts, leading to the advancement of sustainable energy technologies. The outcomes of this study hold the potential to revolutionize the fields of water treatment, photocatalysis, and supercapacitors, ultimately contributing to the realization of a cleaner and more sustainable future.

Acknowledgment

I would like to express my deepest gratitude and appreciation to the following individuals, without whom the completion of this PhD dissertation would not have been possible.

First and foremost, I would like to extend my heartfelt thanks to my family. Their unwavering support, love, and understanding have been my anchor throughout this challenging journey. To my parents, for their constant encouragement and belief in my abilities, I am eternally grateful. Your sacrifices and dedication have been the driving force behind my success. To my siblings, for their patience and understanding during my long hours of work, I am indebted to you.
I am also indebted to my esteemed colleagues and friends, who have been instrumental in shaping my research and providing valuable insights. Their camaraderie and intellectual discussions have enriched my understanding and broadened my perspectives. I am grateful for the stimulating debates, late-night brainstorming sessions, and the shared moments of joy and frustration. Your unwavering support and encouragement have been invaluable.

A special note of appreciation goes to my supervisor, Prof. Dr. Atsunori Matsuda of Toyohashi University of Technology, whose guidance, expertise, and unwavering support have been pivotal in the successful completion of this dissertation. Your mentorship, patience, and constructive feedback have been instrumental in shaping my research and refining my analytical skills. I am grateful for the countless hours you dedicated to reviewing my work, providing valuable suggestions, and pushing me to exceed my limits.

I would also like to extend my thanks to my PhD reviewers Prof. Dr. Muto and Prof. Dr. Kawamura [Toyohashi University of Technology]. Their dedication to academic excellence and their commitment to nurturing young scholars have provided a conducive environment for my intellectual growth and development.

Lastly, I would like to express my gratitude to all the participants and organizations who generously shared their time and resources for the purpose of this research. Without their cooperation and willingness to participate, this study would not have been possible.

In conclusion, I am profoundly grateful to everyone who has supported me in this challenging and rewarding endeavor. Your belief in me, your encouragement, and your unwavering support have been the pillars upon which I have built this academic achievement. I am humbled and honored to have had the opportunity to pursue this PhD, and I am forever grateful for the love and support of my family, the camaraderie of my colleagues, and the guidance of my supervisor.

Thank you all from the bottom of my heart.

[MOHAMED HAMADA MOHAMED ABDELKODOUS]

Table of contents

Chapter 2: Carbon-semiconductor heterojunction based on the nanocomposite $Co_xNi_{1-x}Fe_2O_4$; x=0.9 / SiO_2 / TiO_2 for the efficient wastewater treatment (chloramine-T dye degradation and microbial pathogens' disinfection)

Chapter 3: UV-assisted chloramine-T degradation by multiple nanocomposites of carbon-semiconductor-based heterojunction

Chapter 4: Multifunctional metal-semiconductor-based heterojunction for superior light-assisted degradation of different dyes and microorganisms' deactivation: Theoretical and experimental study

Chapter 5: Overall water splitting over metallic nanoparticles loaded on Al-SrTiO$_3$ perovskite semiconductor photocatalyst supported with RhCr$_2$O$_3$ and CoOOH cocatalysts under wide ranges of light

Chapter 6: Designed Al-$SrTiO_3$/Au/CdS Z-Schemes for efficient H_2 evolution under visible light

Chapter 7: carbon loaded nanocomposite as an efficient electrode material for supercapacitor applications

Chapter 1: General Introduction

Energy storage and conversion applications play a critical role in addressing the growing challenges of energy demand, sustainability, and grid stability. As the world transitions towards cleaner and more renewable energy sources, the efficient storage and conversion of energy become paramount for enabling a sustainable and reliable energy future. By storing excess energy during periods of low demand or high generation, and releasing it during peak demand or low generation, energy storage systems contribute to a stable and reliable power supply. In the face of increasing energy demands and the urgent need for sustainable solutions, energy storage has emerged as a crucial component of the modern energy landscape. The ability to store energy efficiently, reliably, and on a large scale is paramount for the integration of renewable energy sources, grid stability, and the advancement of electric transportation. Among the various energy storage technologies, supercapacitors have gained significant attention due to their unique characteristics and potential to revolutionize energy storage systems. Supercapacitors, also known as electrochemical capacitors or ultracapacitors, are energy storage devices that bridge the gap between conventional capacitors and batteries. Unlike traditional capacitors, which store energy through static charge separation, and batteries, which rely on chemical reactions, supercapacitors store energy electrostatically and electrochemically. This unique mechanism allows them to combine the advantages of capacitors, such as high power density and rapid charge/discharge rates, with the energy storage capacity of batteries.The importance of supercapacitors in the realm of energy storage stems from several key factors. Firstly, their high power density enables rapid energy delivery, making them ideal for applications that require bursts of power, such as regenerative braking in electric vehicles or smoothing out power fluctuations in renewable energy systems. Secondly, their long cycle life and excellent durability make them suitable for applications where frequent charge/discharge cycles are required without significant degradation.Furthermore, supercapacitors offer a sustainable alternative to traditional energy storage technologies. They can be charged and discharged thousands of times, reducing the need for frequent replacements and resulting in lower environmental impact. Additionally, supercapacitors operate efficiently over a wide temperature range and exhibit excellent performance even in harsh environmental conditions, making them reliable and versatile energy storage solutions. Supercapacitors also play a crucial role in improving the overall efficiency of energy systems. By acting as intermediate storage devices, they can buffer intermittent energy sources, such as solar and wind, and provide a stable supply of energy when needed. This not only enhances the reliability and stability of power grids but also contributes to the effective integration of renewable energy sources, reducing reliance on fossil fuels and mitigating the impact of climate change. Moreover, supercapacitors have the potential to revolutionize the transportation sector. Their high power density and rapid charging capabilities make them ideal for electric vehicles, enabling shorter charging times and longer driving ranges. By utilizing supercapacitors in conjunction with batteries, hybrid energy storage systems can be created, offering the advantages of both technologies and addressing the limitations of pure battery systems.

While energy conversion is a crucial process that allows us to harness, transform, and utilize energy in various forms. The field of photocatalysis has emerged as a significant branch of research within the realm of chemistry and materials science, offering promising solutions for various environmental and energy challenges. In recent years, the application of photocatalysis has garnered increasing attention, particularly in the domain of heterogeneous photocatalysis, due to its potential to harness solar energy for diverse applications. Photocatalysis, in its simplest definition, refers to a process in which light energy initiates a chemical reaction by activating a semiconductor material known as a photocatalyst. This activation process generates electron-hole pairs, which subsequently participate in various redox reactions on the surface of the photocatalyst. Heterogeneous photocatalysis specifically involves the use of solid photocatalysts, typically metal oxides, which exhibit excellent photochemical properties. The principle of operation lies in the ability of these photocatalysts to absorb light within a specific wavelength range and subsequently utilize this energy to drive chemical reactions, including pollutant degradation and energy conversion. The applications of heterogeneous photocatalysis are diverse and encompass a wide range of fields. Environmental remediation, for instance, represents a prominent application area, where photocatalysis has demonstrated its potential for pollutant degradation, including the decomposition of organic compounds, elimination of hazardous substances, and disinfection of water and air. Moreover, the field of energy conversion has witnessed significant advancements due to the utilization of photocatalysis. The production of hydrogen as a clean and sustainable energy source, carbon dioxide reduction, and the generation of solar fuels have all been explored using heterogeneous photocatalytic systems. Understanding the history and evolution of photocatalysis provides crucial insights into the development of this field. From the pioneering work of Fujishima and Honda in the 1970s, who discovered the photoelectrochemical properties of titanium dioxide, to the continuous advancements in materials synthesis, characterization techniques, and reactor design, photocatalysis has evolved into a multidisciplinary field of research. The significance of this research lies in its potential to address some of the most pressing environmental and energy challenges of our time. By harnessing the power of sunlight and utilizing photocatalysts, it is possible to develop sustainable and cost-effective solutions for clean energy production and environmental remediation.

In this work, functional, recyclable, and efficient nanocomposite matrix ($Co_xNi_{1-x}Fe_2O_4$; x=0.9 / SiO_2 / TiO_2) was prepared by a layer-by-layer method. The nanocomposite was built from the interior core layer (magnetic layer) to the exterior shell layers (photoactive layers). The photoactive layer employed Titanium oxide (TiO_2) nanoparticles (NPs), due to its plenitude, nontoxicity, oxidizing properties and long stability. TiO_2 NPs can efficiently play a key role in many fundamental applications related to solar energy and environment such as solar water splitting and wastewater purification. However, TiO_2 NPs suffer from rapid electron-hole pair recombination and large bandgap (3.2 eV) inhibiting their technological applications. Many techniques have been reported to tailor the drawbacks of TiO_2 nanomaterials including the incorporation with non-metal ions like sulfur and chlorine or the doping with noble metals such as Ag, Au and Pt. Collection and recycling of the composite after treatment is a critical challenge, to build a recyclable nanostructure, magnetic nanomaterials give a helpful way to reuse nanocomposites when employed in their cores by magnetic separation. Thus, the photocatalytic reaction may happen for many times by collecting TiO_2 nanocomposites from the wastewater being treated for subsequent reuse. Super paramagnetic nanoparticles are one of the most favored materials, especially Fe_3O4 and ferrite nanoparticles, to develop recyclable photocatalysts due to their high polarization and steadiness. Thus, the photocatalyst can be gathered by magnets after effective treatment. However, coating TiO_2 with iron oxide nanoparticles initiates ineffectual and unstable photocatalyst due to photo-dissolution. For example, direct electronic collaborations occur between the photoactive TiO_2 and iron oxide nanoparticles prompting their oxidation and the development of pseudobrookite (Fe_2TiO_5) as an unstable stage affecting the overall quantum efficiency. Thus, separation of the photoactive layer and the magnetic core with a thin silica layer is a must to persist the photocatalytic abilities. To further improve the quantum efficiency, the prepared composite matrix was loaded with different carbon materials with various dimensionalities including (0D C-dots, 1D Single-walled carbon nanotubes (SWCNTs), and 2D reduced graphene oxide (rGO) to form carbon semiconductor heterojunctions (chapters 2-3). Carbon nanomaterials are extensively used in doping the photocatalyst surface due to their phenomenal properties such as charge exchange and outstanding optical properties which opened the best approach to be connected in photocatalysis applications. Similarly, the previously mentioned matrix was loaded with copper (Cu) NPs to form metal-semiconductor heterojunction (chapter 4). Cu NPs which as cost-effective, can affectively absorb visible light, and improve charge separation. After that, the photocatalytic performance of the prepared nanocomposites was tested against many organic, inorganic, and heavy metals under both UV and visible light via adsorption, photolysis, and photocatalysis assays. Kinetics of reactions and many parameters affecting the overall performance (ex: photocatalysts dose, dye concentration, pH, and scavengers) were also investigated. In addition, the antimicrobial potential of the prepared materials was evaluated against multi-drug resistant bacteria and pathogenic fungi through different assays including minimum inhibitory concentration (MIC), zone of inhibition (ZOI), antibiofilm formation, cell content leakage, and the effect of gamma and UV rays' activation was also investigated. While Chapters (5-6) are presenting overall water splitting and H_2 evolution under wide ranges of light through cocatalyst loaded Al-$SrTiO_3$ photocatalyst and Al-$SrTiO_3$/Au/CdS Z-Scheme samples, respectively. Since 1980, $SrTiO_3$ photocatalyst is attracting the interest of many researchers worldwide as a promising material for overall water splitting. $SrTiO_3$ can promote overall water spitting into H_2 and O_2 in a 2:1 stoichiometric ratio. In addition, it possesses a proper band structure with respect to water oxidation and reduction potentials. However, the quantum yield of pristine $SrTiO_3$ is low, due to its wide bandgap energy (3.2 eV), inefficient light absorption, the rapid recombination of photoexcited charge carriers, and the undesired backward reactions. Many efforts have been dedicated to tailor the current limitations of pristine $SrTiO_3$. On the one hand, doping $SrTiO_3$ with lower valence cations such as Al^{+3} ions increased its light absorption and minimized the defects (Ti^{+3}) acting as recombination centers for photogenerated electrons and holes. On the other hand, H_2 and O_2 can be evolved from the surface of $SrTiO_3$ by employing different variety of cocatalysts, improving the migration and separation of charge carriers, and decreasing the activation energy. In addition, to promote the photocatalytic activity under visible light, decorating the main semiconductor photocatalyst with plasmonic nanoparticles such as Au NPs is a very promising technique through plasmonic energy transfer from plasmonic metals to the semiconductor photocatalyst. Plasmonic energy through hot-electron transfer, resonant energy transfer, and light scattering through the localized surface plasmon resonance (LSPR) can foster water splitting performance by visible light active materials. In (Chapter 5), we combined the synergetic impact of visible light-absorbing plasmonic NPs such as (Pt, Au, and Cu) with the efficient cocatalysts for hydrogen evolution ($RhCr_2O_3$) and oxygen evolution (CoOOH) reactions. While in (Chapter 6), we combined a visible-light absorbing semiconductor material (CdS) to from efficient Z-Scheme systems for H_2 evolution under visible light. Combining CdS is a promising approach to improve the performance of $SrTiO_3$ as it has a narrow bandgap (2.4 eV). In addition, CdS possesses a more negative conduction band edge with respect to H^+ to H^2 reduction potential, high flat-band potential, and improved electrochemical performance, making it a very suitable electron donor material. Finally, chapter (7), is evaluating the potential of our previously mentioned carbon-semiconductor heterojunction-based nanocomposite (C-dots / $Co_xNi_{1-x}Fe_2O_4$; x=0.9 / SiO_2 / TiO_2) as an electrode material for supercapacitor applications. The prepared nanocomposite possesses not only a good surface area but also carbon and metal oxide layers which are suitable for supercapacitance applications.

Chapter 2: Carbon-semiconductor heterojunction based on $Co_xNi_{1-x}Fe_2O_4$; x=0.9 / SiO_2 / TiO_2 nanocomposite for the efficient wastewater treatment (chloramine-T dye degradation and microbial pathogens' disinfection)

2.1 Overview

Water scarcity is now a serious global issue resulting from population growth, water decrease, and pollution. Traditional wastewater treatment plants are insufficient and cannot meet the basic standards of water quality at reasonable cost or processing time. In this paper we report the preparation, characterization and multiple applications of an efficient photocatalytic nanocomposite ($Co_xNi_{1-x}Fe_2O_4$; x=0.9 / SiO_2 / TiO_2 / C-dots) synthesized by a layer-by-layer method. Then, the photocatalytic capabilities of the synthesized nanocomposite were extensively-studied against aqueous solutions of chloramine-T trihydrate. In addition, reaction kinetics, degradation mechanism and various parameters affecting the photocatalytic efficiency (nanocomposite dose – chloramine-T initial concentration – reaction pH) were analyzed in detail. Further, the antimicrobial activities of the prepared nanocomposite were tested and the effect of UV-activation on the antimicrobial abilities of the prepared nanocomposite was analyzed. Finally, a comparison between the antimicrobial abilities of the current nanocomposite and our previously-reported nanocomposite ($Co_xNi_{1-x}Fe_2O_4$; x=0.9 / SiO_2 / TiO_2) was been carried out. Our results revealed that the prepared nanocomposite possessed a high degree of crystallinity, confirmed by XRD, while UV-Vis. recorded an absorption peak at 299 nm. In addition, the prepared nanocomposite possessed BET-surface area of (28.29 ± 0.19 m^2/g) with narrow pore size distribution. Moreover, it had semi-spherical morphology, high-purity and an average particle size of (19.0 nm). The photocatalytic degradation efficiency was inversely proportional to chloramine-T initial concentration and directly proportional to the photocatalyst dose. In addition, basic medium (pH = 9) was the best suited for chloramine-T degradation. Moreover, UV-irradiation improved the antimicrobial abilities of the prepared nanocomposite against E. coli, B. cereus, and C. tropicalis after 60 min. The observed antimicrobial abilities (high ZOI, low MIC and more efficient antibiofilm capabilities) were unique compared to our previously-reported nanocomposite. Our work offers significant insights into more efficient water treatment and fosters the ongoing efforts looking at how pollutants degrade the water supply and the disinfection of water-borne pathogenic microorganisms.

2.2 Introduction

Population growth, the continued demand of water and water shortages from one year to another are pushing the world towards a water shortage problem[1-3]. In addition, most of the available potable water on earth is contaminated with many kinds of pollutants such as organic, inorganic materials, heavy metals and pathogenic microorganisms, causing serious diseases[4-7]. Among these pollutants, chloramine-T is gaining a lot of attention due to its adverse effects on public health, and is seriously threatening the aquatic environment [8, 9]. Chloramine-T is an organic compound with a chloro-substituent in the place of an amino hydrogen [10]. It is currently-used in many applications such as antifouling biocides, disinfectant, various food products, and different cosmetics[11-13]. However, several toxicological experiments have shown that chloramine-T is harmful to the skin and eyes of humans [14]. In addition, it causes irritation of the upper respiratory tract [15] and in severe cases nausea, vomiting and diarrhea [16]. Thus, reduction and degradation of chloramine-T into relatively-safe intermediates is important for our environment. Currently, there are many water treatment and purification methods[17-19]. However, these traditional methods are not effective in terms of water quality, time of processing and overall cost of operation. Nanotechnology, through nanomaterials, offers not only more-effective ways of water purification, but also cost-effective and easily-manipulated techniques. Nanomaterials possess outstanding chemical, physical and biological properties compared to their bulk materials, due to the large number of surface atoms compared to the inner mass [20-23]. Recently, there are many reports highlighting various promising nano materials and composites for heavy metal adsorption and dye removal applications [24-28]. With respect to them, titanium dioxide nanoparticles (TiO_2 NPs) have been extensively studied over the past decades (since water splitting by Fujishima and Honda in 1972) due to their cost-effectiveness, high degree of thermal and chemical stabilities, high-oxidizing ability, and their good electronic and optical characteristics [29]. TiO_2 NPs are very promising in many environmental applications like water treatment. However, the technological application of TiO_2 NPs is limited by two main drawbacks [30]. Firstly, they possess a wide energy bandgap (2.96, 3.02 and 3.2 eV) for the brookite, rutile and anatase phases respectively[31]. Thus, TiO_2 NPs are activated only by ultraviolet (UV) light, representing a tiny portion of the total solar spectrum (about 3 %) [32]. Secondly, TiO_2 NPs have short electron-hole recombination time (about 10^{-9} sec), while photocatalytic reactions need times at the order of (10^{-3} sec), that further deteriorates the photocatalytic efficiency of TiO_2 NPs [33, 34]. Various tailoring methods have been reported for increasing the quantum efficiency of TiO_2 NPs such as the formation of mixed TiO_2 phases which reduces the band gap energy [35], doping with ions of non-metals like carbon [36] and sulfur [37] and loading with noble metals like silver (Ag) [38], platinum (Pt) and gold (Au) [39] which elongate electron-hole recombination time. Currently, loading TiO_2 NPs with cheap carbon nanoparticles is gaining significant considerations, such as conjugation with activated carbon which improved the adsorption potential of TiO_2 NPs [40]. Additionally, loading with graphene and carbon nanotubes has shown to provide good electron mobility and reduced the recombination time of the photo-generated charge carriers [41, 42]. Recently, carbon dots (C-dots) have received much interest due to their strong photoluminescence, abundance, cost-effectiveness, ease of manipulation, and chemical inertness, and their role as electron reservoirs which elongates the electron-hole recombination time during photocatalytic degradation [43-46]. In this chapter, single nanoparticles were incorporated into one nanocomposite to gain more benefits. A recyclable TiO_2-based and C-dots-loaded nanocomposite ($Co_xNi_{1-x}Fe_2O_4$; x=0.9 / SiO_2 / TiO_2 / C-dots) was prepared by a layer-by-layer method. A magnetic core ($Co_xNi_{1-x}Fe_2O_4$; x=0.9) was formed to make the nanocomposite recyclable by magnetic separation, SiO_2 layer was used as a protective shell for the TiO_2 NPs (to protect the TiO_2 NPs from the formation of pseudo-brookite due to magnetic core contact), anatase TiO_2 shell was prepared as an efficient photocatalyst with good photocatalytic abilities, and C-dots were loaded onto the TiO_2 surface to act as an electron reservoir to increase TiO_2 quantum efficiency. The photocatalytic abilities of the prepared nanocomposite were tested against chloramine-T degradation (an organic compound). In addition, reaction kinetics, photocatalytic mechanism and different parameters affecting the efficiency of photodegradation (nanocomposite dose, chloramine-T initial concentration and reaction pH) had been analyzed. Moreover, the antimicrobial abilities of the synthesized nanocomposite had been tested against multi-drug- resistant bacteria and pathogenic fungi. Finally, the effect of UV-activation on the antimicrobial abilities of the prepared nanocomposite had been studied.

2.3 Materials & Methods

2.3.1 Materials

Copper acetate monohydrate ($C_4H_8CuO_5$), ascorbic acid ($C_6H_8O_6$), titanium (IV) isopropoxide 97% ($C_{12}H_{28}O_4Ti$), ammonium hydroxide 28% (NH_4OH), tetraethyl orthosilicate (TEOS) 98% [Si

$(OC_2H_5)_4]$, absolute ethanol 99.9 % (C_2H_5OH), hydroxypropyl cellulose (M.W. = 80,000), nickel chloride ($NiCl_2$), cobalt chloride ($CoCl_2$), sodium hydroxide pellets (NaOH), Ferric chloride ($FeCl_3$. $6H_2O$), and chloramine-T trihydrate $C_7H_7ClNNaO_2S$. $3H_2O$ were purchased from Sigma Aldrich (Germany). All reagents were of extra-pure grade and were used as received without further purification.

2.3.2 Method

2.3.2.1 Preparation of the sandwich structure: ($Co_xNi_{1-x}Fe_2O_4$; $x=0.9/SiO_2/TiO_2$) nanocomposite

The detailed preparation steps are reported in our previously-published papers [47, 48].

2.3.2.2 Preparation of carbon nanoparticles (C-dots)

C-dots were prepared according to the method reported by Xiaofang Jia *et. al,* [49]. Briefly, (6.8 g) of ascorbic acid were dissolved in (400 ml) deionized water (D.I.W.). (0.8 g) of copper acetate monohydrate was then added into the above solution, and the solution stirred at room temperature for 10 min. The temperature was then raised to 90ºC and kept for 5 hrs and the remaining solution centrifuged at 9000 rpm for 20 min to remove large particles. Finally, the supernatant containing the C-dotswas dried at 60ºC for 8 hrs.

2.3.2.3 Preparation of ($Co_xNi_{1-x}Fe_2O_4$; $x=0.9 / SiO_2 / TiO_2 /$ C-dots) nanocomposite

The C-dots-loaded nanocomposite was prepared according to the method reported in our previously-published paper [29]. Briefly, 0.8 g of the nanocomposite from part 2.2.1 was mixed with 0.1 g of C-dots from part 2.2.2. Then, 50 ml D.I.W was added, and the mixture dispersed using water-bath sonication for 45 min. The hybrid composite was then centrifuged at 8000 rpm for 15 min. Finally, the collected composite was washed with D.I.W. and dried at 85ºC for 2 hrs. The preparation steps are schematically-represented in **Fig. 2.1.**

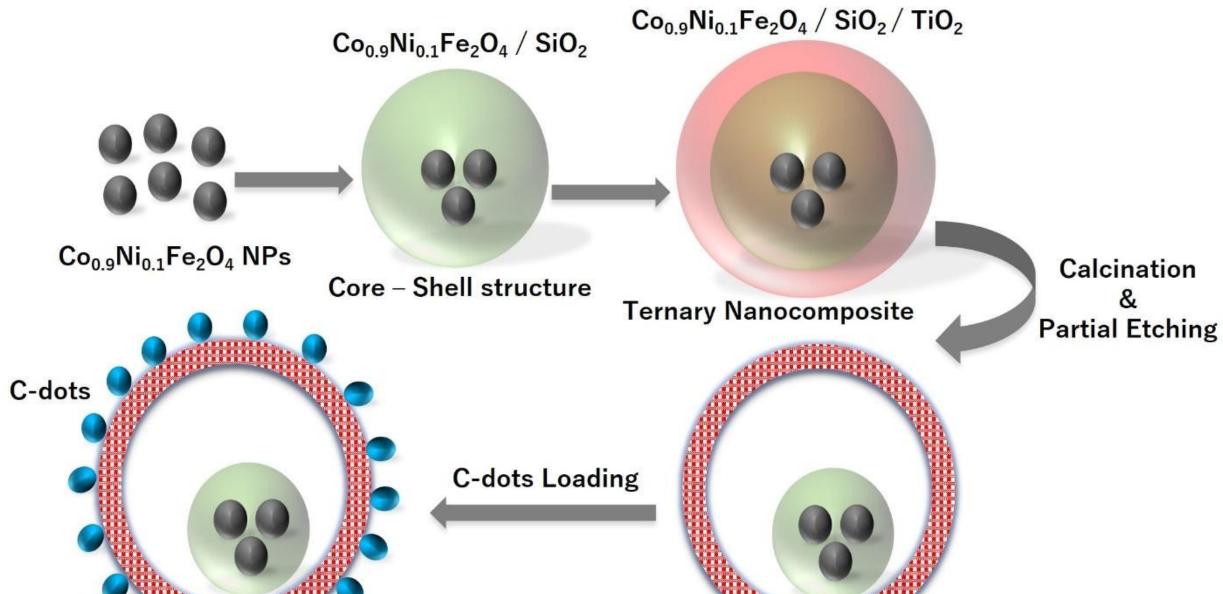

Fig. 2.1: Schematic representation of the mechanism of $Co_xNi_{1-x}Fe_2O_4$; x=0.9 / SiO_2 / TiO_2 / C-dots nanocomposite formation.

2.3.3 Characterization of the prepared nanocomposite

Crystallinity and phase were studied using x-ray diffraction (XRD) analysis on an Ultima IVX-ray diffractometer, Rigaku, Japan, applying a voltage of 40 KV, a current of 30 mA and Cu K_α radiation (λ = 1.540598 Å). UV-Vis. absorption was calculated via a V-670 spectrophotometer, JASCO, Japan. BET and BJH analyses were used to determine surface area and pore size distribution via Tristar II Micromeritics, Japan. The average particle size was determined by a high-resolution transmission electron microscope (HR-TEM), JEM-2100 F, JEOL Ltd., Japan. The morphology, elemental composition and purity of the particles were analyzed by scanning electron microscope (SEM) supported with an energy-dispersive X-ray (EDX) unit, SU8000 Type II, HITACHI high technologies, Japan. FTIR analysis was carried out by an FT-IR 3600, JASCO Infra-Red spectrometer via the KBr pellet method. It was recorded through a wave-number scale from 4000 to 400 cm^{-1}.

2.3.4 Photocatalytic activity of ($Co_xNi_{1-x}Fe_2O_4$; x=0.9 / SiO_2 / TiO_2 / C-dots) nanocomposite against chloramine-T trihydrate

Photocatalytic experiments were carried out at an ambient temperature of 24 ± 2°C. A fixed amount of 10 mg of the synthesized nanocomposite was added to a 50 mL aqueous solution of chloramine-T C_o =10 mgL^{-1} and stirred for 2 hrs. in the dark. After reaching adsorption-desorption equilibrium, the suspension was illuminated by a low-pressure, 10 W mercury lamp with 90% emittance at 254 nm. The lamp was axially-located and held in a quartz immersion tube. At given irradiation time intervals, 1 ml of the suspension was taken out by a syringe equipped with 2.5 µm pore size filter. The filtered supernatant was centrifuged at (5000 rpm) for (10 min), to remove particles of the employed photocatalyst. The changes in chloramine-T concentration during photo-decomposition were determined by measuring the absorbance at λ_{max}= 225 nm as a function of irradiation time in the liquid cuvette configuration. D.I.W. was used as the reference on a UV-Vis. Spectrophotometer (Agilent Technologies Cary60 UV-Vis). The concentration of chloramine-T prior to UV-irradiation was used as the initial value for the measurement of chloramine-T degradation.

2.3.5 Antimicrobial activity of C-dots and $Co_xNi_{1-x}Fe_2O_4$; x=0.9 / SiO_2 / TiO_2 / C-dots nanocomposite

Both C-dots and $Co_xNi_{1-x}Fe_2O_4$; x=0.9 / SiO_2 / TiO_2 / C-dots nanocomposite were dispersed in DMSO to form two tested concentrations for each sample (10 and 15 µg/ml). Next, their antimicrobial activities were individually-tested using the agar well diffusion method [50], against different isolates of infection-causing bacteria such as *Staphylococcus aureus (*MRSA), *Escherichia coli*, *Bacillus cereus*, *Pseudomonas aeruginosa, and Klebsiella pneumoniae.* Furthermore, the antifungal potentials of both samples were checked against unicellular pathogenic fungi (*Candida tropicalis and Candida albicans)*. The tested microorganisms were kindly-gifted from the culture collection of Drug Microbiology Lab., Drug Radiation Research Dep., NCRRT, Cairo, Egypt. It is worth stating that 0.5 McFarland standard of all tested bacterial inoculums was fixed at 3-4 $\times 10^8$ CFU/ml and 2-5 $\times 10^8$ CFU/ml for pathogenic yeast. Growth restraint of the examined pathogenic bacteria and yeast was defined by measuring the zone of inhibition (ZOI) after 24 hrs. of incubation [51]. In addition, conventional antibiotic discs such as nystatin (NS), with 6 mm-diameter, and a ready-to-use solution of Amoxicillin/Clavulanic acid (AMC, 100 µg/ml) were utilized as references to compare the abilities of the developed nanocomposite [52]. A minimum inhibitory concentration (MIC) was defined using Luria–Bertani (LB) broth with suitable serial dilution [53, 54]. A test tube containing the selected microorganism and the nutrient was employed as a positive control, and another tube with just the nutrient was used as a negative control. *C-dots* and the prepared C-dots loaded-nanocomposite (beginning with a concentration of 50 mg/ml) were examined to determine their MIC values. MIC values were measured after 24 hrs. of incubation at 37^{o}C [55, 56]. The examined bacterial inoculums were fixed at 3-5$\times 10^8$ CFU/ml, while *Candida* species were fixed at 2-5$\times 10^7$ CFU/ml. MIC values were determined by ELISA plate reader at absorption wavelength of 600 nm [56, 57].

2.3.6 Antibiofilm activity of $Co_xNi_{1-x}Fe_2O_4$; x=0.9 / SiO_2/ TiO_2/ C-dots nanocomposite

A semi-quantitative investigation of biofilm growth by pathogenic bacteria and yeast and its inhibition by the prepared C-dots loaded nanocomposite were evaluated according to the process described by Christensen *et al.*, [58]. The apparent detection of biofilms created by pathogenic bacteria and yeast throughout the inner walls of test tubes having the tested nanocomposite with a concentration of (15 µg/ml) and tubes without the nanocomposite (control) was carried out. Additionally, nutrient broth (5 ml) was added to all test tubes after setting 0.5 McFarland standards at 2-3 ×10^7 CFU/ml (for the tested bacteria). The tubes were then incubated for 24 hrs. at 37°C. The content of the control tubes and nanocomposite-included tubes was discarded and tubes were washed and cleaned with phosphate buffer saline (PBS, pH = 7.4). After that, tubes were dried[48, 59]. The developed yeast and bacterial biofilms were fixed by 5 ml sodium acetate (3 %) for 15 min, and then all tubes were washed with D.I.W. Bacterial and yeast biofilms were dyed with 0.1% crystal violet (CV) for 10 min, then D.I.W. used to eliminate the excess quantity of CV [60]. Additionally, 4 ml of absolute ethanol was employed to dissolve CV. The formed biofilms were identified by the characteristic stained rings around the walls of test tubes [61]. The bacterial and yeast biofilms were investigated using a UV-Vis. spectrophotometer at 570 nm, and the biofilm suppression percentage (%) was determined by utilizing **equation 2.1** [48, 62].

$$Percentage\ of\ bacterial\ and\ yeast\ biofilm\ inhibition\ (\%) = \frac{O.D.\ of\ the\ control\ sample - O.D.\ of\ the\ treated\ sample}{O.D.\ of\ the\ control\ sample}$$

2.3.7. Effect of UV-irradiation on the antimicrobial abilities of the prepared nanocomposite

To distinguish the influence of UV-irradiation on the antimicrobial potential of the synthesized $Co_xNi_{1-x}Fe_2O_4$; x=0.9 / SiO_2 / TiO_2 / C-dots nanocomposite against microbes, the restraint percentage was defined by measuring the optical density of the viable and dead microbial cells [63]. Three susceptible microbes were selected, including *E. coli* (Gram-negative bacteria), *B. cereus* (Gram-positive bacteria) and *C. tropicalis* (unicellular fungi). For each microorganism, four test tubes were prepared. The first tube was a control, which contained tested microbes and was not UV-irradiated; the second had both tested microbes and the prepared nanocomposite and was not UV-irradiated; the third contained the tested microbes and was UV-irradiated; and the fourth included both tested microbes and the synthesized nanocomposite, and was UV-irradiated. All four tubes had nutrient broth and a fixed number of microorganisms (0.5 McFarland, CFU/ml). A low-pressure mercury lamp emitting UV (10W, 90% emittance at 254 nm) was horizontally-positioned and settled on the laminar flow. Examined tubes were subjected to UV-irradiation for 1 hour at a distance of about 60.96 cm. It is worth to mention that the number of bacteria and yeast was determined every 10 min through a UV-Vis. Spectrophotometer, at a wavelength of 600 nm for bacteria and 630 nm for *Candida species,* for 1 hour and the repression percentage % was estimated by **equation 2.1**.

2.3.8 Reaction mechanism using SEM/EDX analysis of nanocomposite-treated bacterial cells

Obtained bacterial cells from the biofilm-forming test were washed with PBS and fixed with 3 % glutaraldehyde solution. The preserved bacterial specimens were regularly-washed with PBS and evenly-dehydrated with various concentrations of ethanol (30 %, 50 %, 70 %, 80 %, 95 %, and 100 %) for about 20 minutes at 28±2°C [59]. Next, bacterial cells were placed on an aluminum scrap for SEM/EDX analysis [59]. The morphological characteristics of the control (non-treated pathogenic bacteria and yeast) and nanocomposite-treated bacterial and yeast cells were observed using SEM/EDX analysis.

2.3.9 Statistical analysis

Statistical interpretation of our results was performed through the ONE-WAY ANOVA analysis (at $P < 0.05$), using Duncan's multiple series studies, and the least significant difference (LSD) record [64]. The obtained results were also analyzed by SPSS software (version 15).

2.4 Results & discussion

2.4.1 Characterization of the prepared $Co_xNi_{1-x}Fe_2O_4$; x=0.9 / SiO_2 / TiO_2 / C-dots nanocomposite

2.4.1.1 XRD analysis

Crystallinity and phase of the prepared C-dots and the whole nanocomposite were studied using XRD, as depicted in **Fig. 2.2** Several diffraction peaks were recorded, such as the peak at $2\theta = 22.9^o$, plane (002), which corresponds to the C-dots shown in Fig. 2 [65], while peaks recorded at $2\theta = 25.5^o$, plane (101), 38.1^o, plane (004), 48.4^o, plane (200), 53.6^o, plane (105), 55.4^o, plane (211), 63.1^o, plane (213), and 75.6^o, plane(215) correspond to anatase TiO_2 NPs (JCPDS 21-1272). In addition, peaks observed at $2\theta = 37.2^o$, plane (311), 54.3^o, plane (422), and 62.3^o, plane (440) were due to the cobalt and nickel ferrite of $Co_xNi_{1-x}Fe_2O_4$; x=0.9 NPs (JCPDS 10-325 and JCPDS 1-1121). It is worth mentioning that an SiO_2 amorphous halo was suppressed due to the high intensity of C-dots and TiO_2 peaks, as previously-reported in our paper [48].

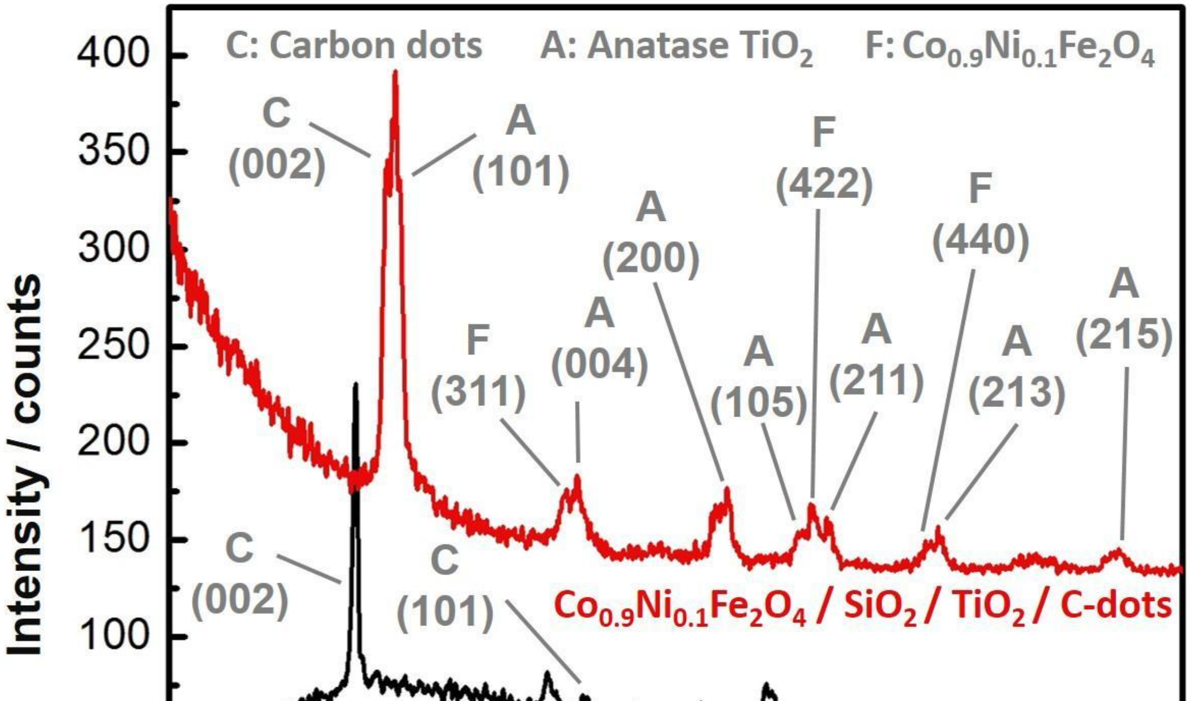

Fig. 2.2: XRD patterns of the prepared C-dots NPs and $Co_xNi_{1-x}Fe_2O_4$; x=0.9 / SiO_2 / TiO_2 / C-dots nanocomposite.

2.4.1.2 UV-Vis. spectroscopic analysis and bandgap calculation

To reveal the optical characteristics of the synthesized nanocomposite and bare C-dots, UV-Vis. analysis was carried out, as shown in **Fig. 2.3**. A strong absorption peak at (299 nm) was recorded for the prepared $Co_xNi_{1-x}Fe_2O_4$; x=0.9 / SiO_2 / TiO_2 / C-dots nanocomposite. While a C-dots absorption peak was recorded at (256 nm), this could be attributed to $\pi \rightarrow \pi^*$ transitions of carbon [66]. It is worth mentioning that the loading of C-dots resulted in a change of the nanocomposite absorption from (365 nm) for the previously-prepared $Co_xNi_{1-x}Fe_2O_4$; x=0.9 / SiO_2 / TiO_2 nanocomposite to (299 nm) for the newly-prepared C-dots-loaded $Co_xNi_{1-x}Fe_2O_4$; x=0.9 / SiO_2 / TiO_2 nanocomposite [48]. This shift could be attributed to the existence of the new transition electronic bands due to loading with carbon [67, 68]. While, band gap energy of the prepared nanocomposite was determined using **Tauc's equation (2.2)** as follows:

$$\alpha h\upsilon = A(h\upsilon - Eg)^n \qquad (2.2)$$

where (α) denotes the absorption coefficient, ($h\upsilon$) represents photon energy, (A and h) are constants, (Eg) is the band gap energy and (n) is a constant depends on the type of electronic transition and $n = 1/2$, in case of indirect band gap semiconductors. By plotting a graph of $(\alpha h\upsilon)$ 1/2 versus $h\upsilon$, linear region's extrapolation gives the value of band gap energy (Eg) as shown in **supplementary Fig.2.2**. The calculated band gap energy of the synthesized nanocomposite has been found to be (3.35 eV).

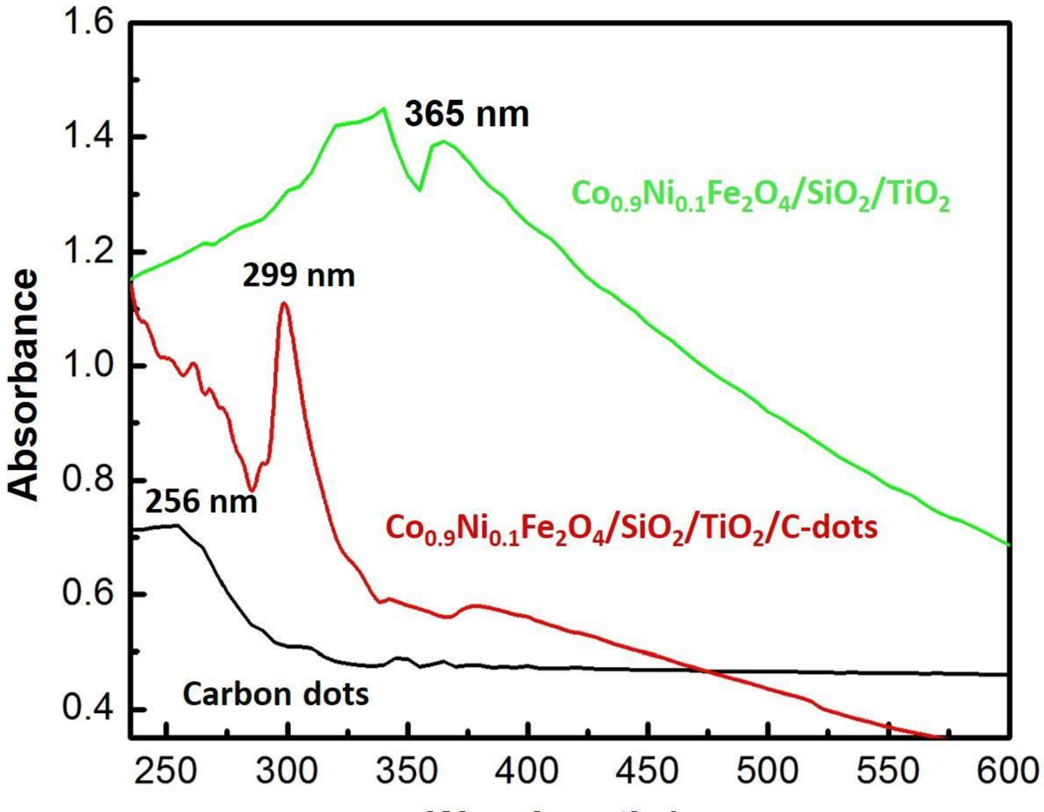

Fig. 2.3: UV-Vis. absorption spectra of the prepared $Co_xNi_{1-x}Fe_2O_4$; x=0.9 / SiO_2 / TiO_2 / C-dots nanocomposite, bare C-dots and $Co_xNi_{1-x}Fe_2O_4$; x=0.9 / SiO_2 / TiO_2 nanocomposite.

2.4.1.3 Surface area and pore size distribution analysis

N_2 adsorption-desorption isotherm and pore size distribution of the prepared nanocomposite are shown in **Fig. 2.4 (a-b)**. According to the IUPAC classification, the obtained isotherm was of type (IV), indicating the presence of mesopores. The uptake of adsorbate was increased when pores became filled, and an inflection point occurred near the completion of the first monolayer [69-71]. In addition, sharp capillary condensation was recorded at higher pressures (0.95–1), which indicated the presence of macropores [48, 72]. The calculated surface area of the prepared nanocomposite was 28.29±0.19 m^2/g and pore volume was 0.001253 cm^3/g. Finally, **Fig. 2.4 (b)** shows the pore size distribution of the prepared nanocomposite. The prepared nanocomposite possessed unimodal and narrow pore size distribution, with an intense peak at (pore diameter = 13.3 nm), confirming the presence of mesopores.

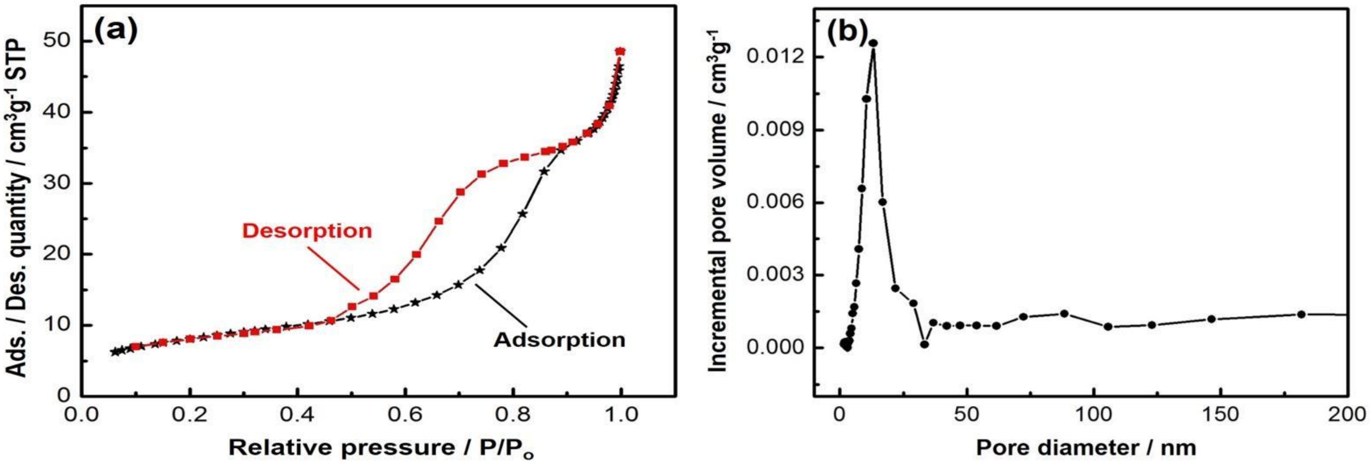

Fig. 2.4: (a) N_2 Adsorption-desorption isotherm of the prepared $Co_xNi_{1-x}Fe_2O_4$; x=0.9 / SiO_2 / TiO_2 / C-dots nanocomposite; (b) Pore size distribution.

2.4.1.4 TEM, HR-TEM analysis and average particle size calculation

A TEM image of the prepared nanocomposite is shown in **Fig. 2.5 (a)**. The primary particles were agglomerated with high interparticle void content. This structure was in good agreement with the N_2-gas adsorption-desorption isotherm shown in **Fig. 2.4 (a)**, where condensation in interparticle voids clearly-appeared at the high relative pressure region of 0.95–1. In addition, the agglomeration mainly occurred during TEM sample preparation, since the nanocomposite was well-dispersed in water solvent and no precipitation was observed for several hrs. The HR-TEM image in **Fig.2.5 (b)** shows that the average crystallite size was 19 nm. Almost all fringes observed were attributed to anatase TiO_2 NPs, which can be attributed to the high content and crystallinity of $TiO_{2,}$ as shown in **Fig. 2.6 (c)**. The selected area electron diffraction pattern in **Fig. 5 (c)** also showed only the characteristic rings of anatase TiO_2. This result was a good match to the recorded XRD pattern in **Fig. 2.2**, where anatase TiO_2 was the predominant crystal phase of the prepared nanocomposite.

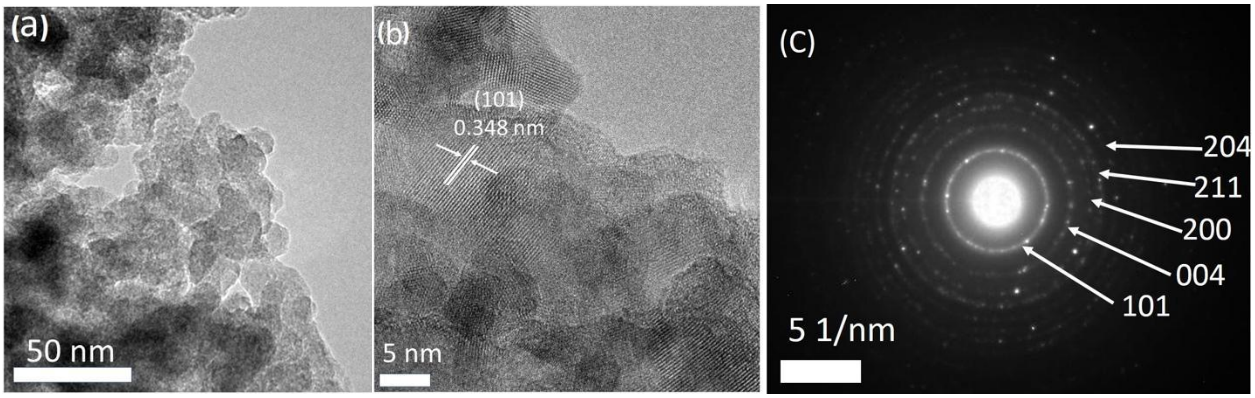

Fig. 2.5: (a) TEM image of the prepared $Co_xNi_{1-x}Fe_2O_4$; x=0.9 / SiO_2 / TiO_2 / C-dots nanocomposite; (b) HR-TEM image; (c) SAED pattern.

2.4.1.5 SEM and EDX analysis

The external morphology, purity, and the elemental composition of the prepared nanocomposite were studied, as shown in **Fig.2.6 (a-c)**. SEM analysis showed that the prepared nanocomposite had a semi-spherical structure, with a uniform distribution of each layer. EDX analysis revealed the high purity of the prepared nanocomposite, as indicated by the presence of atoms characteristic to each component of it and the absence of foreign atoms that may appear as impurity.

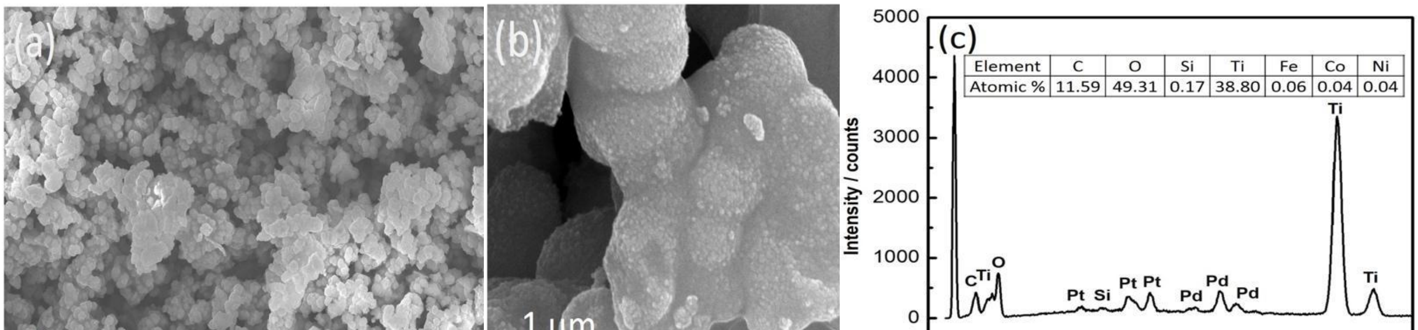

Element	C	O	Si	Ti	Fe	Co	Ni
Atomic %	11.59	49.31	0.17	38.80	0.06	0.04	0.04

Fig. 2.6: (a) SEM image of the prepared $Co_xNi_{1-x}Fe_2O_4$; x=0.9 / SiO_2 / TiO_2 / C-dots nanocomposite; (b) Magnified SEM image; (c) EDX pattern with elemental composition.

2.4.1.6 Surface bonding and functional groups analysis; FTIR analysis of the prepared nanocomposite

Inducing chemical compounds via IR wave's causes either stretching or bending of these bonds and FT-IR was used to identify the functional groups and define the molecular structure of the studied composite. The FT-IR investigation was directed to determine the interaction between $Co_xNi_{1-x}Fe_2O_4$; x=0.9 / SiO_2 / TiO_2 / nanocomposite and the synthesized C-dots **(Fig. 2.7)**. The observed bands around 455.7 cm^{-1} (in both $Co_xNi_{1-x}Fe_2O_4$; x=0.9 / SiO_2 / TiO_2 / nanocomposite and $Co_xNi_{1-x}Fe_2O_4$; x=0.9 / SiO_2 / TiO_2 / C-dots nanocomposite) were assigned to Ti–O stretching

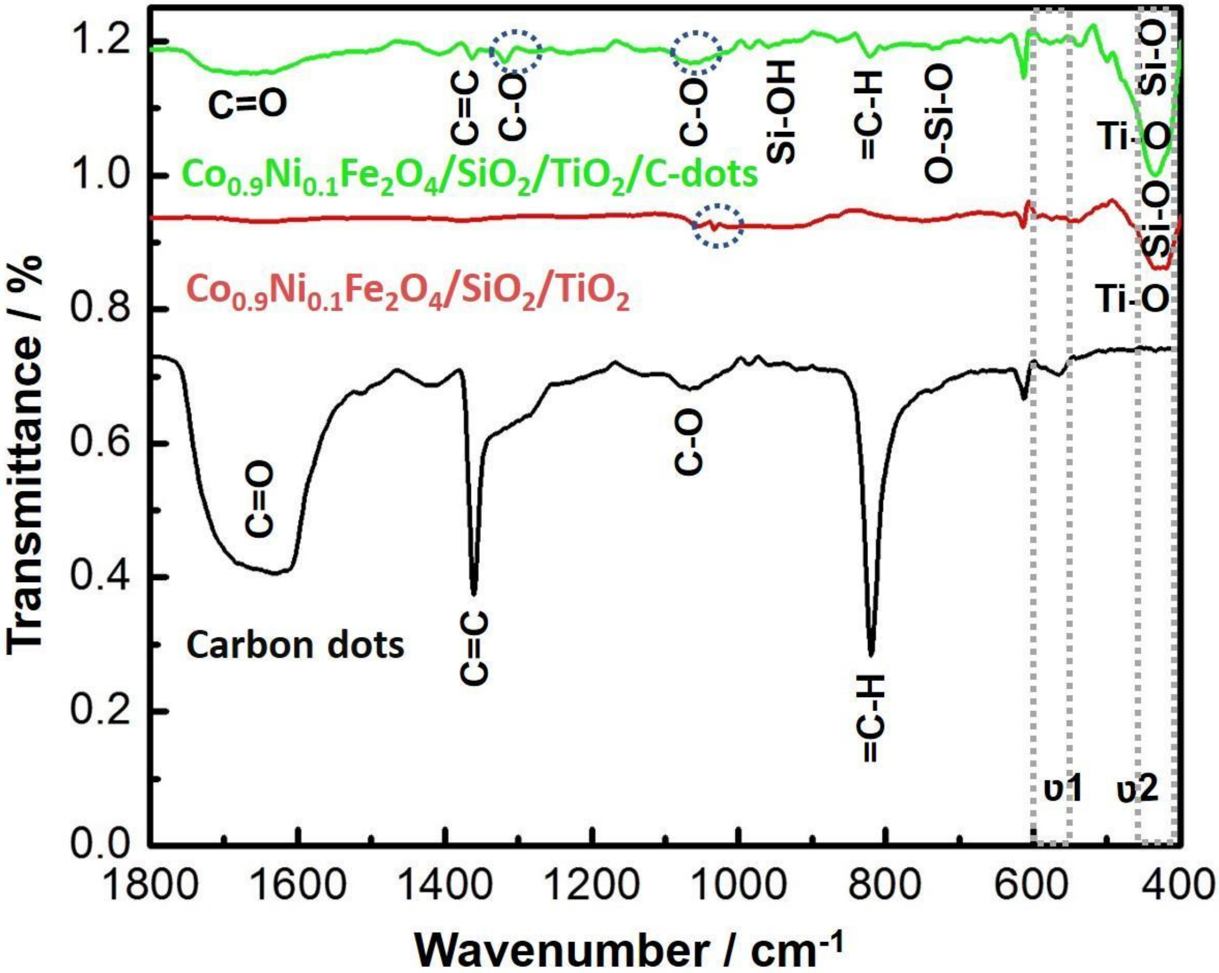

vibration [73]. The presence of free silanol (Si-OH) groups on surface was detected at 920.25 cm^{-1} [74, 75]. In addition, the symmetrical tension of O-Si-O appeared at 789.21 cm^{-1} while the bending of Si-O could be seen at 455.7 cm^{-1} [76]. It is generally known that the spinel ferrites exhibit two FTIR active bands, designated as υ_1 and υ_2. The 'υ_1' was observed at the range (550-600 cm^{-1}) and 'υ_2' was recorded at the range (350-450 cm^{-1}). These two bands refer to the stretching of metal ions and oxygen bonds in the tetrahedral and octahedral sites respectively [77]. Further, the cubic spinal phase of the present samples was successfully-formed [78-81], as shown in **Fig. 2.7**. The peaks at wave number 1155 cm^{-1} were attributed to a bond formation during the synthesis of cobalt nickel ferrite. The stretching of O–H bands can be seen around 1561 cm^{-1}. It is clear that the structure remained in the cubic spinel phase even after the substitution of metals on ferrite nanostructures. It should be noted that, in the FTIR spectrum of the synthesized C-dots, the stretching vibration band of C=O was observed at 1633.3 cm^{-1} (C-dots) and at 1675.0 cm^{-1} ($Co_xNi_{1-x}Fe_2O_4$; x=0.9 / SiO_2 / TiO_2 / C-dots nanocomposite), and the stretching vibration bands of C−O was detected at 1099 cm^{-1} (C-dots) and at 1089.2 cm^{-1} ($Co_xNi_{1-x}Fe_2O_4$; x=0.9 / SiO_2 / TiO_2 / C-dots nanocomposite) [82]. Moreover, the obvious two sharp peaks, at 1359 cm^{-1} (C-dots), 1362 cm^{-1} ($Co_xNi_{1-x}Fe_2O_4$; x=0.9 / SiO_2 / TiO_2 / C-dots nanocomposite) and 818.2 cm^{-1} (C-dots), 824.12 cm^{-1} ($Co_xNi_{1-x}Fe_2O_4$; x=0.9 / SiO_2 / TiO_2 / C-dots nanocomposite),were associated with the stretching and bending vibrations of C=C, and =C-H respectively, suggesting the presence of alkyl groups [83]. Finally, one distinct peak, located at 1319.7 cm^{-1} in $Co_xNi_{1-x}Fe_2O_4$; x=0.9 / SiO_2 / TiO_2 / C-dots nanocomposite, was not detected in C-dots spectrum. It may have corresponded to the C-O functional group, which suggested the conjugation of C atom with O atoms (from SiO_2 and/or TiO_2; inner and outer nanocomposite layers) by a covalent bond. This C-O stretching vibration represented the conjugation of C-dots on the surface of the synthesized $Co_xNi_{1-x}Fe_2O_4$; x=0.9 / SiO_2 / TiO_2 nanocomposite [84, 85]. Our FTIR results were similar to some recently-published research studies [86-89].

Fig. 2.7: FTIR analysis of the $Co_xNi_{1-x}Fe_2O_4$; x=0.9 / SiO_2 / TiO_2 / C-dots nanocomposite, bare C-dots and $Co_xNi_{1-x}Fe_2O_4$; x=0.9 / SiO_2 / TiO_2 nanocomposite.

2.4.2 Photocatalytic Activity of $Co_xNi_{1-x}Fe_2O_4$; x=0.9 / SiO_2 / TiO_2 / C-dots nanocomposite

The photocatalytic activity of the synthesized C-dots-loaded nanocomposite was evaluated via the photocatalytic degradation of an aqueous solution of chloramine-T trihydrate under UV-light irradiation. Upon increasing the UV-irradiation period, the strong absorption bands of chloramine-T recorded at 225 nm (the maximum absorbance wavelength (λ_{max}) for the chloramine-T), reduced continuously, and the removal of chloramine-T solution reached about 80 % after 90 min of UV-light irradiation, as shown in **Fig. 2.8**.

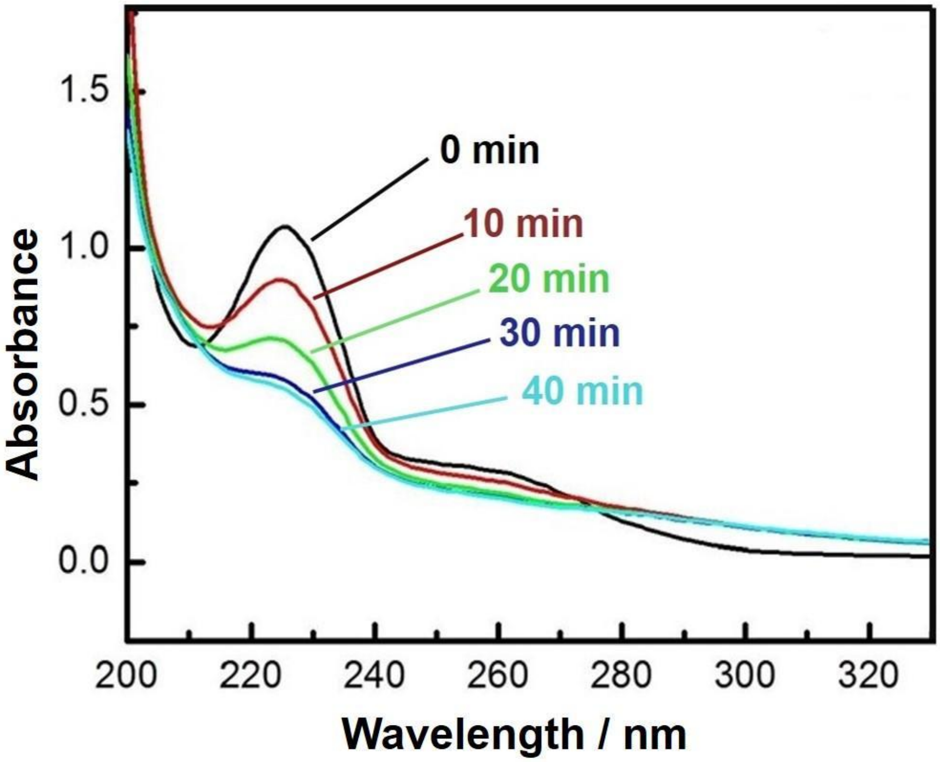

Fig. 2.8: UV-Vis. spectra of chloramine-T solution after photodegradationtest for 0-40 min (10 mg of nanocomposite, 50 ml chloramine-T solution, Temp. = 25 °C and pH = 7).

2.4.2.1 Effect of chloramine-T initial concentration on the degradation efficiency

Degradation efficiency with an irradiation time of chloramine-T via 10 mg of the prepared nanocomposite in (50 ml) chloramine-T solution of initial concentrations (10, 20 and 30 mg/L) is illustrated in **Fig. 2.9**. The color of the solution turned from a turbid white to nearly transparent at the end of the decomposition experiment, with approximately 80 % removal after 90 min. Our results showed that the degradation efficiency of chloramine-T is inversely-proportional to its initial concentration. The decomposed percentage of chloramine-T was measured by using C_t/C_o x 100, where C_t and C_o are the remaining and initial concentrations of chloramine-T, respectively.

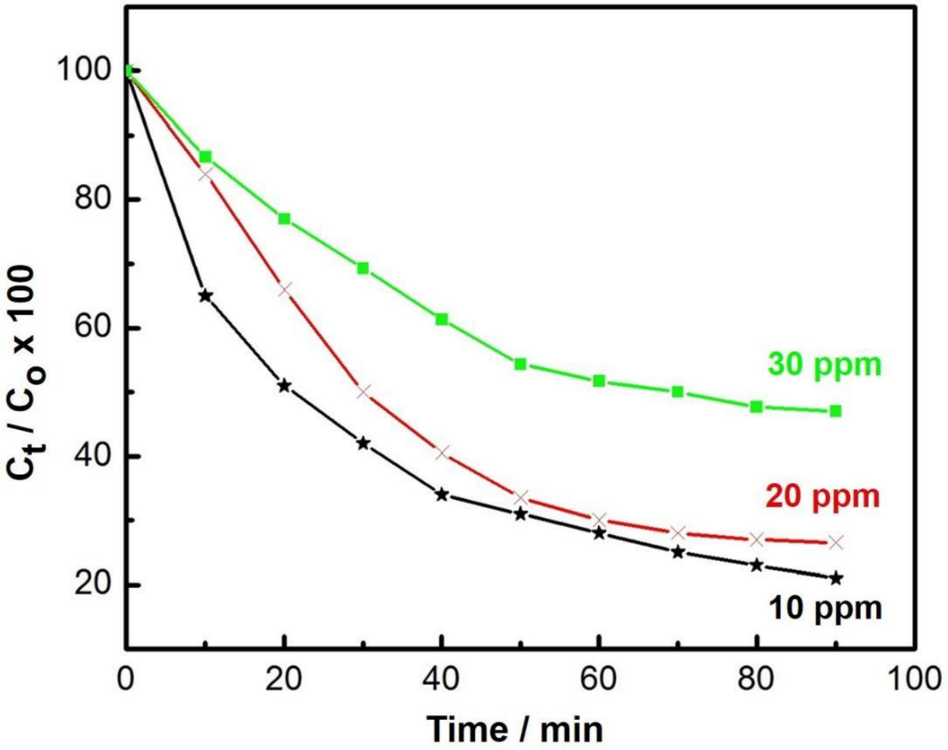

Fig. 2.9: Effect of initial concentration of chloramine-T on the degradation efficiency (10 mg of nanocomposite, 50 ml chloramine-T solution, Temp. = 25 °C and pH = 7).

2.4.2.2 Effect of the nanocompositedose on degradation efficiency

The influence of a nanocomposite dose on the photodegradation of chloramine-T under UV-light was studied by varying the amount of the prepared photocatalyst between 5 mg and 20 mg against a fixed concentration of chloramine-T (20 mg/L), as shown in **Fig. 2.10**. The results showed that by increasing the amount of the employed photocatalyst from (5 to 20 mg), a decrease in the value of C_t/C_o x 100 was observed from 40 to 20, respectively. The results also indicated an increase in the degradation efficiency upon increasing the photocatalyst dose from (5 to 20 mg). The observed increase in degradation efficiency with increasing the amount of the photocatalyst in the reaction could be attributed to the increase in the available active area or active sites of the photocatalyst to volume ratio of chloramine-T solution [90, 91].

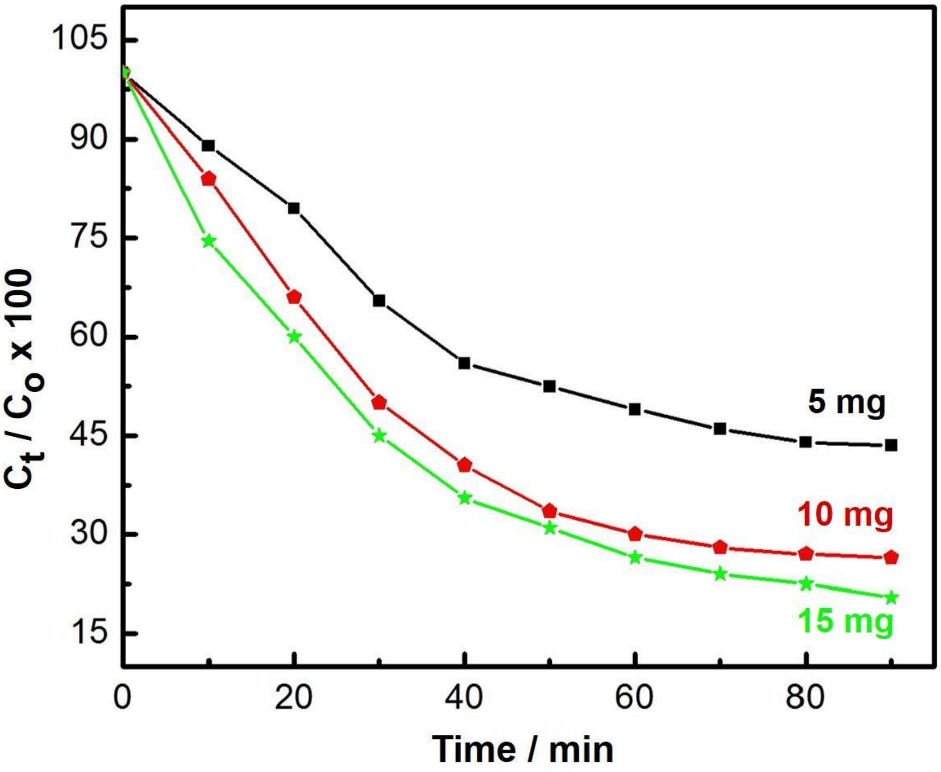

Fig. 2.10: Effect of the photocatalyst dose on the degreadation efficency of chloramine-T (50 ml chloramine-T solution (20 mgL^{-1}), Temp. = 25 °C and pH = 7).

While **Fig. 2.11** shows a plot of 1/$[C]_t$ against time, which gives a straight-line with intercept equal to 1/$[C]_0$ and slope *k*. According to the values of $R^2 > 99.5$, the reactions of chloramine-T degradation with the prepared nanocomposite followed pseudo second-order reaction kinetics. Moreover, as indicated in **Fig. 2.12**, there is a clear inverse dependenceof the apparent pseudo second-order rate constant on the initial concentration of chloramine-T.

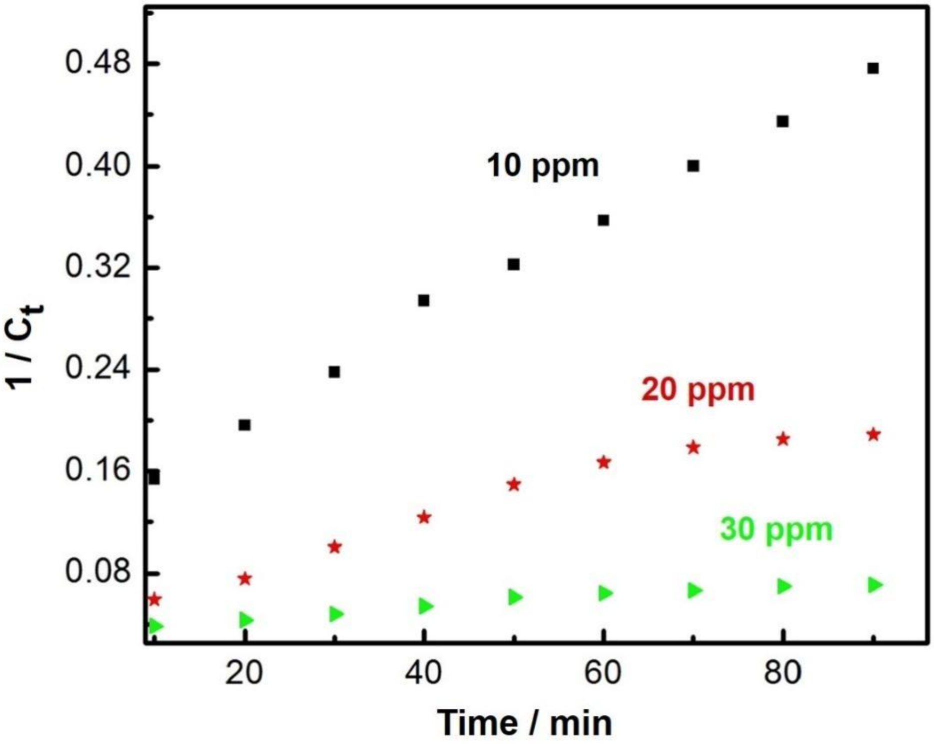

Fig. 2.11: Pseudo second order kinetics of chloramine-T degradation (10 mg of nanocomposite, 50 ml chloramine-T solution, Temp = 25 °C and pH = 7).

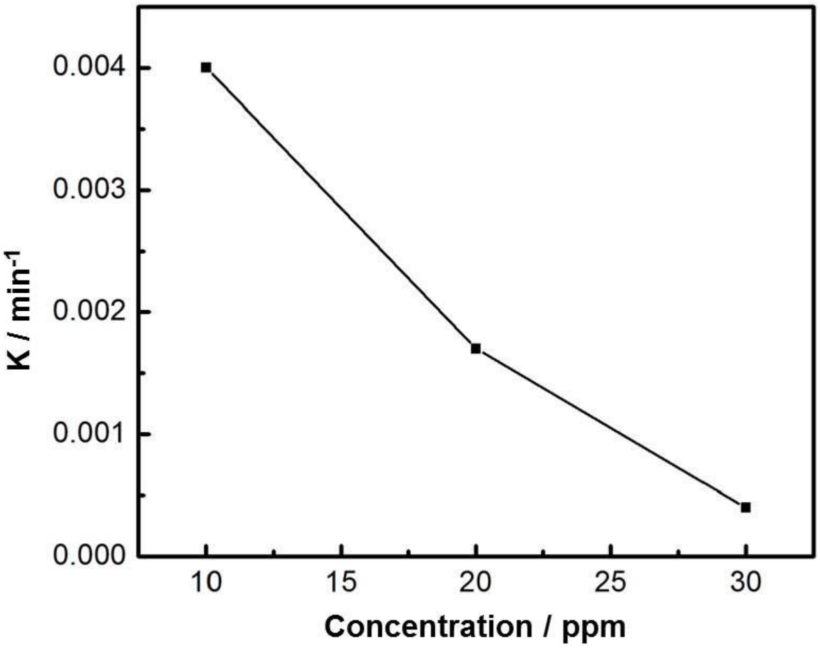

Fig. 2.12: Apparent pseudo second order rate constant vs initial concentration of chloramine-T.

2.4.2.3 Effect of pH value on the photodegradation of chloramine-T

In this part, the role of reaction pH on the photocatalytic degradation of chloramine-T was studied in the pH range from (5 to 9) at room temperature (25ºC ± 2ºC). The initial pH of the chloramine-T solution was set before UV-irradiation and it was not changed during the experiments. The influence of the initial pH on the photodegradation of chloramine-T under UV-irradiation was investigated, and the results are shown in **Fig. 2.13**.

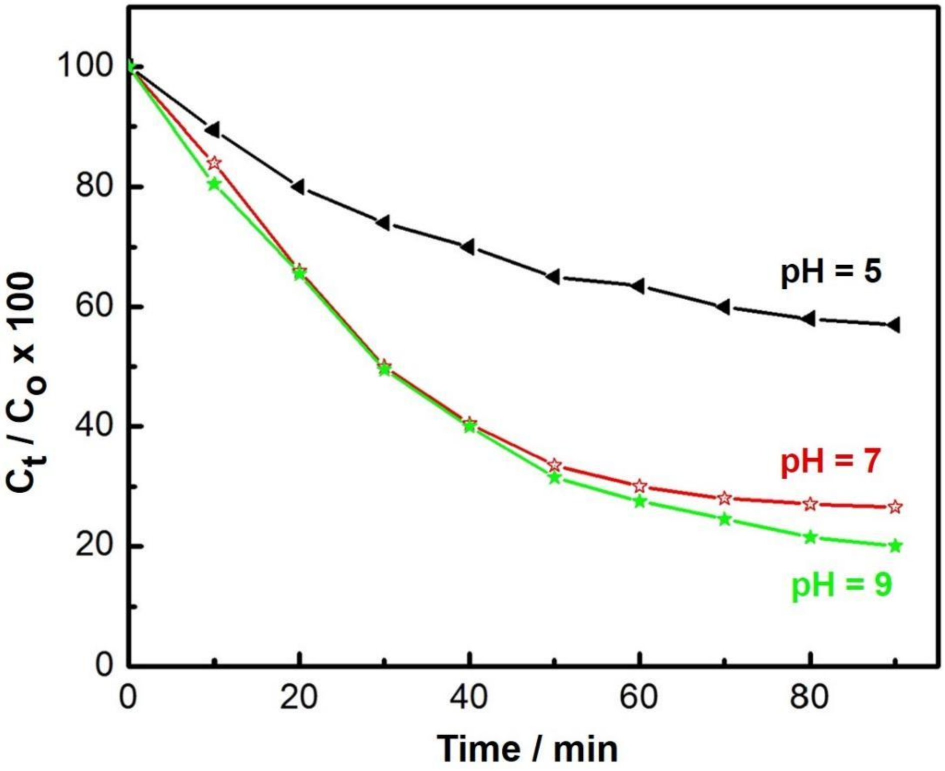

Fig. 2.13: Effect of pH on the degradation of chloramine-T (10 mg nanocomposite, 50 ml chloramine-T (20 mgL^{-1}) and 100 min UV-irradiation).

The photodegradation of chloramine-T was enhanced by increasing the pH. It is well known that, the photocatalytic degradation of chloramine-T is a complicated process, which started with the adsorption on the nanocomposite surface [92]. The photocatalytic performance of the prepared nanocomposite could be attributed to the surface electrical properties, due to the different interlayer anions. The superior surface potential of the nanocomposite facilitated chloramine-T adsorption, which is helpful in promoting the transfer of light-generated charge carriers to the photocatalyst surface [93].

The initial pH of the solution is one of the most remarkable parameters controlling the photocatalytic process and can affect the surface charge nature of the photocatalyst and the extent of agglomeration and its stability [47, 93, 94]. Moreover, pH manipulates a significant role in the reaction mechanisms that can lead to chloramine-T degradation. The photodegradation mechanisms affected by varying the pH values include hydroxyl radical attack, explicit oxidation by the positive holes in the valence band, and explicit reduction by the electrons in the conduction band. In the presence of a photocatalyst, it is assumed that photocatalytic degradation is likely to happen due to the formation of electron-hole pairs on the exterior of the employed photocatalyst, due to UV-irradiation. Oxidative potential of holes either reacts with the–OH groups to form hydroxyl radicals or oxidizes the reactive chloramine-T to form a degradation product [95]. The reactions of chloramine-T and the employed photocatalyst can be summarized as follows **(equations, 2.3- 2.6)**.

$$C - dots\ loaded\ composite + h\upsilon \rightarrow nanocomposite\left(e^{-}_{CB} + h^{+}_{VB}\right) \quad (2.3)$$

$$h^{+}_{VB} + Chloramine - T \rightarrow Chloramine - T^{\bullet +}\ (Oxidation\ of\ the\ compound) \quad (2.4)$$

Or

$$h^{+}_{VB} + OH^{-} \rightarrow OH^{\bullet} \quad (2.5)$$

$$OH^{\bullet} + chloramine - T \rightarrow (Degredation\ product) \quad (2.6)$$

Interestingly, the concentration of $OH^{\bullet}$ radicals is relatively-higher at higher pH values (alkaline medium), and this may also be another reason for the increase in photodegradation of strong alkaline media. In addition, the high pH value (in alkaline media) is beneficial to the formation of

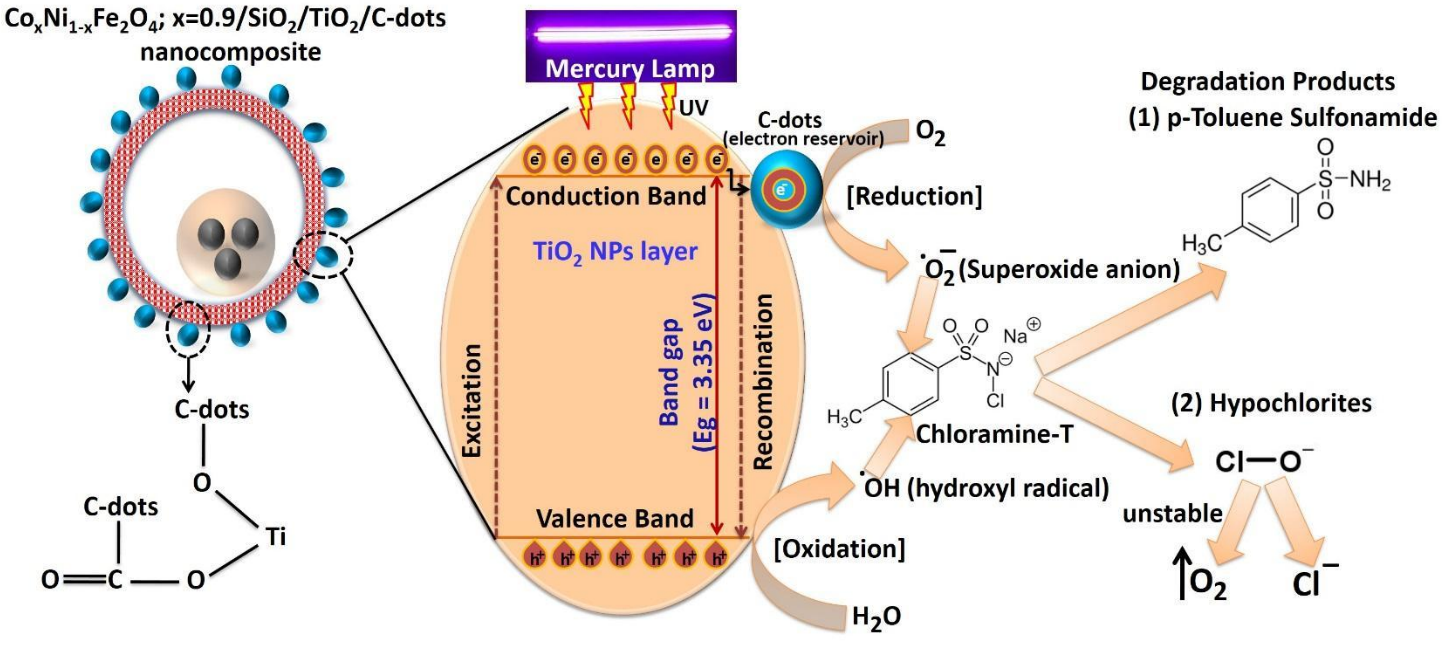

$OH^{\bullet}$ radicals during the reaction between dissolved oxygen and excited state electrons, which makes the degradation of chloramine-T noteworthy [96], while, at low pH values, a decrease in photodegradation efficiency is noticed that may be attributed to the instability of the prepared nanocomposite through a cathodic dislocation of the valence band position, which gives rise to a weakening of the oxidation capability of the holes. In conclusion, the initial reaction pH has an influence on the surface charge of the catalyst and the adsorption characteristics of ions [47, 95].

The proposed mechanism of interaction between the prepared nanocomposite and chloramine-T is shown in **Fig. 2.14**. Upon UV-light excitation of TiO_2 layer, charge carriers will be photogenerated and redox reactions will be initiated. Then, the generated free radicals (such as $OH^{\cdot}$ And $O2^{-2}$) will degrade chloramine-T into two potential products, p-touluene sulfonamide and hypochlorites that can be easily dissociated into O_2 and Cl^- ions. Since, there are no published reports about the degradation of chloramine-T till the moment, more investigations via high-performance liquid chromatography (HPLC) and gas chromatography-mass spectrometry (GC-MS) are required to analyze with more details the degradation products of chloramine-T.

Fig. 2.14: Proposed mechanism of photocatalytic degradation of chloramine-T with the prepared nanocomposite.

2.4.3 In vitro antimicrobial activity of the synthesized $Co_xNi_{1-x}Fe_2O_4$; x=0.9 / SiO_2 / TiO_2 / C-dots nanocomposite

Agar diffusion technique was used to test the antimicrobial potential of the prepared nanocomposite (screening procedure). C-dots loaded nanocomposite (15 µg/ml) showed comparatively-higher antimicrobial potential against all examined bacteria and *Candida species compared with C-dots*. Screening data verified that the fabricated nanocomposite possessed predominant antibacterial efficacy against *E. coli* (36 mm ZOI, **Fig. 2.15 (a),** *P. aeruginosa* (33 mm ZOI) and *B. cereus* (24 mm ZOI, **Fig. 2. 15 (b)** as seen in **Table 2.1**. Interestingly, the synthesized C-dots loaded nanocomposite exhibited more effective antimicrobial capacities than bare C-dots and other conventional antimicrobial agents (AMC). Our previously-prepared $Co_xNi_{1-x}Fe_2O_4$ x=0.9 /SiO_2/TiO_2; nanocomposite [47] exhibited antibacterial action of (16 mm, ZOI) against *E. coli* and an antifungal potential against *C. albicans* of (10 mm, ZOI). Interestingly, by making a comparison, we observed an enhanced antibacterial activity of C-dots loaded nanocomposite (**Fig. 2.15 – Table 2.1**) suggesting the possibilityof synergistic potential between $Co_xNi_{1-x}Fe_2O_4$/SiO_2/TiO_2; x=0.9

nanocomposite and C-dots. It was also noted that the prepared nanocomposites were more effective against Gram-negative than Gram-positive bacteria. One possible cause is in how the bacterial cell walls are constructed, as cell walls of Gram-negative species consist primarily of films (thin layers) of peptidoglycans, lipopolysaccharides, and lipids, while, cell walls of Gram-positive species have thick arrangements of peptidoglycans [97]. The prepared C-dots loaded nanocomposite can be used as a powerful antifungal agent, as it possesses an extraordinary antifungal potency against *C. tropicalis* (35 mm ZOI, Fig. 15 c) and *C. albicans* (28 mm ZOI) as presented in **Table 2.1.** The MIC values of bare C-dots and C-dots loaded nanocomposite against all tested pathogenic bacteria and *Candida* sp. were in the range of 6.25 to 0.024µg/ml, as shown in Table 1. The synthesized nanocomposite possessed MIC values of about 0.024µg/ml against *E. coli, 0.097*µg/ml *against C. tropicalis, and 0.390*µg/ml against *B. cereus*. Surprisingly, by comparing these results with those in our previously-published paper [47], the synthesized $Co_xNi_{1-x}Fe_2O_4$; x=0.9 /SiO_2/TiO_2 nanocomposite possessed MIC values of (3.12µg/ml) against *E. coli* and (12.5 µg/ml) against *C. albicans*. However, the newly-prepared C-dots loaded nanocomposite showed more promising MIC results, of about (0.024 µg/ml against *E. coli*) and (0.781 µg/ml ZOI against *C. albicans*), suggesting it had good antimicrobial abilities at very low concentrations.

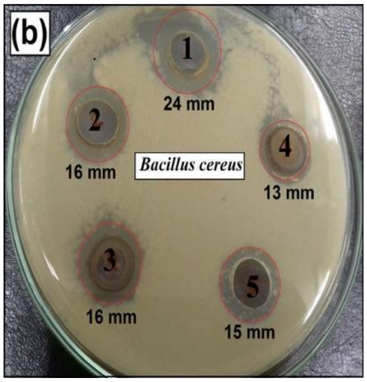

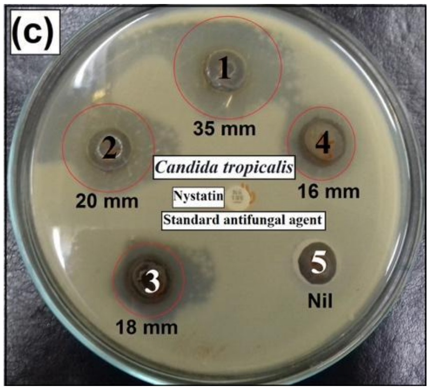

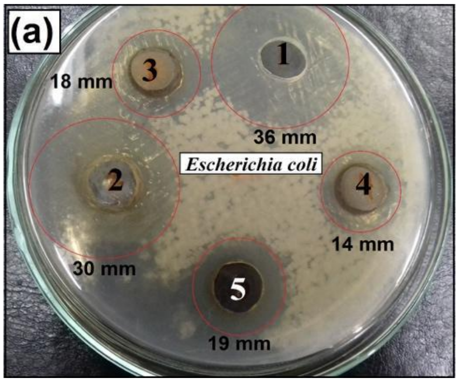

Fig. 2.15: Antibacterial and antifungal activities of bare C-dots and $Co_xNi_{1-x}Fe_2O_4$; x=0.9 / SiO_2 / TiO_2 / C-dots nanocomposite on: (a) *Escherichia coli*, (b) *Bacillus cereus* and (c) *Candida tropicalis* measured as ZOI (mm). 1= $Co_xNi_{1-x}Fe_2O_4$; x=0.9 / SiO_2 / TiO_2 / C-dots nanocomposite (15 µg/ml), 2= $Co_xNi_{1-x}Fe_2O_4$; x=0.9 / SiO_2 / TiO_2 / C-dots nanocomposite (10 µg/ml), 3= bare C-dots (15 µg/ml), 4= bare C-dots (10 µg/ml) and 5= Amoxicillin/Clavulanic Acid (100 µg/ml, standard antibacterial agent).

Pathogenic microbes	**ZOI of bare c-dots (10 µg/ml) (mm)**	**ZOI of bare c-dots (15 µg/ml) (mm)**	**MIC of bare c-dots (µg/ml)**	**ZOI of CoxNi$_{1-x}$Fe$_2$O$_4$; x=0.9 / SiO$_2$ / TiO$_2$ / C-dots (10µg/ml) (mm)**	**ZOI of CoxNi$_{1-x}$Fe$_2$O$_4$; x=0.9 / SiO$_2$ / TiO$_2$ / C-dots (15 µg/ml) (mm)**	**MIC of CoxNi$_{1-x}$Fe$_2$O$_4$; x=0.9 / SiO$_2$ / TiO$_2$ / C-dots (µg/ml)**	**▪ AMC or NS**
Escherichia coli	$14^{d}\pm0.2516$	$18^{d}\pm0.2516$	1.562	$30^{e}\pm0.1000$	$36^{g}\pm0.2516$	0.024	$19^{c}\pm0.2516$
Pseudomonas aeruginosa	$13^{c}\pm0.2081$	$14^{b}\pm0.1154$	1.562	$21^{d}\pm0.3000$	$33^{e}\pm0.4725$	0.195	$10^{a}\pm0.1527$
Staphylococcus aureus; MRSA	$9^{a}\pm0.4041$	$10^{a}\pm0.5291$	12.5	$11^{a}\pm0.2309$	$12^{a}\pm0.4725$	6.25	Nil
Bacillus cereus	$13^{c}\pm0.4509$	$16^{c}\pm0.1000$	0.751	$16^{b}\pm0.4506$	$24^{c}\pm0.1154$	0.390	$15^{b}\pm0.3214$
Klebsiella pneumoniae	$9^{a}\pm0.4509$	$10^{a}\pm0.2516$	6.25	$16^{b}\pm0.4041$	$18^{b}\pm0.1154$	3.125	Nil
Candida albicans	$12^{b}\pm0.4041$	$16^{c}\pm0.2516$	3.125	$16^{b}\pm0.1732$	$25^{d}\pm0.2000$	0.781	Nil
Candida tropicalis	$16^{e}\pm0.3214$	$18^{e}\pm0.2516$	0.781	$20^{c}\pm0.3000$	$35^{f}\pm0.3055$	0.097	Nil
LSD	0.76667	1.50000	-------	4.03333	0.96667	-----	-----

Table 2.1: Antibacterial and antifungal activities of bare C-dots and $Co_xNi_{1-x}Fe_2O_4$; x=0.9/ SiO_2/TiO_2/C-dots nanocomposite, against multi-drug resistant (MDR) bacteria and pathogenic *Candida species*, measured as ZOI (mm) and MIC (µg/ml).

Values are presented as means ± SD (n = 3). Data within the groups were analyzed using one-way analysis of variance(ANOVA) followed by $^{a, b, c, d, e, f, g}$ *Duncan's multiple range test (DMRT), LSD= Least Significant Difference.*

- ● Nil means that no ZOI was measured.
- ▪ AMC = Amoxicillin/Clavulanic Acid (standardantibacterial agent).
- ▪ NS = Nystatin (standardantifungal agent).

Interestingly, there is a correlation between the physical characteristics (surface area) of the prepared nanocomposite and its recorded antimicrobial capabilities. The measured surface area of the C-dots loaded nanocomposite was (28.29 ± 0.19 m^2/g) with a unimodal and narrow pore size distribution, with an average pore diameter of (13.3 nm) and an average pore volume of (0.001253 cm^3/g). The prepared nanocomposite possessed two classes of pores in its outer shell (TiO_2 NPs), mesoporous and macropores [98]. This surface area and pore size distribution expanded its connection areas (active sites) to absorb more microbial cells (diameter of *E. coli* is 0.25µm). These physical features were significant in enhancing its antimicrobial potency at a low concentration (0.024µg/ml) against all tested pathogenic bacteria and *Candida* species.

2.4.4 Effect of UV-irradiation on the antimicrobial potential of $Co_xNi_{1-x}Fe_2O_4$; x=0.9/SiO_2/TiO_2/C-dots *nanocomposite in liquid media*

Comparative study of the repression percentage of *E. coli*, *B. cereus*, and *C. tropicalis* by non-irradiated and UV-irradiated nanocomposite was conducted and is shown in **Fig. 2.16.** The restraint percentage of the examined pathogens due to nanocomposite treatment decreased as a function of time, suggesting that it maintained effective antimicrobial capabilities against the colonies of *E. coli*, *B. cereus*, and *C. tropicalis*. as shown in **Fig. 2. 16 (a-c)**, Interestingly, the UV-irradiated nanocomposite showed higher antimicrobial potential compared with the non-irradiated, as shown in **Fig. 2.16**. The highest recorded hindrance percentages of non-irradiated and UV-irradiated nanocomposites against *E. coli* were 34.12 % and 80.47 %, respectively. Inhibition percentages were 22.56 % and 49.54 % for *B. cereus* and 50.45 % and 78.54 % for *C. tropicalis* after 60 min of UV-irradiation (practice time) as shown by non-irradiated and UV-irradiated nanocomposites, respectively. The effect of UV-irradiation on the nanocomposite can be explained by the photo-created reactive oxygen species (ROS), which can disintegrate bacterial cells. The observed antimicrobial capabilities were also due to the effective UV-absorption by the synthesized nanocomposite. OH radicals can be also produced by irradiating the nanocomposite with UV. Due to the electron shift within the microbial cells and the nanocomposite, OH radicals can damage bacterial cells by reducing co-enzyme contents [99]. In addition, metal oxides (MOs), like TiO_2 (the composite's external layer), possess positive charges in slightly-acidic media, while microbes have negative charges. This creates an electromagnetic attraction between microbes and MOs, resulting in microbial cell oxidization and consequent damage [100]. Moreover, nanomaterials can damage cellular proteins and DNA by binding with electron-donating constructions such as thiols, carbohydrates, indoles, hydroxyls, and amides. Additionally, they can induce cracks in the cell walls of bacteria, causing extensive permeability and cell death [101]. We previously-reported that our $Co_xNi_{1-x}Fe_2O_4$; x=0.9 /SiO_2/TiO_2 nanocomposite had a negative charge in neutral media, but tested microbes media is slightly-acidic (pH = 6), which can change the outside charge of the nanocomposite to positive, which is in a good agreement with our recorded results.

Further, our previous $Co_xNi_{1-x}Fe_2O_4$; x=0.9/ SiO_2/ TiO_2 nanocomposite [47] displayed an inhibition % against *E. coli* of about 70.45 % after UV-activation, while the newly-synthesized $Co_xNi_{1-x}Fe_2O_4$; x=0.9/SiO_2/TiO_2/ C-dots nanocomposite showed an inhibition % of 80.47% **(Fig. 2.16 (a)**. In addition, its repression to *Candida* species reached (78.54%; **Fig. 2.16 (c)** compared with only 50.85 % for the previous $Co_xNi_{1-x}Fe_2O_4$; x=0.9/SiO_2/TiO_2 nanocomposite [47].

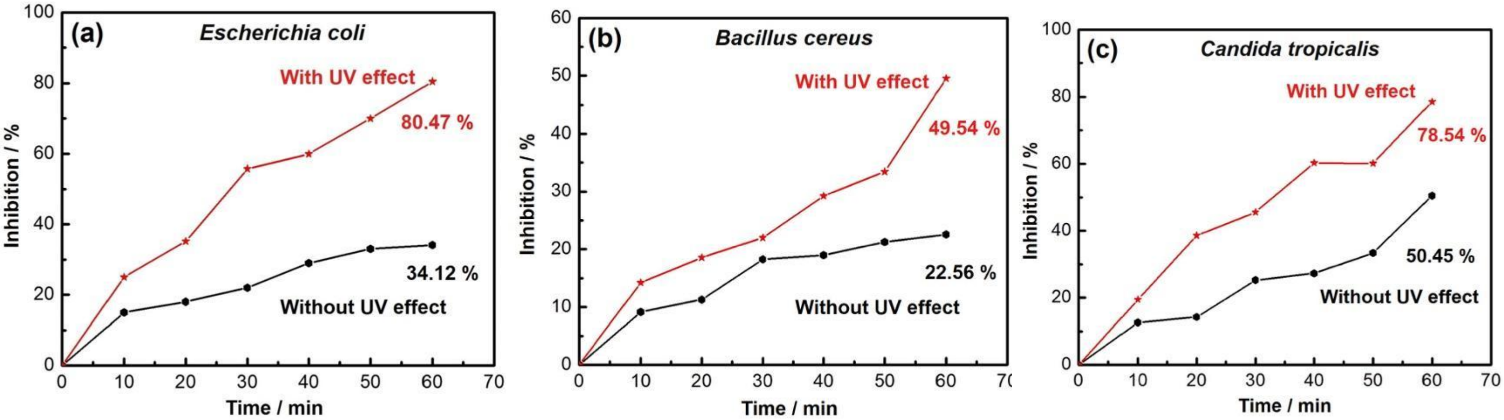

Fig. 2.16: Antimicrobial abilities of UV-irradiated $Co_xNi_{1-x}Fe_2O_4$; x=0.9/SiO_2/TiO_2/C-dots nanocomposite against different pathogenic microbes: (a) *Escherichia coli*, (b) *Bacillus cereus* and (c) *Candida tropicalis.*

2.4.5 Antibiofilm potential of $Co_xNi_{1-x}Fe_2O_4$; x=0.9/SiO_2/TiO_2/C-dots nanocomposite

Biofilm formation is popular in various exopolysaccharide-producing pathogenic microorganisms [59, 102]. Biofilms are formed by the tested pathogenic bacteria and yeast with and without nanocomposite treatment was evaluated by using test tubes process [103]. **Fig. 2. 17 (a)** displays the antibiofilm ability of the prepared nanocomposite against *E. coli*. *E. coli* grew without our nanocomposite and shows a clear whitish-yellow matt in the air-liquid interface of the tubes. This matt was completely-connected to the inner wall of the tubes and resembled ablue circle after CV staining. A blue solution was also formed after dissolving the CV-stained circle by absolute ethanol, as shown in **Fig. 2.17 (a)**.

On the other hand, the restriction of bacterial rings growth was observed in *E. coli* inoculated with tested nanocomposite (15 µg/ml), and the blue color corresponding to CV-stained bacterial cells was faint, as shownin **Fig. 2.16 (a)**. Similar results were observed for *B. cereus* and *C. trobicalis* biofilm suppression (pathogenic yeast), as shown in **Figs. 2.17 (b) - 2.17 (c)** respectively.

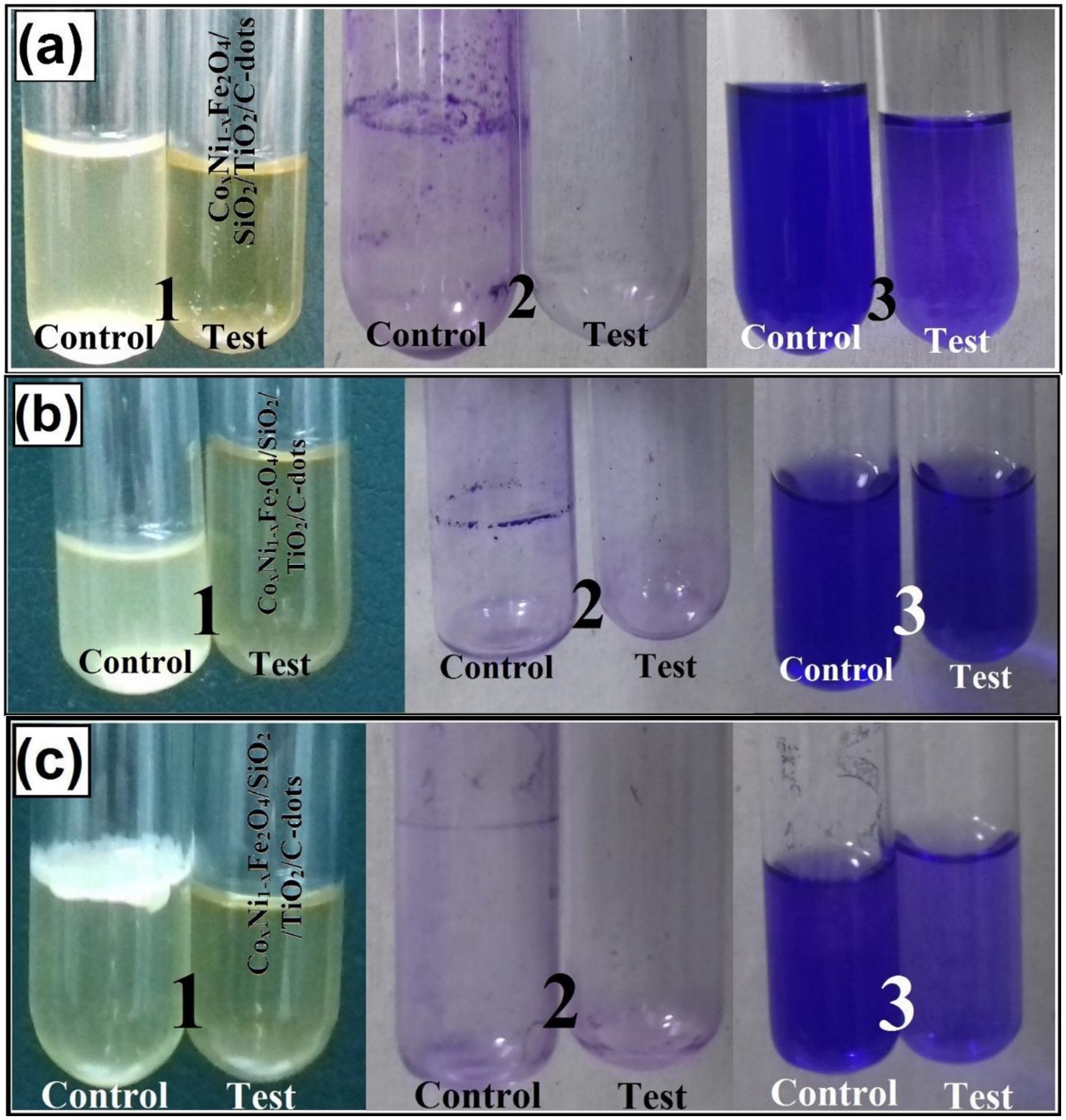

Fig. 2.17: Antibiofilm activity of $Co_xNi_{1-x}Fe_2O_4$; x=0.9/SiO_2/TiO_2/ C-dots nanocomposite (15 µg/ml) using tube method against (a) *Escherichia coli,* (b) *B. cereus* and (c) *C. tropicalis*, showing (1) Growth of the bacterial and yeast cells and biofilm formation (rings) without nanocomposite treatment and the inhibition of bacterial and yeast growth after treatment, (2) Staining of the adherent bacterial and yeast cells with crystal violet and (3) Removal and dissolution of the adherent bacterial and yeast cells inethanol for semi-quantitative biofilm inhibition determination (as shown in table 2).

Bacterial and yeast strains	O.D. of crystal violet stain at 570nm (Control)	O.D. of crystal violet stain at 570 nm (Treated with $Co_xNi_{1-x}Fe_2O_4$; x=0.9 / SiO_2 / TiO_2 / C-dots nanocomposite)	Inhibition %
Escherichia coli	$3.981^{g}\pm0.0206$	$0.242^{a}\pm0.0216$	93.92%
Pseudomonas aeruginosa	$1.254^{b}\pm0.0096$	$0.615^{c}\pm0.0035$	50.35%
Staphylococcus aureus; MRSA	$1.060^{a}\pm0.0055$	$0.564^{b}\pm0.0020$	48.49%
Bacillus cereus	$1.735^{c}\pm0.0291$	$0.606^{c}\pm0.0025$	65.07%
Klebsiella pneumoniae	$2.170^{d}\pm0.0026$	$1.025^{e}\pm0.0020$	52.76%
Candida albicans	$2.225^{e}\pm0.0343$	$0.750^{d}\pm0.0049$	66.29%
Candida tropicalis	$2.904^{f}\pm0.0475$	$0.222^{a}\pm0.0049$	92.35%
LSD	0.07633	0.04300	------------

Table 2.2: Semi-quantitative inhibition of the biofilm formation by non-treated and nanocomposite-treated bacterial and yeast pathogens.

Values are presented as means ± SD (n = 3). Data within the groups were analyzed using one-way analysis of variance (ANOVA) followed by $^{a, b, c, d, e, f, g}$ *Duncan's multiple range test (DMRT), LSD= Least Significant Difference.*

To determine the restraint percentage of bacterial and yeast biofilm, a UV-Vis. spectrophotometer was used (at 570 nm). The optical density (O.D.) was measured after separating the CV-stained bacterial and yeast biofilms through ethanol. **Table 2.2** presents the reduction percentage of the biofilms created by the examined bacteria and yeast strains. The highest suppression percentage was recorded against *E. coli* (93.92%, **Fig. 2. 17 (a)**, followed by *C. trobicalis* (92.35%, **Fig. 2.17 (c)** and *C. albicans* (66.29%, **Table 2.2**) after inoculation with (10 µg/ml) of the prepared nanocomposite.

In addition, the newly-synthesized $Co_xNi_{1-x}Fe_2O_4$; x=0.9/SiO_2/TiO_2/C-dots nanocomposite was more active against biofilm creation than the previously-synthesized $Co_xNi_{1-x}Fe_2O_4$; x=0.9 /SiO_2/TiO_2

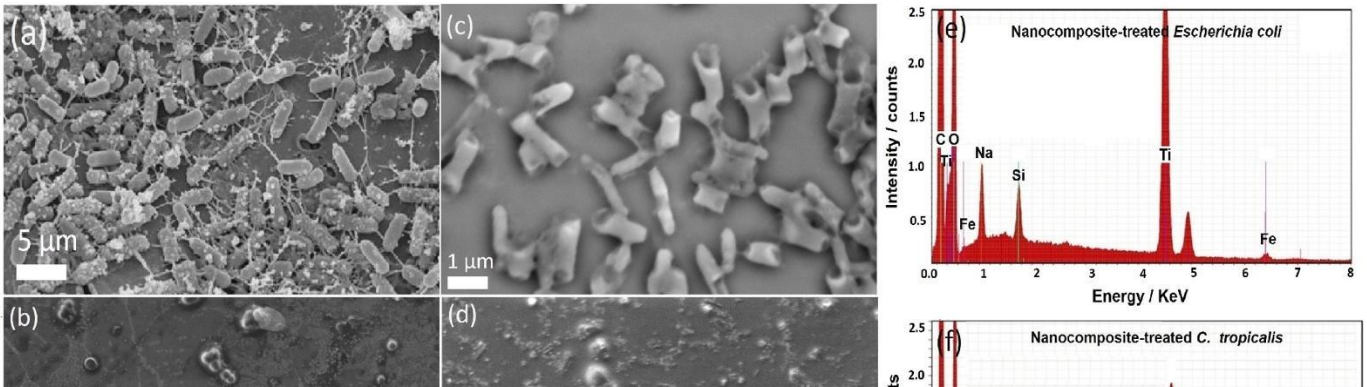

nanocomposite [47]. It exhibited an inhibition against biofilm-producing *E. coli* of (93.92%, **Table 2.2**), compared with (92.82 %) for the $Co_xNi_{1-x}Fe_2O_4$; x=0.9/SiO_2/TiO_2 nanocomposite. Moreover, it inhibited biofilm production by *C. trobicalis* (92.35 %, **Table 2.2**) compared with only (77.84 %) by the $Co_xNi_{1-x}Fe_2O_4$; x=0.9/ SiO_2 / TiO_2 nanocomposite. The prepared nanocomposite was used to control the biofilm growth at its adhesion level (known as the initial level) [104]. The change in the inhibitory percentage can be assigned to different factors such as antimicrobial potential, biosorption (due to the large exterior surface area of the nanocomposite), physical properties (size of particles and porosity), attack abilities, and many chemical characteristics managing the interaction of the synthesized nanocomposite and biofilms [103, 105]. It was also observed that the prepared nanocomposite significantly-repressed *E. coli* by more than 98 % with 0.024 µg/ml (MIC, **Table 2.1**). When the exopolysaccharide construction is inhibited (the essential fragments for biofilm expansion), *E .coli* cannot create its biofilm [59, 103]. To clarify the antibiofilm capabilities of the nanocomposite, we attempted an activity mechanism against *E. coli and C. tropicalis* biofilms using SEM/EDX analysis [48, 106]. SEM images revealed the shape of bacterial and yeast cells before and after nanocomposite treatment. In the control sample (non-treated bacterial and yeast cells), bacterial and yeast colonies were regularly-grown and exhibited normal cellular shapes with healthy cell surface and concentrated biofilm, as shown in **Figs. 2.18 (a, b)**. After nanocomposite treatment, observable morphological changes were recognized in *E. coli and C. tropicalis* cells **(Figs. 2.18 (c, d)**. In addition, an observable lysis of external surface was accompanied by deformations and reductions in the viable number of *E. coli and C. tropicalis* cells. Furthermore, biofilm development was inhibited. EDX elemental analysis revealed the presence of Ti and Si atoms (atoms of nanocomposite's outer shells) and C atoms for C-dots at deformation areas and at the outer surface of the treated *E. coli and C. tropicalis* cells, confirming the action of the tested nanocomposite, as shown in **Figs. 2.18 (e, f)**. One possible reason for the powerful activity against the cells of *E. coli and C. tropicalis* could be the large surface area (28.29 m^2/g), which allows for a conventional immobile connection between the negatively-charged bacterial cell walls and the nanocomposite, as shown in **Fig. 2.18 (c-d)** [107, 108]. This result is in a good agreement with various published reports on the interaction between MO NPs and pathogenic microorganisms by electrostatic potential, resulting in bacterial membrane detachment [107, 109, 110]. A recent study reported that MO NPs could induce oxidative stress in pathogenic microbes [111], and quickly damage their cell membranes upon exposure to increased cellular ROS levels. In this study, the prepared nanocomposite was externally-linked to *E. coli* and *C. tropicalis* cells through electrostatic attraction and reduced bacteria cell numbers via membrane leakages [109]. Our suggested action mechanism started with the adhesion of the nanocomposite to the exterior surface of *E. coli* and *C. tropicalis*. Then, Ti^{2+}, Si^{2+} ions (from the external shell) and Fe^{+2} (from the core) penetrated the tested bacterial and yeast cells and destroyed their biological molecules, such as bacterial mitochondria and DNA. After that, cellular toxicity due to oxidative tension and the generated ROS increased.

Fig. 2.18: SEM and corresponding EDX elemental analysis of *E. coli* and *C. trobicalis*: (a) Normal bacterial cells (*E. coli*) without nanocomposite treatment, (b) Normal yeast cells (*C. tropicalis*) without nanocomposite treatment, (c) Depressed and deformed bacterial cell after nanocomposite treatment, (d) Depressed and deformed *Candida* cell by nanocomposite treatment showing the complete lysis of *Candida* cell and loss of budding formation, (e) Corresponding EDX elemental analysis of the treated *E. coli* cell confirming the cellular internalization of the prepared nanocomposite in *E. coli* cells, and (f) Corresponding EDX elemental analysis of the treated *C. tropicalis* cell confirming the cellular internalization of the synthesized nanocomposite in *C. tropicalis* cells.

2.5 Conclusion

$Co_xNi_{1-x}Fe_2O_4$; x=0.9 / SiO_2 / TiO_2 nanocomposite was prepared using a layer-by-layer approach. It was then decorated with C-dots synthesized using a one-pot hydrothermal method. The prepared nanocomposite was examined using several instruments to understand its phase, crystallinity, UV-absorption, band gap energy, surface area, pore size distribution, average size of particle, morphology and purity. The prepared nanocomposite was designed for wastewater treatment. Thus, two different applications were carried out: photocatalytic degradation of water pollutants, and disinfection of water-borne pathogens. Chloramine-T trihydrate was used as an example of organic pollutants in water, and many multi-drug-resistant bacteria and pathogenic fungi were employed as common water-borne microorganisms. Following this, the photocatalytic abilities of the prepared nanocomposite and the different factors (nanocomposite dose – chloramine-T initial concentration – reaction pH) affecting their efficacy were studied. Our results showed that the photodegradation of chloramine-T followed second order kinetics. In addition, degradation mechanism suggested that holes had a significant role in the photodegradation via chloramine-T oxidation or forming free radicals. Moreover, the prepared nanocomposite showed more promising antimicrobial potential (high ZOI, low MIC) than bare C-dots, and our previously-reported nanocomposite ($Co_xNi_{1-x}Fe_2O_4$; x=0.9 / SiO_2 / TiO_2), suggesting a synergistic effect of C-dots with the nanocomposite. Notably, the antimicrobial ability of the prepared nanocomposite was significantly-increased after

UV-irradiation. Above all, the synthesized nanocomposite showed a high ability for pathogenic-cell destruction as revealed by its good antibiofilm capabilities, suggesting a use for our nanocomposite in fighting multi-drug-resistant bacteria and fungi. Our work provides a revolutionary, nanomaterial-based and cost-effective solution for wastewater treatment to assist in solving global water shortage issues.

Chapter 3: UV-assisted chloramine-T degradation by multiple nanocomposites of carbon-semiconductor-based heterojunction

3.1 overview

The problem of hazardous wastewater remediation is a complicated issue and a global challenge. Herein, a layered $Co_{0.5}$ $Ni_{0.5}$ Fe_2O_4 /SiO_2 /TiO_2 composite matrix was prepared and incorporated with three carbon nanomaterials having different dimensionalities, carbon dots (C-dots, 0D), single-walled carbon nanotubes (1D), and reduced graphene oxide (2D), in an effort to create effective photocatalytic nanocomposites for chloramine-T removal from water. Microstructural analyses confirmed the formation of nanocomposites and revealed their chemistry and structure. Elemental mapping revealed a uniform distribution of elements throughout the nanocomposite matrix that was free of impurities. The spherical shape of the matrix particles (average diameter ~90 nm) and their conjugation with the carbon nanomaterials were confirmed. Nitrogen adsorption–desorption isotherms revealed that the nanocomposites were mesoporous but also contained macropores. The surface chemical compositions of the nanocomposites were investigated and showed a range of available binding energies. The kinetics of photocatalysis by the system were studied, and the effects of different parameters (such as photocatalyst dose and charge-carrier scavengers) on the efficiency of chloramine-T degradation were also investigated. The nanocomposite loaded with 10% C-dots exhibited high UV-assisted photocatalytic activity for chloramine-T degradation (65% removal efficiency).

3.2 Introduction

Hazardous materials polluting water currently present a significant threat to public health by pushing the world toward a global water shortage and increase the number of deaths every year due to water-borne pathogens. Chloramine-T is one of the most serious materials polluting water and can cause several health problems, such as vomiting, diarrhea, nausea, and irritation of the upper respiratory tract [112]. Advances in nanotechnology through the use of nanocomposites, which combine the advantages of several materials, are receiving considerable attention as potential materials that can be employed to face global challenges in water purification. Among nanocomposites, recyclable and TiO_2-based nanocomposites are of great importance due to their cost-effectiveness, relatively high photocatalytic capabilities, chemical and thermal stabilities, versatility in application, and ease of preparation. Recently, Marsooli et al. reported the preparation of an $Fe_3O_4/SiO_2/TiO_2/CeVO_4$ nanocomposite by an ultrasonic-assisted precipitation approach for methylene blue (MB) degradation under visible light [113]. The nanocomposite had an average particle diameter of about 80–100 nm and high purity, as revealed by scanning electron microscope (SEM) and energy dispersive X-ray spectroscopy (EDX) analyses, respectively. However, due to the nanocomposite's core–multi-shell microstructure, it possessed a weak saturation magnetization (M_s) of about 9.2 $emug^{-1}$. In addition, due to the relatively large band gap of both the TiO_2 and $CeVO_4$ nanoparticles (NPs), quantum inefficiency due to the inefficient utilization of visible light could reduce the overall degradation efficiency. Tajareh et al. used multiwalled carbon nanotubes (MWCNTs) to fabricate a TiO_2/Fe_3O_4/MWCNT nanocomposite by a sonochemical method. This nanocomposite was designed for the removal of various organic dyes from water, such as methyl orange, reactive red 77, acid red 14, and acid blue 19 [114]. As an example of their results, the removal efficiency of acid red 14 by the nanocomposite, irradiated by direct sunlight, was 86.27% after 8 h. This nanocomposite employed photoactive TiO_2 NPs in direct contact with the magnetic Fe_3O_4 NPs, which is known to lead to the formation of pseudo-brookite, which can deteriorate its photocatalytic efficiency [47, 112, 115]. Another nanocomposite, $Fe_3O_4/SiO_2/TiO_2$–Co/rGO was synthesized by Fu et al. via sol-gel and hydrothermal methods for water-treatment applications [116]. The nanocomposite exhibited a degradation efficiency of 98.87% against MB under visible light irradiation for 160 min, and indications of long-term stability with an efficiency of about 93.88% after five consecutive uses under identical conditions. Particles of the nanocomposite were relatively large at 500 nm, which implies a low surface area and thus reduced photocatalytic abilities [117]. Previously, we reported the preparation and characterization of a $Co_{0.9}Ni_{0.1}Fe_2O_4/SiO_2/TiO_2$ nanocomposite by a simple layer-by-layer approach. The nanocomposite exhibited good crystallinity, high purity, a high surface area, and colloidal stability [115]. The result encouraged us to investigate its photocatalytic and antimicrobial behaviors against pyridine and pathogenic microorganisms, which were enhanced by UV and gamma irradiation [47]. The quantum efficacy of the material was further enhanced by loading it with carbon dots which acted as electron reservoirs and photons upconverters [112]. Over the past two years, several experiments have been carried out to optimize surface area, particle size, magnetic properties, TiO_2 percentage, and the core–multi-shell microstructure. In this chapter, the optimized nanocomposite matrix of $Co_{0.5}Ni_{0.5}Fe_2O_4/SiO_2/TiO_2$ (CNFST) was first prepared by a layer-by-layer method. Subsequently, the nanocomposite matrix was loaded by three carbon nanomaterials as follows: 0D carbon dots (C-dots), 1D single-walled carbon nanotubes (SWCNTs), and 2D reduced graphene oxide (rGO). These synthesized nanocomposite materials were characterized by several techniques in terms of their structural and morphological features. Finally, photocatalytic properties of these nanocomposites were investigated and compared with P25 (a standard photocatalyst) against chloramine-T trihydrate. The photocatalytic ability of CNFST/C-dots 10% nanocomposite was studied in detail. A kinetics study was carried out and the effects of different parameters (such as photocatalyst dose, pH, chloramine-T initial concentration, and charge carrier scavengers) on the efficiency of degradation were also investigated. Our results showed promising photocatalytic performance of these carbon-loaded nanocomposites which can be employed for effective wastewater treatment.

3.3 Materials & methods

3.3.1 Materials

The starting reagents of cobalt chloride ($CoCl_2$), nickel chloride ($NiCl_2$), ferric chloride ($FeCl_3•6H_2O$), tetraethyl orthosilicate 98% (TEOS) ($Si•(OC_2H_5)_4$), absolute ethanol 99.9% (C_2H_5OH), titanium (IV) isopropoxide 97% ($C_{12}H_{28}O_4Ti$), ammonium hydroxide 28% and 25% (NH_4OH), hydroxypropyl cellulose (M.W. = 80,000), hydrochloric acid (HCl), sodium hydroxide (NaOH), ascorbic acid ($C_6H_8O_6$), copper acetate monohydrate (($C_4H_8CuO_5$)$•H_2O$), sulfuric acid (H_2SO_4), nitric acid (HNO_3), potassium chlorate ($KClO_3$), P25 (standard TiO_2 photocatalyst), and chloramine-T trihydrate ($C_7H_7ClNNaO_2S•3H_2O$) were purchased from Sigma Aldrich and from Wako, Japan. In addition, SWCNTs were obtained from OCSiAl, Japan. All reagents were used as-received without further purification (extra-pure grade).

3.3.2 Method

3.3.2.1 Preparation of composite matrix ($Co_{0.5}Ni_{0.5}Fe_2O_4/SiO_2/TiO_2$)

The complete set of preparation steps for the composite matrix used in this study is reported in our previously-published reports [47, 48, 112].

3.3.2.2 Preparation of C-dots

C-dots were synthesized using a hydrothermal method as reported by Jia *et. al* [49]. In brief, 6.8 g of ascorbic acid was first dissolved in 400 mL deionized water (DIW) and stirred for 10 min. Next, 0.8 g copper acetate monohydrate was added while maintaining the solution at room temperature under constant stirring for 10 min. The container was kept in a water bath and its temperature was gradually increased to 90°C and held for 5 h. The remaining solution was then centrifuged at 9000 rpm for 30 min to remove large particles. The supernatant was further purified by pouring through Millipore filter paper (pore diameter ~0.22 μm) to remove small particles. Finally, purified supernatant containing C-dots was dried in a N_2-supplemented oven at 70°C for 12 h.

3.3.2.3 Preparation of rGO

3.3.2.3.1 Preparation of graphite oxide

Graphite oxide was obtained through a modified Staudenmaier's method [118-120]. Briefly, 5 g of graphite powder was chemically oxidized by an acidic solution containing 90 mL of H_2SO_4

and 45 mL of HNO_3. The solution was constantly stirred at room temperature for 30 min, then was cooled in an ice bath. To reduce the risk of explosion from the exothermic reaction, 55 g of $KClO_3$ was gradually added to solution. To ensure complete oxidation of the graphite powder, the mixture was magnetically stirred for 5 days at room temperature. The resultant graphite powder was then washed with DIW and a 10% HCl solution to remove any sulfate residuals or other ionic impurities. Finally, the processed graphite oxide powder was dried at 70°C in a vacuum oven for 5 h.

3.3.2.3.2 Preparation of microwave assisted rGO

Graphite oxide powder from the previous step was treated by microwave irradiation (IRIS OHYAMA, Japan) at a constant irradiation power of 900 W for 30 s to achieve highly exfoliated rGO [121, 122].

3.3.2.4 Preparation of carbon-loaded nanocomposites

Three nanocomposite samples were prepared by loading the three different carbon nanomaterials into the composite matrix described in Sec. 2.2.1. The three nanocomposite samples were composites loaded at 10% with C-dots, SWCNTs, and rGO. Samples were denoted (CNFST/C-dots 10%), (CNFST/SWCNTs 10%), and (CNFST/rGO 10%), respectively. Briefly, CNFST and each type of carbon nanomaterial was separately dispersed in 50 mL of super dehydrated C_2H_5OH using water bath sonication for 45 min. Next, 1 mL of a NH_4OH 25% solution was incorporated into the mixtures which were left to vigorously stir overnight. The resultant powders were washed several times using DIW and were dried at 80°C for 6 hrs. The preparation steps are shown schematically in **Fig. 3.1**

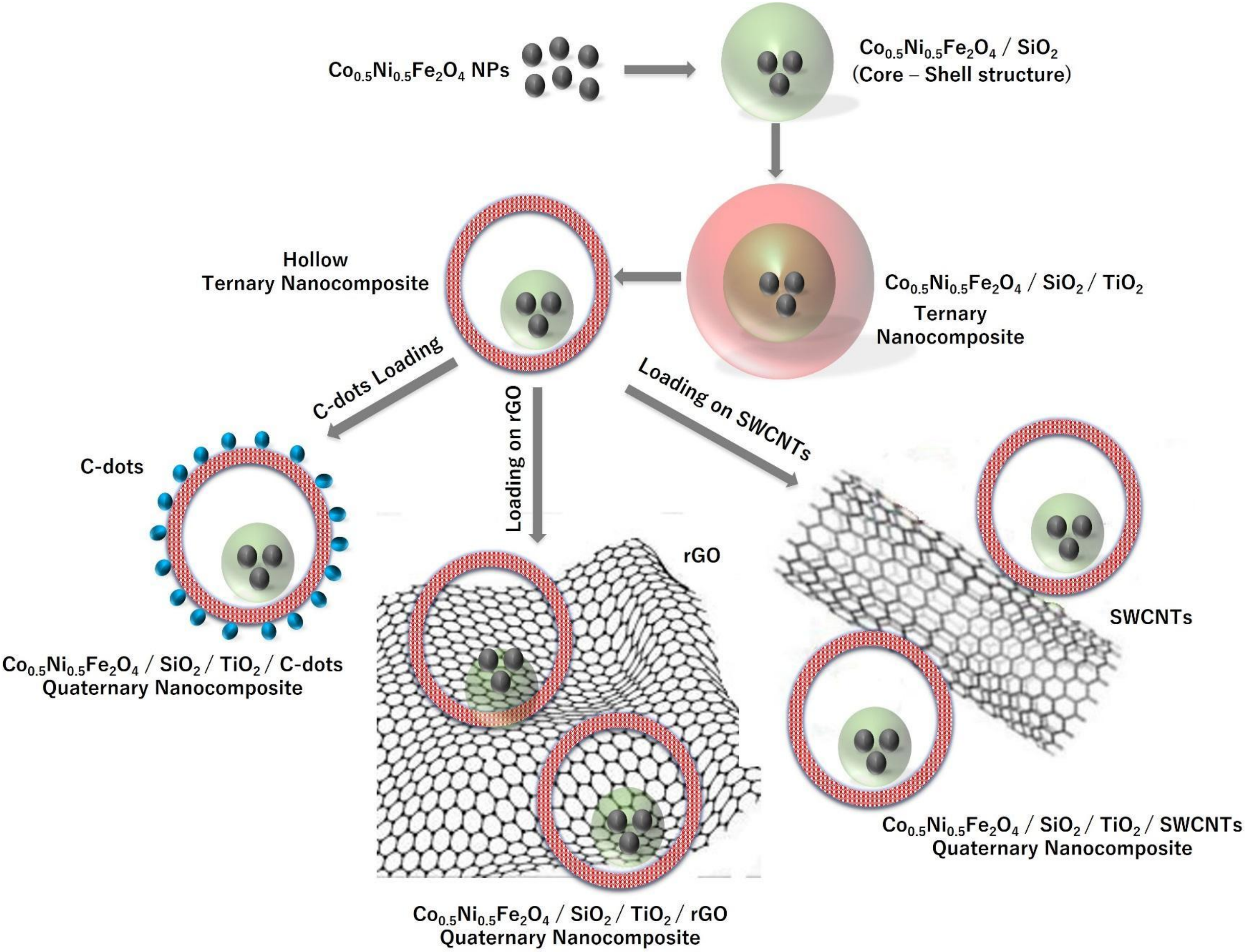

Fig. 3.1: Step-by-step schematic of the nanocomposite synthesis processes.

3.3.2.5 Characterization of the nanocomposites

Phase and crystallinity were investigated by X-ray diffraction (XRD) analysis using an Ultima IV X-ray diffractometer (Rigaku, Japan) employing Cu-Kα radiation ($\lambda = 1.54$ Å) operated at 30 mA and 40 kV. X-ray photoelectron spectroscopy (XPS) was conducted using a PHI Quantera SXM Scanning X-ray Microprobe (ULVAC-Phi, Inc., Japan) to analyze the elemental composition and chemical states of the species present. The morphology, purity, and elemental composition of the samples were characterized using a scanning electron microscope (SEM) supported with an SU8000 Type II energy-dispersive X-ray spectroscopy (EDX) unit (HITACHI high technologies, Japan). Images of the average particle diameters and electron diffraction patterns were collected using a JEM-2100F (JEOL Ltd., Japan) transmission electron microscope (TEM). Surface area and pore-size distribution analyses were measured by Brunauer–Emmett–Teller (BET) analysis and the Barrett–Joyner–Halenda (BJH) method using a Tristar II (Micromeritics, Japan). Fourier transform infrared (FTIR) analysis via the KBr pellet method was used to identify chemical bonding in the samples using an FTIR 3600 (JASCO Infrared spectrometer, Japan). The FTIR pattern was recorded over the 4000 cm^{-1} to 400 cm^{-1} wave-number range. Raman analysis was conducted to reveal molecular interactions, polymorphism, and chemical structure in the samples using an NRS-3100 (JASCO, Japan). Finally, Ultraviolet–Visible light (UV–Vis.) spectroscopy was used to calculate the concentration of chloramine-T during photodegradation using a V-670 spectrophotometer (JASCO, Japan).

3.3.2.6 Photocatalytic degradation of chloramine-T trihydrate

Photocatalytic degradation studies were conducted at room temperature (24°C ± 2°C). As a screening step, a fixed quantity of each nanocomposite (10 mg) was added to a 50 mL aqueous solution of chloramine-T with an initial concentration (C_o) of 10 ppm. Mixtures were stirred for 2 h in darkness to reach an adsorption–desorption steady state. Subsequently, suspensions were irradiated by an axially-located Hg–Xe arc lamp (spot-lure SP-7, Ushio, Japan) with an emittance at 250 nm. At defined intervals of time, 2 mL of each suspension was sampled using a syringe supported by a filter (2.5 µm pore size). The concentration of chloramine-T in these supernatant samples during photo-decomposition was determined using UV–Vis. spectroscopic analysis by measuring the absorbance at λ_{max} = 222 nm (absorption peak of chloramine-T) in the liquid cuvette configuration. DIW was used as a reference for UV–Vis. measurements.

3.4 Results & discussion

3.4.1 Characterization of nanocomposites

3.4.1.1 XRD analysis

XRD analysis was carried out to investigate the phase assemblage and crystallinity of the composites [123]. As shown in **Fig. 3.2**, the XRD pattern of the unloaded composite matrix exhibited several peaks, at 2θ = 25.3°, corresponding to the (101) set of planes; at 37.2°,(004), 47.5°, (200); 52.6°, (105); 54.4°, (211); 63.8°, (204); 69.8°, (116); 71.58°, (220); and 75.6°, (215). The diffraction peaks and corresponding crystallographic planes correspond mainly to the anatase phase of TiO_2 (JCPDS 21-1272) [124, 125], the predominant material of the composite matrix. It is worth noting that the SiO_2 amorphous halo that frequently appears at 2θ = 21.9 ° was not present. Similarly, $CoNiFe_2O_4$ peaks were obscured by the adjacent high-intensity peaks of the TiO_2. The same results were reported in our previous reports, along with an indication of composite formation [47, 48, 112]. Similar peaks were detected in the P25 sample. Some additional peaks corresponding to the rutile phase of TiO_2 were observed at 2θ = 27.5°, (110); 36.2°, (101); 41.5°, (111); and 56.1°, (220), which were found to be in good agreement with the JCPDS card number (21-1276) [126-128]. In the case of the CNFST/C-dots 10% sample, the same peaks of anatase TiO_2 appeared, while the main broad peak of the C-dots (2θ = 21.80°) were not observed, likely due to their low intensity. For the CNFST/rGO 10% sample, a diffraction peak at 2θ = 26.25°, (002) was clearly observable, corresponding to rGO sheets [129]. Finally, for the CNFST/SWCNTs 10% sample, similar peaks from the TiO_2 were present. However, the sharp peak of TiO_2 at 2θ = 25.3°, (101) was slightly shifted and broadened, which could be the result of overlap between the main TiO_2 peak and the weaker peak of SWCNTs at 2θ = 26.3°, (002). In addition to the above results,

Fig. S.3.1 shows XRD patterns of separate samples of the carbon materials (C-dots, rGO, and SWCNTs) used to decorate the nanocomposite matrix. For the C-dots sample, a single broad peak located at 2θ = 21.80° was detected corresponding to the (002) crystallographic plane, which is typical for amorphous carbon [130]. The XRD pattern of the synthesized rGO sample exhibited two diffraction peaks located at 2θ = 26.25° and 42.95°, which correspond to the (002) and (102) planes, respectively [131]. Finally, several diffraction peaks were recorded in the XRD pattern of SWCNTs at 2θ = 22.81°, 44.24°, and 45.10°, which correspond to the planes (002), (100), and (101), respectively [132]. The absence of other peaks in the XRD patterns (**Fig. S.3.1**) confirmed the purity of the synthesized samples, which is a favorable result related to the fabrication and grafting processes expected to result in high performance in the assigned applications.

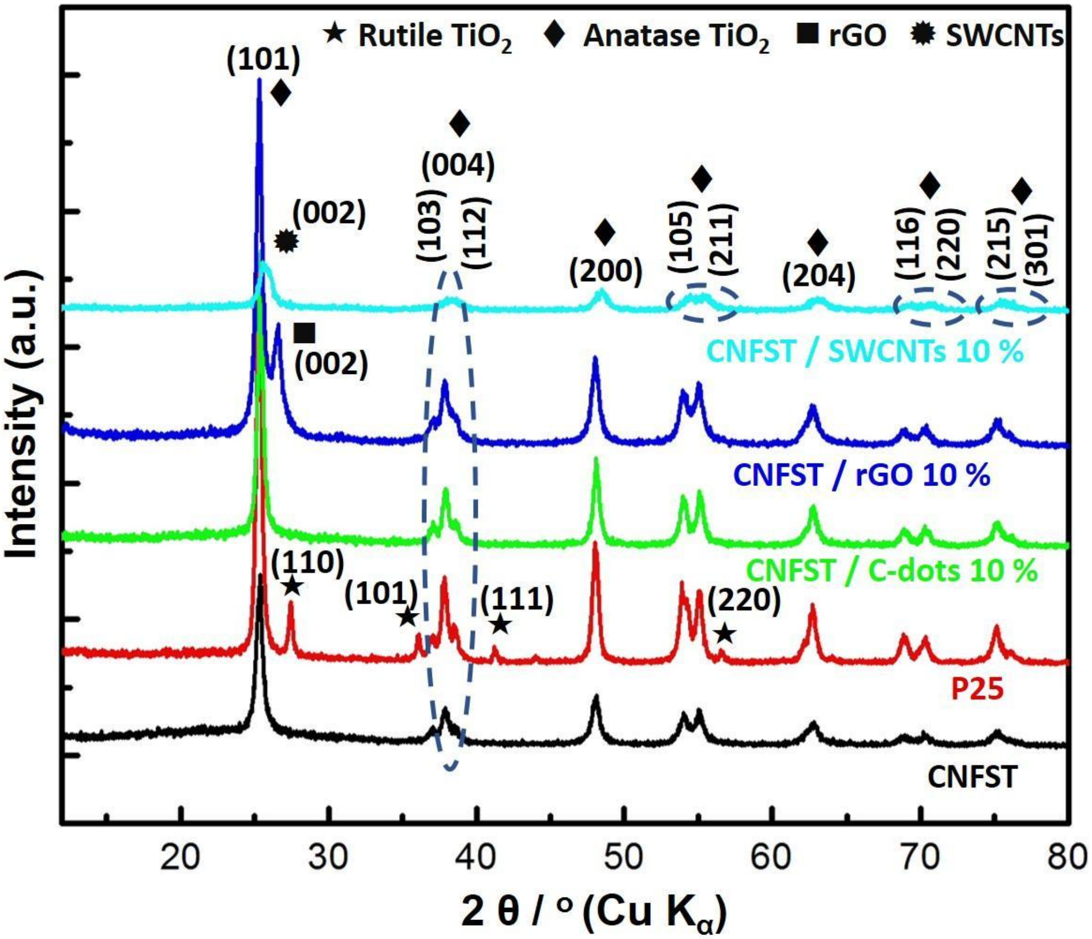

Fig. 3.2: XRD θ–2θ patterns of the nanocomposites.

3.4.1.2 SEM, elemental mapping, and EDX analysis

SEM, EDX analysis, and elemental mapping were conducted to gain a complete perspective regarding the surface morphology, purity, and grain sizes of the nanocomposites [133]. **Fig. 3.3** shows the surface morphology, elemental mapping, and elemental analysis of the CNFST/C-dots 10% nanocomposite. It can be seen that the C-dots are distributed over the upper surface of the CNFST, as shown in **Fig. 3.3 (a)**. While **Fig. 3.3 (b–h)** confirmed the presence of all elements constituting the composite, such as C, Ti, Si, O, Fe, Ni, and Co, and that they were uniformly-distributed throughout the composite matrix without any foreign elements, indicating the high purity of the prepared samples. Ti was the dominating element with the highest ratio, as revealed by the EDX analysis in **Fig. 3.3 (i).** However, Fe, Ni, and Co atoms localized to the core and exhibited relatively-lower ratios. Similarly, **Fig. 3.4** presents SEM analysis, EDX elemental mapping, and EDX spectra of the synthesized CNFST/rGO 10% nanocomposite. The typical cracks and fissures of rGO materials were clearly detected, as shown in **Fig. 3.4 (a)**. In addition, the CNFST matrix is uniformly distributed with the large surface area of rGO. This revealed the presence of all of the elements involved—C, Ti, Si, O, Fe, Ni, and Co—shaping its structure, as shown in **Fig. 3.4 (b–h)**. Interestingly, the color density (intensity) of shell-layers' forming elements such as C, Ti and Si is more dense than the core-forming elements such as Co, Ni, and Fe. In addition, the samples' purity is here confirmed by the lack of other detectable elements in the EDX analysis, as shown in **Fig. 3.4 (i)**. Unlike the CNFST/C-dots 10% composite, C content in the CNFST/rGO 10% composite is nearly two times greater, which is attributable to a better loading efficiency due to the higher surface area of rGO compared with C-dots. **Fig. 3.5** shows the surface morphology, elemental mapping, and EDX analysis of the CNFST/SWCNTs 10% nanocomposite. The SWCNTs appear as sheet-like soots which are black colored rubbery soots. SWCNTs are uniformly crosslinked with the CNFST matrix as shown in **Fig. 3.5 (a)**, while elemental mapping shows all elements comprising the composite, including C, Ti, Si, O, Fe, Ni, and Co, as presented in **Fig. 3.5 (b–h)**. The EDX spectrum shows small ratios of Na and Al,

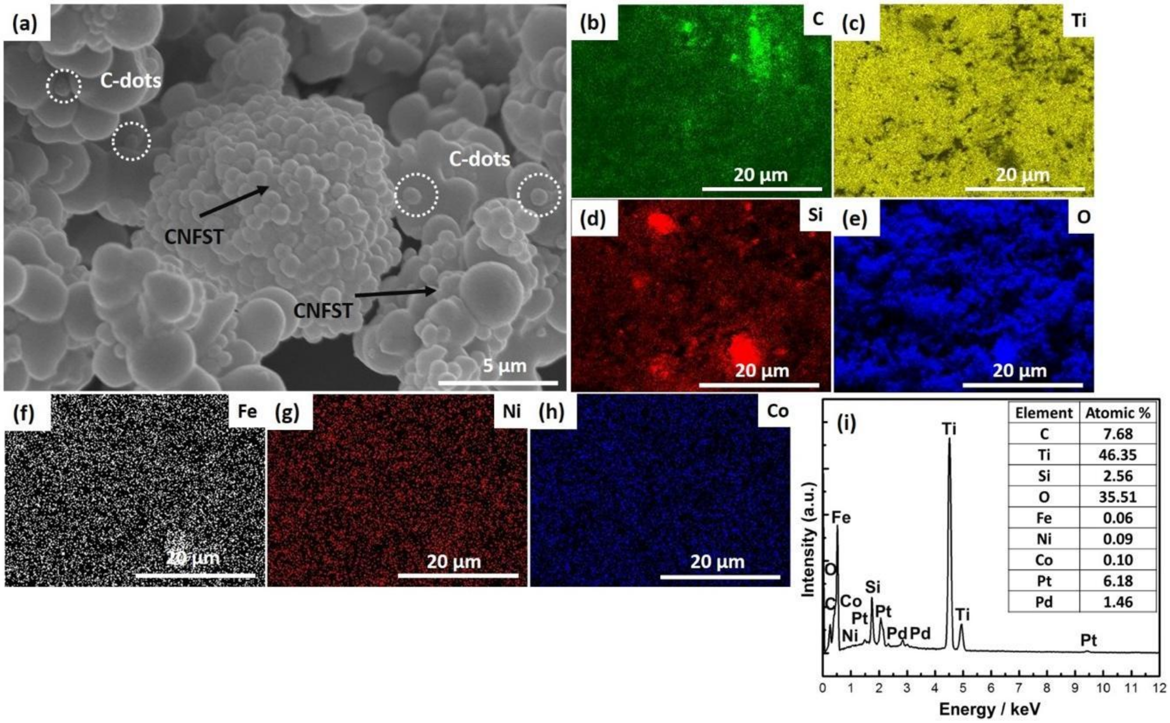

Element	Atomic %
C	7.68
Ti	46.35
Si	2.56
O	35.51
Fe	0.06
Ni	0.09
Co	0.10
Pt	6.18
Pd	1.46

Fig. 3.3: (a) SEM image of the CNFST/C-dots 10% nanocomposite, (b–h) EDX elemental mapping and (i) EDX spectrum.

which arise from the commercial SWCNTs. In addition, the C ratio is relatively higher than all of the other prepared composites, which may be the result of strong crosslinking of CNFST matrix with SWCNTs as shown in **Fig. 3.5 (i).** Additionally, SEM images of the carbon nanomaterials showing the typical features of each sample are shown in **Fig.S.3.2**.

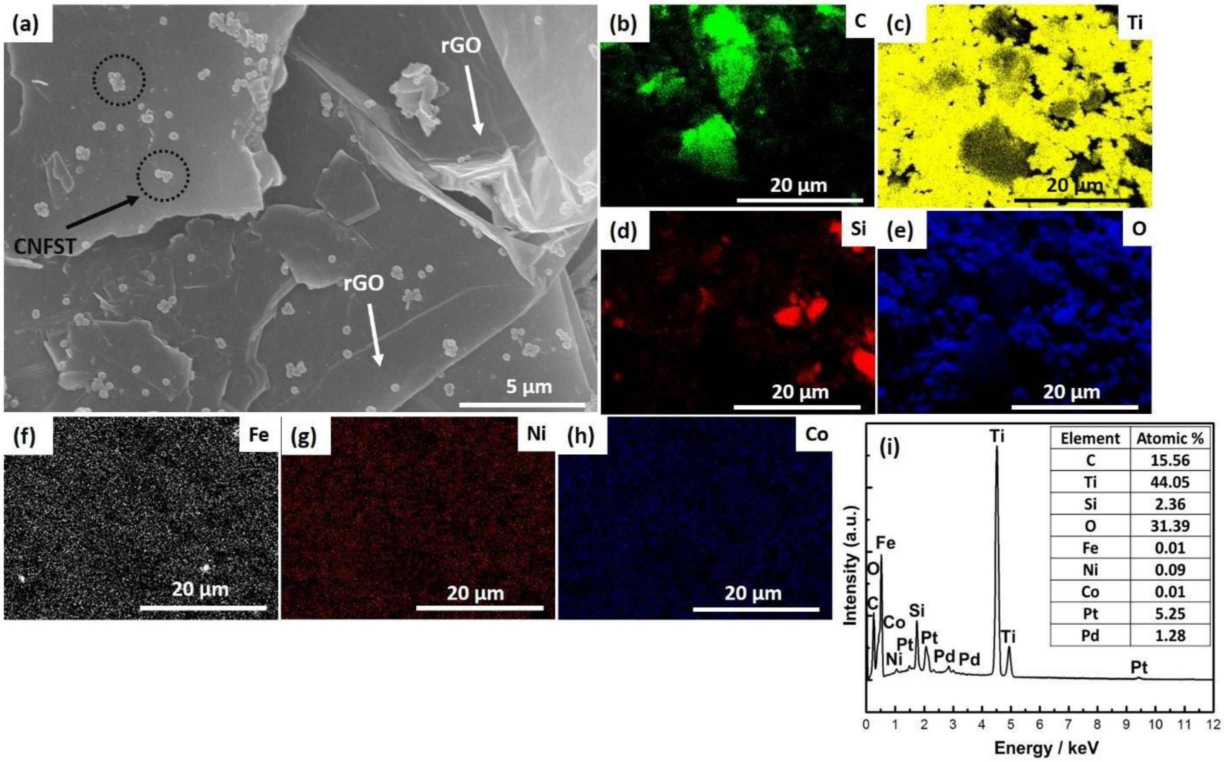

Fig. 3.4: (a) SEM image of the CNFST/rGO 10% nanocomposite, (b-h) EDX elemental mapping and (i) EDX spectrum.

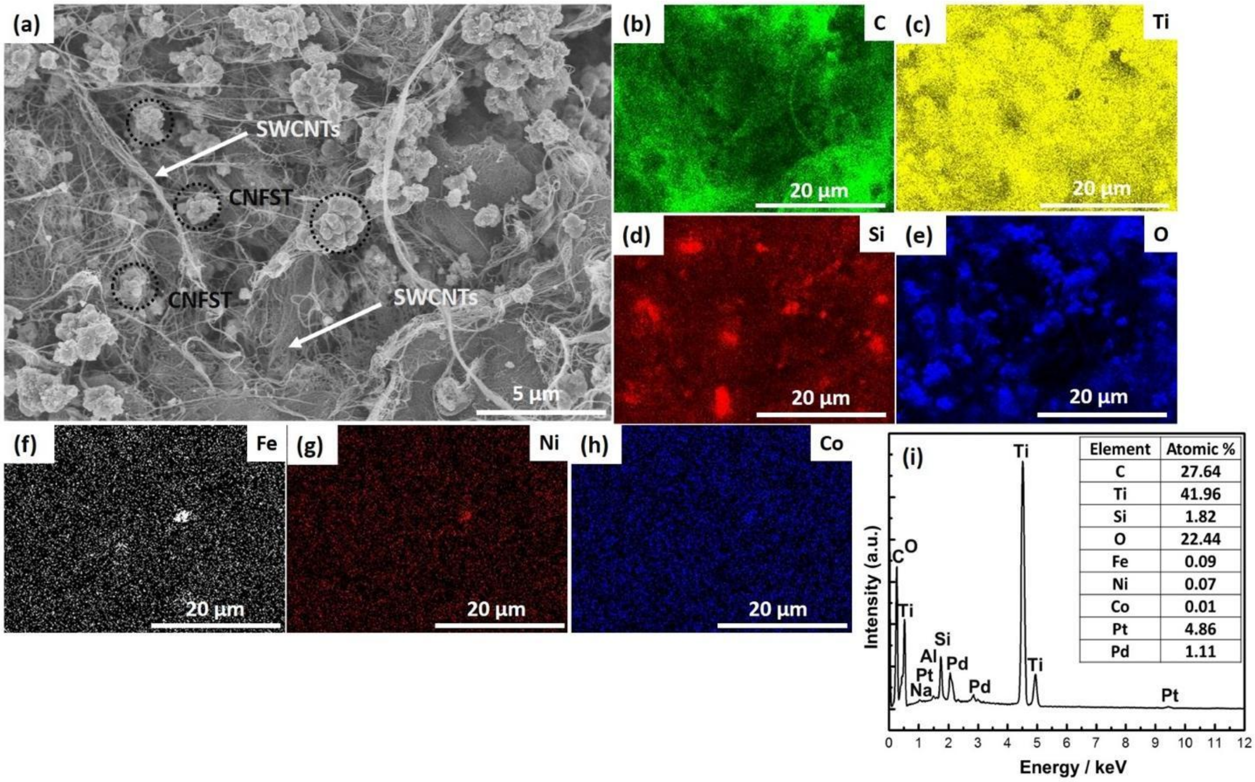

Fig. 3.5: (a) SEM image of the CNFST/SWCNTs 10% nanocomposite, (b–h) EDX elemental mapping and (i) EDX spectrum.

3.4.1.3 TEM, high-resolution TEM, and electron diffraction pattern analyses

TEM analysis was performed to measure the average diameter of the composite matrix, to identify the *d*-spacings of lattice planes, and to confirm the phase by analysis of the crystallographic plane reflections present in selected-area electron diffraction (SAED) patterns. **Figs. 3.6 (a, d, and g)** are TEM micrographs of the CNFST/C-dots 10%, CNFST/rGO 10%, and CNFST/SWCNTs 10% nanocomposites, respectively. The matrix particles are spherical in shape, with an average diameter of 90 ± 14 nm, as shown in **Fig. S.3.3**. Slight agglomeration occurred,

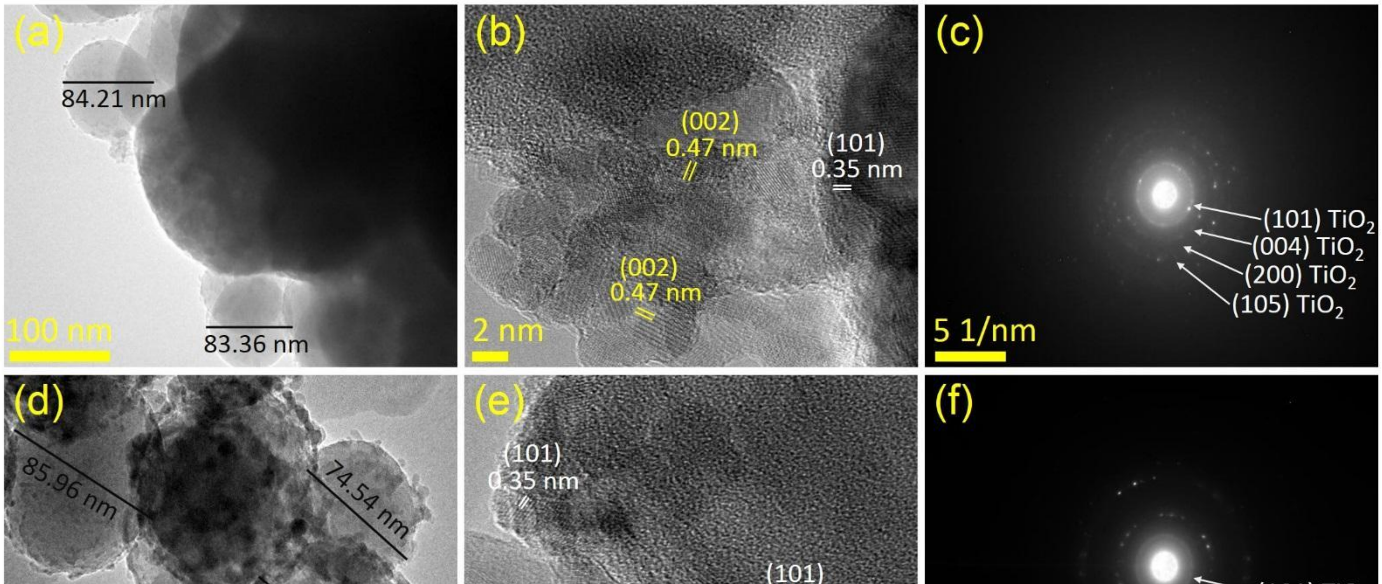

mainly during sample preparation. The interparticle void content percentage matches the result of the BET analysis (below). The N_2 adsorption–desorption isotherm is presented in **Fig. 3.7 (a)**, which shows that at the high relative pressure region of 0.87 to 1, condensation clearly occurred in the interparticle voids. The composite matrix is uniformly conjugated with carbon components. For example,

Fig. 3. 6 (g) shows a bundle of $SWCNT_S$ conjugated with the composite matrix. Lattice fringes in high-resolution TEM (HRTEM) images are primarily attributed to the anatase form of TiO_2, in agreement with the interpretation of the XRD data of **Fig. 3.2**, which showed predominantly anatase. Interpretation of the HRTEM images confirmed the presence of carbon by analysis of the shape and characteristic crystallographic (002) planes of a spacing of 0.47 nm, as shown in **Figs. 3.6 (b, e, and h)**. Analysis of the SAED patterns, **Figs. 3.6 (c, f, and i)**, similarly confirmed the presence of carbon nanoparticles within the nanocomposite matrix, especially for rGO and SWCNTs.

Fig. 3.6: TEM image, HRTEM image and SAED pattern of (a–c) the CNFST/C-dots 10% nanocomposite, (d–f) the CNFST/rGO 10% nanocomposite and (g–i) the CNFST/SWCNTs 10% nanocomposite.

3.4.1.4 BET surface area and BJH pore size analyses

The BET measurement's N_2 adsorption–desorption isotherms and the BJH pore-size distribution of the nanocomposites, along with P25, are shown in **Figs. 3.7 (a, b)**. In addition, isotherms of separate matrix and carbon powders are shown in **Fig. S.3.4**. Considering the IUPAC classification scheme, all samples show type (III) isotherms corresponding to weak adsorbate-adsorbent interactions (N_2 gas and the prepared sample particles), as shown in **Fig. 3.7 (a)**. Adsorption occurred when the N_2 interaction with an adsorbed layer was greater than its interaction with sample's surface. The sharp capillary condensation observed at relatively higher relative pressures, from 0.87 to 1, indicates the presence of macropores [134]. The calculated values of surface area, pore volume, and pore area of the prepared nanocomposites, along with P25 and the separate carbon nanomaterials, are listed in **Table 3.1**.

Table 3.1: Calculated surface areas, pore volumes, and pore areas of the prepared materials and their nanocomposites.

No.	Sample	BET Surface area ($m^2 \cdot g^{-1}$)	Pore volume ($cm^3 \cdot g^{-1}$)	Pore area ($m^2 \cdot g^{-1}$)
1	CNFST	3.28 ± 0.16	0.001	3.52
2	rGO	78.33 ± 3.8	0.086	167.19
3	SWCNTs	634.53 ± 13.98	0.194	386.91
4	C-dots	4.19 ± 2.53	< 0.001	< 0.001
5	P25	48.48 ± 0.12	0.002	5.46
6	CNFST / C-dots 10%	1.24 ± 0.20	0.004	7.76
7	CNFST / rGO 10%	5.05 ± 0.21	0.002	4.61
8	CNFST / SWCNTs 10%	28.37 ± 1.15	0.018	35.39

Compared to the synthesized nanocomposites, the P25 sample has the greatest surface area (48.48 ± 0.12 $m^2 \cdot g^{-1}$), which can be attributed to the relatively smaller particle size of only 21 nm (as indicated from TEM analysis by the supplier). The decreased surface area of the prepared nanocomposites is the result of increasing the size of the particles. The average diameter of particles in the nanocomposites' matrices is approximately 90 nm, as confirmed by the TEM analysis shown in **Figs. 3.6 (a, d, and g).** Upon grafting of the composite matrix with the SWCNTs, the overall surface area of the resulting nanocomposite increased significantly due to the relatively high surface area of SWCNTs. On the other hand, upon loading C-dots and rGO into the composite matrix, their overall surface area was not greatly increased, a condition which can be the result of poor loading efficiency or the occurrence of agglomeration. **Fig. 3.7 (b)** shows the pore size distribution of the prepared nanocomposites. All samples possess a multimodal and broad pore-size distribution, reflecting the presence of two types of pores–mesopores with pore diameters of 2–50 nm and macropores with pore diameters greater than 50 nm.

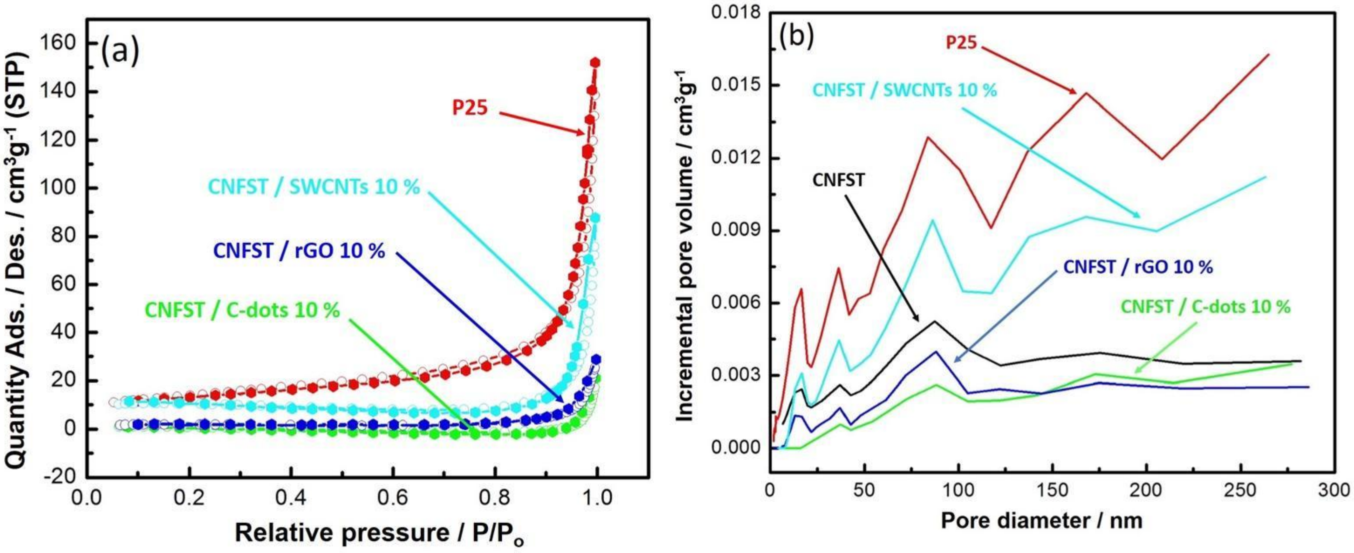

Fig. 3.7: (a) N_2-adsorption–desorption isotherms of the prepared composites with respect to P25 and (b) the BJH pore size distribution.

3.4.1.5 FTIR Surface bonding and analysis of functional groups

Results of the FTIR analysis, shown in **Fig. 3.8,** reveal surface-bonding and functional groups of the prepared CNFST/C-dots 10% nanocomposite, CNFST matrix, and C-dots samples (as a representative sample). The band at approximately 3425 cm^{-1} in all FTIR spectra is attributed to O–H stretching due to water molecules adsorbed onto the surface of the synthesized materials [135]. The strong peaks observed in all samples, at 2480 cm^{-1}, are attributed to CO_2 from the surrounding environment [136]. The main peak detected at 1650 cm^{-1} in the C-dots sample, and at 1666 cm^{-1} for the CNFST/C-dots 10% sample correspond to the stretching vibration bands of

C=O. This band was not detected in CNFST matrix, which might confirm the binding of the C-dots with the CNFST matrix via this bond [137, 138]. The peak observed at 1190 cm^{-1} in the CNFST/C-dots 10 % and at 1178 cm^{-1} in the CNFST composite matrix correspond to Si-O-Si bonding [139-141]. Generally, spinel ferrites exhibit two identical FTIR bands, characterized as υ_1 and υ_2, where "υ_1" appears in the range from 500 to 600 cm^{-1} and "υ_2" appears in the range from 300 to 450 cm^{-1} [142, 143]. These two bands are related to the stretching of oxygen bonds and to metal ions in the octahedral and tetrahedral sites, respectively [78-81], confirming the cubic spinel phase in both the CNFST/C-dots 10 % and the CNFST composite matrix. In addition, the peaks observed in the range from 460 to 560 cm^{-1} are attributable to Ti–O–Ti bonding, which is a characteristic of metal oxides [144]. Finally, the appearance of free silanol groups (Si–OH, located in the inner regions of the composite) are indicated by the bands detected at 980.25 cm^{-1} and 981.84 cm^{-1} for the CNFST/C-dots 10 % and for the CNFST matrix, respectively [74, 75]. Our results are in good agreement with similar recently-reported research articles [86-89, 115, 137, 145].

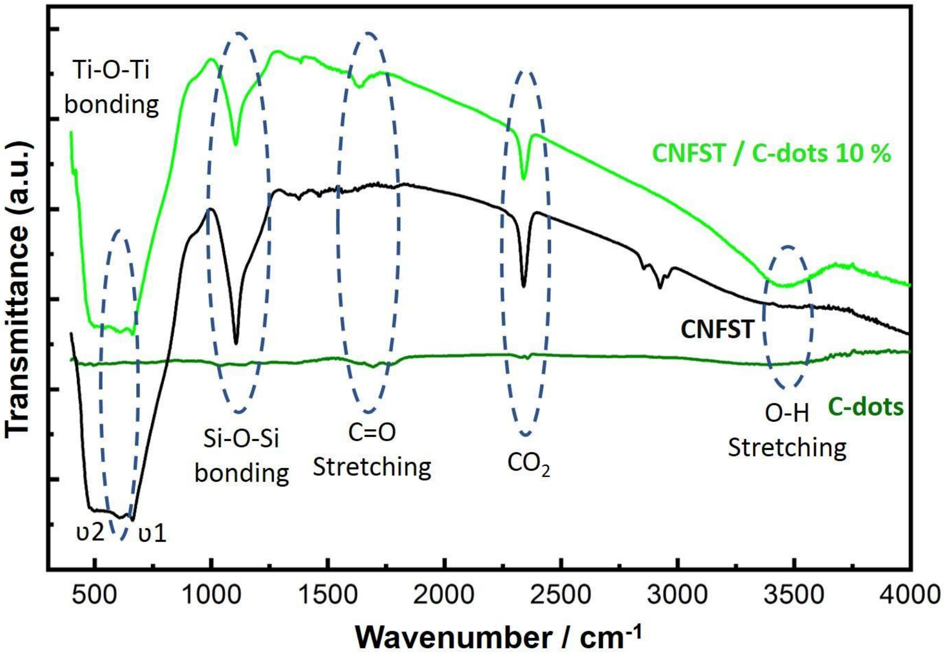

Fig. 3.8: FTIR spectra of the CNFST matrix, the C-dots, and the CNFST/C-dots 10% nanocomposite.

3.4.1.6 XPS analysis

XPS analysis was performed to determine the elemental composition and chemical states of the synthesized nanocomposites, particularly the main constituents of C and Ti, and also from different locations of the samples. **Figs. 3.9 (a–f)** show the detailed, deconvoluted XPS spectra that reveal the binding energy related to the C 1*s* and Ti 2*p* elements of the prepared nanocomposites.

Figs. 3.9 (a–b) correspond to the CNFST/C-dots 10% nanocomposite, **(c–d)** to the CNFST/rGO 10% nanocomposite, and **(e–f)** to the CNFST/SWCNTs 10% nanocomposite. Depending upon the C bonding configuration, the C 1*s* energies were found to vary from the binding energy of 283.5 eV to 285.3 eV. The deconvoluted C1*s* core-level XPS spectra in **Fig. 3.9 (a, c, and e)** exhibit peaks of different C species, such as sp^2–C and sp^3–C, with peaks at ~284.5 eV and ~285.2 eV, respectively [146]. The peak at 283.5 eV corresponds to a material containing both C and Si, but the peak at 284.5 eV can be assigned to either C–C bonds or C–Si–O bonds [147-149]. The XPS measurements revealed the different binding energies for C available for the binding in materials with a CNFST matrix. The deconvoluted Ti 2*p* core-level XPS spectra in **Figs. 3.9 (b, d, and f)** are the Ti $2p_{1/2}$ and Ti $2p_{3/2}$ peaks at binding energies of ~464.1 eV and ~458.2 eV, respectively, which confirms the presence of the Ti^{4+} state in the TiO_2 [150, 151]. The XPS analysis revealed that each carbon-loaded CNFST nanocomposite exhibited slight changes in their binding for C and Ti.

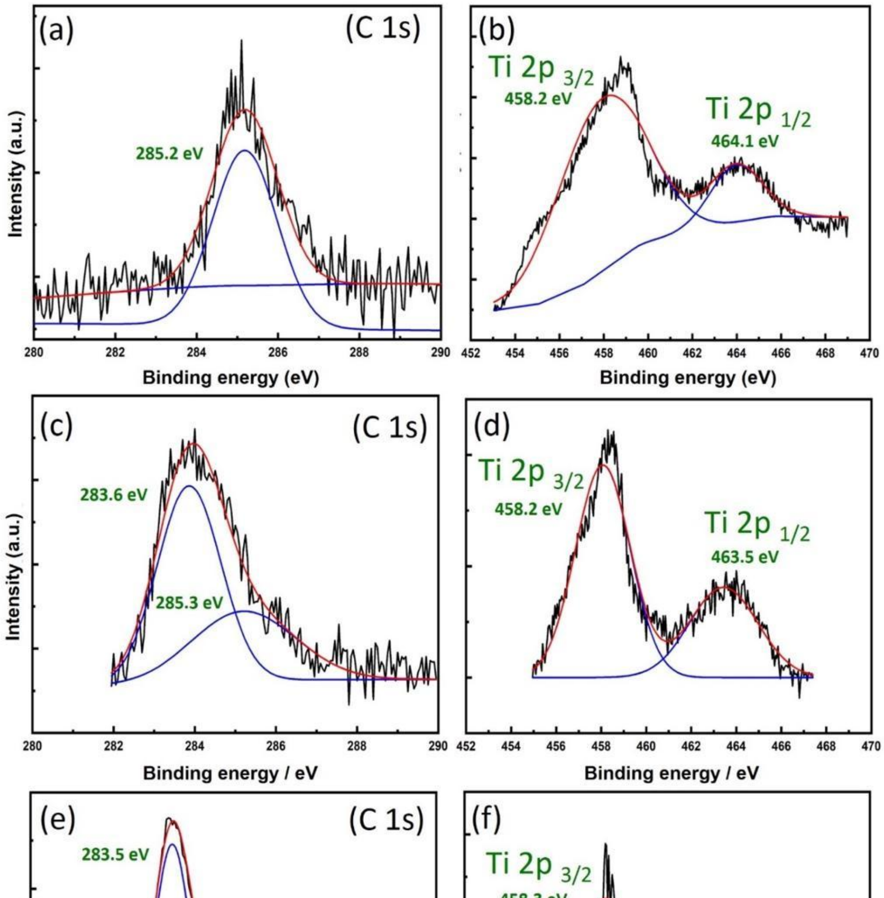

Fig. 3.9: XPS spectra showing the binding energy of C and Ti for (a–b) CNFST/C-dots 10% nanocomposite, (c–d) CNFST/rGO 10% nanocomposite, and (e–f) CNFST/SWCNTs 10% nanocomposite.

3.4.1.7 Raman analysis of polymorphism, structure, and molecular interactions

Raman analysis was carried out to analyze the chemical structure, polymorphism, and molecular interactions, and also to seek to confirm the conjugation of the CNFST matrix with the carbon nanomaterials during the formation of the samples and of P25. The results are shown in **Figs. 3.10 (a–f)**. Anatase TiO_2 is the dominant phase present in the particles of the core-shell CNFST matrix. As a result, four Raman-active bands corresponding to anatase TiO_2 are present at 236.8, 293.3, 515.9, and 638.4 cm^{-1}, corresponding to E_{g1}, B_{1g}, A_{1g}, and E_{g2} modes, respectively. Upon loading C-dots into the composite matrix to form the CNFST/C-dots 10% nanocomposite, two other carbon-characteristic peaks appeared at approximately 1379.1 and 1589.7 cm^{-1} and are attributed to the D and G bands, respectively, as shown in **Figs. 3.10 (a–b)**. The D band corresponds to sp^3 defect sites due to vacancies and grain boundaries [152, 153]. The G band represents scattering of E_{2g} phonons of sp^2 C atoms [154]. As predicted, similar peaks are present for the CNFST/rGO 10% and CNFST/SWCNTs 10% nanocomposites, with a slight peak shift and a slight change in the value of (I_D/I_G) because of the reduction of sp^3 into sp^2, and also to the reduction in the sp^2 domain size of C atoms upon their interaction with the CNFST matrix, as shown in **Figs. 3.10 (c, d, and e)** [155, 156]. It is important to note that the radial breathing mode is observed at 185 cm^{-1} in the CNFST/SWCNTs 10% nanocomposite, indicating the conjugation with SWCNTs; it can also be used to estimate SWCNTs' diameter [157]. Finally, P25, which contains both polymorphs of anatase and also rutile, exhibits recorded peaks in good agreement with the literature [158, 159].

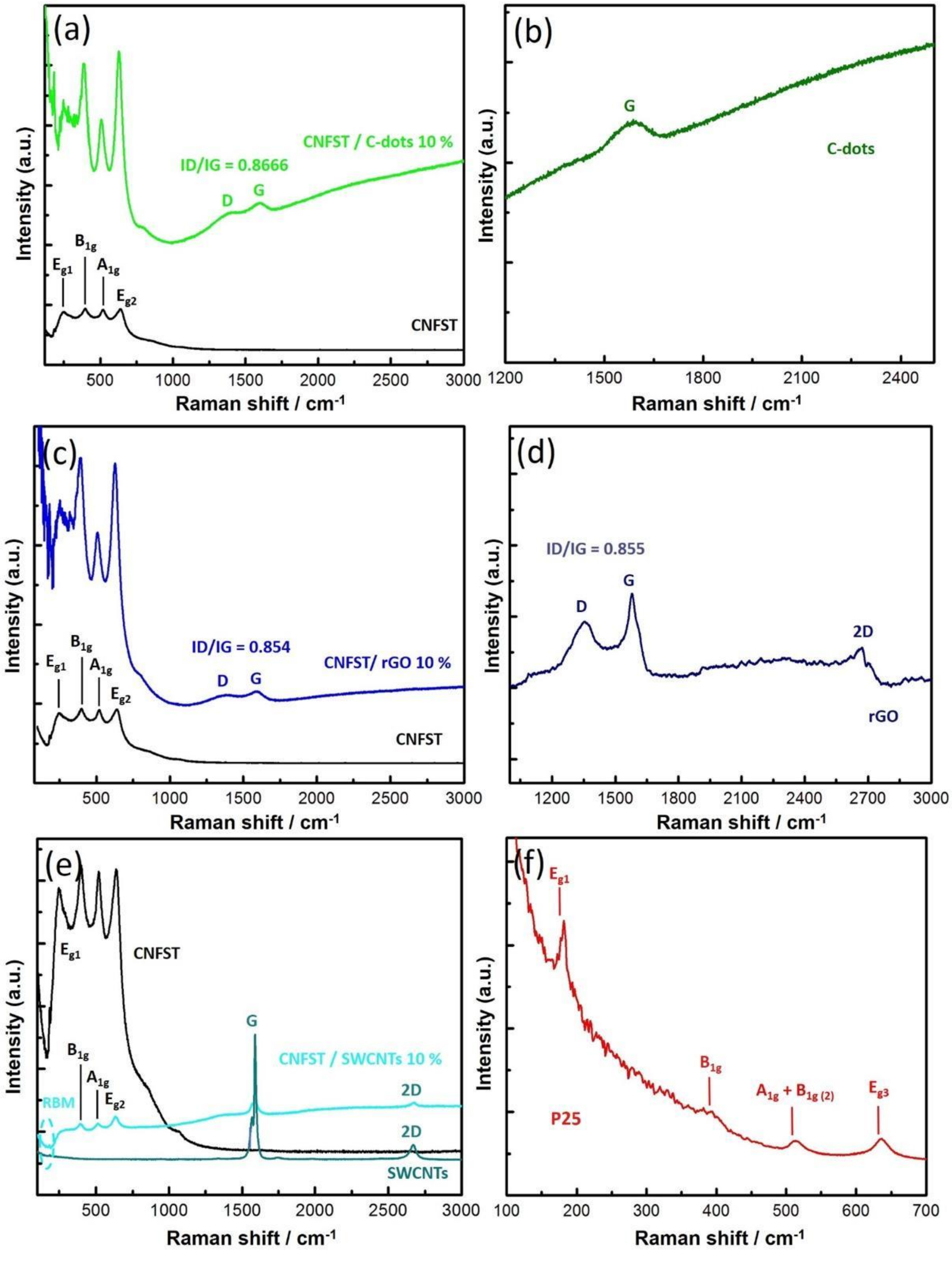

Fig. 3.10: Raman spectra of (a) CNFST and the CNFST/C-dots 10% nanocomposite, (b) C-dots, (c) CNFST and the CNFST/rGO 10% nanocomposite, (d) rGO, CNFST, SWCNTs, and the CNFST/SWCNTs 10% nanocomposite, and (f) P25.

3.4.2 Photocatalytic degradation of chloramine-T

We conducted a comparative study of CNFST/C-dots 10%, CNFST/rGO 10%, and CNFST/SWCNTs 10% nanocomposites, as applicable as photocatalysts for the decomposition of chloramine-T dye. Additionally, a pure P25 sample was used as a reference photocatalyst for comparison [160, 161]. As shown in **Figs. 3.11 (a–d)**, the distinctive absorption band of chloramine-T (about 222 nm) declined continuously with continuing irradiation by UV-light. Furthermore, the distinctive absorption band of chloramine-T in the presence of the prepared nanocomposites shifted with the irradiation time [162].

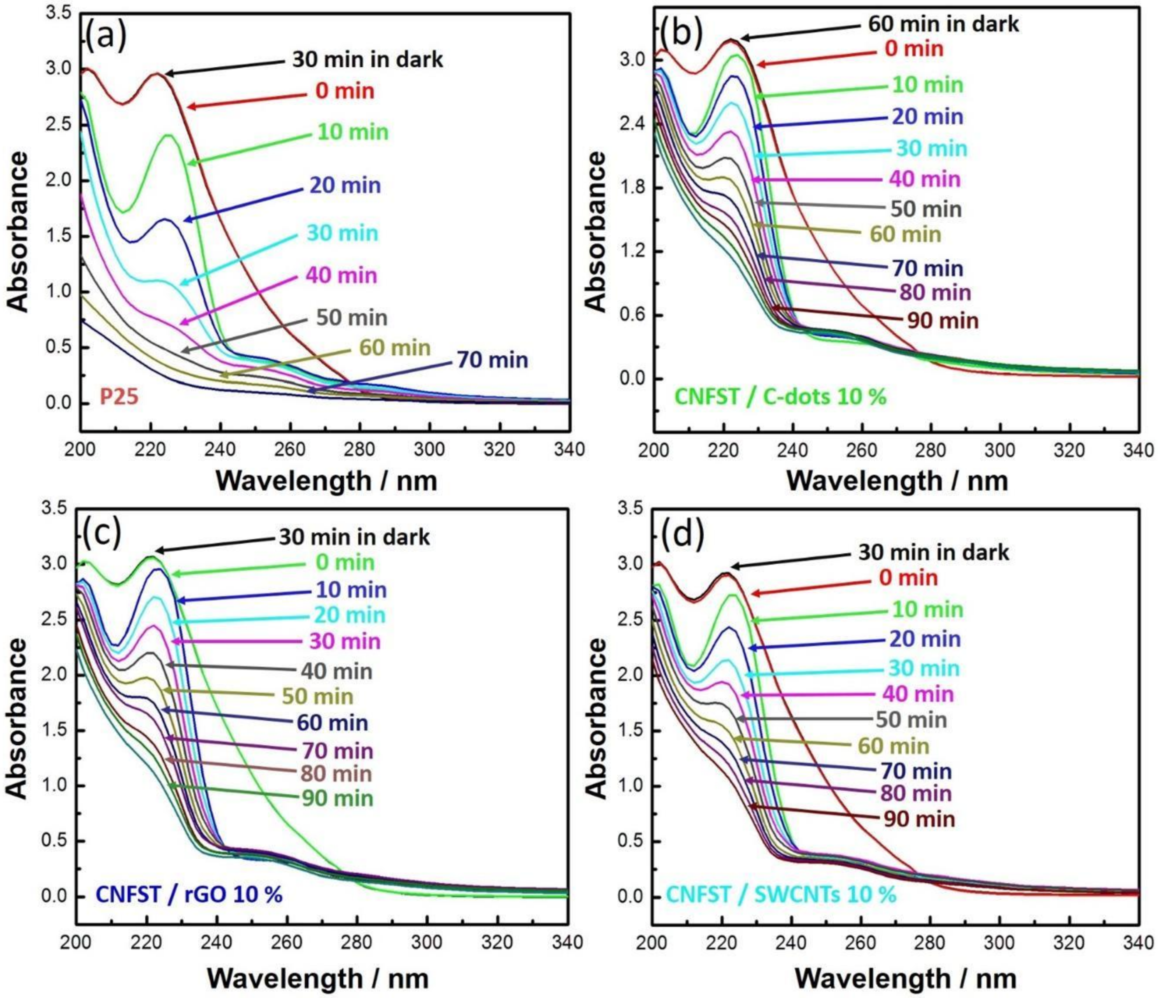

Fig. 3.11: UV–Vis. absorption spectra of the aqueous solutions of chloramine-T over (a) P25, (b) CNFST/C-dots 10%, (c) CNFST/rGO 10%, and (d) CNFST/SWCNTs 10% nanocomposites under UV irradiation.

Fig. 3.12 shows the reduction in chloramine-T dye concentration with time of UV irradiation in the presence of the photocatalysts examined. After 40 min of UV light irradiation, the CNFST/C-dots 10%, CNFST/rGO 10%, and CNFST/SWCNTs 10% nanocomposites degraded by approximately 28%, 32.7%, and 41.6%, respectively, of the initial concentration of the chloramine-T. The value for P25 was about 75%. This greater removal ability is attributed to the relatively-higher content of TiO_2 NPs, relatively smaller size of the NPs, and the greater surface area with respect to the prepared nanocomposites, as determined by EDX, TEM, and BET examination, respectively [163, 164]. In addition, as the contact time approached 90 min, the three prepared nanocomposites exhibited nearly identical ratios of chloramine-T degradation under identical conditions [165]. The CNFST/SWCNTs 10% nanocomposite, however, shows the greatest potential for photodegradation of chloramine-T with respect to the other prepared nanocomposites. This result is attributed to the relatively higher surface area of SWCNTs versus C-dots or rGO, and versus the nanocomposite employing SWCNTs, as revealed by the BET results shown in **Table 3.1** [166, 167]. In addition, the C ratio in the CNFST/SWCNTs 10% nanocomposite is higher than the ratio in the other two nanocomposites; carbon is essential for acting as an electron reservoir and thus the lifetime of the photogenerated charge carriers can be prolonged, which leads to higher photocatalytic efficiency [167, 168]. Moreover, electron mobility was likely enhanced by the large electrically conducting surface of the SWCNTs [167]. The degradation rate-constants of chloramine-T degradation by the tested samples are listed in **Table 3.2**.

Table 3.2: Apparent rate-constant values of chloramine-T degradation by P25 and the prepared nanocomposites.

Material	Apparent rate constant ($ppm^{-1}\cdot min^{-1}$)
P25	1.822×10^{-3}
CNFST/C-dots 10%	0.164×10^{-3}
CNFST /rGO 10%	0.172×10^{-3}
CNFST /SWCNTs 10%	0.184×10^{-3}

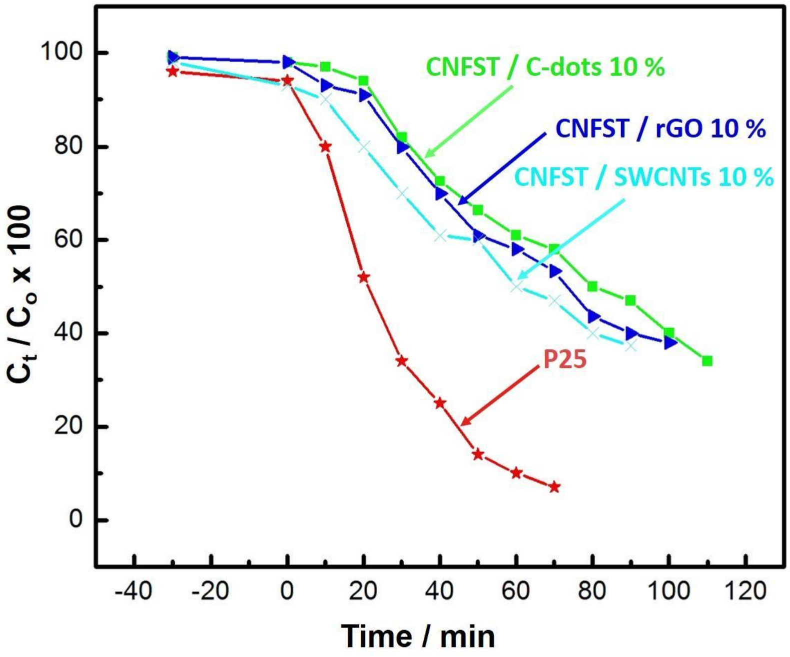

Fig. 3.12: Comparison of photocatalytic degradation of chloramine-T (conc. = 100 ppm, pH = 7, *T* = 25°C, 10 mg of photocatalyst used) by P25 and the prepared nanocomposites.

Due to their ease of preparation and cost-effectiveness, the CNFST/C-dots 10% nanocomposite was selected as the model for the remaining experiments investigating chloramine-T degradation.

In addition, a procedure for describing the sorption kinetics was carried out, where the outcomes of tests of the linearized integration of the pseudo-first and pseudo-second order models were compared [169, 170].

$$\ln ln\left(1 - \frac{q_t}{q_e}\right) =- k_1 t;\ (3.1)$$

$$\frac{t}{q_t} = \frac{1}{k_2 q_\infty^2} + \frac{t}{q_\infty};\ (3.2)$$

Where q_t is the average current concentration, q_∞ is the equilibrium current concentration in the sorbent, and *k* is the rate constant. If the experimental behaviors observed match with Eq. (1) (i.e., a greater correlation coefficient), we can expect that the degradation process is occurring via the diffusion mechanism. If they match with Eq. (2), then we can expect that the degradation process is facilitated by adsorbate-adsorbate interactions [169]. Herein, the kinetics plots for chloramine-T degradation under UV light using the prepared nanocomposites fit well with the pseudo-second-order model, indicating an inclination toward chemisorption as shown in **Fig. 3.13** [96]. In addition, the relationship between the apparent rate constant and the concentration of chloramine-T is shown in **Fig. 3.14.**

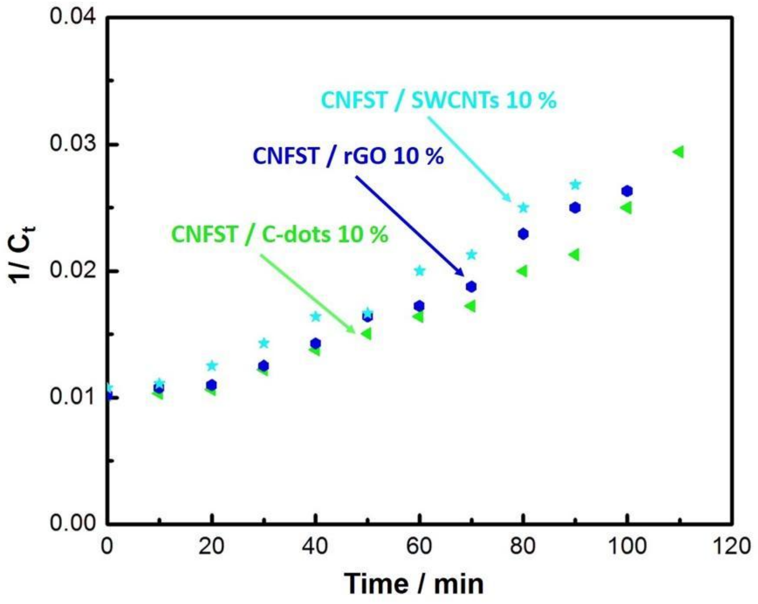

Fig. 3.13: Pseudo-second-order kinetics of the removal of chloramine-T solution (conc. = 50 ppm, pH = 7, nanocomposite dose = 10 mg, and *T* = 25°C).

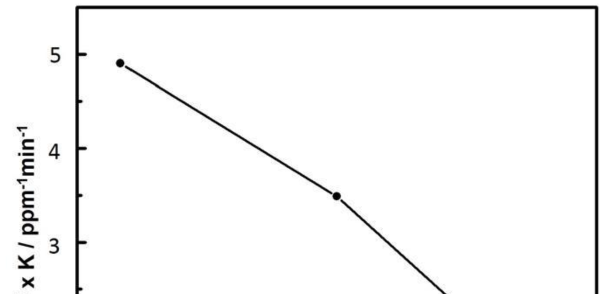

Fig. 3.14: Relationship between the apparent pseudo-second-order rate constant and the initial concentration of chloramine-T.

3.4.2.1 Influence of various parameters on the chloramine-T degradation efficiency

3.4.2.1.1 Effect of photocatalyst dosage of the CNFST/C-dots 10% nanocomposite

The influence of photocatalyst dosage on the efficiency of degradation of chloramine-T was examined by varying the dose of the CNFST/C-dots 10% photocatalyst from 5 to 15 mg in the presence of 50 mL of chloramine-T solution with an initial concentration of 100 ppm. **Fig. 3.15** shows that the photodegradation rate was enhanced by increasing the photocatalyst dosage, which confirms that the nature of this heterogeneous photocatalysis and can be ascribed to the increment of potential active sites and to the ease of free radical generation [165].

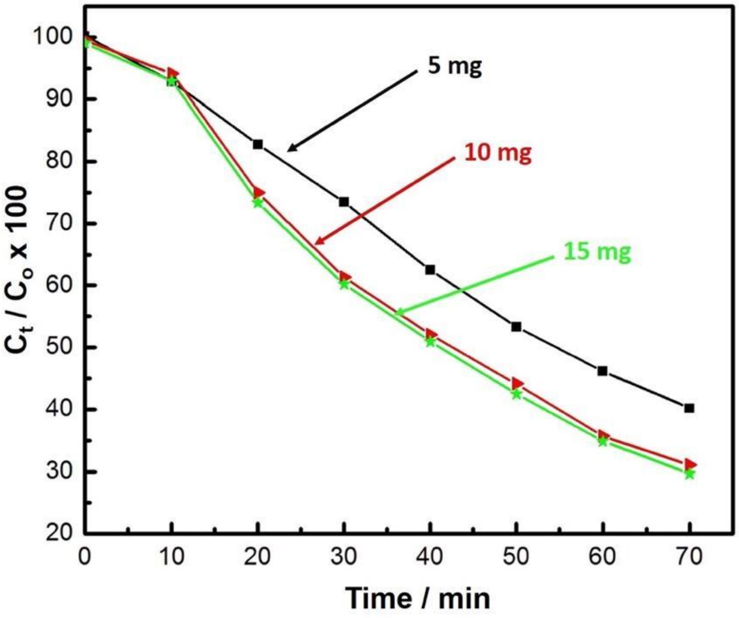

Fig. 3.15: Photocatalyst dose influence on the photodegradation of chloramine-T (conc. = 50 ppm., *T* = 25°C, and pH = 7).

3.4.2.1.2 Effect of initial chloramine-T concentration

Photocatalytic degradation of chloramine-T with different initial concentrations (50, 75, and 100 ppm) of the CNFST/C-dots 10% nanocomposite is illustrated in **Fig. 3.16**. It can be deduced that the degradation efficiency is enhanced by reducing the initial concentration of chloramine-T. In the case of 50 mg/L of chloramine-T, the removal efficiency was 70% after 70 min. However, the removal efficiency of chloramine-T with initial concentrations of 75 and 100 mg/L was lesser, at 65% and 45%, respectively, after the same time of exposure [171]. This behavior could be illustrated as a result of the insufficiency of active radical sources, and the constant amount of active photocatalyst sites could not eliminate the higher concentration of chloramine-T as effectively. The rate of photodegradation is reduced by increasing the initial concentration of chloramine-T. These results are compatible with other reports [165, 171-173].

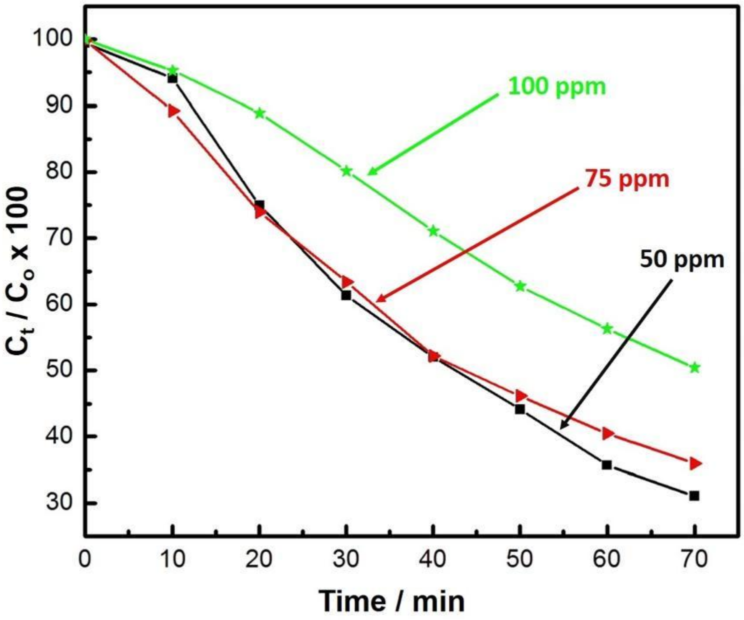

Fig. 3.16: Influence of the initial chloramine-T concentration on the photodegradation efficiency (photocatalyst dose = 10 mg, pH = 7, and *T* = 25°C).

3.4.2.1.3 Effect of pH

Solution pH was found to be a prominent parameter for determining the rate of chloramine-T photodegradation in the presence of the CNFST/C-dots 10% nanocomposite. This is understood to be because free radicals are generated due to the interfacial interactions between organic dyes and the surfaces of the photocatalysts employed, which is dependent upon the pH of the medium [174, 175]. The pH is a complex parameter since it is associated with the state of the photocatalyst surface, which affects the adsorption of chloramine-T on the CNFST/C-dots 10% nanocomposite. The effect of pH value on the photoreaction was investigated over CNFST/C-dots 10% nanocomposite and the results are represented in **Fig. 3.17 (a)**. In the alkaline solution (pH 10), degradation of 35% of chloramine-T within 70 min occurred. Whereas, chloramine-T degradation reached 58 % in the neutral solution (pH 7) after the same time. In the acidic solution (pH 3), chloramine-T concentration decreased by 65 % of its original concentration [171]. So, the activity of the CNFST/C-dots 10% nanocomposite was superior in the acidic solution and weak in the alkaline solution. As mentioned above, an acidic solution made the reaction surface of the photocatalyst to acquire opposite charge (positive charge) which is beneficial for chloramine-T adsorption on the CNFST/C-dots 10% nanocomposite [171, 176].

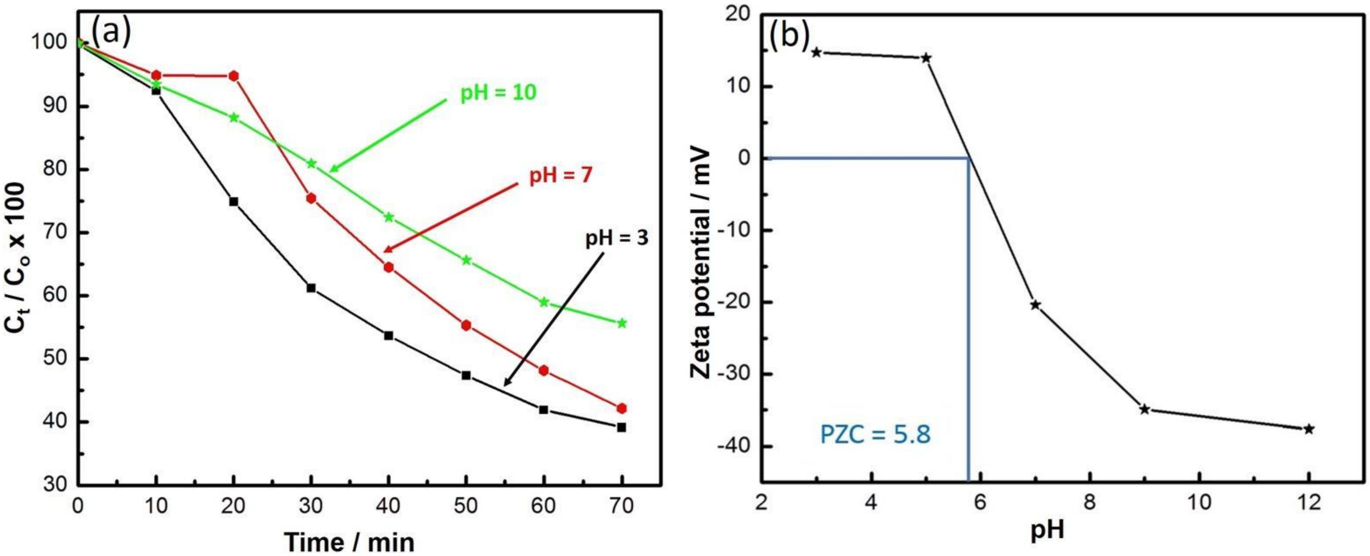

Fig. 3.17: (a) Effect of pH on the photocatalytic degradation of chloramine-T (conc. = 50 ppm, dose = 10 mg, and *T* = 25°C) and (b) point of zero charge.

Surface charge plays a significant role in facilitating the interaction between adsorbent and adsorbate [177]. Toward verifying this point, zeta potential measurements were conducted versus pH, and the results are shown in **Fig. 3.17 (b)**. The point of zero charge (pH_{PZC}) was identified in order to demonstrate the relationship between the pH and photodegradation efficiency. pH_{PZC} was calculated for different pH values from 3 to 12. In strongly acidic media (pH = 3), the composite exhibited a positive charge of approximately +15 mV; this decreased slightly at pH = 5. However, in neutral media (pH = 7), the CNFST/C-dots 10% nanocomposite exhibited a negative charge of −20 mV, while in alkaline media (pH = 9), the nanocomposite also exhibited a negative charge, in this case −35 mV. At pH = 12, the nanocomposite exhibited a negative charge of approximately −40 mV. pH_{PZC} was determined to be at a pH of 5.8. The variation in zeta potential and surface charge can be understood based on pH. During the dispersion of the CNFST/C-dots 10% nanocomposite in water, the surface displayed an anionic nature and an increment in surface area that would lead to more coverage of OH^- groups from the water. This behavior induces the production of rare H^+ ions in solution and therefore decreases the pH. The zeta potential would be negative if $pH_{solution} > pH_{PZC}$ and vice versa. As a consequence, chloramine-T can be efficiently attracted to the positively-charged surface of the CNFST/C-dots 10% photocatalyst by electrostatic attraction forces, and thereby photodegradation activity can be improved [178, 179].

3.4.2.1.4 Effect of scavengers on chloramine-T degradation

Reactive oxygen species (ROS) generation occurs by trapping photogenerated electrons or holes via various species, mainly dissolved oxygen, hydroxyl ions, and water molecules existing in the solution. The most significant ROS species are hydroxyl ($^{\cdot}OH$), superoxide ($^{\cdot}O_2^-$), and singlet oxygen ($^1O_2$). Various additives act as scavengers for one or more ROS species and for photogenerated charge carriers [180, 181]. The influence of various scavengers on the photocatalytic degradation process was investigated to evaluate the most active species. Isopropanol, methyl viologen, and benzoquinone were used to trap $OH^{\cdot}$, e^- and $O_2^{\cdot}$, respectively [180]. **Fig. 3.18** shows the efficiency of photodegradation of chloramine-T for an irradiation time of 70 min in the absence and presence of scavengers present in concentrations of 5 ppm. The efficiency decreased from 47% to approximately 43%, 41%, and 40% in the presence of methyl viologen, benzoquinone, and isopropanol, respectively. Isopropanol and benzoquinone were the most influential scavengers. The photodegradation of chloramine-T by the CNFST/C-dot 10% was reduced (40%) upon adding isopropanol, revealing that the $OH^{\cdot}$ radical was the principal species responsible for chloramine-T degradation. Also, the degradation rate was reduced upon adding benzoquinone to 41%, demonstrating that the $O_2^{\cdot}$ radical contributed significantly to chloramine-T degradation [182]. Finally, the proposed reaction mechanism of chloramine-T degradation by the nanocomposites is shown in **Fig. S.3.5**. In addition, the resulted products as a result of photodegradation of chloramine-T were discussed in detail in our recently-published manuscript [112]. To better understand the photocatalytic ability of the prepared nanocomposite, a comparison of values between it and those from recently reported articles is listed in **Table 3.3.** Where we mentioned closely-related, TiO_2-based nanocomposites against the most commonly-used dyes such as Rhodamine B and Methyl orange.

Table 3.3: Photocatalytic activity of TiO_2-based nanocomposites for the decolorization of different dyes in aqueous solutions.

Name of catalyst	Pollutant	Decolorization (%)	Ref.
MnCo–Ferrite/TiO_2	Methyl orange (MO)	73	[183]
Ni–Cu–Zn ferrite/SiO_2/TiO_2/Ag	Methylene blue (MB)	83.9	[184]
TiO_2 nanotube/rGO	Rhodamine B	78.5	[185]
ZnO-graphene-TiO2	Rhodamine B	92	[186]
$NiFe_2O_4$/SiO_2/N-TiO_2	Methyl orange (MO)	90	[187]
TiO_2–$ZrTiO_4$–SiO_2	Rhodamine B	95	[188]
CNFST/C-dots 10%	Chloramine-T	65	Current work

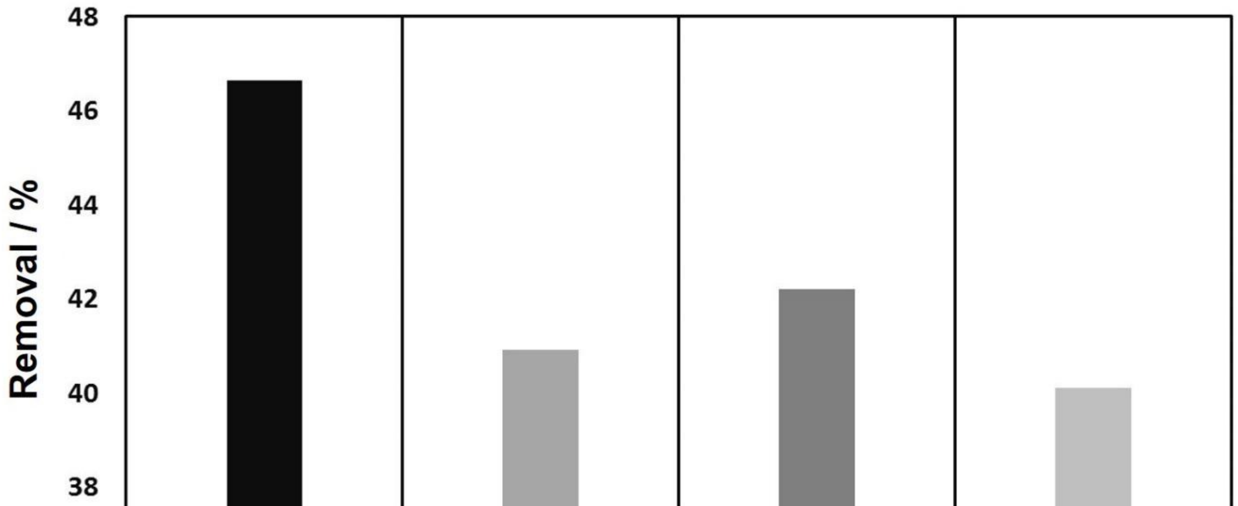

Fig. 3.18: Effect of different scavengers on photocatalytic degradation of chloramine-T (scavengers conc. = 5 ppm, chloramine-T conc. = 50 ppm, photocatalyst dose = 10 mg, pH = 7, and *T* = 25°C).

3.5 Conclusion

In this paper we described a composite matrix ($Co_{0.5}Ni_{0.5}Fe_2O_4/SiO_2/TiO_2$) that was prepared using a layer-by-layer method. The matrix was then loaded by three carbon nanomaterials. The synthesized nanocomposites were fully characterized to determine their: phase, crystallinity, morphology, elemental distribution, purity, average particle diameter, surface area, pore size distribution, effective functional groups, chemical bonding, and chemical structure. Photocatalytic degradation of organic, water-polluting chloramine-T trihydrate catalyzed by the nanocomposites was investigated and compared with P25, which exhibited a relatively higher photocatalytic efficiency due to its larger surface area and pure TiO_2 content. Additionally, kinetics studies and the effects of various parameters (photocatalyst dose, pH, chloramine-T initial concentration, and charge carrier scavenger species) were also evaluated. XRD patterns of the nanocomposites showed the phase and good crystallinity of the prepared nanocomposites. SEM analysis revealed that the CNFST matrix was uniformly distributed over the large surface area of the rGO and SWCNTs. However, C-dots were uniformly-loaded over the relatively greater surface of the CNFST matrix. EDX spectra confirmed the purity of the prepared nanocomposites. The TEM characterization revealed that the composite matrix comprised spherical grains with an average diameter of ~90 nm. Interestingly, the composite matrix was exceptionally conjugated with bundles of carbon nanotubes. Considering IUPAC classification, all samples showed a type (III) isotherm corresponding to weak adsorbate-adsorbent interactions. All samples had multimodal and broad pore-size distributions, reflecting the presence of two types of pores, mesopores and macropores. The FTIR spectra exhibited numerous peaks, among them one at 1650 cm^{-1} in the C-dots sample, and one at 1666 cm^{-1} in the CNFST/C-dots 10% sample, corresponding to the stretching vibration bands of C=O. This band was not detected in the CNFST matrix, which might be reflective of the type of bonding between the C-dots and the CNFST matrix, a covalent bond (C=O). Regarding the photodegradation of chloramine-T, its distinctive absorption bands (around 222 nm) decreased continuously with increasing UV irradiation time, and its distinctive absorption bands in the presence of the nanocomposites exhibited a significant blue shift. After 40 min of UV irradiation, the CNFST/C-dots 10%, CNFST/rGO 10%, and CNFST/SWCNTs 10% nanocomposites had degraded about 28%, 32.7% and 41.6%, respectively, of the initial concentration of chloramine-T. Kinetics plots for chloramine-T degradation under UV irradiation in the presence of the nanocomposites fit well to the pseudo-second-order model, indicating a tendency toward chemisorption. By analyzing the degradation efficiency, the photodegradation rate was found to be enhanced by increasing the photocatalyst dosage, which is attributable to the increment of potential active sites and the ease of free-radical generation. When 50 mg/L of chloramine-T was used as an initial concentration, the removal efficiency was 70% by the CNFST/C-dots 10% after 70 min. Removal efficiency for 75 and 100 $mg \cdot L^{-1}$ concentrations was 65% and 45%, respectively, under the same conditions. Additionally, the degradation efficiency decreased from 65% to 35% as the solution pH rose from 3 to 10. Under acidic conditions, degradation of chloramine-T was faster than that under neutral or alkali conditions, an effect attributed to the electrostatic interaction that occurred between the negatively-charged chloramine-T and the positively-charged CNFST/C-dots 10%, which led to an increment in the activated sites. Finally, chloramine-T photodegradation efficiency decreased from 47% to about 43%, 41%, and 40% in the presence of methyl viologen, benzoquinone, and isopropanol, respectively. This result confirmed that the $OH^{\cdot}$ radical was the principal species responsible for chloramine-T degradation. Our work informs the formulation of new nanocomposites for effective water treatment.

Chapter 4: Multifunctional metal-semiconductor-based heterojunction for superior light-assisted degradation of different dyes and microorganisms' deactivation: Theoretical and experimental study

4.1 overview

Due to modern industrialization and population growth, access to clean water has become a global challenge. In this study, a metal–semiconductor heterojunction was constructed between Cu NPs and $Co_{0.5}Ni_{0.5}Fe_2O_4/SiO_2/TiO_2$ composite matrix for the photodegradation of potassium permanganate, hexavalent chromium Cr(VI) and p-nitroaniline (pNA) under UV light. In addition, the electronic and adsorption properties after Cu loading were evaluated using density functional theory (DFT) calculations. Moreover, the antimicrobial properties of the prepared samples toward pathogenic bacteria and unicellular fungi were investigated. Photocatalytic measurements show the outstanding efficiency of the Cu-loaded nanocomposite, compared to that of bare Cu NPs and composite matrix. Degradation efficiencies of 44% after 80 min, 100 % after 60 min, and 71% after 90 were obtained against potassium permanganate, Cr(VI), and pNA, respectively. Similarly, the antimicrobial evaluation showed high ZOI, lower MIC, higher protein leakage amount, and cell lysis of nearly all microbes treated with Cu-loaded nanocomposite.

4.2 Introduction

In pursuit of a modern industrial revolution, pharmaceuticals, agricultural waste, and hazardous chemical compounds are produced. To deal with these environmental pollutants, waste disposal and management have become significant global challenges [189] . Some of the hazardous compounds that contaminate water, soil, and the environment are highly toxic and have the potential to cause serious health problems, pollutants such as potassium permanganate, chromium ions, and 4-nitroaniline or p-nitroaniline (pNA). Potassium permanganate is an inorganic dye that is used in many applications, including water treatment [190]. However, its existence in potable water may cause many chronic health problems, such as liver damage and skin irritation [191]. Chromium, which exists in water either in trivalent or hexavalent oxidation states, the hexavalent state has raised concerns due to its high toxicity [192]. Moreover, nitroaromatic compounds, such as pNA, are major water-soluble noxious pollutants that have been classified as priority contaminants by the U.S. Environmental Protection Agency [193]. In addition to this, millions of people die every year from diseases caused by waterborne pathogens (bacteria and fungi), including diarrhea, typhoid fever, and hepatitis A [47]. Recently, these microorganisms have begun to show resistance toward all currently known antibiotics, which poses a real danger to humans and marine life [194]. The aforementioned pollutants are detected in wastewater and are detrimental to aquatic organisms and may lead to long-term pollution of the environment. Therefore, eliminating these compounds from industrial wastewater is of particular importance. Many wastewater purification techniques are available, such as coagulation, flocculation, adsorption, ultra-filtration, oxidation, and membrane methods [195]. However, these techniques have many limitations as a result of their high cost, complexity, and time-consuming processes. Consequently, particulate photocatalysis has received much attention due to its outstanding photocatalytic characteristics, which include the direct conversion of light energy into chemical energy via a series of redox reactions that occur on the surface of a material known as a photocatalyst. Heterogeneous photocatalysis using semiconductor-based nanocomposites is important because it combines the effects of different nanoparticles. Titania (TiO_2)-based nanocomposites exhibit desirable advantages, such as cost-effectiveness, extraordinary efficiency, unique stability, and excellent reproducibility. The photocatalytic properties of TiO_2-based photocatalysts have been assessed in the degradation of many organic compounds, with the majority of them displaying superior photocatalytic performance toward several pollutants under different conditions [196]. However, TiO_2-based photocatalysts demonstrate remarkable photocatalytic activity only under UV light due to their wide bandgap energy (3.2 eV for anatase TiO_2) [197]. In addition, the rapid recombination process of electron–hole pairs on the surface of TiO_2-based photocatalysts is another serious limitation that hinders their vast applications in water remediation. Thus, to enhance the performance of TiO_2-based photocatalysts, many tailoring methods have been carried out. Among them, the construction of a metal–semiconductor heterojunction is a promising route due to the efficient charge separation and increase in the redox reaction time [198]. The decoration of TiO_2 photocatalysts with carbon nanomaterials or noble metal particles, such as gold (Au), silver (Ag), and platinum (Pt), has been reported to enhance their photocatalytic performance [199]. Some of these noble metals (Au–Ag) also act as co-catalysts to improve the absorption of photocatalysts in the visible light range [200]. However, the utilization of such metals is limited due to their extraordinary cost, toxicity, and low natural abundance. In the same context, copper (Cu) is more abundant, cost effective, eco-friendly, and exhibits photocatalytic properties, and can be employed as a co-catalyst to prevent rapid electron–hole recombination [201]. To further increase the efficiency of TiO_2 NPs, the utilization of a SiO_2 matrix to enhance the absorption capability of TiO_2 and to provide a framework for the dispersion of TiO_2 particles has been studied. Excellent adsorption capability has been shown to improve the photoactivity of a TiO_2/SiO_2 system [202]. At the same time, the uniform distribution of TiO_2 NPs onto a SiO_2 matrix has been shown to lead to an enhancement in the composite specific surface area [203, 204], as well as the increased thermal stability of TiO_2 NPs. In heterogeneous photocatalysis, it is difficult to separate the employed photocatalyst from wastewater streams. Consequently, more interest has been directed toward the utility of nanocomposites with magnetic cores for water treatment applications, as these can be readily removed from water using a magnet [117]. Among these magnetic materials, spinel nickel–cobalt ferrite ($NiCoFe_2O_4$) has been extensively used in diverse applications, such as gas sensing, water desalination, energy storage, radar, and stealth applications [205], due to its excellent chemical and thermal stabilities, as well as its superparamagnetism [206]. Besides this, it exhibits excellent permeability, significant saturation magnetization, and soft coercivity. These properties are essential for exploring its feasibility in several possible industrial and environmental applications [207]. Herein, the optimized preparation of a recyclable, magnetic $Co_{0.5}Ni_{0.5}Fe_2O_4/SiO_2/TiO_2$ (CNFST) nanocomposite matrix via a layer-by-layer method is reported. Cu NPs were loaded onto the external surface of the prepared matrix (TiO_2 layer) to construct a metal–semiconductor heterojunction of the $Co_{0.5}Ni_{0.5}Fe_2O_4/SiO_2/TiO_2/Cu$ 10% (CNFST/Cu 10%) enhanced photocatalyst. The photocatalytic properties of the prepared photocatalyst were examined in the photodegradation of aqueous solutions containing three different types of pollutants (potassium permanganate (an inorganic dye), hexavalent chromium (a heavy metal), and p-nitroaniline (pNA, an organic dye)) under UV-light radiation. In addition, the electronic and adsorption properties of the photocatalyst were analyzed via density functional theory (DFT) analysis. Finally, the antimicrobial activities of the prepared photocatalyst were evaluated against many multi-drug-resistant bacteria and pathogenic fungi and the results compared with those of standard antibacterial and antifungal agents.

4.3 Materials and methods

4.3.1 Materials

The starting reagents copper acetate monohydrate (($C_4H_8CuO_5$)•H_2O), ascorbic acid ($C_6H_8O_6$), hydroxypropyl cellulose (molecular weight = 80,000), ammonium hydroxide 28% (NH_4OH), sodium hydroxide (NaOH), cobalt chloride ($CoCl_2$), titanium(IV) isopropoxide 97% ($Ti(OC_3H_7)_4$), nickel chloride ($NiCl_2$), hydrochloric acid (HCl), ferric chloride ($FeCl_3$•$6H_2O$), absolute ethanol 99.9% (C_2H_5OH), tetraethyl orthosilicate 98% (TEOS) (Si•$(OC_2H_5)_4$), ethylenediaminetetraacetic acid ($C_{10}H_{16}N_2O_8$, EDTA), sulfuric acid (H_2SO_4), potassium permanganate ($KMnO_4$), potassium dichromate ($K_2Cr_2O_7$), and pNA ($C_6H_6N_2O_2$) were purchased from Sigma Aldrich-Germany, Wako-Japan and Merck-USA. Chemicals were of extra pure grade and used as received.

4.3.2 Methods

4.3.2.1 Preparation of the composite matrix ($Co_{0.5}Ni_{0.5}Fe_2O_4/SiO_2/TiO_2$), Cu NPs and Cu-loaded nanocomposite ($Co_{0.5}Ni_{0.5}Fe_2O_4/SiO_2/TiO_2/Cu$)

Detailed preparation steps of the composite matrix (CNFST), Cu NPs, and CNFST/Cu nanocomposite are presented in supplementary materials and are shown in **F. S. 4(1-3)**.

4.3.2.2 Characterization of the prepared samples

The crystallinity and formed phases of the photocatalyst samples were analyzed by X-ray diffractometry (XRD) using an Ultima IV X-ray diffractometer (Rigaku, Japan) operated at 40 kV and 30 mA using CuK_α radiation (λ = 1.54 Å). The atomic composition and chemical states were investigated using X-ray photoelectron spectroscopy (XPS) on a PHI Quantera SXM scanning X-ray microprobe (ULVAC-Phi, Inc., Japan). In addition, the external morphologies, purities, and mass compositions of the prepared samples were evaluated via scanning electron microscopy (SEM) and energy-dispersive X-ray spectroscopy (EDX) (SU8000 Type II - HITACHI high technologies, Japan). Transmission electron microscopy (TEM) (JEM-2100F (JEOL Ltd., Japan) was used to determine the average particle size and crystallographic planes calculations, while scanning tunneling electron microscopy (STEM) analysis was carried out to reveal the distribution of Cu on the composite matrix. A Tristar II (Micromeritics, Japan) instrument was used to estimate the surface areas and porosities of the photocatalyst samples, facilitated by Brunauer–Emmett–Teller (BET) and Barrett–Joyner–Halenda (BJH) analyses. Fourier-transform infrared (FTIR) analysis using the potassium bromide (KBr) method was conducted to reveal the type of chemical bonding using an FTIR 3600 Jasco infrared spectrometer (Japan). Raman spectroscopy (NRS-3100, Jasco, Japan) was performed to investigate the chemical structures, molecular interactions, and polymorphism of the photocatalyst samples. The stability of the prepared samples was analyzed by carrying out zeta potential calculations using an ELS-Z1NT instrument (Photal Otsuka Electronics, Japan). Finally, diffuse-reflectance analysis and calculations using the Kubelka−Munk equation were employed to determine the absorption and bandgap energy using a V-670 spectrophotometer (Jasco, Japan).

4.3.2.3 Photocatalytic degradation and antimicrobial activity evaluation

Detailed experimental steps for the evaluation of both Photocatalytic and antimicrobial performance of the prepared samples are shown in supplementary materials.

4.4 Results and discussion

4.4.1 Characterization of the prepared samples

XRD analysis of the prepared samples shows strong and intense peaks, indicating their crystallinity as shown in **Fig. S. 4.4**. For Cu NPs, several diffraction peaks were recorded at 2*θ* = 44.3°, 50.4°, and 74.3°, which correspond to the (111), (200), and (220) lattice planes, and are a good match to the standard peaks of Cu (JCPDS no. 71-4610) [208]. In addition, this recorded pattern confirms the formation of a face-centered cubic (FCC) crystal structure, which is in good agreement with the selected area electron diffraction (SAED) analysis **Fig. 4.1(c)**. While, the diffraction peaks of bare composite matrix (CNFST) were recorded at 2θ = 25.3°, 36.1°, 37.4°, 38.5°, 48.5°, 54.6°, 55.4°, 64.8°, 69.8°, 71.58°, and 75.6°, which correspond to the (101), (103), (004), (112), (200), (105), (211), (204), (116), (220), and (215) crystallographic planes, respectively. The recorded diffraction peaks and their corresponding planes can be mainly attributed to anatase TiO_2 (JCPDS 21-1272) [124, 125], the principal external layer of the

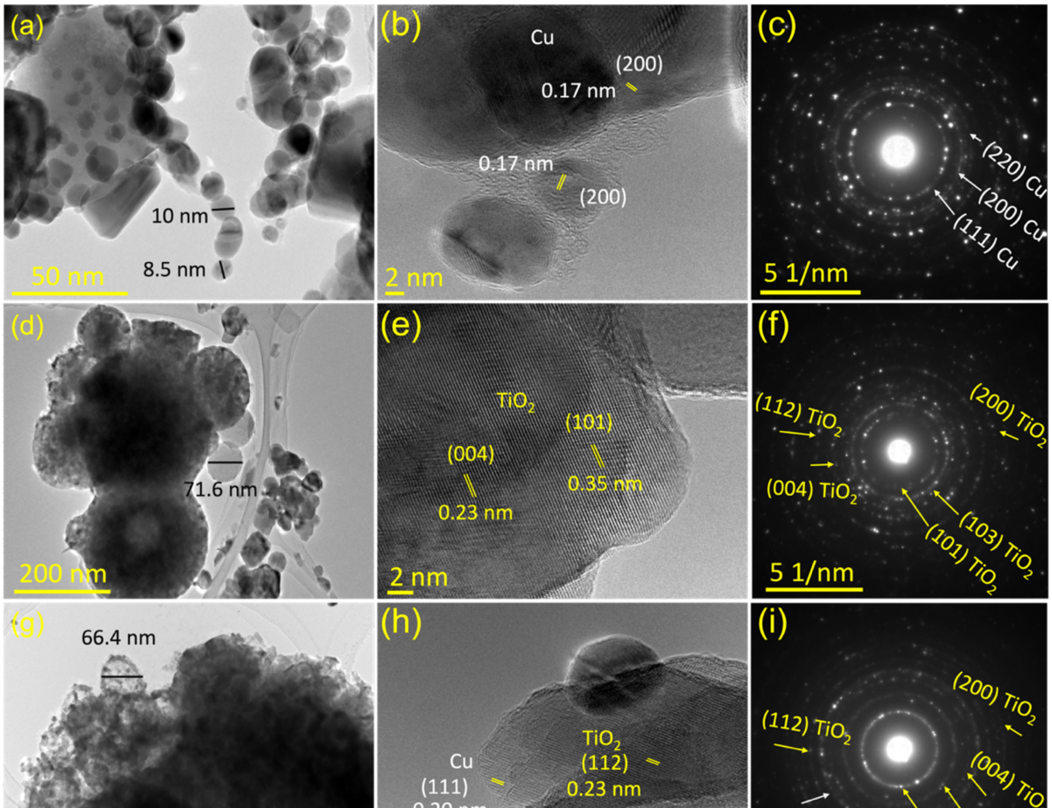

composite matrix. This conclusion was confirmed from the mass percentage analysis of the EDX **Fig. S. 4.5(b-d)** and atomic percentage analysis using XPS (**Fig. 4.3**). A combination of peaks of the bare composite matrix and Cu NPs can be observed in the pattern of the Cu-loaded composite (CNFST/Cu), indicating their conjugation, as supported by the SEM observation **Fig. S. 4.5(c)**, STEM mapping **Fig. S. 4.5(f)**, and TEM analysis **Fig. 4.1 (g)**. It is worth mentioning that a small amount of the loaded Cu NPs over the CNFST surface was oxidized into Cu_2O (JCPDS No. 05-0667) [209], which is indicated by two small peaks at 36.8° (111) and 42.3° (200) in the XRD pattern. Finally, the calculated crystal sizes from Scherrer equation were 38.29, 16.04, and 22.78 nm for the Cu NPs, CNFST, and CNFST/Cu samples, respectively. (**Fig. S. 4.5)** shows SEM-observed surface morphology and EDX mass percentages of the bare CNFST and CNFST/Cu nanocomposite. It is obvious that bare CNFST composite matrix exhibits homogeneous spherical-shaped structures as presented in

Fig. S 4.5(a). While its EDX analysis confirms that Ti has the highet mass ratio, followed by O forming the external TiO_2 layer of CNFST nanocomposite. In addition, SEM observations reveal that Cu NPs are uniformly distributed as clusters on the external layer of the CNFST matrix as shown in **Fig. S. 5(c)**. These results are in a good agreement with STEM mapping shown

in **Fig. S. 4.5(f)**. While, **Fig. 4.1(a, d,** and **g)** show the TEM analysis of the prepared Cu NPs, bare CNFST matrix, and CNFST/Cu 10% nanocomposite, respectively. The Cu NPs and matrix particles are almost spherical in shape, with average diameters of around 9 and 70 nm, respectively. The CNFST/Cu nanocomposite exhibits almost the same average diameter as that of bare CNFST sample. The high-resolution TEM (HR-TEM) images confirm the conjugation of Cu NPs with TiO_2 layer as shown in **Fig. 4.1(h)**, because of the presence of characteristic crystallographic planes of both Cu and TiO_2 that have d-spacings of 0.17 nm (200) and 0.20 nm (111) for Cu NPs, and 0.238 nm (004) and 0.233 nm (112) for the TiO_2 NPs. It is worth mentioned that the observed lattice fringes shown in **Fig. 4.1 (e)** and **(h)** can be ascribed to the anatase TiO_2, confirming that TiO_2 is the main layer of the composite matrix, and matching both XRD and EDX results. Finally, analysis of SAED patterns confirms the formation of Cu NPs with a FCC crystal structure as shown in **Fig. 4.1(c)**, the dominance of anatase TiO_2 in the nanocomposite matrix, as shown in **Fig. 4.1(f)**, and the conjugation of the Cu NPs with TiO_2 to form the CNFST/Cu nanocomposite, as shown in **Fig. 4.1(i)**.

Fig. 4.1: TEM analyses, HR-TEM observations, and SAED patterns of the (a–c) Cu NPs, (d–f) CNFST matrix, and (g–i) CNFST/Cu 10% nanocomposite.

N_2 adsorption–desorption isotherms and BJH pore size distribution analysis are shown in **Fig. S.4.6**. According to the IUPAC classification, the bare CNFST matrix exhibits a type III adsorption isotherm, indicating the weak interactions between the adsorbate and adsorbent (N_2 gas and CNFST), as shown in **Fig. S. 4.6(a)**. However, upon loading Cu NPs over the CNFST matrix, the adsorption type changes from type III to V, which pointing out to the formation of mesopores (2-50 nm). In addition, the resultant nanocomposite shows an improved surface area, as shown in **Table 4.1**.

Table 4.1: Calculated BET surface areas, pore areas, and pore volumes of the prepared samples.

No.	**Sample**	**BET Surface area (m^2/g)**	**Pore volume (cm^3/g)**	**Pore area (m^2/g)**
1	CNFST	4.78 ± 0.05	0.0008	1.63

2	CNFST / Cu 10 %	11.34 ± 0.08	0.0007	1.54

While, Fig. S. 4.6(b-c) shows the BJH pore size distributions of the samples. The prepared samples exhibit both multimodal and wide porosity distribution. On the one hand, bare CNFST matrix showed 2 weak peaks in the mesoporous region (2-50 nm) and large increasing portion in the macroporous region (> 50 nm). On the other hand, CNFST/Cu nanocomposite possessed larger ratio of mesopores and less decreasing volume of macropores. As a result of the formation of more mesopores after Cu loading, the observed surface area was improved. **Table 4.2** shows the zeta potential values, net charge, and corresponding stability of the prepared samples. it can be seen that Cu NPs exhibit net positive charge and high tendency to be agglomerated in aqueous solutions, while the negatively-charged CNFST matrix shows moderate stability that can be attributed to its higher zeta potential value [210]. Finally, CNFST/Cu nanocomposite exhibited a net positive charge, and its zeta potential and stability index was found to be in the middle between both samples [194].

Table 4.2: Zeta potentials and the corresponding colloidal stability of the prepared samples.

No.	**Sample**	**Zeta potential (mV)**	**Stability**
1	Cu	+ 4.22	Strong agglomeration
2	CNFST	- 38.62	Moderate stability
3	CNFST / Cu 10 %	+ 22.08	Incipient instability

Chemical bonding and functional groups of the prepared samples were revealed by FTIR spectra, shown in **Fig. S. 4.7**. The absence of Cu–O stretching vibrations suggests that, the volume fraction of Cu oxide is very small, and Cu NPs were loaded onto the TiO_2 surface via weak electrostatic van der Waals forces. **While,** XPS analysis was carried out to investigate the chemical states and to estimate the atomic ratios of the main elements constituting CNFST/Cu nanocomposite, as shown in **Fig. 4.2(a–d)**. **Fig. 4.2(a)** shows the survey XPS spectrum of the nanocomposite, from which multiple peaks corresponding to all constituting elements were recorded. **Fig. 4.2(b–d)** show the deconvoluted peaks of the main elements, Cu, Ti, and O. For Cu 2p three peaks were detected, one at 951.6 eV and two peaks at 932.3 and 933.9 eV, which are characteristic of metallic copper Cu(o) or Cu(I) and Cu(II), respectively [211]. This confirms the presence of oxidized Cu on the surface of the nanocomposite, matching XRD analysis. For Ti 2p, two peaks at binding energies of 464.5 and 458.2 eV can be observed that confirm that the Ti^{4+} state is dominant in the TiO_2 layer [151]. Finally, O 1s is represented by two peaks, one at 531.3 eV, which is due to the presence of hydroxyl groups on the surface of the composite or adsorbed water molecules, and the second at 529.6 eV corresponding to metal oxides of Ti and Cu. In addition, the observed shoulder (> 531.3 eV) toward higher binding energies corresponds to a large number of oxygen vacancies that are present on the surface of the material, which is favorable for increased photocatalytic efficiency due to them acting as electron reservoirs [212, 213].

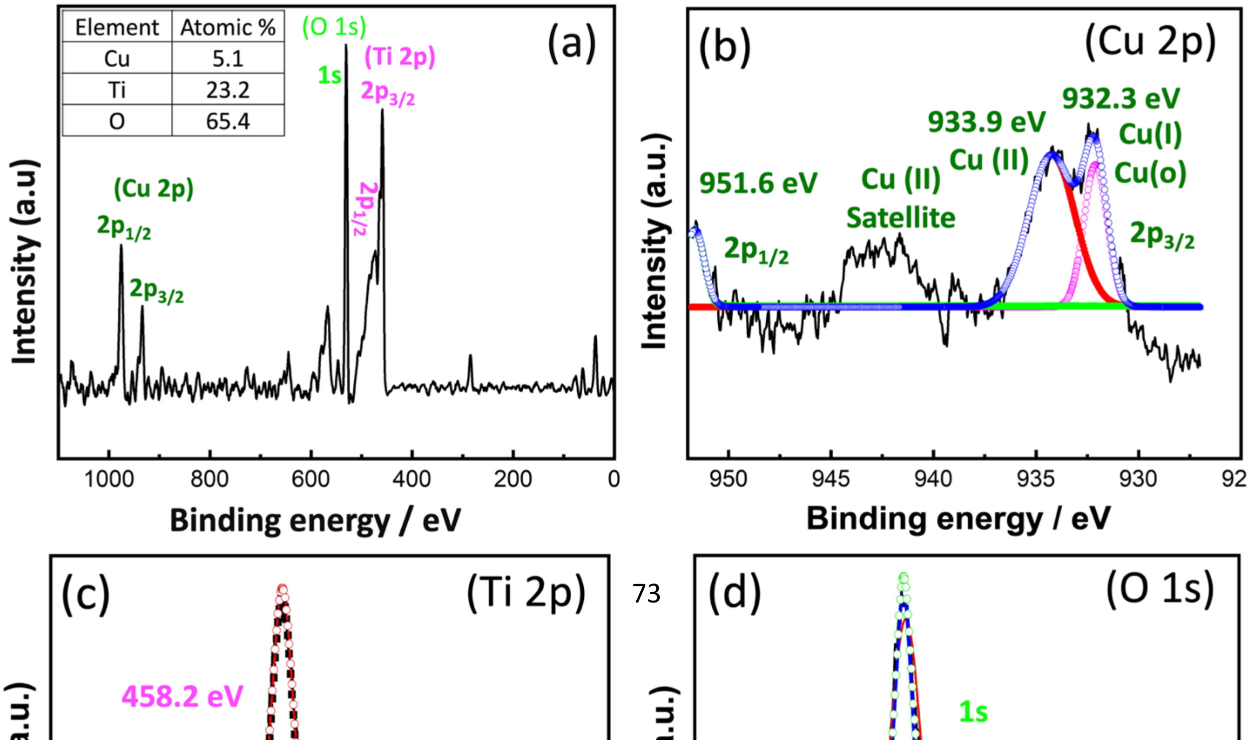

Fig. 4.2: XPS a) survey analysis and atomic ratios and b) deconvoluted Cu 2p, c) Ti 2p, and d) O 1s spectra.

Finally, diffuse-reflectance spectra were recorded, and bandgap energy values were calculated using the Kubelka–Munk equation as shown in **Fig. 4.3**. Both nanocomposites exhibit absorption in the UV region at around 350 nm **Fig. 4.3 (a)**, while bandgap calculations show that, upon Cu loading the bandgap energy slightly increased from 3.1 to 3.15 eV, as presented in **Fig. 4.3(b)**. This result may be attributed to the fact that Cu NPs absorb visible light, and that the absorption wavelength range overlaps with that of TiO_2, affecting the extrapolation used to calculate the bandgap energy value.

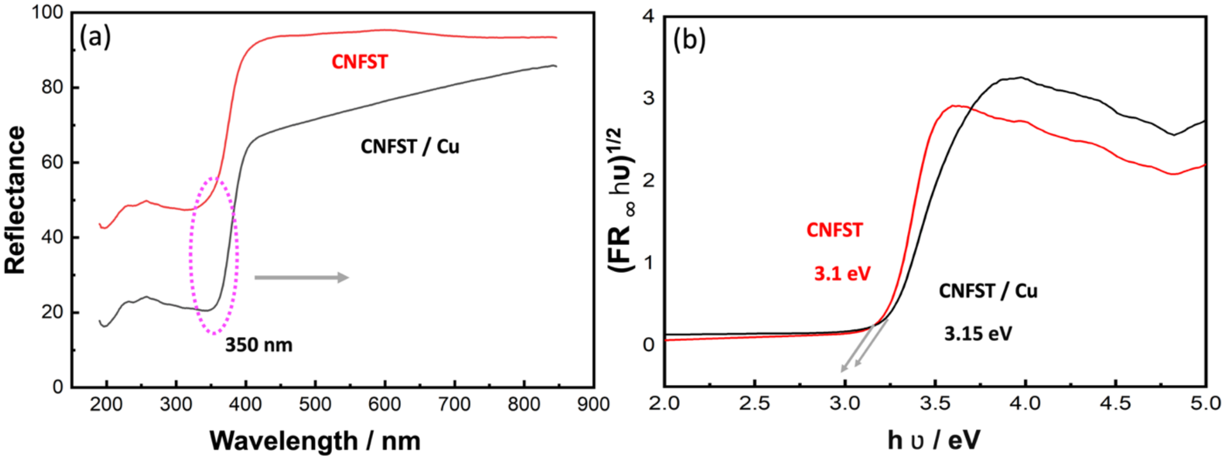

Fig. 4.3: a) Diffuse-reflectance spectra of the CNFST and CNFST/Cu 10% nanocomposites and b) bandgap energy calculations acquired using the Kubelka–Munk equation.

4.4.2 Photocatalytic activity of the prepared samples

4.4.2.1 Potassium permanganate degradation (inorganic dye)

Fig. 4.4(a–c) shows a comparison of the photocatalytic degradation of potassium permanganate inorganic dye by the prepared samples along with dye photolysis and dye removal due to adsorption in the dark. From the graph, it can be clearly observed that in the absence of the prepared samples the employed UV light degrades only around 11% of the dye after 4 h, as shown in **Fig. 4.4(a)**, while adsorption in the dark leads to almost 17% removal of the dye at the same time, as shown in **Fig. 4.4(b)**. However, photocatalytic removal by the prepared samples is more efficient, as shown in **Fig. 4.4(c)**. The prepared CNFST/Cu sample shows the highest dye removal efficiency, with around 44% dye removal after only 80 min. This improved photocatalytic activity can be ascribed to the synergistic effect between the Cu NPs and the prepared CNFST nanocomposite.

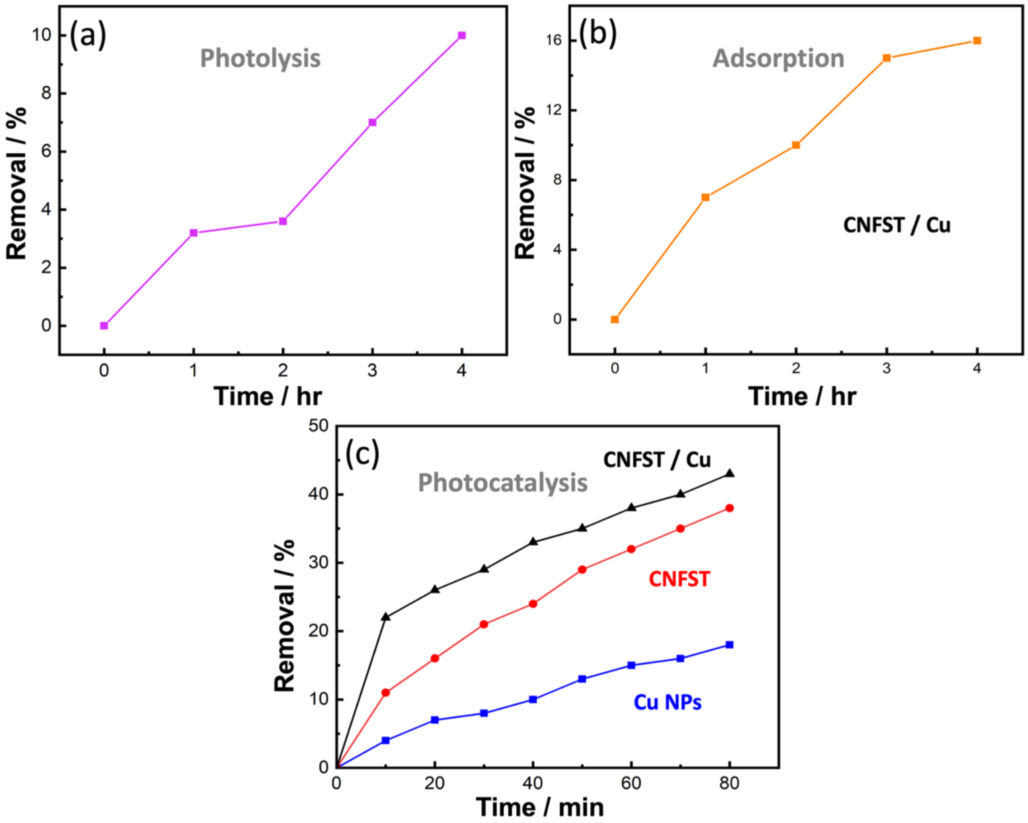

Fig. 4.4: Potassium permanganate degradation by a) photolysis (no photocatalysts), b) adsorption in dark (no light), and c) photocatalytic degradation by the prepared samples under UV irradiation.

4.4.2.2 Chromium(VI) reduction

The photocatalytic reduction of chromium ions by the prepared samples was investigated at different pH values in the range of 2–5 using 1 mM of EDTA as a hole scavenger, with the results shown in **Fig. 4.5(a–b)**. Similarly, the CNFST/Cu sample exhibits much more enhanced Cr(VI) reduction efficiency compared to the bare CNFST nanocomposite and the Cu NPs. **Fig. 4.5(a)** reveals that almost 57% of Cr(VI) ions were reduced to Cr(III) ions after 120 min at pH 5 compared to only 19% and 25% by the Cu and bare CNFST nanocomposite, respectively, while at pH 2, the CNFST/Cu sample exhibits superior Cr(VI) reduction ability, with almost 100% of Cr(VI) being reduced after 60 min, as revealed in **Fig. 4.5(b)**.

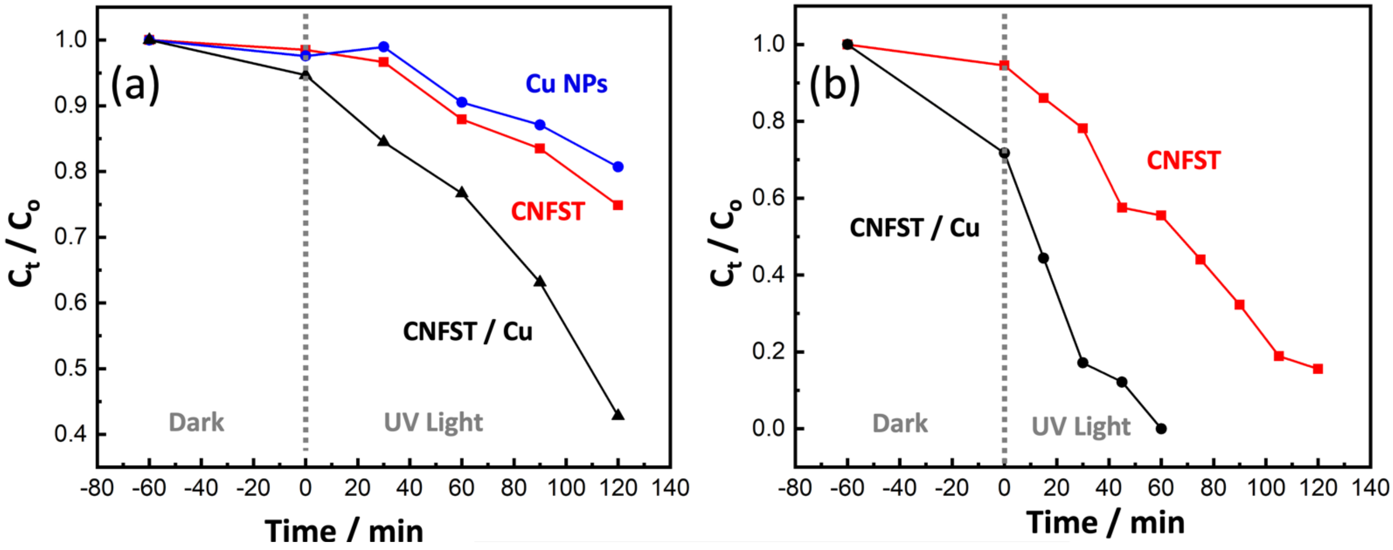

Fig. 4.5: Cr(VI) reduction evaluation a) 10 mg of photocatalyst, 20 ppm of a Cr(VI) solution at pH 5 and 1 mM of EDTA, and b) 20 ppm of a Cr(VI) solution at pH 2 and 1 mM EDTA.

4.4.2.3 pNA degradation (organic dye)

It can be clearly observed from **Fig. 4.6(a)** that the degradation of pNA due to photolysis after 4 h was only 9%, while the removal due to adsorption in the dark was around 18% after the same amount of time, as shown in **Fig. 4.6(b)**. While, **Fig. 4.6(c)** shows the progressive decline in the absorption peaks (at λ_{max} = 380 and 230 nm) due to photodegradation by the CNFST/Cu photocatalyst under UV irradiation [162]. **Fig. 4.6(d)** shows that CNFST/Cu photocatalyst possesses the highest photocatalytic activity (65% removal) toward pNA compared to bare Cu dots (22% removal) and the bare CNFST nanocomposite (26% removal), after 90 min under UV irradiation. This improved photocatalytic efficiency can be attributed to the effect of the constructed metal–semiconductor heterojunction of the nanocomposite, which facilitates charge separation and the absorption of incident light. In addition, it features a relatively higher surface area (11.34 m^2/g) and a network of mesopores that facilitate the photocatalytic reaction, as confirmed from the BET surface area and porosity analyses.

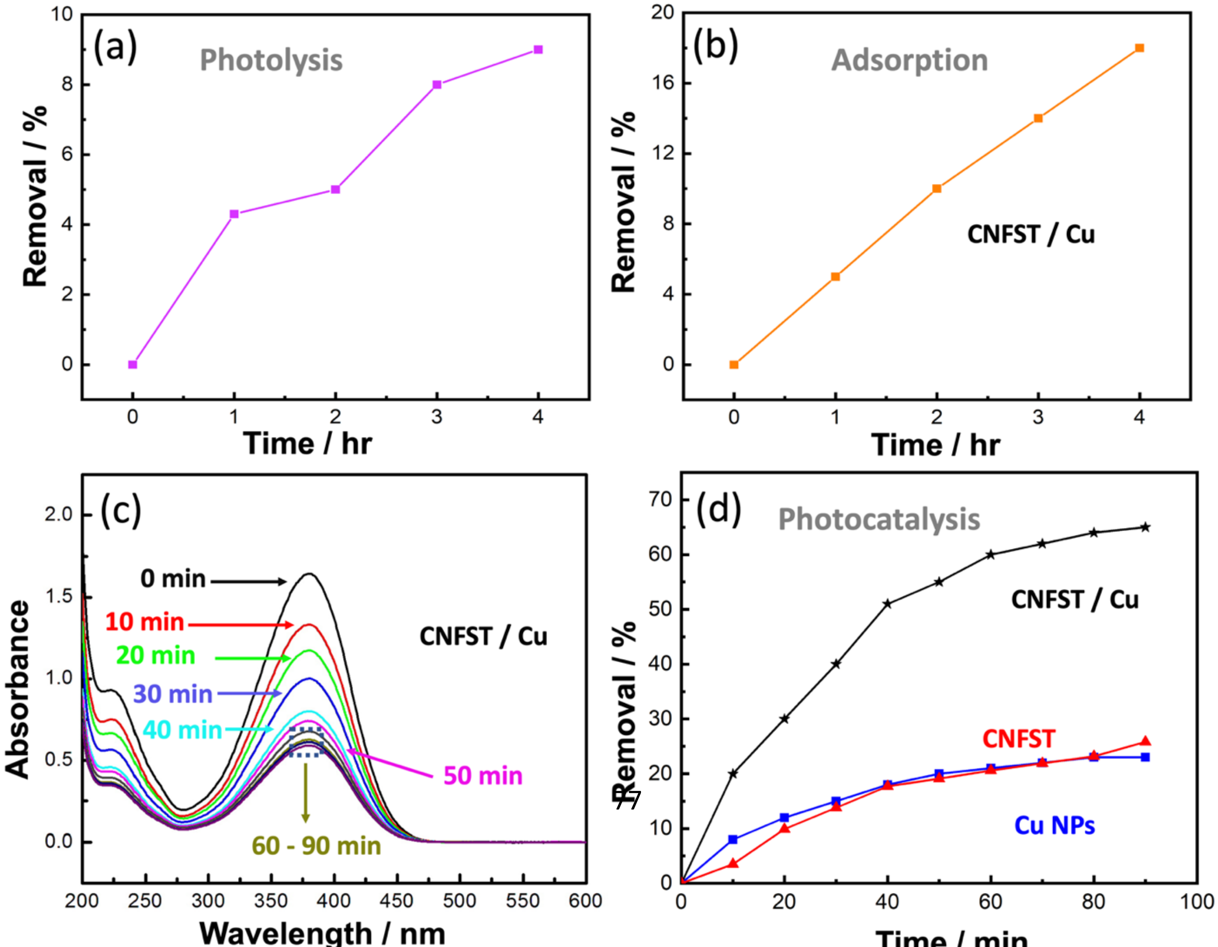

Fig. 4.6: Removal of pNA by a) photolysis, b) adsorption, c) absorbance reduction with time due to the CNFST/Cu nanocomposite, and d) a comparison of the photocatalytic degradation of the prepared samples.

4.4.2.3.1 Effect of the photocatalyst dose and initial pNA concentration

The effects of photocatalyst dose and initial pNA concentration on the photocatalytic performance were analyzed, as shown in **Fig. S. 4.8(a–b).** Upon increasing the photocatalyst dose from 5 to 20 mg in an aqueous solution of pNA, the percentage of pNA removal increases from 43% to 95% after 90 min of irradiation under UV light as shown in **Fig. S. 4.8(a)**. As the amount of the CNFST/Cu photocatalyst increases, there is an increase in the number of active sites available for pNA removal. In other words, by increasing the number of active sites on the surface of the employed photocatalyst, the number of absorbed photons increases, thus leading to more redox reactions and enhanced efficiency. Consequently, more charge carriers and more free radicals are likely to be generated. Secondly, it was observed that, as the initial concentration of pNA increases from 5 to 15 ppm, the percentage removal of pNA decreases from 84% to 46.67% as shown in **Fig. S. 4.8(b)**. The increase in the concentration of pNA leads to the formation of aggregates on the surface of the photocatalyst. Consequently, a few photons can reach and stimulate redox reactions over the surface of the photocatalyst, thus leading to a reduction in the degradation efficiency [214]. In addition, after a specific time the vacant sites of the CNFST/Cu photocatalyst become saturated with the adsorbed pNA molecules. Moreover, repulsive forces occur between pNA and the CNFST/Cu photocatalyst, which lead to the negligible degradation of pNA. This implies that after equilibrium case is reached, further irradiation does not lead to more degradation [215, 216].

4.4.2.3.2 Reaction kinetics and apparent rate constant

The reaction kinetics of the degradation of pNA under UV light using the prepared CNFST/Cu photocatalyst are a good fit to a pseudo first-order model, as shown in the results presented in **Fig. S. 4.9(a)**. In addition, it can be observed that the value of the reaction rate constant, *k*, decreases in line with an increase in the initial concentration of pNA, as shown in **Fig. S. 4.9(b)**, which is in a good agreement with the degradation performance results. As the concentration of pNA increases, fewer H_2O molecules are adsorbed onto the surface of the CNFST/Cu photocatalyst and the number of created hydroxyl radicals is reduced [217].

4.4.2.3.3 Effect of initial pH and the point of zero charge (PZC)

The impact that solution pH has on the elimination rate of pNA in the presence of the CNFST/Cu photocatalyst is shown in **Fig. S. 4.10(a)**. In acidic solution (pH 5), pNA concentration is reduced by 18% compared to its original concentration after 90 min under UV light, while the degradation of pNA reaches around 66% in neutral solution (pH 7). However, after the same contact time, around 71% of pNA is degraded in alkaline solution (pH 9). This result can be ascribed to the electrostatic interactions that occur between pNA molecules and CNFST/Cu photocatalyst in alkaline medium, which lead to an enhancement in the number of redox reactions that take place [171]. The pH of the PZC was recorded at pH 7.5 as shown in **Fig. S. 4.10(b)**, which implies that the surface charge of the CNFST/Cu composite is positive in the acidic medium, whereas, it possesses negative charge in the alkaline media. Furthermore, at neutral pH, surface charge is zero and the electrostatic forces that occur between the CNFST/Cu composite surface and pNA molecules can be disregarded [218]. The proposed photocatalytic reaction mechanism of the prepared CNFST/Cu photocatalyst is shown in **Fig. S. 4.11**.

4.4.3 Molecular modeling

To explain the interaction between the modified TiO_2 (external layer) and the tested pNA, DFT calculations were employed to determine the electronic and adsorption properties of TiO_2 before and after its modification using the Cu NPs [219].

4.4.3.1 Computational model and structure

DFT calculations were performed using the Gaussian 16 software at the M062X/6-31(d,p) level of theory [220]. To account for the possibility of the occurrence of van der Waals interactions between the adsorbent (TiO_2) and the adsorbate (pNA), Grimme's dispersion correction (gd3) was added to the M062X functional. As shown in **Fig. S. 4.12(a)**, the TiO_2 layer is represented by a finite nanoflake. Thus, to study the effect that adding Cu NPs and Cu oxides has on the adsorption properties of the nanoflake, Cu, CuO, and Cu_2O were attached, as shown in **Fig. S. 4.12(b–d)**. These constructed structures were then allowed to interact with pNA initially placed at 3.5 Å above them, as shown in **Fig. S. 4.12(g)**. It can be observed from **Fig. S. 4.12(f–h)** that the addition of Cu and Cu oxides improves the adsorption of pNA (with respect to the unmodified TiO_2

in **Fig. S. 4.12(e)**), because of the formation of several chemical bonds between the O and C atoms of pNA and the Cu atoms of the chemically-modified TiO_2 nanoflake. To confirm these findings, the adsorption energy (E_a) was calculated before and after the addition of Cu and its oxides, as summarized in **Table 4.3**, where E_a was calculated using the formula: $E_a = (E_{ad} + E_{pNA} - E_r)/n$, where E_{ad} is the ground state energy of the adsorbent (TiO_2, TiO_2–CuO, etc.), E_{pNA} is the ground state energy of pNA, E_r is the ground state energy of the product after adsorption, and n is the total number of atoms. From the values of E_a shown in **Table 4.3**, the attachment of Cu oxides increased the adsorption energy by double the original value before the attachment, from ~ 0.05 eV for TiO_2/pNA to 0.1 eV for TiO_2– CuO/pNA or TiO_2–CuO–Cu_2O/pNA. It is worth mentioning that the increase in the adsorption energy in the case of the TiO_2–CuO–Cu/pNA structure is unique, which can be ascribed to the closeness of the Cu atoms in this system, leading to strong interactions occurring between them, as presented in **Fig. S. 4.12(g)**.

Table 4.3: Calculated HOMO/LUMO energy gaps (E_g) and adsorption energies (E_a) of the selected structures.

Structure	E_g(eV)	E_a (eV)
TiO_2	3.73	--
pNA	6.78	--
TiO_2-CuO	3.93	--
TiO_2-CuO-Cu	3.27	--
TiO_2-CuO-Cu_2O	3.08	--
TiO_2/pNA	3.12	0.0496
TiO_2-CuO/pNA	3.68	0.0961
TiO_2-CuO-Cu_2O/pNA	2.76	0.1070
TiO_2-CuO-Cu/pNA	3.19	0.0798

4.4.3.2 Electronic density of states

The electronic density of states of Cu-modified TiO_2 before and after the adsorption of pNA is shown in **Fig. 4.7**. In this representation, the molecular orbitals are represented by Gaussian functions with a broadening of $\alpha = 0.032$ eV. The highest occupied molecular orbital (HOMO) distributions are also presented to show the effect that chemical modification and the adsorption of pNA have on this electronic orbital. The energy gap of TiO_2, as shown in **Table 4.3** and **Fig 4.7(a)**, is 3.73 eV which is slightly higher than the experimental value of 3.1 eV. This increase in the energy gap is the result of a quantum size effect, where the smaller the TiO_2 nanoflake, the higher the energy gap. Attaching one CuO molecule to the structure increased the energy gap to 3.93 eV, with this increases expected to be due to the passivation of the interactive electrons of the Ti atoms at the edge. This effect seen in **Fig. 4.7(c)** results from a decrease in the intensity of the distribution cubes on the Ti atoms around the CuO. However, further addition of Cu atoms or Cu_2O molecules decreases the energy gaps to 3.27 and 3.08 eV, respectively.

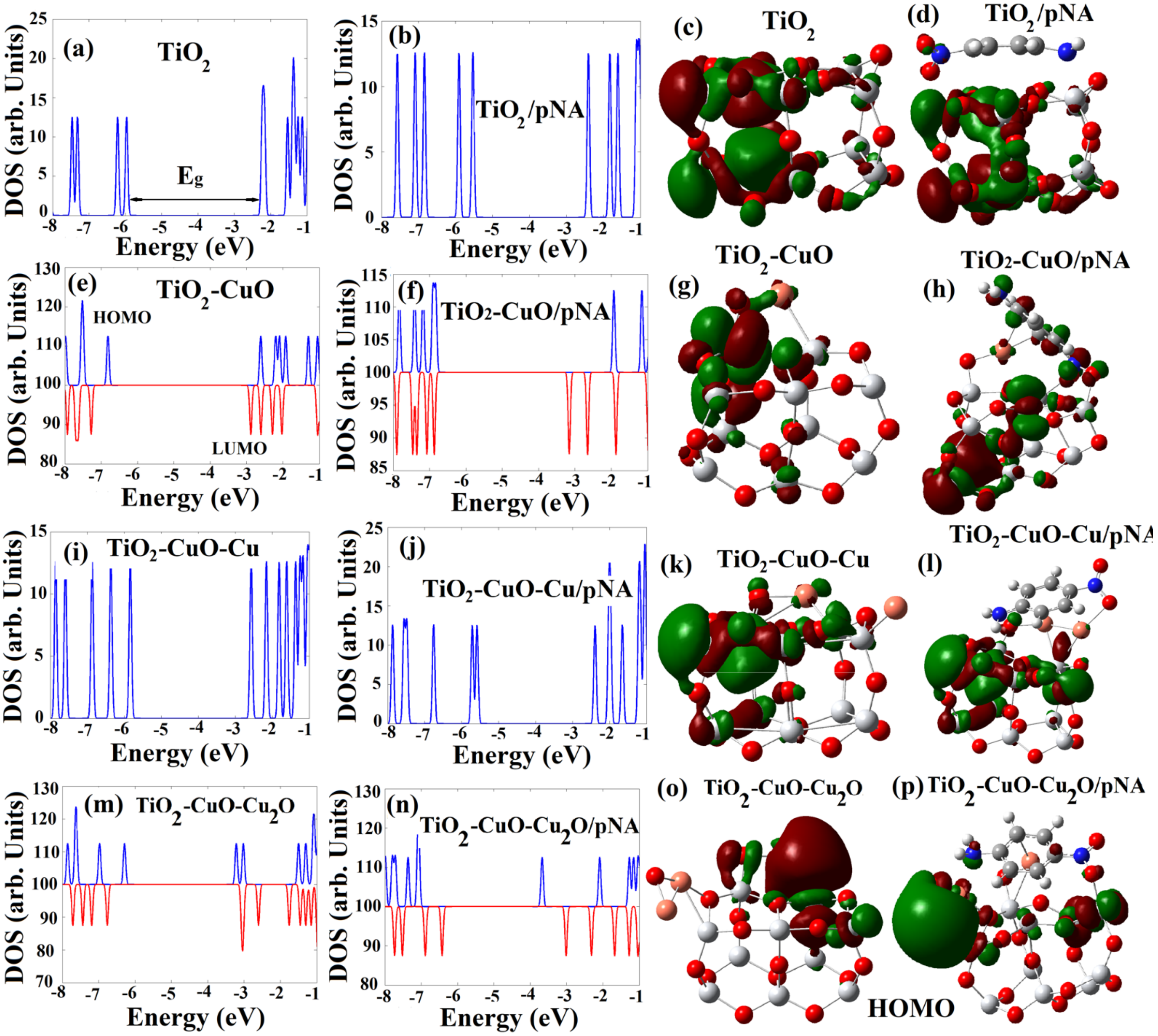

Fig. 4.7: Electronic density of states and the corresponding HOMO of the studied TiO_2-structures before and after adsorption of pNA. The blue and red peaks in the DOS spectra represent spin up and spin down molecular orbitals, respectively. Dark red and blue cubes in the HOMO distribution represent the positive and negative signs of the molecular orbital wave function.

Increasing the number of attached Cu and Cu oxides increases the interactions between them and TiO_2, leading to the creation of low-energy electronic states within the energy gap, and thus reducing it [221, 222]. For example, the HOMO of TiO_2–CuO–CuO_2 is almost located around the attached CuO. In other words, it originates from the weaker bonds between CuO and TiO_2. Therefore, Cu and Cu oxides can be used to enhance the photocatalytic properties of TiO_2 by decreasing its energy gap toward the visible light region. The energy gap further decreases after the adsorption of pNA due to the same reason, where the highest decreases to 2.76 eV for TiO_2–CuO–CuO_2/pNA corresponds to the highest interaction and thus the highest absorption. **Fig. 4.7** shows the HOMO distributions before and after the adsorption of pNA, which provides additional confirmation for the improved adsorption capability of the system upon the addition of Cu and Cu oxides. In the first case, as shown in **Fig. 4.7(d)**, the HOMO is distributed only on the TiO_2, which implies moderate physical adsorption, while in the other cases, the HOMO is distributed on both the TiO_2 and pNA due to the formation of chemical bonds between TiO_2 and pNA.

4.4.3.3 Molecular electrostatic potential (MESP)

Fig. S. 4.13. shows MESP contour maps, which indicate the computation of the surrounding charges, nucleus, and electron concentration at a particular position, using the colors red, orange, yellow, green, and blue, where red represents the lowest MESP level and blue represents the highest MESP level. The red color indicates positions with the highest electrostatic repulsion and more reactivity, whereas the blue color show positions with the lowest electrostatic repulsion. For the pNA and TiO_2 model, the red color is localized around the oxygen atoms of NO_2 and around the oxygen atoms of the TiO_2 corners. When pNA and TiO_2 interact, the color distribution of TiO_2 varies, resulting in the red color spreading around the TiO_2 oxygen atoms, reflecting the increase in the TiO_2 reactivity. Furthermore, in the case of TiO_2/CuO, the presence of CuO increases the reactivity of TiO_2, resulting in the red color being concentrated around the TiO_2 structure. The interaction of Cu with TiO_2–CuO leads to a significant change in the color distribution of TiO_2–CuO, with an increase in the red color around the oxygen atoms of TiO_2 reflecting the increase in reactivity. Meanwhile, in the case of TiO_2–CuO–CuO_2, the oxygen atoms of TiO_2 as well as those of CuO are red in color, meaning that it is more active. The color distribution of the TiO_2–CuO–Cu/pNA structure indicates an increase in reactivity around the TiO_2, as observed in the expansion of the red color around it. Finally, in terms of the interactions of pNA with TiO_2–CuO and TiO_2–CuO–CuO_2, the red color density increases across the surface of the structure, indicating that the presence of pNA enhances the reactivity of the structure.

4.4.4 Antimicrobial activity of the synthesized nanocomposites

4.4.4.1 Well diffusion methods

As presented in **Fig. 4.8** and **Table 4.4**, both nanocomposites hinder the microbial growth of the tested pathogenic bacteria and unicellular fungi. However, upon the loading of Cu NPs into the nanocomposite, the antimicrobial activity was improved. The prepared CNFST/Cu sample shows significant growth inhibition against all tested microbes (except for *P. vulgaris*) with respect to the positive control (amoxicillin and nystatin) and bare CNFST nanocomposite. It is worth mentioning that the highest antimicrobial activity of the prepared CNFST/Cu sample was recorded against the bacterial strain *S. aureus*, which led to a ZOI of around 35.6 ± 0.58 mm compared to only 20.5 ± 0.76 mm for bare CNFST sample and around 14.5 ± 0.53 mm for the positive control.

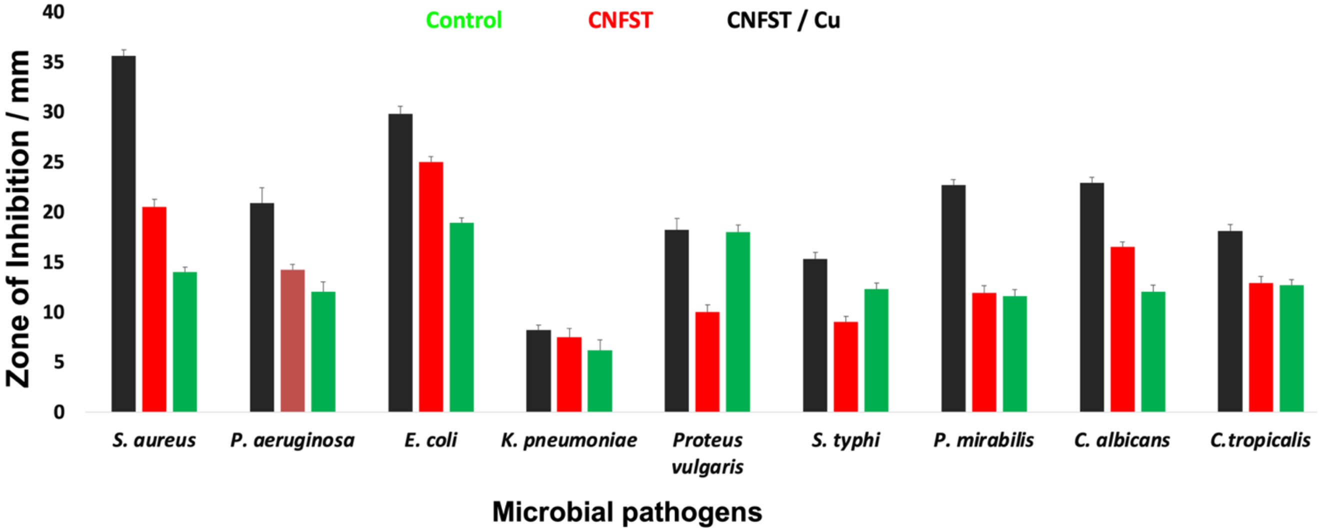

Figure 4.8: ZOI antimicrobial testing of the prepared nanocomposites against different pathogenic bacteria and unicellular fungi.

The MIC results (Table 4) show the promising application of the prepared nanocomposites as antimicrobial agents. The lowest recorded MIC concentration exhibited by the bare CNFST nanocomposite and the positive control is 0.48 µg/mL against *E. coli.* While, CNFST/Cu nanocomposite showed MIC concentration of around 0.03 µg/mL against *S. aureus.* In addition, it possessed dual functionality, acting as bacteriostatic at low concentrations, and as bactericidal at high concentrations. This enhanced activity can be attributed to the synergistic effect of the Cu NPs and the prepared CNFST nanocomposite.

Test organism	**CNFST/Cu**		**CNFST**		**Amoxicillin/Nystatin**	
	ZOI (mm)	**MIC µg/ml**	**ZOI (mm)**	**MIC µg/ml**	**ZOI (mm)**	**MIC µg/ml**
Staphylococcus aureus	35.6±0.58^{a}	0.03	20.5±0.76^{b}	7.81	14.0±0.46^{c}	250
Pseudomonas aeruginosa	20.9±1.53^{f}	7.81	14.2±0.58^{d}	62.5	12.0±1.00^{d}	250
Escherichia coli	29.8±0.76^{bc}	0.12	25.0±0.53^{a}	0.48	18.9±0.50^{a}	0.48
Klebsiella pneumoniae	8.2±0.50^{h}	250	7.5±0.87^{fg}	250	6.2±1.00^{f}	500
Proteus vulgaris	18.2±1.15^{g}	31.25	10.0±0.69^{d}	31.25	18.0±0.68^{b}	31.25
Salmonella typhi	15.3±0.64^{e}	125	9.0±0.58^{f}	125	12.3±0.61^{d}	250
Proteus mirabilis	22.7±0.52^{ef}	7.81	11.9±0.72^{e}	31.25	11.6±0.66^{c}	62.5
Candida albicans	22.9±0.58^{de}	0.48	16.5±0.50^{c}	7.81	12.0±0.70^{d}	250
Candida tropicalis	18.1±0.66^{e}	1.95	12.9±0.68^{d}	31.25	12.7±0.52^{d}	250

Table 4.4: Antimicrobial ZOI and MIC values of the prepared nanocomposites against different bacteria and *Candida* strains.

ZOI: zone of inhibition, MIC: minimum inhibition concentration. Values are means ± SD (n = 3). Data within the groups were analyzed using one-way analysis of variance (ANOVA) followed by $^{a, b, c, d, e, f, g, h}$ *Duncan's multiple range test (DMRT).*

4.4.4.2 Growth curve assay

The repression impact of the prepared nanocomposites on *S. aureus* is presented in **Fig. 4.9(a)**. the extension rate of *S. aureus* in the untreated control group is fast, with the most potent optical density (at λ = 600 nm) (OD_{600}) value of around 2.78 nm. By contrast, the OD_{600} values of the nanocomposites are lower, showing a repression impact. This performance of both nanocomposites can be attributed to two main factors. Firstly, the presence of Co– Ni ferrite NPs, which exhibit good antibacterial potential against different bacterial strains (*S. aureus, P. aeruginosa*, and *E. coli)* and unicellular fungi [143]. Secondly, the positively-charged liberated metal ions (Co^{2+},Cu^{2+}, Fe^{2+}, Ni^{2+}, Si^{2+}, and Ti^{2+}) from the prepared nanocomposite facilitate the electrostatic interactions with the negatively-charged membrane of *S. aureus* [223]. The generated ROS on the surface of the prepared samples results in protein oxidation, DNA injury, and lipid peroxidation, which destroy bacterial cells [224]. CNFST/Cu sample shows the best performance due to the presence of Cu NPs exhibiting unique antibacterial activity, as described in previous studies [225, 226]. It is worth mentioning that the higher hypersensitivity of the Gram-positive bacteria toward the nanocomposites may be explained as a consequence of their less turgid cell membrane [227].

4.4.4.3 Effect of UV activation: disinfectant potential of the prepared samples

The effect of UV activation of the prepared samples on *S. aureus* is shown in **Fig. 4.9(b)**. With respect to the untreated control group, the growth of *S. aureus* is significantly reduced after the treatment of both nanocomposites, with the CNFST/Cu sample showing excellent disinfectant potential upon UV exposure. In water and air, and upon photon absorption, active hydroxyl ($^{\cdot}OH$) and ROS (O_2^{-}, and H_2O_2) species are generated in the presence of O_2 and H_2O [228]. The ROS produced, particularly H_2O_2, can penetrate cell membranes and produce active oxidative hydroxyls via a reaction within the bacterial cells that ultimately leads to bacterial disinfection [229, 230].

4.4.4.4 Determination of protein leakage from bacterial cell membranes

The amount of protein leakage in the suspension of the treated *S. aureus* cells by the prepared samples was calculated using the Bradford method [231]. From **Fig. 4.9(c)**, it can be observed that the quantity of cellular protein leakage from *S. aureus* is proportional to the concentrations of the employed nanocomposites. Protein leakage of 205.95 and 219.58 μg/mL was detected after treatment with 1 mg/ml of CNFST and CNFST/Cu nanocomposites, respectively, confirming the strong antibacterial characteristics of the synthesized nanocomposites, and indicating the creation of holes in the cell membrane of *S. aureus* that led to the leakage of protein from the *S. aureus* cytoplasm. Related studies [232] describe comparable outcomes with ferrites, which revealed concentration-dependent destabilization in the cell membrane of bacterial cells and the leakage of their intracellular substance into the extracellular form (bacterial cell suspension). It can thus be assumed that the disruption of membrane permeability is a vital process in the repression of bacterial mass.

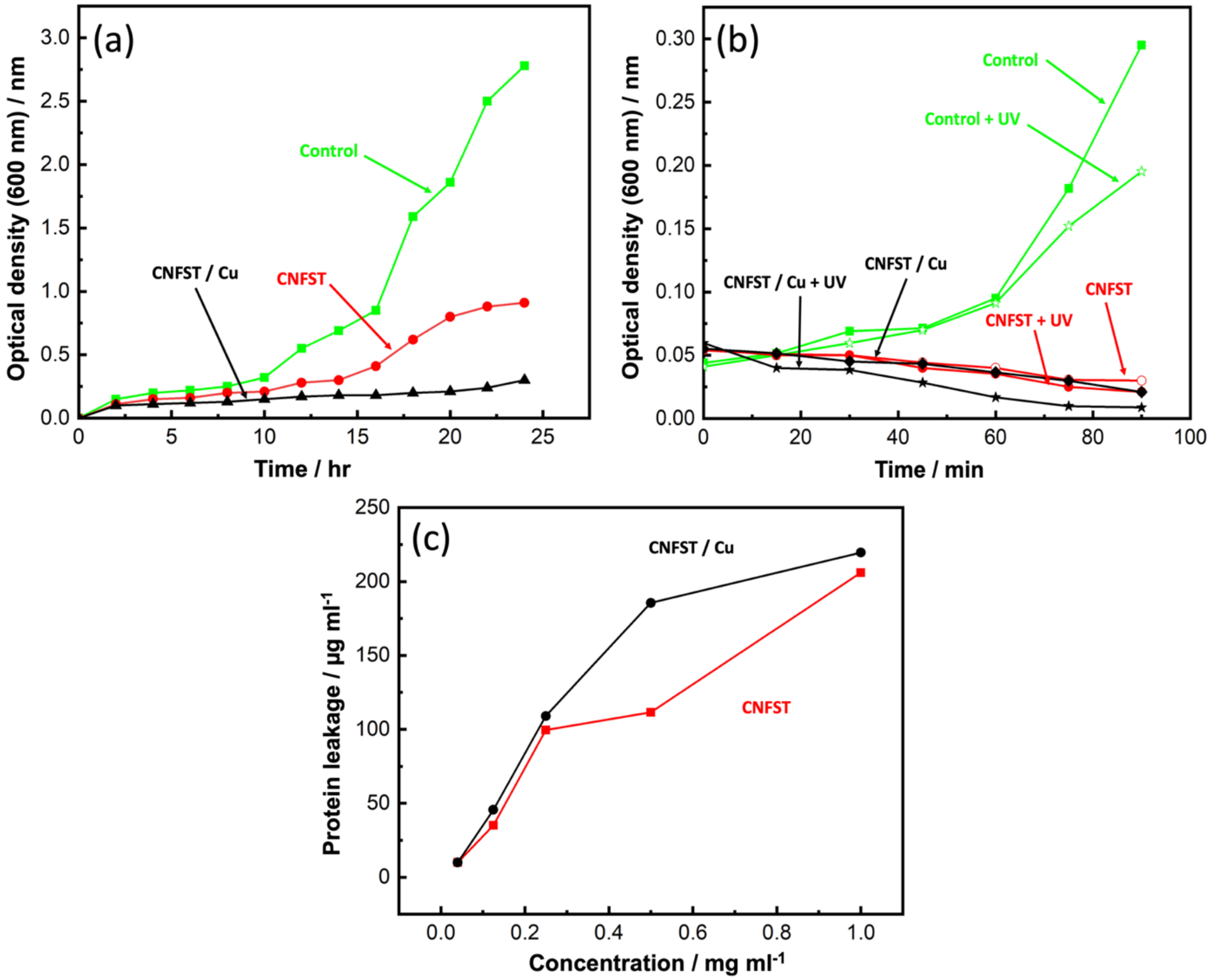

Fig. 4.9: a) The effect of the prepared nanocomposites on the growth curve of *S. aureus, b)* UV activation effect of the prepared nanocomposites against *S. aureus,* and c) Impact of the prepared nanocomposites on the protein leakage from *S. aureus* cell membranes.

4.4.4.5 Reaction mechanism estimation by SEM analysis

SEM analysis was carried out to determine the possible antimicrobial mechanism against *S. aureus*, with the results presented in **Fig. 4.10**. SEM analysis of the control (untreated) bacterial cells shows prolonged shaped cells with regular surfaces, as displayed in **Fig. 4.10(a)**. However, after treatment with the CNFST nanocomposite, unusual morphological irregularities of the *S. aureus* cells were identified, including semi-lysis of their outer surfaces and some deformations, as can be observed in **Fig. 4.10(b)**. Upon treatment with the CNFST/Cu nanocomposite, complete lysis of the bacterial cells (cell malformation) was achieved, decreasing the total viable number, as shown in **Fig. 4.10(c)**, creating holes on the surface of the bacterial cells, as can be observed in **Fig. 4.10(d)**, which is in good agreement with the membrane leakage assay.

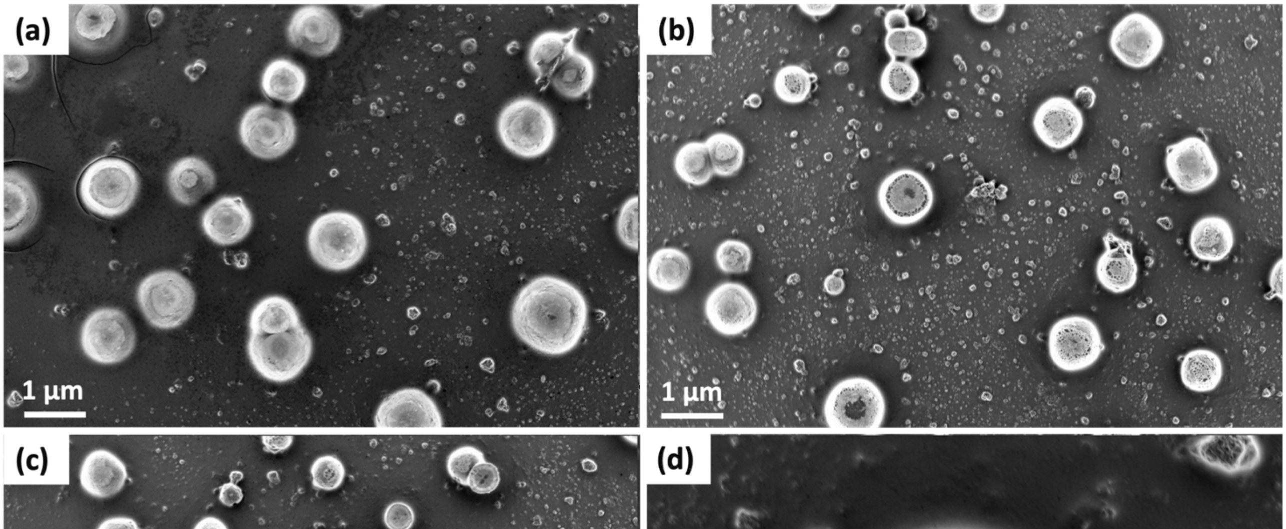

Fig. 4.10: Estimation of the reaction mechanism from SEM analysis, a) control untreated *S. aureus cells,* b) cells treated with the CNFST nanocomposite, c) cells treated with the CNFST/Cu nanocomposite, and d) magnified bacterial cell treated with the CNFST/Cu nanocomposite, confirming the creation of holes on the surface of treated *S. aureus* bacterial cells.

The possible antimicrobial mechanism is presented in **Fig. S. 4.14**. There are many possible factors that contribute toward this mechanism, such as ROS (superoxide anions, O_2^-) [233], the liberated ions from the metal and metal oxides inside the pathogenic microbes, and the alkaline conditions. In addition, ferrites and Cu NPs exhibit good antimicrobial properties, meaning that these materials can alter the microbial morphology, diminish the microbial membrane permeability, and generate oxidative stress due to H_2O_2 production [233, 234].

The CNFST/Cu nanocomposite initiates its activity by adhesion at the exterior surface of the microbial cells, leading to membrane damage, the formation of pits, and the switching off of the ion transport activity [235]. Then, the liberated metal ions destroy all intracellular macromolecules, such as DNA, plasmids, and essential bacterial organs. In addition, cellular toxicity takes place because of the oxidative pressure facilitated by the production of ROS. Finally, in acidic medium, cellular toxicity and genotoxicity occur due to the actions of the core ferrite and the surface Cu NPs [235].

4.5 Conclusion

An optimized layer-by-layer approach was used to prepare a Cu-loaded $Co_{0.5}Ni_{0.5}Fe_2O_4/SiO_2/TiO_2$ nanocomposite, for the photodegradation of three types of pollutants under UV light. DFT analysis was carried out to investigate the adsorption and electronic properties of the prepared CNFST/Cu sample. Moreover, the antimicrobial performance against many pathogens was studied using various assays, such as well diffusion, UV-light activation assessment, and protein leakage. The results in this study show that FCC Cu NPs are formed and uniformly distributed on the surface of the prepared nanocomposite matrix as, revealed from XRD, SEM, and STEM mapping results. Upon Cu loading, the crystalline size, diameter of the particles, and the bandgap of the CNFST matrix slightly increase. However, the BET surface area is largely improved due to more mesopores being formed with respect to macropores, as shown in the BJH pore size distribution curves. The FTIR analysis shows no Cu–O stretching, suggesting that the Cu NPs loading occurs via van der Waals forces. The prepared nanocomposite exhibits strong absorption in the UV region at around 350 nm. Finally, XPS analysis shows the atomic ratios of the main elements that constitute the composite and confirms the existence of oxygen vacancies over the Cu-loaded composite. The photocatalytic properties of the prepared nanocomposite were tested and compared with those of bare Cu and CNFST samples, with the prepared Cu-loaded nanocomposite showing outstanding photocatalytic properties toward all tested pollutants. This efficiency can be attributed to the improved surface area, porosity, and the constructed heterojunction separating photogenerated charge carriers and elongating the reaction time. In addition, the effect of the pH on the photocatalytic properties of the prepared nanocomposite varied from one type of pollutant to another. Similarly, Cu-loaded nanocomposite shows significant antimicrobial properties toward almost all pathogenic microbes. This performance can be ascribed to the synergetic effect between the composite matrix and the loaded Cu NPs.

Chapter 5: Overall water splitting over metallic nanoparticles loaded on Al-$SrTiO_3$ perovskite semiconductor photocatalyst supported with $RhCr_2O_3$ and CoOOH cocatalysts under wide ranges of light

5.1 overview

Developing new renewable, carbon-neutral fuels to diminish the amount of released CO_2 in the atmosphere and to solve global challenges such as global warming and climate change is significant. Among them, hydrogen (H_2) is attracting much attention due to its high energy density, ease of transportation, and multiple means of production. To meet the global demand of $H_{2,}$ photocatalytic water splitting is one of the most promising methods for large scale production.

Herein, Al-doped $SrTiO_3$ photocatalyst (Al-$SrTiO_3$) was prepared by a molten flux method. Then, plasmonic metal nanoparticles (Au, Cu, Pt), and cocatalysts Rh/Cr_2O_3 and CoOOH were selectively deposited onto the reductive and oxidative active sites of Al-$SrTiO_3$ using multi-step photodeposition-impregnation methods for water splitting and H_2 production under UV-rays, UV-Vis. light, and visible light ($\lambda \geq 400$ nm). Our results showed that, compared with Pt and Cu loaded Al-$SrTiO_3$ photocatalyst supported with Rh/Cr_2O_3 and CoOOH cocatalysts, Au-loaded samples showed the highest H_2 production efficiency under both UV (920 µmol/h - EQE = 41 % at 365 nm) and UV-Vis (100.5 µmol/h) rays. In addition, the amount of evolved H_2 decreased by increasing the weight ratio of Au nanoparticles (NPs) due to the overlap between Au NPs and Rh/Cr_2O_3 cocatalyst. Although Au 0.3 wt.%-loaded sample showed high activity under both UV and UV-Vis. rays, it exhibited almost no efficiency under visible light because of the large bandgap of Al-$SrTiO_3$ (3.1 eV) and the poor absorption in the visible region. visible light absorption was then enhanced by increasing the loaded amount of Au NPs and by separating Au NPs and Rh/Cr_2O_3 cocatalyst responsible for H_2 evolution by combining both photodeposition and impregnation methods. Under visible light, Rh/Cr_2O_3-loaded Al-$SrTiO_3$ with 4 wt. % Au NPs showed the highest H_2 evolution efficiency (41 µmol/3h). This was attributed to the efficient hot electron transfer from Au NPs to Al-$SrTiO_3$ then to $RhCr_2O_3$, resulting in charge separation needed for efficient H_2 generation.

5.2 Introduction

Photocatalytic overall water splitting is a promising process for the scalable production of sustainable hydrogen [236, 237]. However, it is an uphill reaction (+237 kJ mol^{-1} Gibbs energy) that requires a continued series of an efficient transfer of the photogenerated charge carriers to the reaction sites before their recombination, and without backward reactions. In addition, the injection of two-electrons and four-holes for the hydrogen and oxygen evolution reactions (HER - OER) is needed, respectively [238]. In order to design an efficient photocatalyst for overall water splitting, many requirements should be considered including the control of charge migration and separation which is significantly affected by photocatalyst's particle size, crystallinity, and doping [239]. Since 1980, $SrTiO_3$ photocatalyst is attracting the interest of many researchers worldwide as a promising material for overall water splitting [240]. $SrTiO_3$ can promote overall water spitting into H_2 and O_2 in a 2:1 stoichiometric ratio. In addition, it possesses a proper band structure with respect to water oxidation and reduction potentials [241]. However, the quantum yield of pristine $SrTiO_3$ is low, due to its wide bandgap energy (3.2 eV), inefficient light absorption, the rapid recombination of photoexcited charge carriers, and the undesired backward reactions [242]. Many efforts have been dedicated to tailor the current limitations of pristine $SrTiO_3$. On the one hand, doping $SrTiO_3$ with lower valence cations such as Al^{+3} ions increased its light absorption and minimized the defects (Ti^{+3}) acting as recombination centers for photogenerated electrons and holes [243]. On the other hand, H_2 and O_2 can be evolved from the surface of $SrTiO_3$ by employing different variety of cocatalysts, improving the migration and separation of charge carriers, and decreasing the activation energy [244]. Liu et al., used modified flux treatment and photooxidation methods for the preparation of $SrTiO_3(Al)/CoO_x$ loaded with Ni single atoms confined in N-doped graphene as a HE cocatalyst [245]. The prepared photocatalyst exhibited 498 μmol g^{-1} h^{-1} HE and 230 μmol g^{-1} h^{-1} OE rates due to Ti–O–C bonds which improved charge separation and transfer. While, Zong et al., loaded 1 % CoP as HE cocatalyst to replace noble metals on the surface of Al-doped $SrTiO_3$ by a photodeposition-phosphorization route [246]. The prepared photocatalyst exhibited 2106 and 1002 μmol $h^{-1}g^{-1}$ production rates for H_2 and O_2, respectively. In addition, by photodepositing Cr_2O_4 to inhibit the undesired backward reactions, the prepared photocatalyst showed an apparent quantum efficiency of about 7.1% at 350 ± 10 nm. While Takata et al., used a 3-step photodeposition method to load $RhCr_2O_3$ and CoOOH cocatalysts for the promotion of H_2 and

O_2, respectively over Al-doped $SrTiO_3$ prepared by a molten flux method [247]. Their designed material possessed an external quantum efficiency (EQE) of (96% at 360 nm). However, EQE measured at 380 nm was only 33.6%. Developing an effective photocatalyst capable of harvesting wide ranges of the solar spectrum (UV and visible regions) is still a challenge. To promote the photocatalytic activity under visible light, decorating the main semiconductor photocatalyst with plasmonic nanoparticles is a very promising technique through plasmonic energy transfer from plasmonic metals to the semiconductor photocatalyst [248, 249]. Plasmonic energy through hot-electron transfer, resonant energy transfer, and light scattering through the localized surface plasmon resonance (LSPR) can foster water splitting performance by visible light active materials. In addition, inhibiting the recombination of electron-hole pairs using sacrificial agents such as methanol, ethanol, lactic acid, and triethanolamine (TEOA) as hole scavengers and silver nitrate $AgNO_3$ as electron scavengers is a promising technique [250, 251]. In this chapter, we combined the synergetic impact of visible light-absorbing plasmonic NPs with the efficient cocatalysts for HER and OER. First, a flux-mediated method was used to prepare Al-doped $SrTiO_3$ photocatalysts. Then, multi-step photodeposition method was adapted to load three types of metal nanoparticles (Au, Cu, and Pt) (HE), along with $RhCr_2O_3$ (HE), and CoOOH (OE) cocatalysts. After that, overall water splitting performance was evaluated under UV and UV-vis rays. In addition, we designed a new system capable of harvesting wide regions of the solar spectrum for the efficient hydrogen production under visible light without any sacrificial agents, by combining photodeposition and impregnation methods, to control the location of cocatalysts over the active sites of the main photocatalyst and inhibit their overlap.

5.3 Materials and methods

5.3.1 Materials

$SrTiO_3$, $SrCl_2$, Al_2O_3, $RhCl_3{\cdot}3H_2O$, K_2CrO_4, $Co(NO_3)_2{\cdot}6H_2O$, $HAuCl_4.3H_2O$, H_2PtCl_6, and $CuCl_2$ were purchased from Sigma Aldrich, Germany. All chemicals were of extra pure grade and were used as received.

5.3.2 Methods

5.3.2.1 Preparation of Al-doped $SrTiO_3$ photocalysts

Al-$SrTiO_3$ photocatalysts were prepared by a molten flux method as reported by Goto et al. [242]. $SrTiO_3$, $SrCl_2$, and Al_2O_3 with a molar ratio of (1:10:0.02) were grinded in an agate mortar. Then mixed powder was transferred into an alumina crucible. The alumina crucible was placed in a muffle furnace and heated at 1150ºC for 10 h in air. After cooling down to room temperature naturally, the formed powder was collected from the crucible by ultrasonication for 30 min. After that, collected powder was washed 6 times by distilled water (D.W.) to remove excessive $SrCl_2$. Finally, remaining powder was dried at 60ºC in air overnight.

5.3.2.2 Photodeposition of cocatalysts and metal NPs

Typically, $RhCr_2O_3$ (Rh = 0.1 wt.% & Cr = 0.05 wt.%) and CoOOH (Co = 0.05 wt.%) cocatalysts along with three metal NPs (Au, Cu, and Pt) with various wt.%, were selectively loaded onto Al-$SrTiO_3$ microparticles by a UV-assisted photodeposition method as reported by Takata et al. [247]. In this process, firstly, (100 mg) of Al-$SrTiO_3$ powder was dispersed in (220 mL) D.W. using ultrasonication for 30 min inside the cell used for water splitting evaluation. Secondly, (50 μL) freshly prepared $RhCl_3{\cdot}3H_2O$ aqueous solution (2 mg/mL) was added to the Al-$SrTiO_3$ dispersion and the mixture was UV-irradiated by a HgXe lamp (275 W, SP-11, USHIO, Japan) for 10 min. Thirdly, (25 μL) K_2CrO_4 aqueous solution (2 mg/mL) was added to the mixture and UV-irradiated for another 5 min. Fourthly, (25 μL) $Co(NO_3)_2{\cdot}6H_2O$ aqueous solution (2 mg/mL) was further UV-irradiated for 5 min. Finally, calculated volumes of (2 mg/mL) $HAuCl_4.3H_2O$, H_2PtCl_6, and $CuCl_2$ aqueous solutions were added to the above mixture and UV-irradiated for 15 min for each. Water splitting evaluation experiments were carried out directly after cocatalysts and matal NPs loading.

5.3.2.3 Loading Au NPs by Impregnation method

Au NPs were randomly deposited onto Al-$SrTiO_3$ photocatalyst by impregnation method as reported by Chen et al. [252]. In brief, Al-$SrTiO_3$ particles were dispersed in a minimum amount of D.W. containing calculated amounts of $HAuCl_4.3H_2O$ aqueous solution. Then, the mixture was placed on a hot plate until water evaporation (slowly). Finally, the dried particles were calcined at 350 ºC for 1 h in air.

5.3.2.4 Characterization of the prepared samples

Crystallinity and phase were investigated by X-ray diffraction (XRD) analysis via X-ray diffractometer, Ultima IV (Rigaku, Japan) applying Cu-Kα radiation (λ = 1.54 Å), operating at 40 kV and 30 mA. While morphology of samples was analyzed by scanning transmission electron microscopy (STEM) by JEM-2100F (JEOL Ltd., Japan), supported with an energy-dispersive X-ray spectroscopy (EDS) unit, JED-2300T. Diffuse-reflectance and bandgap calculations were recorded using a V-670 spectrophotometer (JASCO, Japan).

5.3.2.5 Online water splitting and H_2 production evaluation

The photocatalytic water splitting and H_2 production reactions were carried out in a reaction cell possessing quartz-window connected with a gas circulation system (Makuhari Rikagaku Garasu Seisakujo, Japan). The light sources used for UV, UV-Vis, and visible light irradiations were HgXe lamp (275 W, SP-11, USHIO, Japan), Xenon lamp (HAL-320, 350-1100 nm, ASAHI SPECTRA, Japan), and HAL-320 Xenon lamp supported with (400 nm UV cut filter), respectively. Before photocatalytic evaluation, 100 mg photocatalyst was dispersed in (220 mL) D.I.W by ultrasonication for 30 min. Then, metallic NPs and/or cocatalysts were loaded using photoadaptation method. To remove the dissolved air from the final suspension, it was vacuumized. At regular time intervals, the evolved gases were detected using an online gas chromatography (GC) system, GC-8A (Shimadzu, Japan), employing Argon gas as a carrier and supported with a thermal conductivity detector (TCD). External quantum efficiency (EQE) calculations were performed under UV light using (365 nm UV bandpass filter) using the following **equations (5.1 - 5.2).**

$$\text{EQE \%} = \frac{Number\ of\ reacted\ electrons}{Number\ of\ incident\ photons}\ x\ 100 \qquad (5\text{-}1)$$

$$\text{EQE \%} = \frac{2\ x\ Number\ of\ evolved\ H2\ molecules}{Number\ of\ incident\ photons}\ x\ 100 \qquad (5\text{-}2)$$

5.4 Results and discussion

5.4.1 Photocatalytic water splitting evaluation under UV rays

5.4.1.1 Effect of changing the photodeposition order of cocatalysts and metal NPs

The effect of changing the photodeposition order of cocatalysts and metal NPs on the H_2 production efficiency under UV irradiation is shown in **Fig. 5.1**. As presented, changing the order of deposition resulted in a variety of performances. Comparing the types of metal NPs, Au NPs loaded samples showed the highest H_2 production ability after 15 min-UV irradiation. It is worth mentioning that changing the photodeposition order of Cu NPs loaded samples significantly affected the H_2 production efficiency which could be due to the lower chemical stability of Cu NPs with respect to the highly stable Au and Pt NPs.

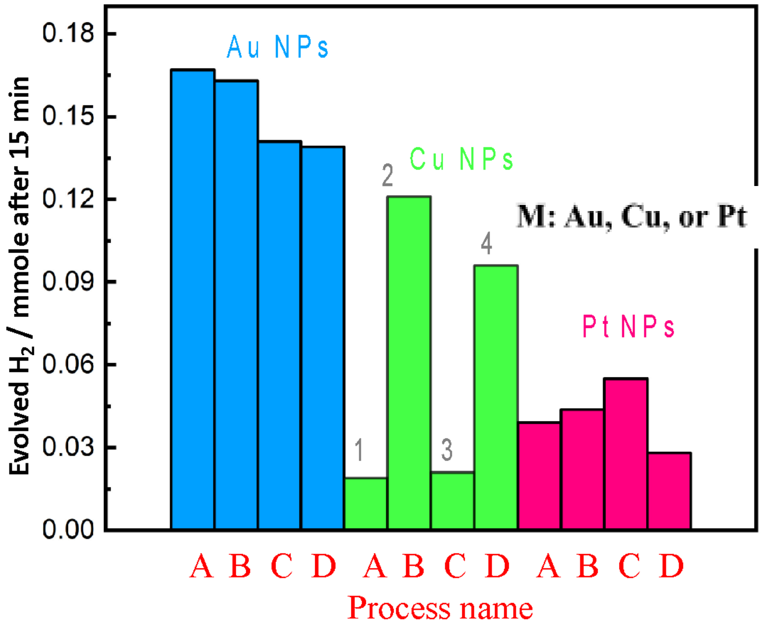

		Photodepositio		
		1	**2**	**3**
Process name	**A**	**Rh**	**Cr**	**Co**
	B	**M**	**Rh**	**Cr**
	C	**Rh**	**Cr**	**M**
	D	**Co**	**Rh**	**Cr**

Fig. 5.1: Effect of changing the photodeposition order of cocatalysts and metal NPs on the photocatalytic H_2 production under UV rays for 15 min. Rh = 0.1 wt. %, Cr = 0.05 wt. %, Co = 0.05 wt. %, M (Au, Cu, Pt NPs) = 0.3 wt.%.

5.4.1.2 Effect of changing the deposited amount of Au NPs on the photocatalytic H_2 production under UV rays

As the highest H_2 production efficiency was exhibited by Au NPs loaded samples, the concentration effect of Au NPs of the sample with the optimized photodeposition order, was investigated as presented in **Fig. 5.2**. It is clear that, by increasing the deposited amount of Au NPs from 0 to 3 wt. %, the evolved H_2 amount under UV rays declined.

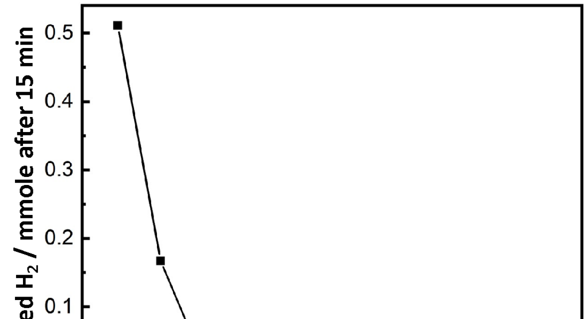

Fig. 5.2: Effect of changing the deposited amount of Au NPs on the H_2 production efficiency under UV rays after 15 min. Rh = 0.1 wt. %, Cr = 0.05 wt. %, Co = 0.05 wt. %.

This result can be ascribed to the possible overlap between Au NPs and $RhCr_2O_3$ cocatalyst responsible for H_2 evolution. With the photodeposition process, both Au NPs and $RhCr_2O_3$ cocatalyst are deposited onto the same (100) $SrTiO_3$ facets, which are active sites for reductive photodeposition [247]. Therefore, the highly efficient H_2 evolution by $RhCr_2O_3$ cocatalyst is hindered by the overlapped Au NPs. This explanation was confirmed via STEM-EDX mapping as exhibited in **Fig. 5.3 (b)**. It is clear that $RhCr_2O_3$ cocatalyst and Au NPs were observed at the same positions. Increasing Au amount resulted in further deterioration of H_2 evolution rate.

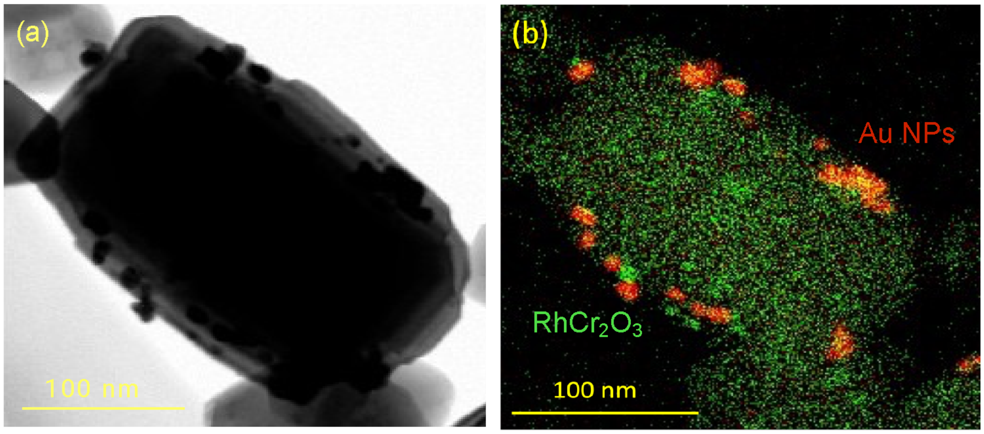

Fig. 5.3: a) STEM image of Al-$SrTiO_3$ (150 nm) loaded with $RhCr_2O_3$, CoOOH cocatalysts, and Au NPs and b) the corresponding EDX mapping image showing the overlap between $RhCr_2O_3$ and Au NPs on the Al-$SrTiO_3$ (100) facets.

5.4.1.3 Effect of UV irradiation time on the overall water splitting under UV rays

After optimizing the type of metal NPs, photodeposition order, and the concentration of the metal NPs, the effect of UV irradiation time on the overall water splitting efficiency was studied as shown in **Fig. 5.4**. By increasing the UV irradiation time, the amount of evolved gases increases accordingly. It is worth to mention that, after 45 min, the amount of O_2 gas exceeded the lower limit of detection, and a stoichiometric ratio of (1:2) with respect to H_2 was confirmed.

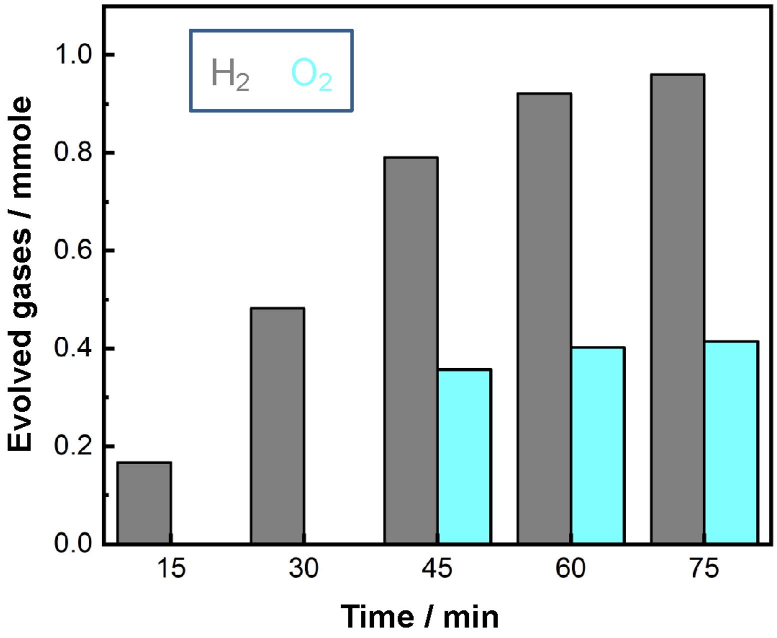

Fig. 5.4: Overall water splitting under UV rays by Al-$SrTiO_3$ loaded with $RhCr_2O_3$ (Rh = 0.1 wt. % - Cr = 0.05 wt. %), CoOOH (Co = 0.05 wt. %.) cocatalysts and Au NPs (Au = 0.3 wt.%).

5.4.1.4 H_2 production stability under UV rays: Cycle test

The effect of increasing the cycle number on the H_2 production rate by the optimized sample was analyzed and presented in **Fig. 5.5**. It is obvious that, by increasing the number of H_2 production cycles up to 15, the photocatalytic H_2 production rate gradually decreases until 51% of the initial rate. This might be attributed to the peeling of cocatalysts and Au NPs off the surface of the main photocatalyst during the washing process between cycles, in addition to the deactivation of the sample during water splitting reaction.

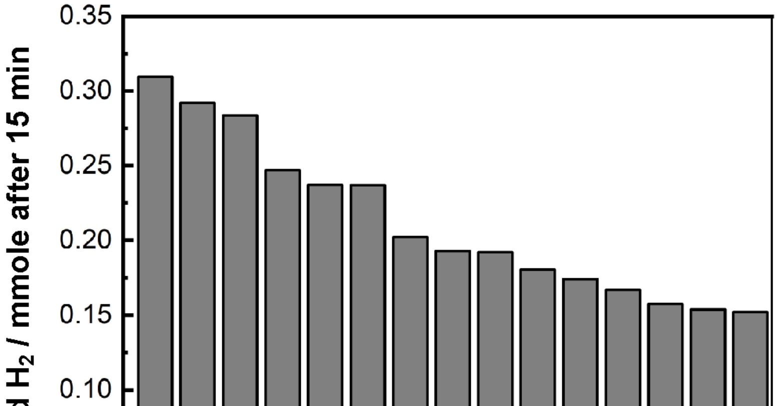

Fig. 5.5: Effect of increasing the cycle number on H_2 production efficiency by Al-$SrTiO_3$ loaded with $RhCr_2O_3$ (Rh = 0.1 wt. % - Cr = 0.05 wt. %), CoOOH (Co = 0.05 wt. %.) cocatalysts and Au P. NPs (Au = 0.3 wt.%).

5.4.2 Photocatalytic hydrogen production under UV-Vis. light

Before evaluating the H_2 production efficiency under UV-Vis. light, the concentration of Au NPs was optimized as shown in **Fig. 5.6 (a)**. It can be found out that, by increasing the concentration of Au NPs, the quantum efficiency and H_2 production rate declined, which is the same tendency as the data obtained under UV rays. While, the H_2 evolution rate by the optimized sample (0.3 wt% Au) with time is shown in **Fig. 5.6 (b)**. It is clear that, by increasing the irradiation time, the amount of produced H_2 increases linearly, where the amounts of generated H_2 gas after 15 and 30 min irradiation were less than the lower limit of detection.

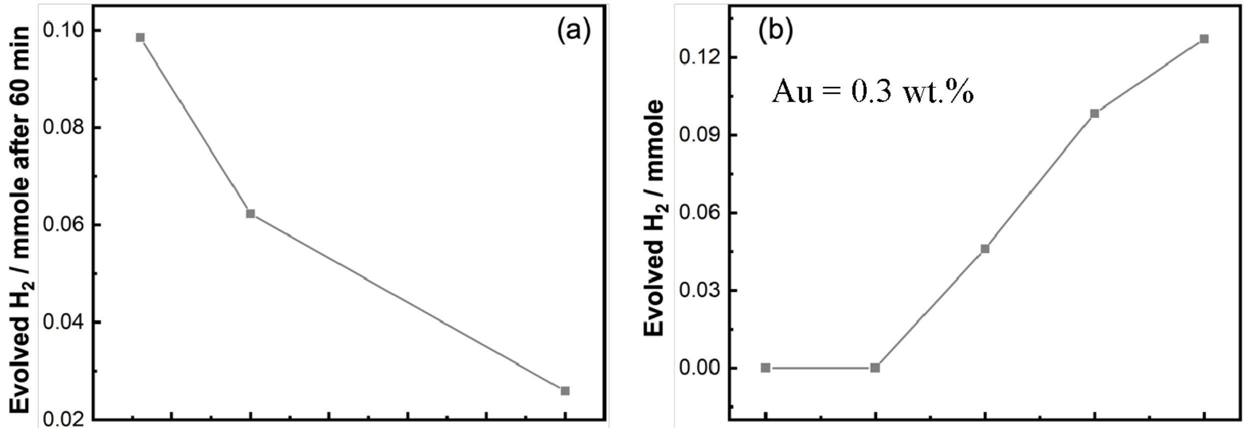

Fig. 5.6: a) Effect of deposited amount of Au NPs on the H_2 production evolution under UV-Vis. rays after 60 min. Rh = 0.1 wt. %, Cr = 0.05 wt. %, Co = 0.05 wt. % and b) Evolved H_2 over time with Au NPs of 0.3 wt.%.

5.4.3 Photocatalytic hydrogen production evaluation under visible light

To obtain satisfactory H_2 production efficiency under visible light, the overlapping of $RhCr_2O_3$ and Au NPs must be suppressed. Consequently, the plasmonic Au NPs and HE $RhCr_2O_3$ were loaded with impregnation and photodeposition methods, respectively. Thus, Au NPs were deposited on Al-$SrTiO_3$ surface randomly, while $RhCr_2O_3$ were deposited selectively on the reductive sites. **Fig. 5.7** shows H_2 production efficiency under visible light of samples loaded with different concentrations of Au NPs. As presented, Al-$SrTiO_3$ loaded with $RhCr_2O_3$ (Rh = 0.1 wt. % - Cr = 0.05 wt. %) and 4 wt.% Au NPs showed the highest potential due to the efficient light absorption. This result is in a good agreement with previously-reported results, where Au-TiO_2 system was investigated in detail [253].

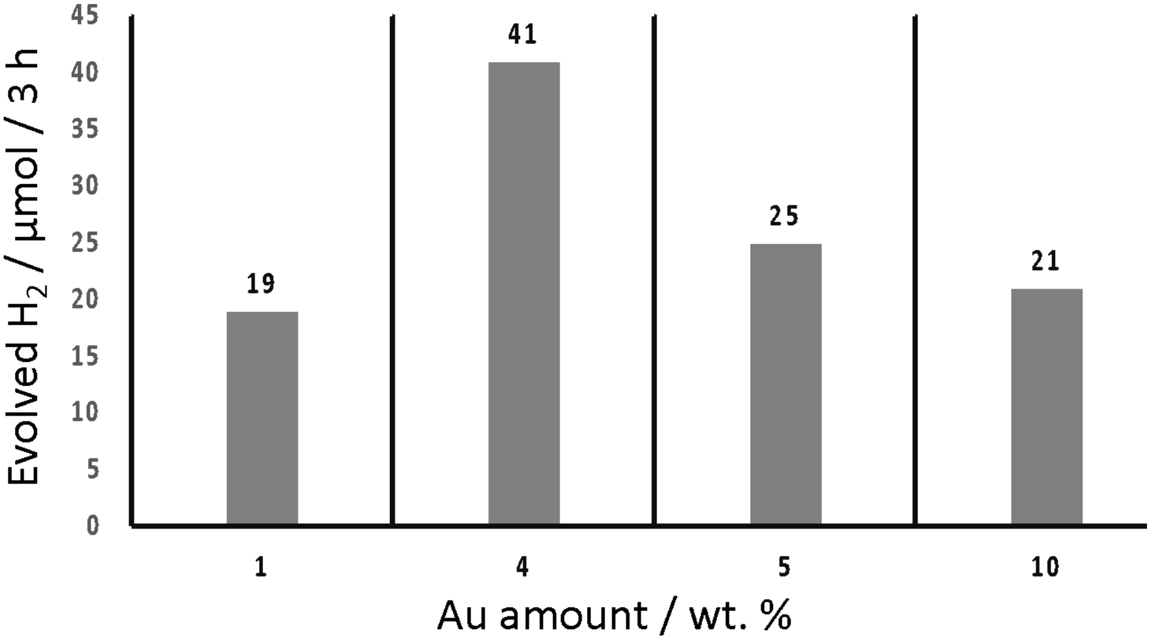

Fig. 5.7: Effect of deposited amount of Au NPs (loaded by impregnation method) on the evolved H_2 formed after 3 h under visible light by Al-$SrTiO_3$ loaded with $RhCr_2O_3$ (Rh = 0.1 wt. % - Cr = 0.05 wt. %) (loaded by photodeposition method).

5.4.4 Reaction mechanism

The mechanism of H_2 and O_2 evolution by the Al-$SrTiO_3$ loaded with $RhCr_2O_3$,CoOOH, and Au NPs is divided into two parts as shown in **Fig. 5.8**. First, under UV rays, the incident light has higher energy than the bandgap of $SrTiO_3$ (3.1 eV). Thus, photogenerated charge carriers (electrons and holes) are formed in Al-$SrTiO_3$. Holes are then oxidize water into positively-charged protons and negatively-charged oxygen anions. Then, the formed electrons migrate to the reaction sites, where $RhCr_2O_3$ reduces protons and promotes the evolution of H_2 (through Rh) and inhibits the backward reactions (through Cr_2O_3 shell). While, oxygen anions are oxidized into O_2 by CoOOH. Similarly, Au NPs promotes the reduction of protons into H_2. Second, under visible light, photons are mainly absorbed by Au NPs resulting in the generation of plasmonic hot-electron transfer to Al-$SrTiO_3$ and then to $RhCr_2O_3$ which promotes H_2 evolution, Therefore, higher amounts of H_2 can be generated under visible light through the hot-electron transfer and photocatalytic enhancement by the near field excitation [254]. However, the generated holes possess lower oxidative potential which is not sufficient for oxidizing water to generate oxygen anions for O_2 evolution. That's the reason why no O_2 was generated under visible light.

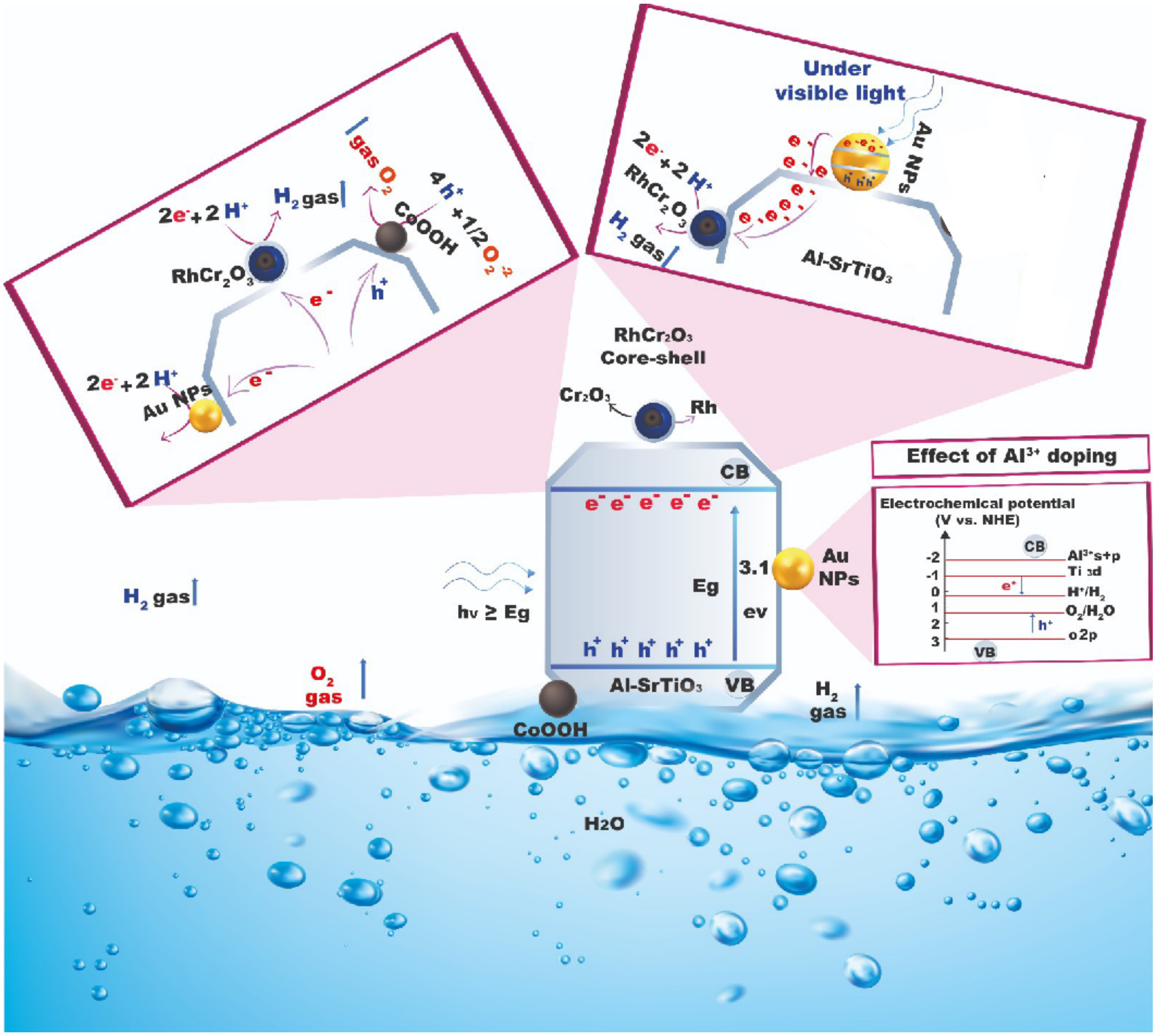

Fig. 5.8: Proposed reaction mechanism of water splitting and H_2 production by the prepared cocatalysts and Au NPs-loaded Al-$SrTiO_3$ under different light sources.

5.4.5 Characterization of the optimized sample under visible light irradiation

5.4.5.1 XRD analysis

Phase and crystallinity of the prepared samples were analyzed using XRD analysis as shown in **Fig. 5.9**. Many Bragg peaks were recorded at 2θ = 22.7°, 32.5°, 40.2°, 46.6.5°, 53.3°, 58.6°, 68.2°, 73.7°, and 78.6° from all samples, which correspond to the (100), (110), (111), (200), (210), (211), (220), (300), and (310) crystallographic planes of perovskite $SrTiO_3$ (JCPDS No. 73-0661) [255]. Neither doped Al^{+3} ions nor loaded cocatalysts ($RhCr_2O_3$ / 1 wt.% Au NPs), could change the crystal structure of the main photocatalyst $SrTiO_3$ due to their relatively lower ratio and high dispersion [250]. However, upon increasing the deposited ratio of Au NPs (from 4 wt.% to 10 wt.%) small new peaks at 2θ =38.1°, 44.3°, and 64.5° were recorded which are attributed to (111), (200), and (220) planes of face-centered cubic Au (JCPDS No. 04-0784) [256].

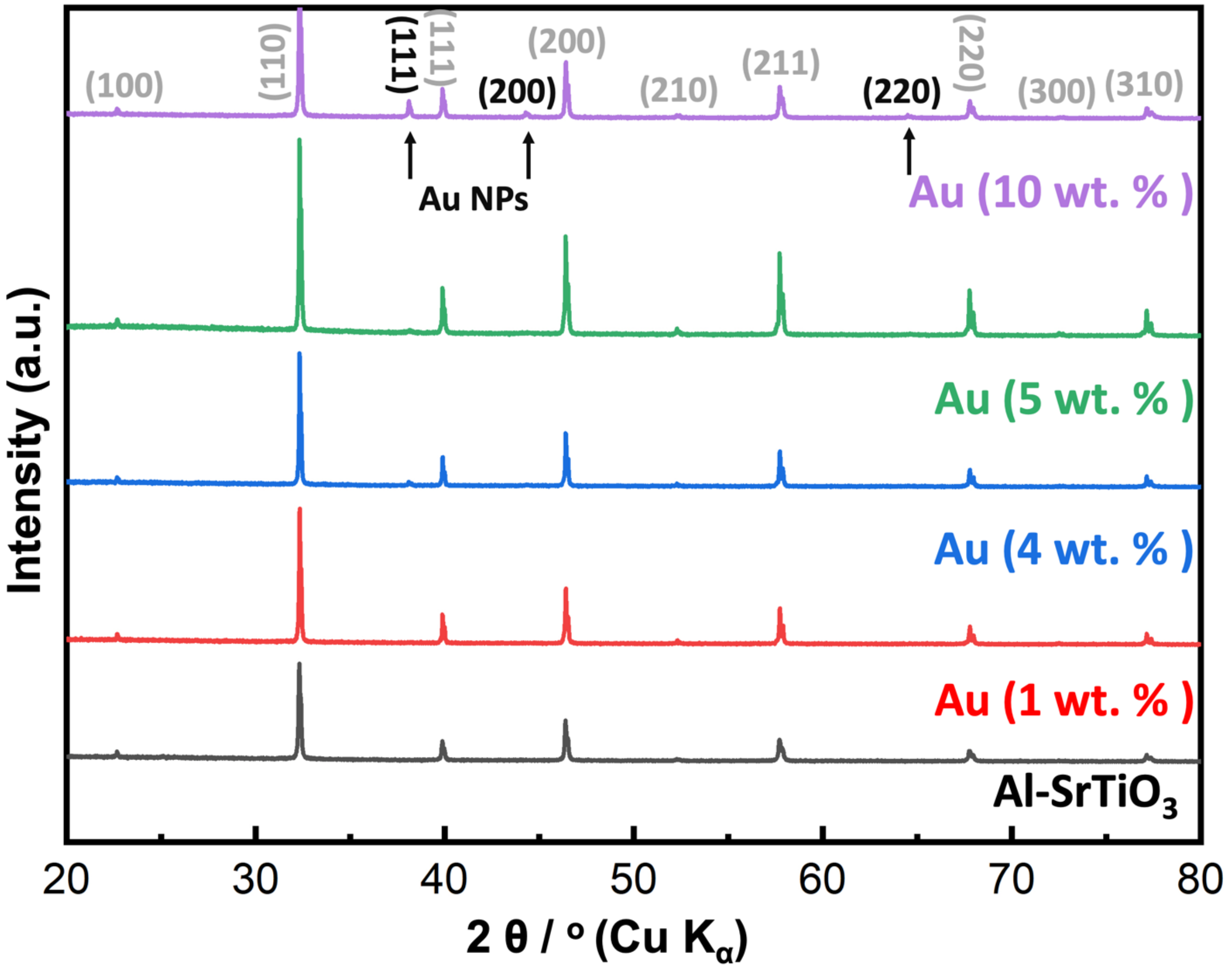

Fig. 5.9: XRD patterns of pristine Al-$SrTiO_3$ and Al-$SrTiO_3$ photocatalyst loaded with $RhCr_2O_3$ cocatalyst (Rh = 0.1 wt.% - Cr = 0.05 wt.%) and different weight ratios of Au NPs.

5.4.5.2 STEM-EDX analysis

To analyze the morphology and dispersion states of $RhCr_2O_3$ cocatalyst and Au NPs on Al-$SrTiO_3$, STEM-EDX analysis was carried out as shown in **Fig. 5.10 (a-c)**. It is clear that, the Al-$SrTiO_3$ maintained cubic morphology distinguishing perovskite materials even after Au and $RhCr_2O_3$ deposition. With respect to **Fig. 5.10 (a-b)** which shows homogeneous distribution of cocatalysts, **Fig. 5.10(c)** revealed that 10 wt.% Au deposition resulted in an agglomeration and a formation of large Au particles (up to 200 nm), which generally do not exhibit efficient LSPR. On the other hand, **Fig. 5.10 (d)** shows the EDX mapping of Al-$SrTiO_3$ loaded with $RhCr_2O_3$ and 4 wt.% Au NPs. Compared with **Fig. 5.3**, Au NPs and $RhCr_2O_3$ cocatalyst were separately deposited [257]. This is because Au NPs were deposited by the impregnation method, which results in a random deposition onto Al-$SrTiO_3$, while $RhCr_2O_3$ cocatalyst was site-selectively deposited by the photodeposition method onto (100) facet of Al-$SrTiO_3$ particles.

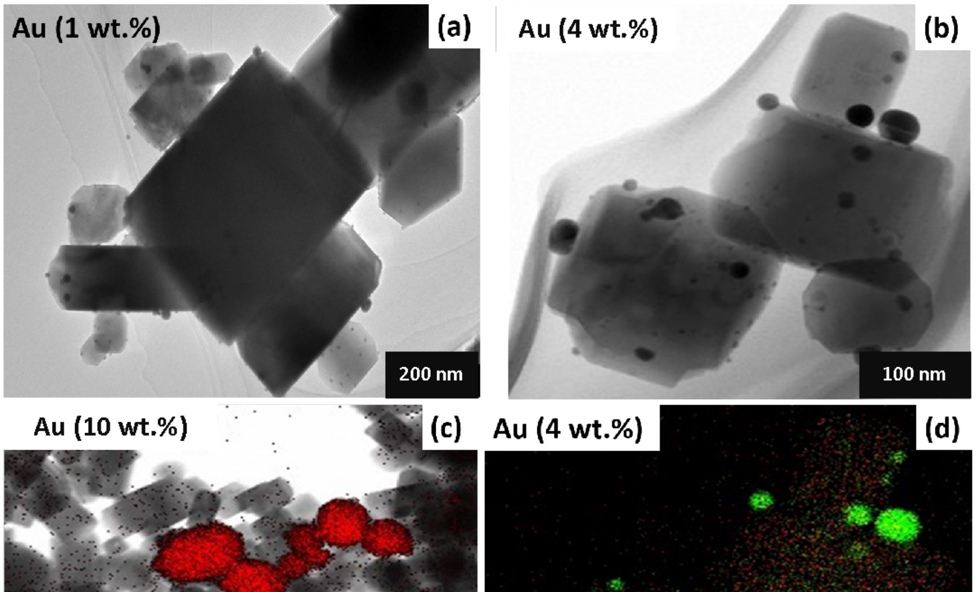

Fig. 5.10: a) STEM image of Al-$SrTiO_3$ photocatalyst loaded with $RhCr_2O_3$ cocatalyst and Au NPs with different ratios a) 1 wt.%, b) 4 wt.%, c) 10 wt.% (overlapped with an Au EDX mapping (red color), and d) the corresponding EDX mapping image of sample deposited with (Au = 4 wt.%).

By preventing the overlap between the two cocatalysts responsible for H_2 evolution, enhanced photocatalytic performance is expected.

5.4.5.3 UV-Vis. diffuse reflectance and bandgap calculations

UV-Vis. diffuse reflectance spectra and the calculated bandgap of the prepared samples are presented in **Fig. 5.11.** Al-$SrTiO_3$ loaded with $RhCr_2O_3$ without any Au NPs, showed a strong absorption in the UV range and faint absorption in the visible range. In addition, its calculated bandgap energy was 3.1 eV that's why it exhibited high performance under UV-rays and no activity under visible light. On the other hand, by increasing the deposited ratio of Au NPs, Al-$SrTiO_3$ exhibited obvious absorption increase in the visible region. The visible light absorption observed at around 550 nm is well matched with localized surface plasmon resonance wavelength of Au NPs [258]. The strongest visible light absorption was observed in the sample loaded with 4 wt.% Au NPs which showed the best H_2 production efficiency under visible light. In addition, it possessed the lowest apparent bandgap energy of about 2.8 eV as shown in Fig. **5.11 (b)**.

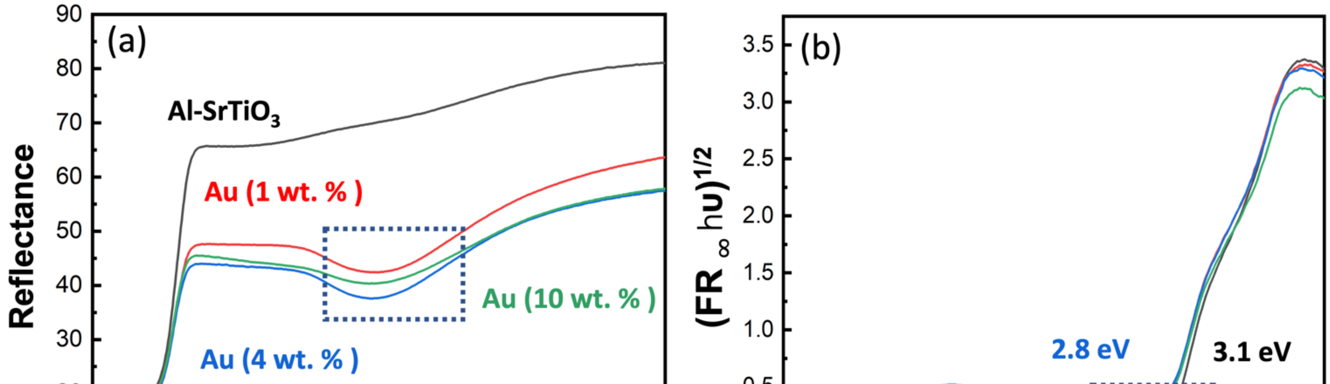

Fig. 5.11: a) UV-Vis. diffuse reflectance spectra of pristine Al-$SrTiO_3$ and Al-$SrTiO_3$ loaded with $RhCr_2O_3$ (Rh = 0.1 wt. % - Cr = 0.05 wt. %), and Au NPs with different wt.%, b) the corresponding Tauc plot of KM formula for the calculation of bandgap energies.

5.5 Conclusion

Molten flux method was used for the preparation of highly crystalline Al-doped $SrTiO_3$ photocatalyst with an average particle size of 150 nm. The prepared particles were highly crystalline and possessed cubic morphology of the perovskite materials. The most outstanding overall water splitting performance was exhibited under UV-rays due to the large bandgap of Al-$SrTiO_3$ particles (3.1 eV). In addition, our results showed that, by changing the photodeposition order of the cocatalysts and metal NPs, the photocatalytic H_2 production efficiencies changed. Moreover, loaded samples with Au NPs exhibited the highest photocatalytic water splitting performance compared with Cu and Pt loaded samples under UV and UV-Vis. light, which could be ascribed to their higher chemical stability, efficient light absorption, and good charge separation. Also, Au NPs concentration is significant due to the possible agglomeration and overlap with $RhCr_2O_3$ cocatalyst responsible for efficient HE. Finally, developed Al-$SrTiO_3$ loaded with $RhCr_2O_3$ (Rh = 0.1 wt%, Cr = 0.05 wt%) and Au NPs (4 wt.%) showed the highest H_2 evolution under visible light. This was attributed to the efficient hot electron transfer from Au NPs to Al-$SrTiO_3$ photocatalyst then to $RhCr_2O_3$.

Chapter 6: Designed Al-$SrTiO_3$/Au/CdS Z-Schemes for efficient H_2 evolution under visible light

6.1 Overview

Development of sustainable solar fuels to meet the continued increase in the energy need worldwide is of particular importance. In addition, reducing carbon emissions could be the last hope to solve global challenges such as global warming and climate change. For this endeavor, different Al-$SrTiO_3$/Au/CdS Z-Scheme samples were developed by changing the weight percentage (wt. %) of gold nanoparticles (Au NPs) and the wt. % ratio of Al-$SrTiO_3$ to CdS NPs using post annealing of mixed powders method. The prepared samples were characterized using several physicochemical techniques to reveal their properties, then their photocatalytic H_2 evolution performance was evaluated under visible light using photodeposited $RhCr_2O_3$ as H_2 evolution cocatalyst. Our results showed that, Al-$SrTiO_3$ particles possessed high crystallinity and cubic perovskite phase, Au NPs exhibited face-centered cubic (FCC) structure, and CdS NPs had cubic Zinc Blende phase as confirmed by XRD analysis. Our UV-Vis. diffuse reflectance analysis revealed that all prepared Z-scheme samples obtained a strong absorption in both UV and visible regions. SEM analysis confirmed the cubic morphology of the perovskite Al-$SrTiO_3$ particles which were randomly deposited by Au NPs of relatively smaller size. While CdS NPs showed semi-spherical shape and were conjugated with Al-$SrTiO_3$ directly to form the proposed Z-Schemes as proposed by our STEM mapping analysis. The highest amount of H_2 (656.7 μ mole) was evolved by Al-$SrTiO_3$/ 4 wt.% Au / CdS (1:1) Z-scheme sample after 3 h of visible light irradiation. This sample had 4 wt. % of Au NPs and equimolar ratio of Al-$SrTiO_3$ and CdS NPs. This relatively higher activity might be because of the efficient light absorption, prolonged lifetime of the photogenerated charge carriers and improved charge separation as revealed by the PL analysis. Our study can promote the ongoing efforts toward more carbon neutral societies.

6.2 Introduction

Every year, the global demand of energy is increasing due to the expansion in technological applications and continued increase in population. In addition, the sooner depletion of fossil fuels and the raised issues of global warming and climate change are driving the world toward carbon neutrality. The photocatalytic water splitting for the production of solar fuels such as hydrogen (H_2) is currently a promising approach to mitigate issues related to energy and the environment [259]. However, the current light harvesting ability and quantum yield efficiency are still low especially under visible light and cannot meet the technological applications [260]. Although many efforts have been devoted, there are still many challenges for the photocatalytic water splitting and H_2 production such as light absorption, redox ability of photogenerated charge carriers, and charge separation [261]. To design an efficient photocatalyst for photocatalytic water splitting, deep understanding of the entire process is required. Water splitting begins with the absorption of water molecules on the surface of the employed photocatalyst, in other words the adsorption capability of the developed photocatalyst is essential, and thus the large specific surface area is more favorable [262, 263]. Additionally, the energy bandgap of the photocatalyst must be less than the photon energy of the incident light for the generation of electron-hole pairs [264]. Furthermore, reducing the recombination rate and promoting mobility of the photogenerated electron-hole pairs is significant for their migration to the photocatalyst surface where redox reaction occurs [265]. Consequently, crystallinity of the photocatalyst, size, doping, and phase are crucial [239]. Moreover, after water oxidation by holes into oxygen (O_2) and reduction of protons by electrons into H_2, inhibition of any possible backward reactions is necessary to increase the quantum efficiency. Therefore, using proper cocatalyst to reduce the activation energy, promoting the formation of products, and enabling charge separation should be considered [266]. Finally, product diffusion/desorption from the surface of the photocatalyst after redox rection [267, 268]. Perovskite n-type strontium titanate ($SrTiO_3$) semiconductor is one of the most widely used photocatalysts for water splitting because of its promising photocatalytic properties, low-cost, structural flexibility, and stability [269-271]. However, its solar energy conversion efficacy under visible light is very low because of its wide band gap (3.1 eV). One approach to tailor the drawbacks of $SrTiO_3$, is through doping with metal ions such as Aluminum (Al^{+3}). According to ionic radii, Al^{+3} shall replace Ti^{+3} acting as recombination centers for the photogenerated charge carriers, thus enhancing the overall efficiency by increasing the lifetime of the redox species [243]. Similarly, Chen et al.

prepared Cr / Ta co-doped $SrTiO_3$ photocatalyst by polymerizable complex (PC) method for the photocatalytic water splitting under visible light [272]. Their UV-Vis. diffuse-reflectance analysis revealed that, absorption edge of $SrTiO_3$ sample was extended towards the visible light region after Cr / Ta co-doping at the wavelength of 540 nm. The improved photocatalytic performance was mainly due to the formation of new impurity states within the forbidden gap of $SrTiO_3$ through Cr 3d and O 2p orbits, thus electrons with lower energy can be excited. Another approach to improve the performance of $SrTiO_3$ is through combining a narrow band-gap semiconductor such as cadmium sulfide (CdS) [273]. In addition to its narrow band gap (2.4 eV), CdS possesses a more negative conduction band edge with respect to H^+ to H_2 reduction potential, high flat-band potential and improved electrochemical performance, making it a very suitable electron donor material [274]. Pan et al. studied the effect of introducing oxygen vacancies (O_v) through Ti^{+3} ion doping and the synergetic effect after conjugating CdS NPs on the Hydrogen evolution (HE) performance of CdS / Ti^{3+}-$SrTiO_3$ nanospheres [275]. Their study found that pure $SrTiO_3$ nanospheres have low intrinsic photocatalytic HE performance of approximately 60.35 μmol/g·h. However, when Ti^{3+}/O_v was introduced, the Ti^{3+}-$SrTiO_3$ nanospheres demonstrated an increase in performance to around 83.31 μmol/g·h. While after conjugating CdS NPs, the HE performance further improved to approximately 660.66 μmol/g·h, or about 10 times more. Additionally, noble metal deposition between the two semiconductor materials, to construct a ternary composite, might enhance its photocatalytic efficiency because of the improved mobility and separation of the photogenerated charge carriers. In addition, noble metal nanoparticles such as gold (Au) exhibit surface plasmon resonance (SPR) originating from electrons collective oscillation which could further enhance the efficiency of the composite via hot electron transfer. Chang et al. reported unique ternary composites based on three dimensionally ordered macroporous (3DOM) $SrTiO_3$ / Au / CdS for H_2 production under visible light ($\lambda > 420$ nm) [276]. The constructed systems achieved remarkable performance with an apparent quantum efficiency of about (42.2% at 420 nm) due to the synergistic effect of improved carrier separation, slow photon effect, and Au SPR effect. Recently, Z-scheme and ternary systems are receiving considerable interest due to possessing wide range of light absorption and strong redox capability of electron-hole pairs compared to traditional heterojunctions (type I and type II) [277]. In the present chapter, highly crystalline Al-doped $SrTiO_3$ particles were prepared by a molten flux method. Then impregnation method was adopted for the deposition of plasmonic Au NPs onto Al-$SrTiO_3$. After that, CdS NPs were combined with

Au-loaded Al-$SrTiO_3$ to construct Z-Scheme samples using post annealing of mixed powder method. The physicochemical properties of the prepared samples were studied in detail using several techniques including XRD, UV-Vis., PL, Raman, XPS, SEM, TEM, HR-TEM, and STEM mapping analyses. Finally, the photocatalytic water splitting / H_2 production performance was evaluated under visible light.

6.3 Materials and methods

6.3.1 Materials

$Cd(NO_3)_2.4H_2O$, $Na_2S.9H_2O$, $HAuCl_4.3H_2O$, $SrTiO_3$, Al_2O_3, $SrCl_2$, $RhCl_3{\cdot}3H_2O$, and K_2CrO_4 were obtained from Sigma Aldrich, Japan. Received chemicals were of extra pure grade and were used without any further purification.

6.3.2 Methods

6.3.2.1 Preparation of Al-doped $SrTiO_3$ photocatalyst

Molten flux method was used for the preparation of Al-$SrTiO_3$ particles as reported previously [278]. Firstly, pristine $SrTiO_3$, Al_2O_3, and the flux agent $SrCl_2$, with a molar ratio of (1: 0.02: 10) were grinded in an agate mortar then placed in a pure alumina crucible. Secondly, the mixed powders were heated at 1150ºC in air for 10 h using a muffle furnace. Thirdly, ultrasonication was used to dissociate the formed powder from the walls of the crucible after cooling down to room temperature naturally. Fourthly, via distilled water (D.W.), collected powder was washed many times to eliminate any residual $SrCl_2$. Finally, washed powder was dried overnight at 60ºC in air.

6.3.2.2 Loading of Au NPs on the prepared Al-$SrTiO_3$

Al-$SrTiO_3$ sample (obtained from the previous step) was loaded with Au NPs using the impregnation method reported by Chen et al., [252]. Firstly, dried Al-$SrTiO_3$ particles were dispersed in a small volume of D.W. (4 mL) using ultrasonication for 10 min. Then, calculated volumes of $HAuCl_4.3H_2O$ aqueous solution was added to the dispersion to deposit Au NPs with 1 wt. %, 2 wt.%, 3 wt.%, 4 wt.%, and 5 wt.% (with respect to Al-$SrTiO_3$). After water evaporation on a hot plate (at 80ºC), dried powder was calcined at 350 ºC for 1 h in air.

6.3.2.3 Preparation of CdS NPs

CdS NPs were prepared using a co-precipitation method as previously reported [279]. In brief, (1 m mole) of $Cd(NO_3)_2.4H_2O$ and (1 m mole) of $Na_2S.9H_2O$ aqueous solutions were prepared separately in (30 mL) D.W. Then, $Na_2S.9H_2O$ aqueous solution was slowly added to $Cd(NO_3)_2.4H_2O$ solution drop-by-drop under constant stirring at room temperature. After that, the orange mixture was left under continued stirring for 1h. Then, the formed precipitate was collected using centrifugation and washed many times using D.W. and ethanol. Finally, collected powder was dried at 60ºC in air for 12h.

6.3.2.4 Preparation of Al-$SrTiO_3$ / Au / CdS Z-Scheme

Al-$SrTiO_3$ / Au / CdS Z-Scheme samples were prepared by a modified post annealing of mixed powders technique reported by Wang et al., [280]. Firstly, fixed amounts of Au-loaded Al-$SrTiO_3$ and CdS NPs were mixed in a ceramic crucible. Finally, mixed powders were annealed at 300ºC for 30 min in air. Different samples were prepared by changing the wt.% of Au-loaded Al-$SrTiO_3$ with respect to CdS NPs (1:1), (1:2), (1:3), (1:4), (2:1), (3:1), and (5:1).

6.3.2.5 Characterization of the prepared samples

Crystallinity and the formed phase were investigated by X-ray diffraction (XRD) analysis performed on Ultima IV X-ray diffractometer (Rigaku, Japan), operating at 40 kV - 30 mA and using Cu-Kα radiation ($\lambda = 1.54$ Å). While morphology of samples, mean diameter, conjugation of Z-Scheme elements, and possible alignments were analyzed via scanning transmission electron microscopy (STEM) on JEM-2100F (JEOL Ltd., Japan), supported with (JED-2300T) energy-dispersive X-ray (EDX) spectroscopy unit. In addition, to reveal the optical properties of samples, diffuse-reflectance and bandgap calculations were conducted via V-670 spectrophotometer (JASCO, Japan). Moreover, charge recombination affinity was investigated through recording PL spectra on a laser spectroscopy unit (KIMMON KOHA, Japan) with 325 nm excitation wavelength. While elemental structure and valence states were analyzed via X-ray photoelectron spectroscopy (XPS) analysis using (ULVAC-Phi, QuanteraSXM, Al Kα, Japan). Finally, chemical composition of samples was studied by Raman analysis carried out by JASCO, NRS-4500 laser Raman spectrometer.

6.3.2.6 Photocatalytic H_2 evaluation

(100) mg of each sample was dispersed in (220 mL) D.W. containing a mixture of (0.1 M) $Na_2S.9H_2O$ and (0.1 M) Na_2SO_3 as sacrificial agents, using ultrasonication for 30 min. Then, $RhCr_2O_3$ as hydrogen evolution (HE) cocatalyst (Rh = 0.1 wt.% - Cr = 0.05 wt.%) was loaded using photodeposition method as previously described in our article [278]. After that, the photocatalytic cell (containing sample, sacrificial agents, and HE cocatalyst) was evacuated to remove any dissolved gases using a gas circulation system (Makuhari Rikagaku Garasu Seisakujo, Japan). Then, the photocatalytic cell was irradiated by (HAL-320, 350–1100 nm) Xenon lamp, ASAHI SPECTRA, Japan), supported with UV cut filter (λ > 400 nm). Finally, evolved gases were evaluated via an online-connected gas chromatography (GC) system, GC-8A (Shimadzu, Japan) supported with a thermal conductivity detector (TCD), and employing Argon (Ar) as a carrier gas.

6.4 Results and discussion

6.4.1 Photocatalytic H_2 evolution under visible light

The photocatalytic H_2 evolution performance of the prepared Z-Scheme samples with different wt. % of Au NPs and fixed ratios of Al-$SrTiO_3$ and CdS NPs (1:1), is shown in **Fig. 6.1**. It is clearly observed that, sample loaded with 4 wt. % Au NPs exhibit the highest efficiency (656.7 µ mole) after 3 h of visible light irradiation followed by the sample loaded with 1 wt. % of Au NPs. In addition, increasing the wt. % of Au NPs significantly (up to 5 wt. %), resulted in a considerable reduction of H_2 evolution efficiency (144 µ mole after the same time of light irradiation). This observation could be due to the possible agglomeration and / or interference between Au NPs and $RhCr_2O_3$ cocatalyst responsible for H_2 evolution as previously explained and confirmed in our published article [278].

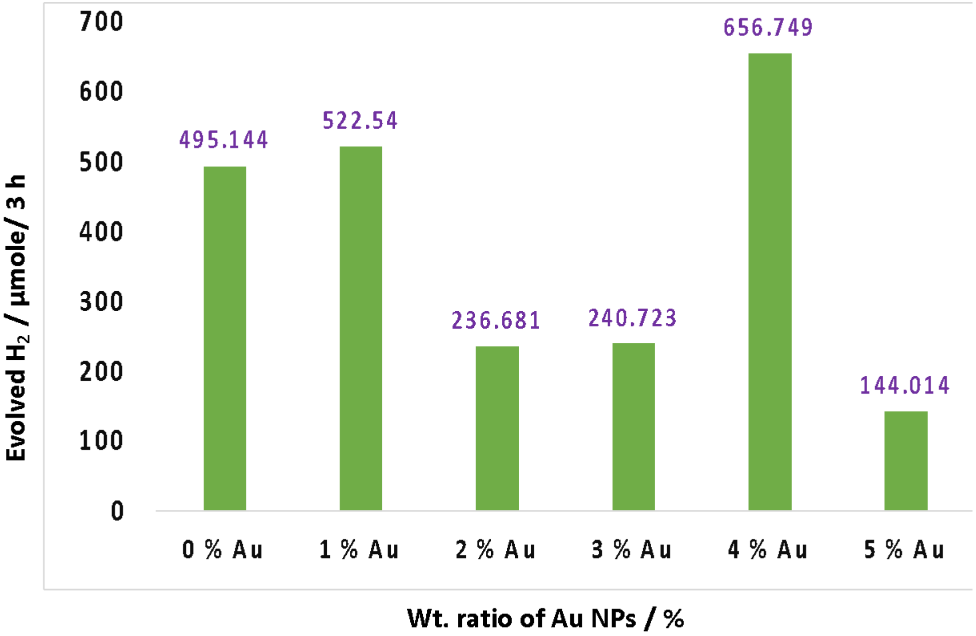

Fig. 6.1: Evolved H_2 under visible light ($\lambda > 400$ nm) by Al-$SrTiO_3$/Z Au/CdS (1:z:1) using 0.1 M Na_2S. $9H_2O$ – 0.1 M Na_2SO_3 as sacrificial agents and $RhCr_2O_3$ (0.1 wt. % - 0.05 wt. %) as HE cocatalyst.

While the effect of changing the wt.% of Al-$SrTiO_3$ to CdS NPs (while fixing the wt. % of Au NPs to the best value - 4 wt.%) on the evolved H_2 is presented in **Fig. 6.2**. Clearly observed that, sample having the wt. % of Al-$SrTiO_3$ to CdS NPs = (1:1) is superior compared to other prepared Z-Scheme samples due to the balance between number of electrons produced at one side and the number of electrons utilized on the other side as previously reported [281].

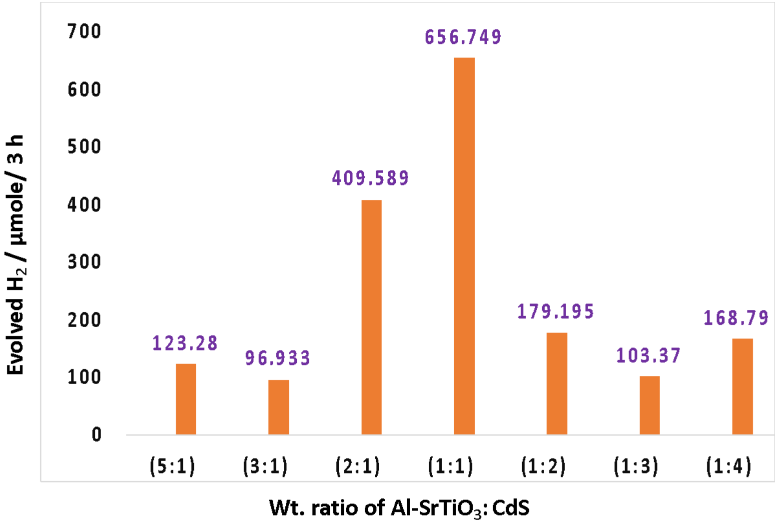

Fig. 6.2: Evolved H_2 under visible light ($\lambda > 400$ nm) by x Al-$SrTiO_3$/4 wt. % Au/ y CdS (x:y) using 0.1 M Na_2S. $9H_2O$ – 0.1 M Na_2SO_3 as sacrificial agents and $RhCr_2O_3$ (0.1 wt. % - 0.05 wt. %) as HE cocatalyst.

The possible reaction mechanisms of H_2 evolution by the prepared Z-Scheme samples are shown in **Fig. 6.3 (a-b)**. Upon light excitation, photogenerated charge carriers (electrons and holes) are generated from CdS having proper bandgap energy (2.17 eV) smaller than the energy of the incident light, holes oxidize water into protons and oxygen anions and some of them are consumed by the sacrificial agents ($Na_2S.9H_2O$ and Na_2SO_3) to promote their separation. Then electrons from both the conduction band (CB) of CdS (having more reductive potential than the CB of Al-$SrTiO_3$) and hot electrons / plasmons transfer to the CB of Al-$SrTiO_3$ (with relatively lower reductive potential) where the H_2 evolution core-shell cocatalyst ($RhCr_2O_3$) promotes the reduction of protons into H_2.

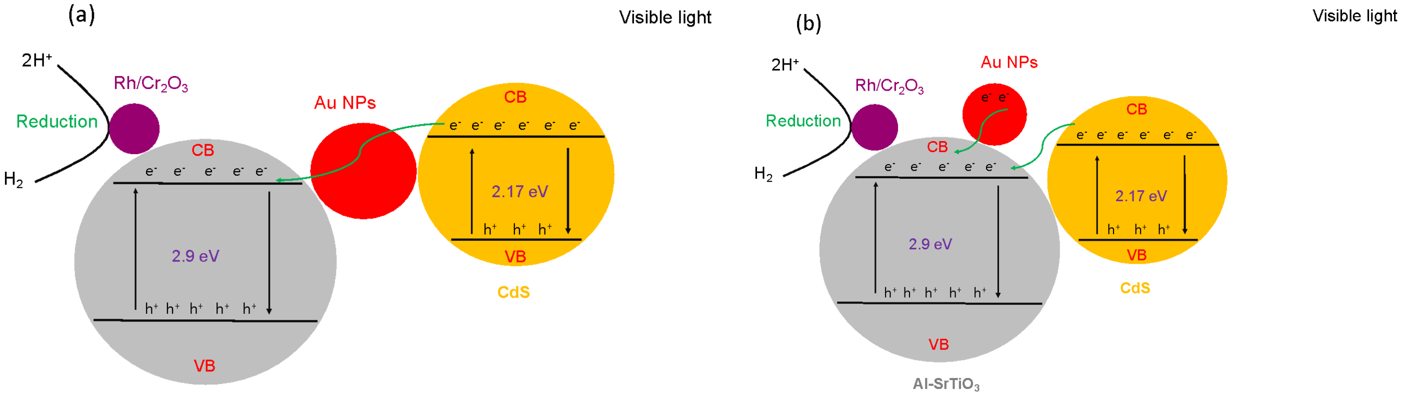

Fig. 6.3: Possible reaction mechanisms of H_2 evolution under visible light by the prepared Z-Scheme samples.

6.4.2 UV-Vis. diffuse reflectance analysis

Fig. 6.4 shows the UV-Vis. diffuse reflectance analysis of the prepared Z-Scheme samples with different wt. % of Au NPs. For all samples, a strong absorption in the UV region (nearly at 350 nm) is exhibited, due to the presence of Al-$SrTiO_3$. While the absorption in the visible light region (475-500 nm) is due to the presence of CdS and Au NPs [282, 283]. It is worth to mention that, by changing the wt. % of Au NPs from 1 to 5, the absorption in the visible light region was changed where the sample loaded with 2 wt. % Au NPs, possesses the best absorption.

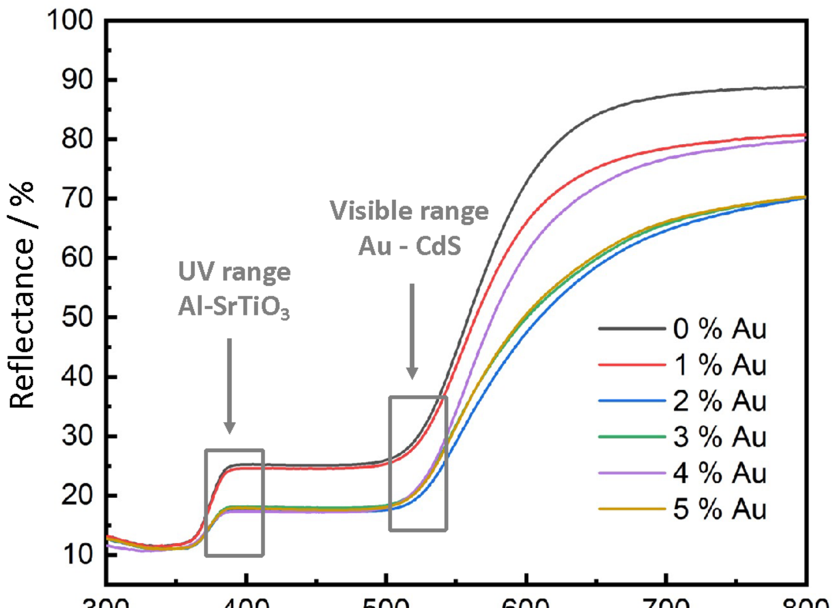

Fig. 6.4: UV-Vis. Diffuse Reflectance of the prepared Z-scheme samples (Al-SrTiO$_3$ / z wt. % Au / CdS (1:1).

6.4.3 Photoluminescence (PL) analysis: estimation of charge carrier lifetime

To get insights on the lifetime of the photogenerated charge carriers playing a significant role in the photocatalytic H_2 evolution, PL analysis of the prepared Z-Scheme samples was carried out and the result is depicted in **Fig. 6.5**. In PL analysis, high intensity means fast recombination rate of electron-hole pairs causing a deterioration of the photocatalytic abilities. It is clearly-observed that, the fastest recombination rate of charge carriers is shown by Al-SrTiO$_3$/ 2 wt.% Au / CdS (1:1) Z-Scheme sample having the highest PL intensity. While, Al-SrTiO$_3$/ 4 wt.% Au / CdS (1:1) Z-Scheme sample exhibits more prolonged lifetime of electron-hole pairs indicated by the considerable decrease in PL intensity, which is a remark of superior photocatalytic performance. This result might be attributed to the synergetic effect of Al^{+3} ion doping which replaced Ti^{+3} known as a recombination center for charge carriers [243] or the optimized ratio of Au NPs, which adjusted the Fermi energy levels [284] and / or the dominance of oxygen vacancies on the surface which acted to electron reservoirs and thus led to an improved charge separation [285].

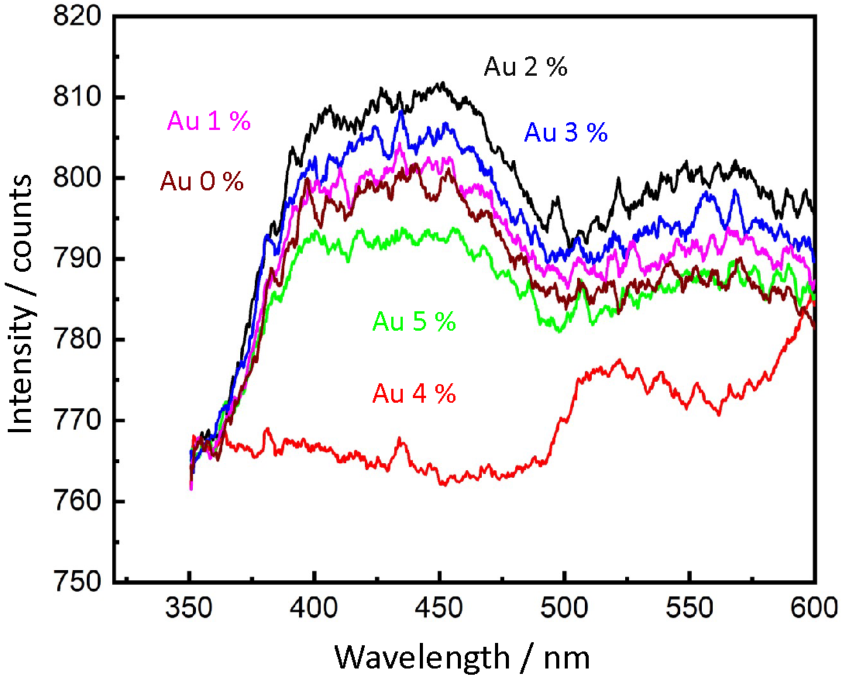

Fig. 6.5: PL analysis of the prepared Z-scheme samples (Al-SrTiO$_3$ / z wt. % Au / CdS (1:1).

6.4.4 XRD (crystallinity and phase) analysis

XRD analysis was carried out to reveal the crystallinity and phase of the prepared samples [194] as shown in **Fig. 6.6**. For Al-SrTiO$_3$ sample, many bragg peaks are detected at 2θ = 22.7° (100), 32.5° (110), 40.2° (111), 46.6.5° (200), 53.3° (210), 58.6° (211), 68.2° (220), 73.7° (300), and 78.6° (310). The recorded peaks and their corresponding crystallographic planes are in a good agreement with those reported for the cubic perovskite phase of SrTiO$_3$ (JCPDS No. 73-0661) [255]. It is worth mentioned that, doping with Al^{+3} ions, could not affect the crystal composition of SrTiO$_3$, which can be ascribed to their high dispersion and / or lower ratio [250]. For Au-loaded Al-SrTiO$_3$ sample, same peaks of Al-SrTiO$_3$ were detected along with the characteristic peaks of the face-centered cubic Au, appeared at 2θ = 38.1° (111), 44.3° (200), and 64.5° (220) (JCPDS No. 04-0784) [256]. In addition, due to the preparation method using high temperature, all Al-SrTiO$_3$ based samples have high crystallinity as indicted by their intense and sharp peaks. Moreover, their crystallite size is relatively small as shown by the narrow width of their peaks. While for bare CdS sample, three peaks at 2θ = 27.2° (111), 44.1° (220), and 52.7° (311) are observed indicating the formation of Cubic Zinc Blende CdS (JCPDS No. 10-0454) [286]. Finally, for the prepared Z-Scheme sample, characteristic peaks indicating the presence and conjugation of all constituting elements (Al-SrTiO$_3$, Au NPs, and CdS) are detected.

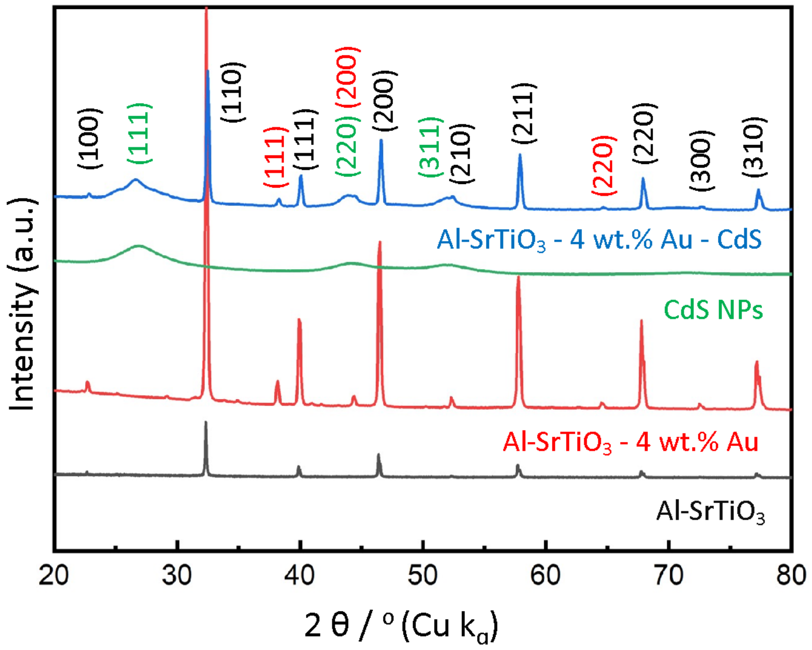

Fig. 6.6: XRD analysis of the prepared Al-SrTiO$_3$ / 4 wt. % Au / CdS (1:1) Z-Scheme sample.

6.4.5 Raman (chemical composition) analysis

Raman analysis was performed to investigate the chemical structure of the prepared Al-SrTiO$_3$/ 4 wt.% Au / CdS (1:1) sample, as presented in **Fig. 6.7**. For Al-SrTiO$_3$, Several peaks are recorded at 190 cm^{-1}, 250 - 348 cm^{-1}, 539 cm^{-1}, and 621 - 718 cm^{-1} corresponding to TO2 (O-Sr-O), TO3 (O-Sr-O), TO4 (O-Sr-O), and LO (Ti-O-Ti), respectively [287]. While for CdS, two characteristic peaks are observed at 301 cm^{-1} and 620 cm^{-1} indicating the fundamental optical phonon mode (1LO) and the first over tone mode (2LO) of CdS, respectively [288].

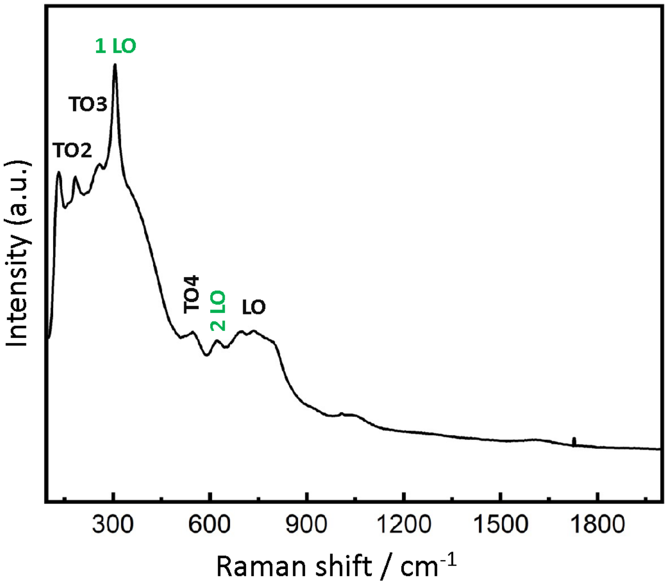

Fig. 6.7: Raman analysis of the prepared Al-SrTiO$_3$ / 4 wt. % Au / CdS (1:1) Z-Scheme sample.

6.4.6 XPS (valence states and elemental structure) analysis

To analyze the elemental structure and valence states of the prepared Al-SrTiO$_3$/ 4 wt.% Au / CdS (1:1) Z-Scheme sample, XPS analysis was conducted as presented in **Fig. 6.8 (a-g)**. **Fig. 6.8 (a)** shows the survey study, where several peaks characteristic to all constituting elements are recorded

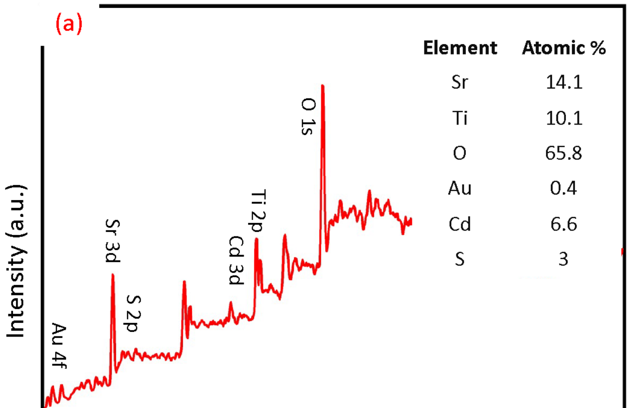

along with their atomic ratios. While the deconvoluted peaks of the substantial elements (Sr, Ti, O, Au, Cd, and S) are presented in **Fig. 6.8 (b-g)**. For Sr 3d, two main peaks at (133.3 eV and 134.2 eV) are observed conforming with (3d $_{5/2}$ and 3d $_{3/2}$), and confirming the presence of Sr^{+2} state [289]. While for Ti 2p, the two characteristic peaks detected at (457.6 eV and 463.3 eV) pointing to (2p $_{3/2}$ and 2p $_{1/2}$), prove the dominance of Ti^{+4} state [151]. This finding affirms the replacement of Ti^{+3} by Al^{+3} ions due to the doping process. Ti^{+4} state is more desirable for an enhanced photocatalytic ability. For O1s, two peaks are detected, characteristic peak of oxygen in metal oxides at (529.5 eV) and another peak at (531.4 eV) showing the presence of hydroxyl groups or adsorbed water molecules. While, at higher binding energies, a flat shoulder is detected assuring the presence of oxygen vacancies at the surface which well-matched with PL results (**Fig. 6.5**) and showing the high potential of the prepared sample for more enhanced photocatalytic performance [212]. For Au, two peaks can be observed at 83.6 eV (4f $_{7/2}$) of the metallic Au and 87.4 eV (4f $_{5/2}$) of Au (I) oxidation state which is unstable state and tend to donate electrons to form more stable compounds [290]. For Cd 3d, two peaks at 405.3 eV and 411.8 eV are detected, which corresponding to (3d $_{5/2}$ and 3d $_{3/2}$) and indicating the presence of Cd^{+2} state. While for S 2p, recorded peaks at 161.8 eV (2p $_{3/2}$) and 162.7 eV (2p $_{1/5}$) pointing to the S^{-2} state in sulfides [283].

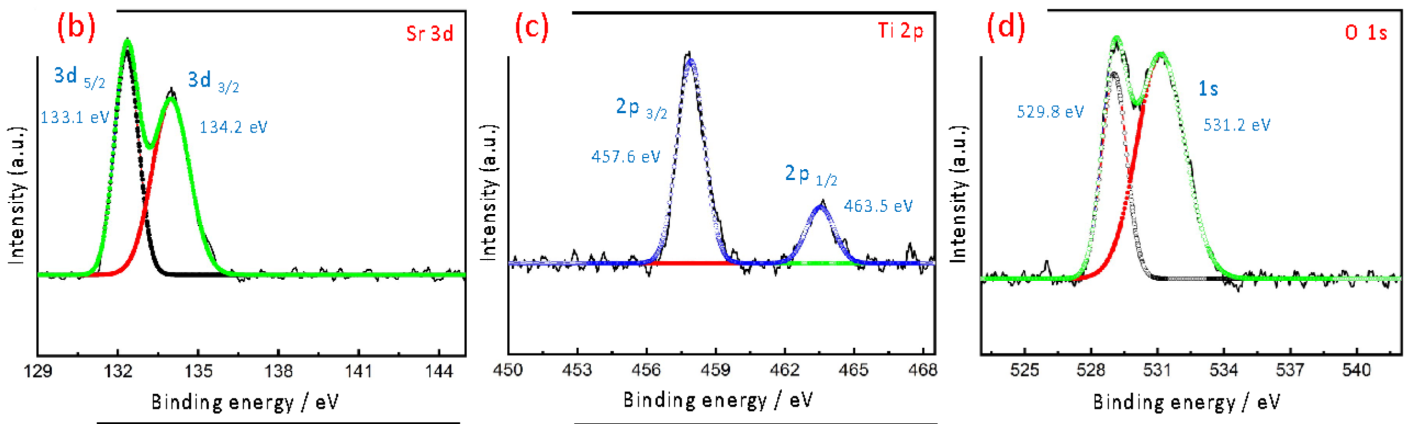

Fig. 6.8: XPS analysis of the prepared Al-SrTiO$_3$ / 4 wt. % Au / CdS (1:1) Z-Scheme sample, a) survey analysis, b-g, deconvoluted peaks of Sr, Ti, O, Au Cd, and S.

6.4.7 SEM (morphology) analysis

There is a tight relation between the performance of photocatalysts and their morphology according to several recent studies, that's the reason why SEM analysis was conducted to analyze the morphology of the prepared Al-SrTiO$_3$/ 4 wt.% Au / CdS (1:1) Z-Scheme sample as presented in **Fig. 6.9**. Al-SrTiO$_3$ possesses cubic morphology characteristic to the perovskite materials as found by XRD analysis (**Fig. 6.6**). While, semi-spherical and relatively smaller Au NPs are randomly deposited onto the surface of Al-SrTiO$_3$ because of the impregnation method used during preparation. Similarly, CdS NPs shown in the vicinity of Al-SrTiO$_3$ exhibit semi-spherical shape.

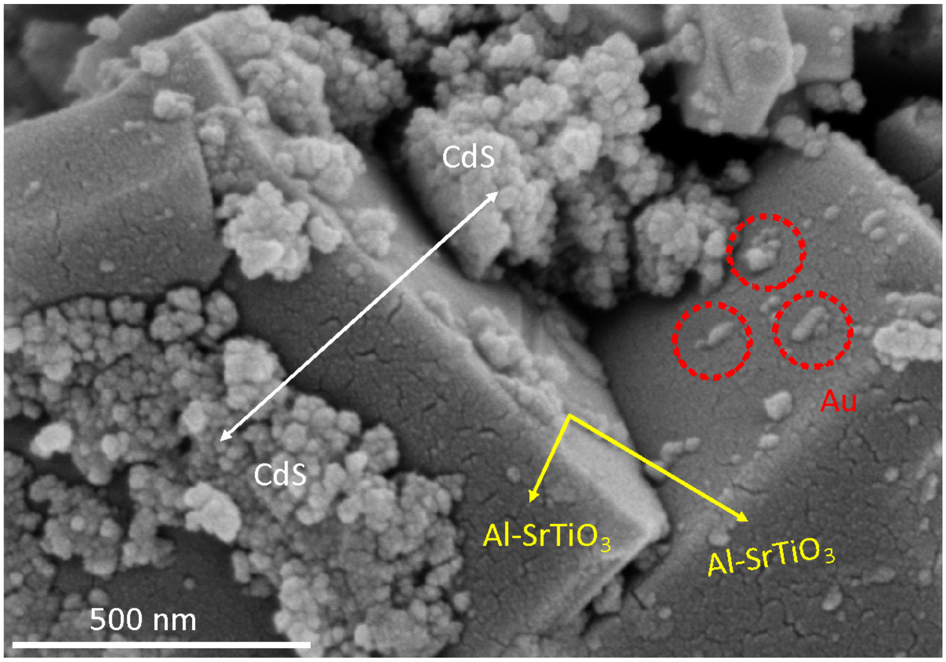

Fig. 6.9: SEM analysis of the prepared Al-SrTiO$_3$ / 4 wt. % Au / CdS (1:1) Z-Scheme sample.

6.4.8 TEM and STEM mapping analyses

Mean diameter, conjugation, phase, and suggested alignments of the prepared Al-SrTiO$_3$/ 4 wt.% Au / CdS (1:1) Z-Scheme sample were investigated using TEM, HR-TEM, SAED, and STEM

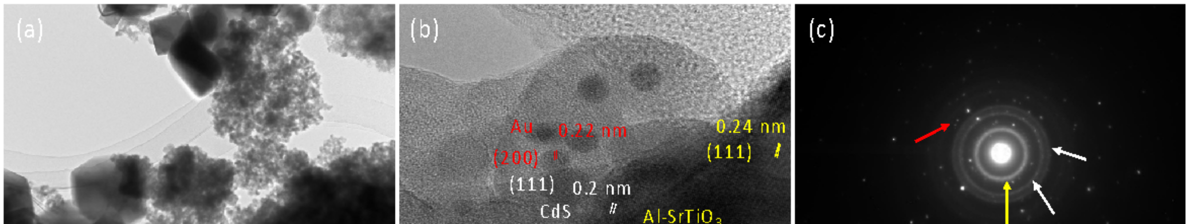

mapping analyses as shown in **Fig. 6.10 (a-m)**. The mean diameter of Al-SrTiO$_3$ particles were found to be 150 nm **Fig. 6.10 (a)**. While HR-TEM analysis in **Fig. 6.10 (b)** and SAED analysis in **Fig. 6.10 (c)**, confirm the conjugation of the constituting elements to form the Z-Scheme indicated by the presence of their crystallographic planes and confirm the formed phase of elements which is in a good agreement with the result obtained by XRD analysis (**Fig. 6.6**). While STEM mapping **Fig 6.10 (d-i)** reveals the purity and elemental uniform distribution. Furthermore, STEM mapping overlap **Fig. 6.10 (j-k)** was conducted to reveal the possible alignments

Fig. 6.10 (l-m) of the Z-Scheme sample.

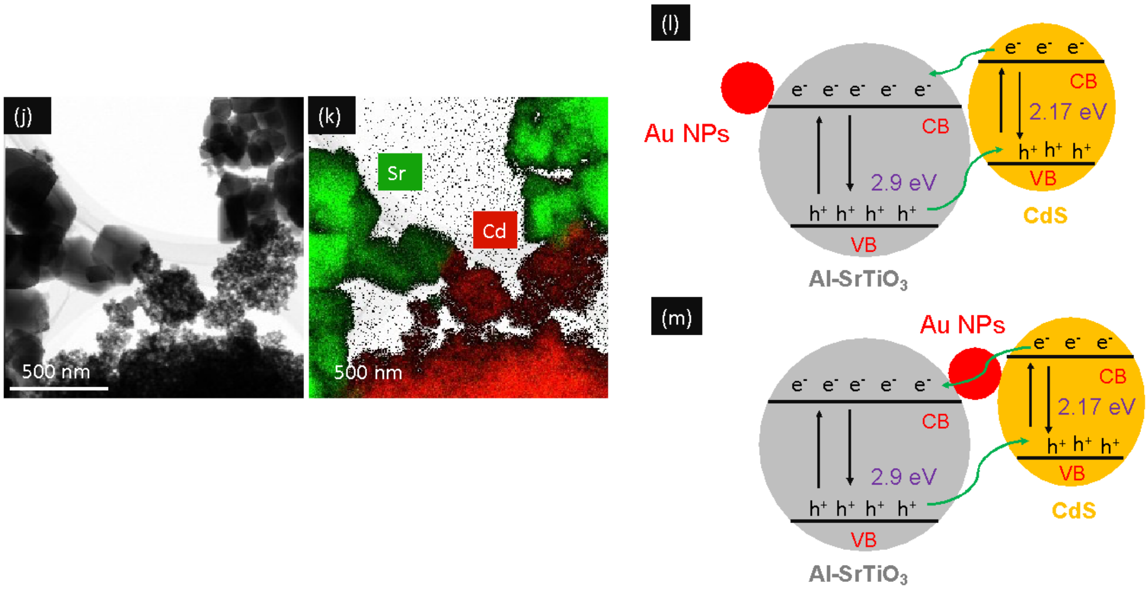

Fig. 6.10: a) TEM analysis, b) HR-TEM analysis, c) SAED pattern, d-I, STEM mapping, j-k, STEM overlap analysis, and l-m) possible alignments of the prepared Al-SrTiO$_3$ / 4 wt. % Au / CdS (1:1) Z-Scheme sample.

6.5 Conclusion

In the present study, many Z-Scheme samples were prepared by a modified method known as post annealing of mixed powders, where Al-SrTiO$_3$ was combined with CdS and Au NPs for the

photocatalytic H_2 evolution under visible light (λ > 400 nm). The phase, purity, and crystallinity of the prepared samples were confirmed along with the efficient conjugation of the constituting elements to build the proposed structure. While, Our H_2 evolution results confirmed that changing either the wt. % of Au NPs, or the wt. % ratio of Al-$SrTiO_3$ to CdS, possesses a significant effect on the H_2 evolution efficiency. The best sample was found to be Al-$SrTiO_3$/
4 wt.% Au / CdS (1:1) which gave the maximum amount of evolved H_2 656.7
μ mole) after 3 h of visible light irradiation. This relatively higher activity is ascribed to an efficient light absorption, prolonged lifetime of the photogenerated charge carriers, and charge separation. Our study opens the way toward carbon neutrality and the efficient production of sustainable solar fuels.

Chapter 7: carbon loaded nanocomposite as an efficient electrode material for supercapacitor applications

7.1 Overview

Naturally, a combination of metal oxides and carbon materials enhances the electrochemical performance of supercapacitor (SC) electrodes. We report on two different materials with highly conductive carbon dots (CDs) and $Co_{0.5}Ni_{0.5}Fe_2O_4/SiO_2/TiO_2$ nanocomposite with a high power density, a high specific surface area, and a nanoporous structure to improve power and energy density in energy storage devices. A simple and low-cost process for synthesizing the hybrid SC electrode material $Co_{0.5}Ni_{0.5}Fe_2O_4/SiO_2/TiO_2$/CDs, known as CDs-nanocomposite, was performed via a layer-by-layer method; then, the CDs-nanocomposite was loaded on nickel foam substrate for SC electrochemical measurements. A comparative study of the surface and morphology of CDs, $Co_{0.5}Ni_{0.5}Fe_2O_4/SiO_2/TiO_2$ nanocomposite and CDs-nanocomposite was carried out using X-ray diffraction (XRD), scanning electron microscopy (SEM), transmission electron microscopy (TEM), energy-dispersive X-ray spectroscopy (EDX), BET surface area, and Raman spectroscopy. The synthesized CDs-nanocomposite electrode material displayed enhanced electrochemical performance, having a high specific capacitance of 913.7 F/g at a scan rate of 5 mV/s and capacitance retention of 72.2%, as well as remarkable long-life cyclic stability over 3000 cycles in the three-electrode setup and 1 M KOH electrolyte. It also demonstrated a superior energy density of 130.7 Wh/kg. The improved electrochemical behavior of the CDs-nanocomposite for SC electrodes, together with its fast and simple synthesis method, provides a suitable point of reference. Other kinds of metal oxide nanocomposites can be synthesized for use in energy storage devices.

7.2 Introduction

Over the last century, the energy used by humans has come primarily from fossil fuels. Conventional fossil fuel resources continue to be consumed at an alarming rate to meet soaring energy demands. Global climate change caused by the excessive burning of fossil fuels has worsened and become an urgent problem [291-293]. Consequently, researchers seek new forms of renewable energy to reduce carbon dioxide emissions and enable the transition to clean and eco-friendly energy sources [294, 295]. Such technologies also help to control and reduce the cost of electricity, improve the consistency and flexibility of electrical systems, replace aging power infrastructure, and provide consistent power to remote areas [296]. However, renewable energy sources are prone to fluctuations. Therefore, energy storage systems will be required to buffer these fluctuations to ensure a stable energy supply [297-300]. Supercapacitors (SCs), unlike batteries or fuel cells, are the key to efficient electrochemical energy storage as they demonstrate high power density, a fast charge–discharge rate, a long life cycle, and a simple operational mechanism [301, 302]. These properties come from two common mechanisms: the electric double-layer capacitance (EDLC) and the pseudocapacitance (PC). In EDLC, the capacitance comes from the high charge accumulation rate at the electrolyte–electrode interface. Therefore, a large surface area and porous structure are required in this case. In contrast, the PC mechanism employs a fast oxidation–reduction reaction [303-305]. Activated carbon-based materials, such as carbon nanotube (CNT), carbon dots (CDs), and graphene, are commonly used in the construction of EDLC electrodes due to their high porosity, low cost, chemical and physical stability, and ease of production from renewable sources [306-308]. However, the specific capacitance of activated carbon electrodes is still lower than that of many other materials, such as conductive polymers and inorganic oxides, which are generally used in PC electrodes [309]. Therefore, the electrical performance of carbon-based SCs must improve before they are useful for practical applications. This can be accomplished by incorporating pseudocapacitive properties and combining carbon-based materials with materials that have a large surface area and appropriate pore size, such as metal oxides, metal hydroxides, and polymers, or with materials containing oxygen or nitrogen functional groups. Such energy storage systems are known as hybrid SCs [310, 311]. Titanium dioxide (TiO_2) is widely used as a photocatalyst and semiconductor in dye-sensitized solar cells. However, researchers recently turned their attention to using TiO_2 as an electroactive material for SCs. TiO_2 possesses semiconducting properties, low-cost production, high stability, and is environmentally friendly. However, TiO_2 has some drawbacks, such as slow ion diffusion and low electrical conductivity, which worsen its performance. Its low specific capacitance range of 90–120 $\mu F/cm^2$ is much lower than those of other transition metal oxides (e.g. $Co(OH)_2$, Co_3O_4, $NiOH_2$, spinel cobaltites etc.) [312-317]. TiO_2 performance must improve to enable the production of low-cost, practical TiO_2-based SCs. This can be achieved by combining TiO_2 with a range of carbon-based materials or conjugated polymers to form composites with mutual EDLC and PC properties, enhancing the SC electrode materials [318]. TiO_2-based CDs demonstrate excellent suitability for supercapacitor applications due to their nanometer size, unique electronic and surface functionalities, large surface area, simple synthesis, low environmental risk, and high charge–discharge rate [319, 320]. The hybridization of carbon allotropes with metal oxides will improve the hybrid system's conductivity and structural stability. TiO_2- based CDs has excellent electron mobility, conductivity, high transmittance, Young's modulus, and large SSA. As a result, it has been used in energy storage applications as an additive with TiO_2 electrodes [321-323]. In this chapter, TiO_2-based CDs nanocomposite ($Co_xNi_{1-x}Fe_2O_4$;, x = 0.5/SiO_2/TiO_2/CDs), termed CDs-nanocomposite, is synthesized via a layer-by-layer method. Loading CDs-nanocomposite electrode materials on nickel foam (NF) substrate improves supercapacitive performance. The experimental results display superior specific capacitance magnitudes of 913.7 F/g at a scan rate of 5 mV/s and capacitance retention of 72.2%. In addition, the results demonstrate a higher energy density of 130.7 Wh/kg and exceptional long-life cyclic stability over 3000 cycles. CDs-nanocomposite electrode materials also demonstrate significant values of power and energy density. Consequently, this makes CDs-nanocomposite on NF a promising candidate for use as a hybrid supercapacitor electrode material.

7.3 Materials and methods

7.3.1 Materials

Ascorbic acid ($C_6H_8O_6$), titanium (IV) isopropoxide (97%, $C_{12}H_{28}O_4Ti$), copper acetate monohydrate ($C_4H_8CuO_5$), tetraethyl orthosilicate (TEOS, 98%, $Si(OC_2H_5)_4$), ammonium hydroxide (28%, NH_4OH), hydroxypropyl cellulose (MW = 80,000), absolute ethanol (99.9%, C_2H_5OH), cobalt chloride ($CoCl_2$), nickel chloride ($NiCl_2$), sodium hydroxide pellets (NaOH), and ferric chloride hexahydrate ($FeCl_3 \cdot 6H_2O$), were purchased from Sigma Aldrich (Germany). All reagents were of extra-pure grade and were used as received from the supplier without further purification.

7.3.2 Methods

7.3.2.1 Preparation of the composite matrix

$Co_{0.5}Ni_{0.5}Fe_2O_4/SiO_2/TiO_2$ nanocomposite matrix was prepared using a layer-by-layer method. $Co_xNi_{1-x}Fe_2O_4$; x = 0.5 core was firstly-prepared using a coprecipitation route. Cobalt chloride (12.5 mg), Ferric chloride 45% (0.05 ml), and Nickel chloride (12.5 mg) were mixed with deionized water (D.I.W.) (50 ml) at 80 °C. Then, pH was adjusted to 8 using few drops of NaOH aqueous solution (2 M) leading to the precipitation of ferrite black particles. Then, formed particles were washed using D.I.W and dried at 70 °C for 3 hrs. Finally, dried particles were calcined for 4 hrs. at 300 °C. Secondly, core-shell structure (Ferrite/SiO_2) was prepared. Ferrite powder (180 mg) (obtained in the previous step) was dispersed in (64 ml) D.I.W. via water-bath sonication for 45 min. Then, absolute ethanol (320 ml) and ammonia solutions (25%) (8 ml) were added directly into the dispersion at room temperature. After mixing, TEOS (3.2 ml) was added dropwise to the mixture, which was left under stirring for 16 hrs. The precipitate was collected by centrifugation and was washed with D.I.W. and ethanol. Finally, the precipitate was dried at 50 °C in air. To load TiO_2 layer onto the formed core-shell structure, (obtained powder from the previous step) was dispersed in a mixture of absolute ethanol (100 ml), hydroxypropyl cellulose (0.2 g), and (0.48 ml) D.I.W. via sonication for 30 min. Then, dissolved titanium(IV) isopropoxide (4 ml) in absolute ethanol (18 ml) was dipped directly into the mixture under vigorous stirring at 85ºC. The reaction was left under reflux conditions for 100 min. The obtained powder was collected and washed with ethanol, then it was re-dispersed in D.I.W. (20 ml) to partially etch the silica layer to form a hollow structure. The dispersion was mixed with (3.5 ml) NaOH solution (2 M) under fixed stirring for 1 h. The powder was then collected, washed several times with D.I.W. and dried for 4 hrs. at 90 °C. Finally, dried powder was calcined for 4 hrs. at 550 °C.

7.3.2.2 Preparation of CDs

CDs were prepared using a hydrothermal method. In brief, ascorbic acid (6.8 g) was dissolved in (400 ml) D.I.W. Then, copper acetate monohydrate (0.8 g) was added to the formed solution at room temperature under fixed stirring for 10 min. Reaction temperature was then increased gradually to 90 °C and the mixture was left for 5 hrs. The formed supernatant was purified through Millipore filter paper (0.22 μm). Finally, supernatant containing CDs was freeze-dried for 12 h.

7.3.2.3 Preparation of CDs-nanocomposite

Prepared CDs and composite matrix (1:10 wt./wt.) were dispersed in super dehydrated ethanol solution (50 ml) using water bath sonication for 30 min. Next, (1 ml) of NH_4OH 25% solution was added into the mixture which was kept at vigorous stirring overnight. Finally, collected powder was washed many times using D.I.W. and dried for 6 hrs. at 80 °C.

7.3.2.4 Loading of CDs-nanocomposite electrode materials on NF substrate for hybrid supercapacitor application

Initially, 1 mg of CDs-nanocomposite powder was dispersed in a solution of 1 ml isopropanol, 1 ml deionized water, and 50 μl Nafion (0.5 wt%) and sonicated for 30 min until homogeneous. Then, using a micropipette, 0.5 mg of this solution was loaded on a clean NF substrate of a defined area of 1.5 × 1.5 cm^2. Finally, the NF loaded with CDs-nanocomposite was heated in an oven at 60°C for 2 h or until completely dry. The CDs-nanocomposite on NF electrode was then ready to be used for electrochemical measurements as shown in the schematic diagram in **Fig. 7.1**.

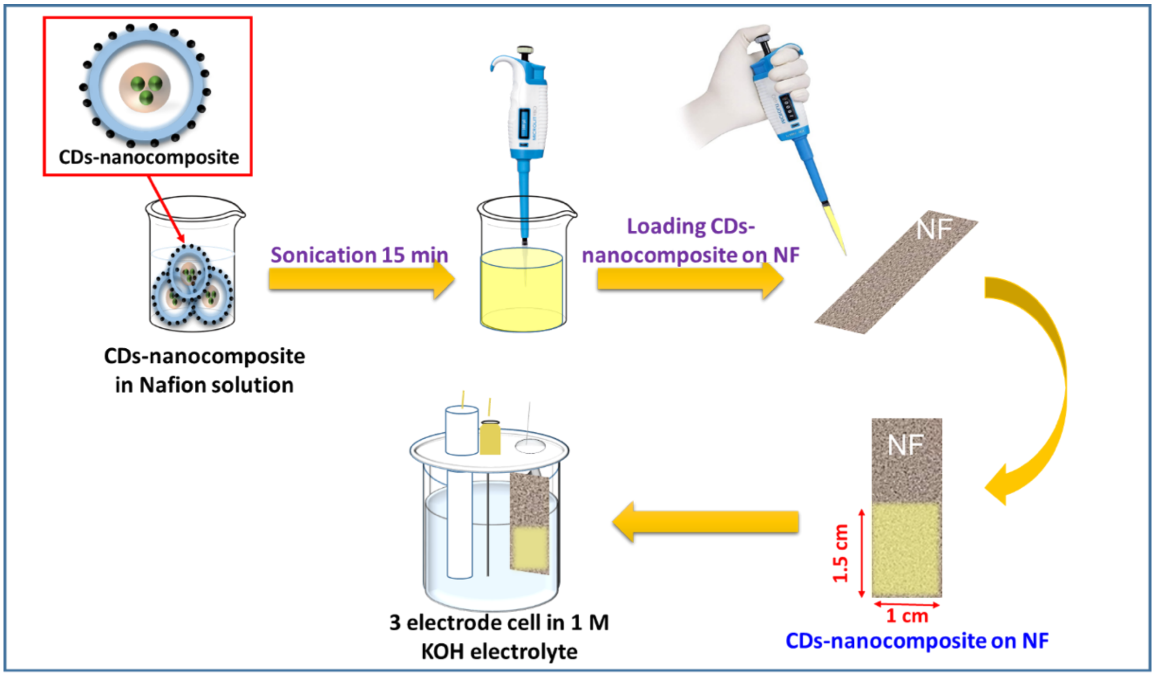

Fig. 7.1: Schematic diagram for the detailed steps of loading CDs-nanocomposite on nickel foam (NF) substrate and preparing it for electrochemical measurements.

7.3.2.5 Characterization of the prepared samples

X-ray diffraction (XRD) patterns were recorded using a Rigaku Ultima IV X-ray diffractometer (Japan) with Cu Kα radiation (λ = 1.5418A°) operating at 40 kV and 60 mA. While, SEM analysis was performed via SEM (Hitachi SU 8000 Type II) connected with energy-dispersive X-ray spectroscopy (EDX). In addition, BET surface area and BJH pore size distribution analyses were conducted by a Tristar II analyzer (Micromeritics, Japan). In addition, TEM analysis was carried out via JEM-2100F (JEOL, Japan). Moreover, Raman analysis was performed on a JASCO NRS-3100 micro-spectrometer with excitation radiation.

7.3.2.6 Electrochemical analysis

The electrochemical performance of the electrode materials was tested in a three-electrode configuration system using a Solartron SI 1286 electrochemical workstation with 1 M KOH as an electrolyte.

7.4 Results and discussion

7.4.1 Characterizations

7.4.1.1 XRD analysis

The formed phase and crystallinity of the synthesized samples were investigated by XRD analysis as shown in **Fig 7.2**. The XRD pattern of the bare composite matrix displayed many diffraction peaks, such as peaks at $2\theta = 25.6°$ (101), at $2\theta = 37.4°$ (004), at $2\theta = 48.2°$ (200), at $2\theta = 53.6°$ (105), at $2\theta = 55.4°$ (211), at $2\theta = 62.8°$ (204), at $2\theta = 68.8°$ (116), at $2\theta = 71.4°$ (220), and at $2\theta = 75.4°$ (215). The observed Bragg peaks and their corresponding crystallographic planes were in good accordance with the anatase TiO_2 phase (JCPDS 21–1272). Therefore, the TiO_2 layer is the dominating material in the composite matrix. It is worth noting that the amorphous halo of the SiO_2 material, usually detected at $2\theta = 21.5°$, was suppressed due to the sharp peaks of the crystalline TiO_2 layer. Similarly, the corresponding peaks of the $Co_{0.5}Ni_{0.5}Fe_2O_4$ material disappeared, which may be attributable to its relatively small ratio and its presence in the internal core of the composite matrix. Similar findings were obtained and reported in our previous studies [47, 112, 115, 324]. For the CDs-amorphous sample, a single characteristic broad peak was recorded at nearly $2\theta = 21.80°$ (002), indicating the formation of amorphous carbon material [325]. For the CDs-nanocomposite, same peaks of bare nanocomposite were recorded, because the single broad peak of CDs was suppressed due to its amorphous nature.

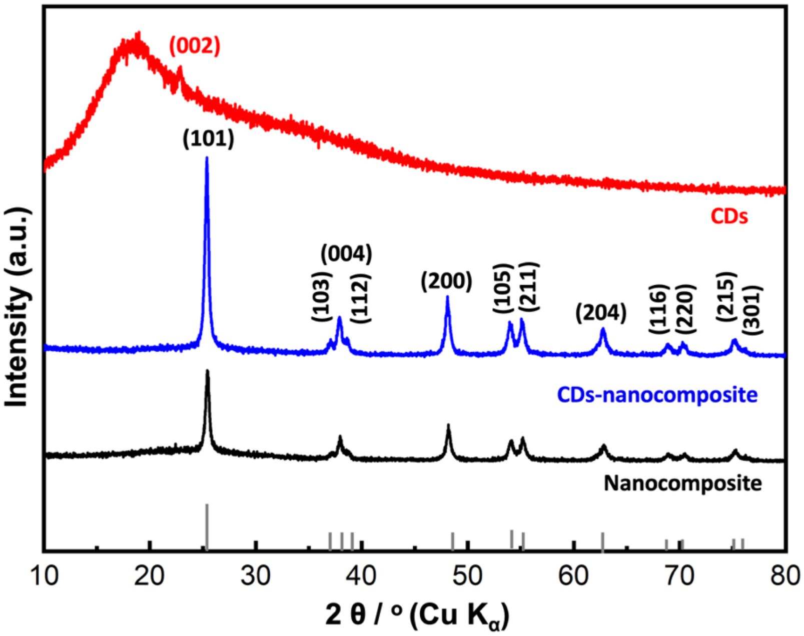

Fig. 7.2: XRD analysis of CDs, nanocomposite, and CDs-nanocomposite.

7.4.1.2 SEM, EDX analysis, and elemental mapping techniques

SEM, EDX analysis, and elemental mapping were performed to analyze the surface morphology, atomic composition, purity, and homogenous distribution of the elements forming the nanocomposite, as shown in **Fig. 7.3**. Analysis of the external morphology of the prepared sample confirmed the homogenous distribution of CDs over the surface of the composite matrix, as exhibited in **Fig. 7.3 (a)**. Elemental mapping techniques showed all the elements (C, Ti, Si, O, Fe, Ni, and Co) forming the nanocomposite in a homogenous distribution, as illustrated in **Fig. S.7.1.** Finally, EDX analysis confirmed the purity of the prepared nanocomposite by revealing a lack of foreign elements. In addition, the atomic analysis revealed that Ti and O (forming the TiO_2 layer) possessed the highest atomic ratios, and the internal Co, Ni, and Fe elements (forming $Co_{0.5}Ni_{0.5}Fe_2O_4$) possessed the lowest atomic ratios, as presented in **Fig. 7.3 (b)**. This result is in good agreement with our XRD analysis.

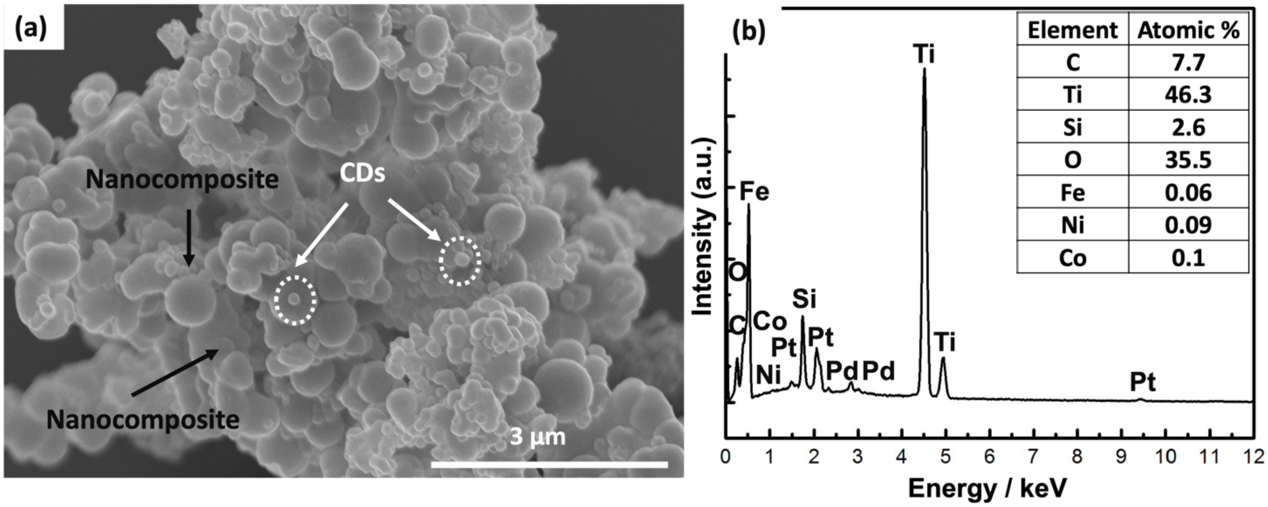

Element	Atomic %
C	7.7
Ti	46.3
Si	2.6
O	35.5
Fe	0.06
Ni	0.09
Co	0.1

Fig. 7.3: (a) SEM analysis of CDs-nanocomposite and (b) EDX atomic analysis.

7.4.1.3 BET surface area and BJH pore size distribution analysis

The BET surface area and BJH pore size distribution of the synthesized samples were investigated as shown in **Fig. 7.4 (a) and (b)**. According to the IUPAC classification, all samples possessed type (III) adsorption isotherms, which indicate weak interactions between the adsorbate and the prepared adsorbent, as exhibited in **Fig. 7.4 (a)**. In this case, adsorption occurred when the N_2 interaction with an adsorbed layer was greater than its interaction with the surface of the synthesized samples. At higher relative pressures (0.87–1), sharp capillary condensation occurred, corresponding to the formation of macropores. The BET surface area, pore volume, and pore area values are summarized in **Table 7.1**. Upon CDs loading onto the composite matrix, the BET surface area declined which can be the result of increasing the particle size of the new CDs-nanocomposite. While **Fig. 7.4 (b)** illustrates the BJH pore size distribution. All samples exhibited a broad, multimodal pore size distribution, confirming the existence of two types of pores: mesopores (2–50 nm) and macropores (>50 nm).

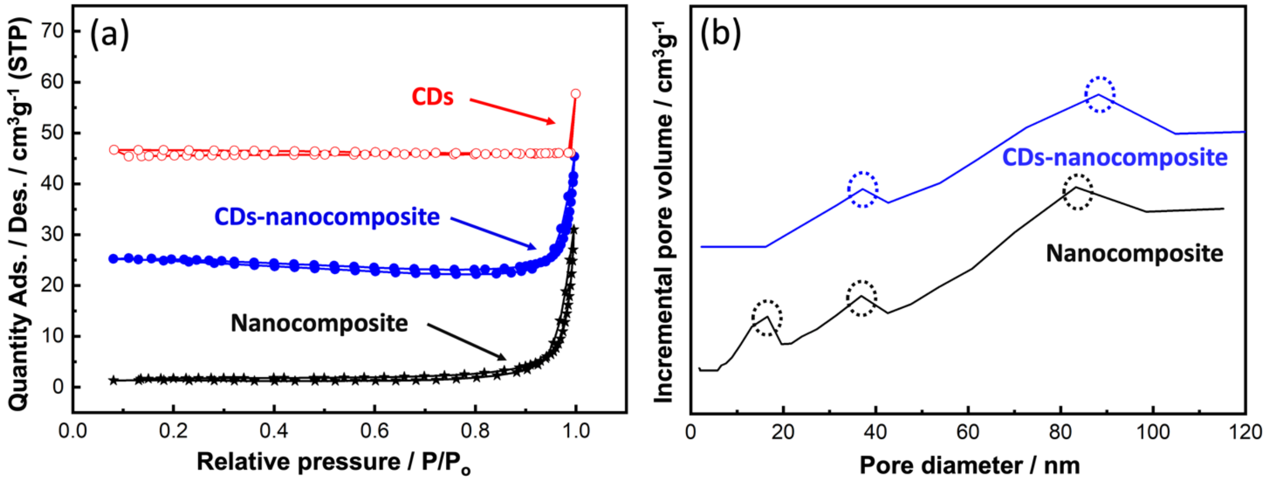

Fig. 7.4: (a) BET surface area analysis of CDs, nanocomposite, and CDs-nanocomposite, and (b) BJH pore size distribution analysis.

Table 7.1: BET surface area, pore volume, and pore area of CDs, nanocomposite, and CDs-nanocomposite.

No.	Sample	BET Surface area (m^2/g)	Pore volume (cm^3/g)	Pore area (m^2/g)
1	CDs	4.2 ± 2.5	< 0.001	< 0.001
2	nanocomposite	3.3 ± 0.2	0.001	3.5
3	CDs-nanocomposite	1.2 ± 0.2	0.004	7.8

7.4.1.4 TEM, HR-TEM, and selected area electron diffraction (SAED) analysis

TEM, HR-TEM, and SAED analyses were performed to calculate the average diameter of the prepared composite matrix, the d-spacings of the lattice planes, and to confirm the formed phase and crystallinity of the synthesized samples, as shown in **Fig. 7.5 (a–c)**. **Figure 7.5 (a)** displays a TEM micrograph of the CDs-nanocomposite where CDs are distributed uniformly over the external surface of the composite matrix. This is similar to the observation made using SEM.

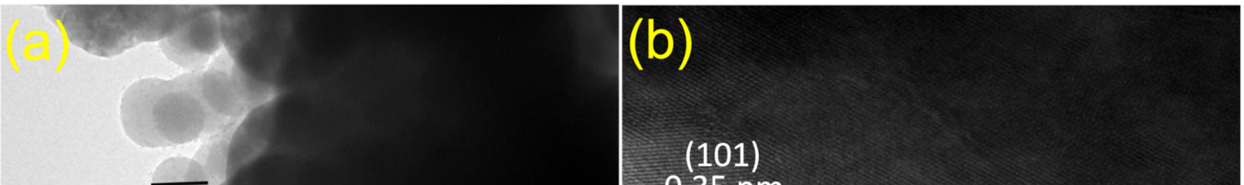

Before CD loading, the average diameter of the matrix was approximately 90 ± 11 nm, and it possessed a spherical shape. After CD loading, the diameter increased. At higher relative pressures, condensation took place in the interparticle voids, which is consistent with the BET results in **Fig. 7.4 (a)**.**Fig. 7.5 (b)** reveals the lattice fringes in HR-TEM images, which confirms the conjugation between the predominant anatase TiO_2 nanoparticles of the matrix and the loaded CDs, characterized by the d-spacing of (002) planes at 0.47 nm. The SAED pattern in **Fig. 7.5 (c)** shows only the fringes of anatase TiO_2 and is consistent with the XRD analysis in **Fig. 7.2**.

Fig. 7.5: (a) TEM analysis of CDs-nanocomposite, (b) HR-TEM analysis, and (c) SAED pattern.

7.4.1.5 Raman analysis

The chemical structure and molecular interactions of the nanocomposite and CDs-nanocomposite were analyzed via Raman analysis. **Fig. 7.6** shows the results. As anatase TiO_2 is the main component of the nanocomposite, three Raman-active bands linked to anatase TiO_2 are detected at 293.4, 515.7, and 638.6 cm^{-1} corresponding to B_{1g}, A_{1g}, and E_{g2} modes, respectively. Upon loading CDs into the composite matrix, the characteristic D and G bands attributed to carbon materials appeared at approximately 1379.6 and 1589.3 cm^{-1}, respectively. The D band represents *sp*^{3} defect sites due to grain boundaries and vacancies, while the G band corresponds to the scattering of $E_{2\,g}$ phonons from *sp*^{2} C atoms. The I_D/I_G value was approximately 0.8666.

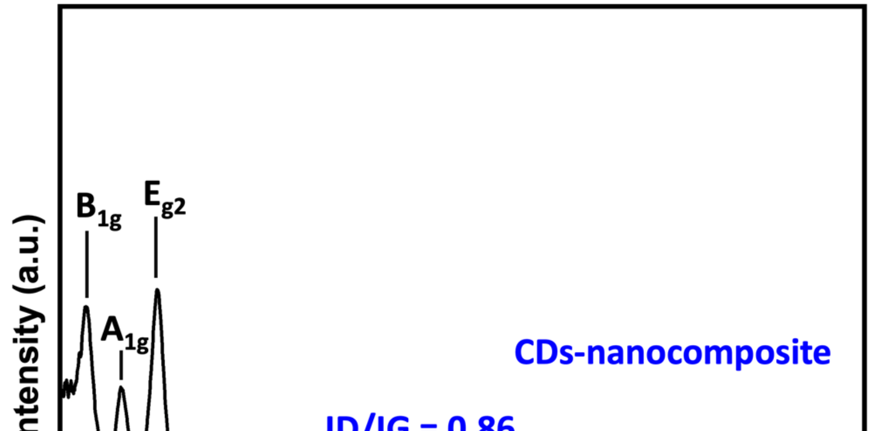

Fig. 7.6: Raman spectra of the nanocomposite and CDs-nanocomposite.

7.4.2 Electrochemical measurements

Fig. 7.7 (a) shows a comparison between the CV curves of the CDs, nanocomposite, and CDs-nanocomposite at a scan rate of 50 mV/s within a potential window of 0–0.75 V. It is accepted that the area of the CV curve is directly proportional to the specific capacitance value. **Fig. 7.7 (a)** shows the area and current of the CV curve of the CDs-nanocomposite are much greater than that of the CDs and nanocomposite CV curves, which emphasizes the enhanced specific capacitance of the CDs-nanocomposite. Moreover, the CDs curve displays a rectangular shape that reflects EDLC behavior. The shape of the CDs-nanocomposite curve illustrates two redox peaks due to Faradaic processes as shown in the following **equation (7-1)** [326], which confirms the presence of the composite and its PC mechanisms [327, 328].

$$TiO_2^-M^+ \leftrightarrow TiO_2 + M^+ + e^- \qquad (7\text{-}1)$$

Where M^+ indicates the protons and alkali metal cations (Na^+, Li^+, and K^+) in the electrolyte.

Fig. 7.7 (b) further demonstrates the properties of the electrode material, illustrating the CV curves of the CDs-nanocomposite tested at different scan rates ranging from 5 to 80 mV/s. All the curves possess two redox peaks. As the scan rate increases, the oxidation peak of the CDs-nanocomposite shifts to a higher potential, and the reduction peak shifts to a lower potential. This can be ascribed to the relatively slow kinetics of the electrochemical reactions at higher scan rates and suggests that the electron transfer process is quasi-reversible or reversible [329, 330]. In addition, as the scan rate increases, the height of the redox peak also increases, and, consequently, the area of the CV curve increases, indicating good electron conduction [331]. There is no substantial change in the shape of the curves even at the highest scan rate (80 mV/s), which suggests that the CDs-nanocomposite has fast charge transfer properties [332]. **Fig. 7.7 (c)** shows the specific capacitance of the CDs-nanocomposite at different scan rates. These values were calculated using

equation (7-2) [333]:

$$C_s = \frac{\int I\, dv}{m\, v\, \Delta V} \qquad (7\text{-}2)$$

where I is the current, v is the potential, dv is the potential window, ν is the scan rate, and m is the mass of the electroactive materials on the electrode. The specific capacitance values were found to be 913.7, 851.3, 831.1, 811.0, 793.7, 782.2, and 755 F/g at scan rates 5, 10, 15, 30, 40, 50, and 80 mV/s, respectively. The curves at different current densities ranging from 10 to 30 A/g were compared, as illustrated in **Fig. 7.7 (d)**, by controlling the measured currents of the CDs-nanocomposite according to the mass of active substance coated on the NF substrate. These values were calculated using **equation (7-3)** [334]:

$$C_s = \frac{I \times \Delta t}{m \times \Delta V} \qquad (7\text{-}3)$$

where C_s is the specific capacity, m is the mass of active substance coated on the substrate, I is the discharge current, and Δt is the discharge time [335]. The specific capacitance values of the CDs-nanocomposite were found to be 837, 741.8, 710.7, 654.2, 594.3, 561.5, 515, 483.2, and 462.6 F/g at current densities 10, 12, 14, 16, 18, 20, 24, 28, and 30 A/g, respectively.

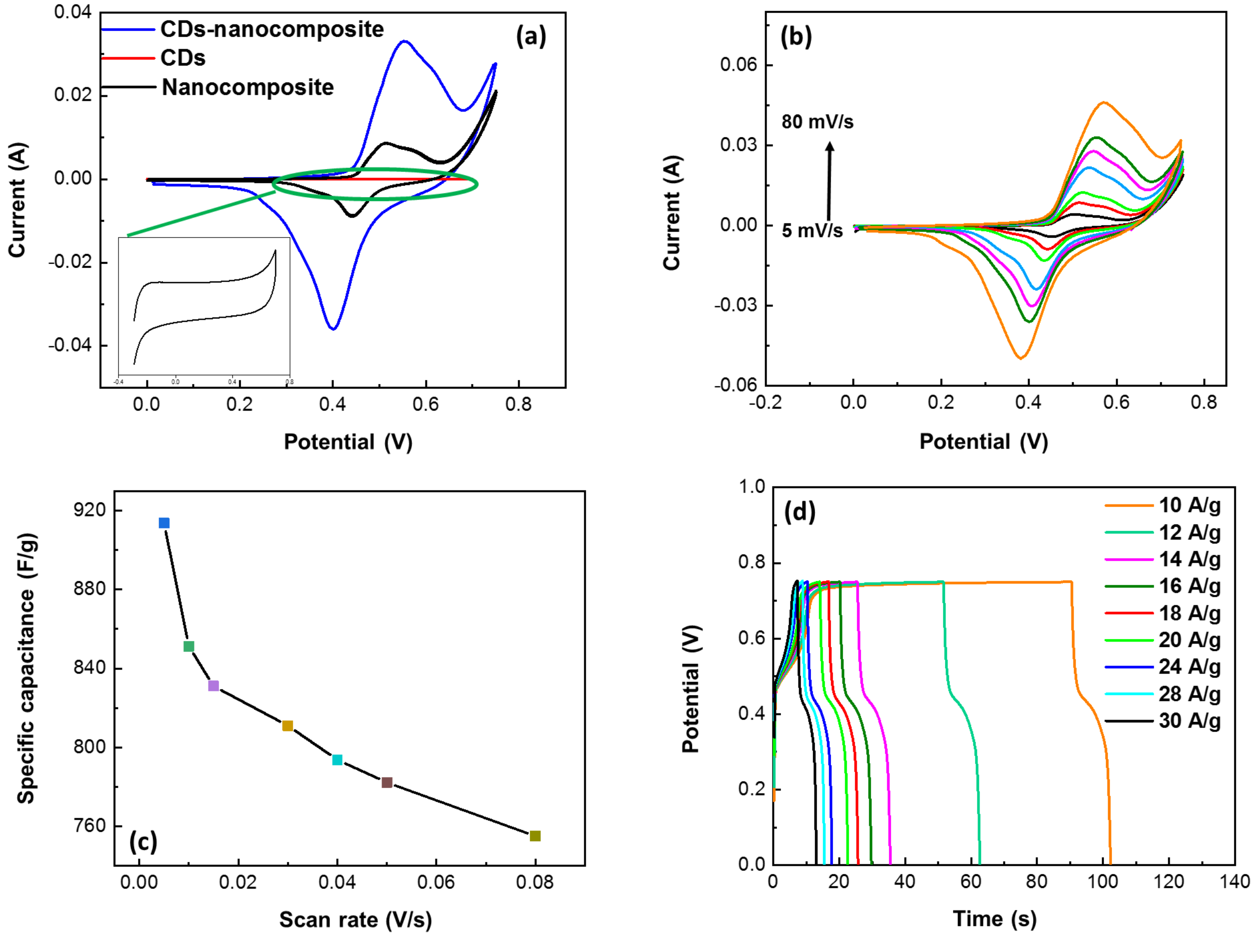

Fig. 7.7: The electrochemical performance of CDs-nanocomposite on NF electrode material (a) Comparison of the CV curve of CDs, nanocomposite (inset), and CDs-nanocomposite at a scan rate of 50 mV/s (b) CV curves of CDs-nanocomposite at various scan rates (c) specific capacitance of CDs-nanocomposite at various scan rates and (d) galvanostatic charge–discharge curves of CDs-nanocomposite at various current densities.

The cycling stability of the electrode material was analyzed using the CV technique continuously for 3000 cycles at a constant scan rate of 80 mV/s within a potential window of 0–0.75 V to evaluate the electrochemical behavior of the CDs-nanocomposite further. The results presented in **Fig. 7.8 (a)** show that the CDs-nanocomposite electrode material delivers 72.2% capacitance after 3000 cycles, signifying its remarkable long-life cyclic stability. More helpful technique to understand the electrochemical performance and the energy storage mechanism for CDs-nanocomposite as hybrid SCs is electrochemical impedance spectroscopy (EIS) technique. EIS is a very significant technique to analyze the electrochemical behavior occurring at different frequencies in SCs. The EIS provides a total overview of all the frequency behavior of a system and gives information about the capacitive behavior, the resistance, and the diffusion-limited processes. EIS techniques make it easy to differentiate between EDLC and Faradaic reaction capacitance in redox-active materials since these two processes occur at different frequencies. The ideal Nyquist plot produced by EIS consists of a semicircle at high frequency, a tilted linear variation of the impedance in the middle frequency range, and a vertical tail at low frequency [336, 337]. **Fig. 7.8 (b)** shows the Nyquist plots for the CDs, nanocomposite, and CDs-nanocomposite obtained in the frequency range of 1.0 to 200 kHz with an ac voltage amplitude of 10 mV. Semicircles are as the charge transfer resistance (Rct) is the charge transfer resistance at the electrode–electrolyte interface, and R_s is the solution resistance, calculated from the semicircle's intercept with the x-axis [338, 339]. It can be noticed that, R_s of CDs-nanocomposite gives intermediate value of 1.5 **Ω** compared to nanocomposite and CDs. This value of R_s indicates the difference in conductivity of the electrode materials, the lower R_s value of CDs-nanocomposite shows the higher conductivity due to a good contact between composite with highly conductive CDs and also short electron path-length as the presence of CDs helps the electrons to migrate to the surface of the electrode active materials which is favorable to redox reactions [329]. The very small semicircle that appears in the region of high frequency has very low diameter, showing low R_{ct} (0.4 **Ω**). The line with a sharp slope at low frequency is specific for the electrode capacity, that looks vertically in ideal capacitors [340]. As shown in **Fig. 7.8 (b)**, the linear part of the CDs-nanocomposite curve looks more vertical, with a smaller practical impedance value, and its shape looks closer to the ideal form. Therefore, it can be noted that the modification of the nanocomposite with CDs enhances the electrochemical performance of hybrid SCs.**Fig. 7.8 (c)** shows the Ragone plot (power density *vs.* energy density) of the CDs-nanocomposite. The values of energy density and power density were calculated from **equations (7-3, 7-4)** [341, 342]:

$$E = \frac{C(\Delta V)^2}{2} \qquad (7\text{-}3)$$

$$P = \frac{E}{t} \qquad (7\text{-}4)$$

where E (Wh/ kg) is energy density of the supercapacitor, C (F/ g) is the total specific capacitance, P (kW/ kg) is power density, and t is the discharge time (h). **Table 7.2** details the energy density and specific capacitance of the TiO_2–carbon-based material synthesized in this work compared with those synthesized in other studies.

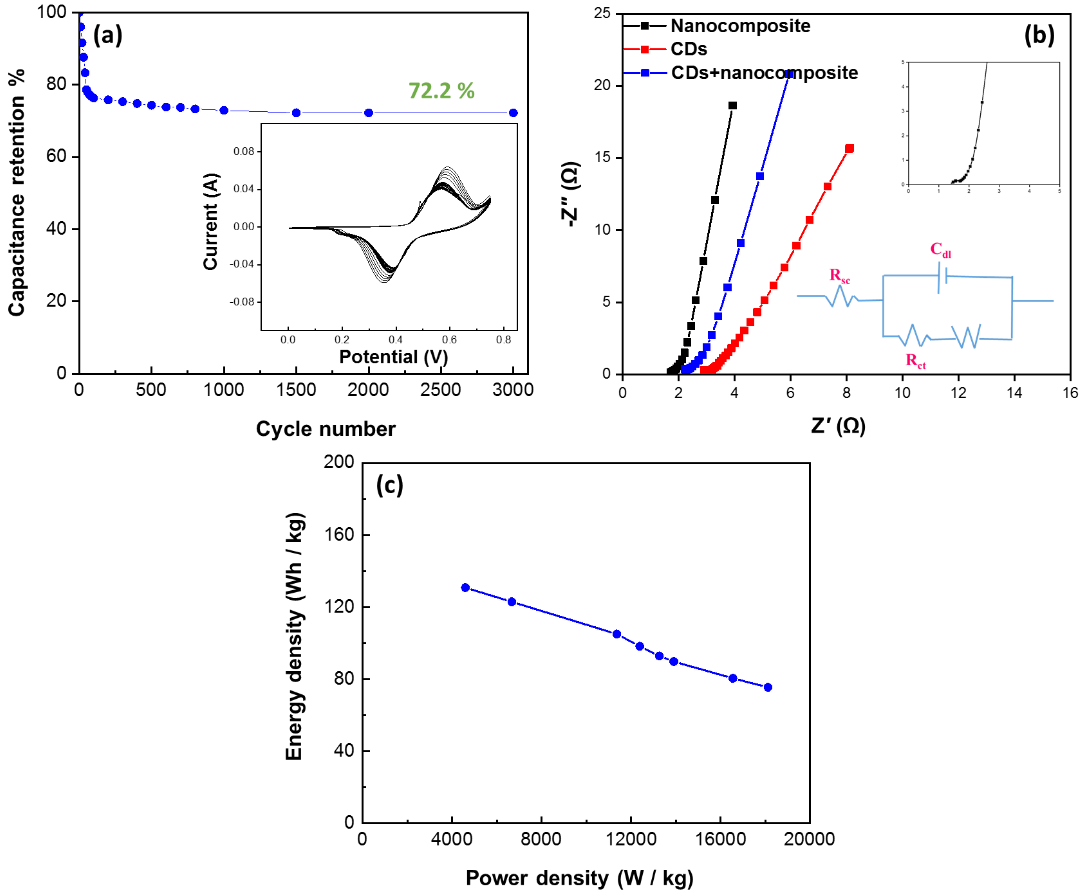

Fig. 7.8: (a) Long-life cyclic stability (over 3000 cycles) of CDs-nanocomposite at a scan rate of 80 mV/s in 1M KOH electrolyte (inset is the CV curve for the initial and final few cycles of CDs-nanocomposite), (b) Nyquist plot of nanocomposite, CDs-nanocomposite and CDs on NF (inset fig. is the high frequency region of CDs-nanocomposite at the top, and EIS equivalent circuit at the bottom) and (c) Ragone plots of the CDs-nanocomposite.

Table 7.2: Comparison of the electrochemical performance (specific capacitance and energy density) of TiO_2–carbon-based materials synthesized by different methods for SC application.

Electrode material	Method	Electrolyte	Specific capacitance	Power density	Energy density	Ref.
TiO_2-CNT film	Electrochemical deposition	PVA-H_2SO_4	345.7 F/g at 1 A/g	9.4 kW/kg	82.5 Wh /kg	[343]
CNT/TiNiW	Dr. Blade technique	PVA/H_3PO_4	549.1 F /g at 1 A/g	-	336.7 Wh /kg	[344]
Co_3O_4/TiO_2/Activated carbon on NF	Simple solgel	6M KOH	946 F/g at 5 mV/s	-	-	[345]
SWCNTs /TiO_2	Hydrothermal	PVA/H_2SO_4	144 F/ g at 1 A/g	62.5 W/ kg	20 Wh/kg	[346]
CDs/TiO_2	Chemical reduction & pyrolysis	2M KOH	2,200 mF/ cm^2 at 5 mV/s	635 $\mu W/cm^2$	51.3 $\mu Wh/cm^2$	[312]
CDs/PPy/TiO_2 nanotube arrays	Anodization	0.15 M pyrrole monomer & 0.1 M ($LiClO_4$)	482 F/ g at 0.5 A/g	150 W/ kg	42.5 Wh /kg	[347]
CDs-nanocomposite	layer-by-layer and hydrothermal methods	1M KOH	913.7 F/g at 5 mV/s	20 kW/ kg	130.7 Wh /kg	**This work**

7.5 Conclusion

TiO_2-based nanocomposite ($Co_xNi_{1-x}Fe_2O_4$, x = 0.5/SiO_2/TiO_2) was synthesized using a simple layer-by-layer approach. It was then enhanced with CDs synthesized using a one-pot hydrothermal method, loaded on NF substrate, and investigated as a potential electrode material for hybrid SCs. The calculated specific capacitance value of the CDs-nanocomposite was 913.7 F/g at a scan rate of 5 mV/s, and it demonstrated good cyclic stability over 3000 cycles with capacitance retention of 72% and a superior energy density value of 130.7 Wh/kg. In conclusion, we suggest that the CDs-nanocomposite developed in this study has the potential to enhance the electrochemical performance of hybrid SCs and that the simple synthesis method can be applied to similar TiO_2 nanocomposites to create favorable electrode materials for advanced energy storage systems.

Chapter 8: General Conclusion

XRD patterns showed the phase and good crystallinity of the prepared nanocomposites.

SEM analysis revealed that the CNFST matrix was uniformly distributed over the large surface area of the rGO and SWCNTs. However, C-dots were uniformly-loaded over the relatively greater surface of the CNFST matrix. EDX spectra confirmed the purity of the prepared nanocomposites. The TEM characterization revealed that the composite matrix comprised spherical grains with an average diameter of ~90 nm. Interestingly, the composite matrix was exceptionally conjugated with bundles of carbon nanotubes. Considering IUPAC classification, all samples showed a type (III) isotherm corresponding to weak adsorbate-adsorbent interactions. All samples had multimodal and broad pore-size distributions, reflecting the presence of two types of pores, mesopores and macropores. The FTIR spectra exhibited numerous peaks, among them one at 1650 cm^{-1} in the C-dots sample, and one at 1666 cm^{-1} in the CNFST/C-dots 10% sample, corresponding to the stretching vibration bands of C=O. This band was not detected in the CNFST matrix, which might be reflective of the type of bonding between the C-dots and the CNFST matrix, a covalent bond (C=O). Regarding the photodegradation of chloramine-T, its distinctive absorption bands (around 222 nm) decreased continuously with increasing UV irradiation time, and its distinctive absorption bands in the presence of the nanocomposites exhibited a significant blue shift. After 40 min of UV irradiation, the CNFST/C-dots 10%, CNFST/rGO 10%, and CNFST/SWCNTs 10% nanocomposites had degraded about 28%, 32.7% and 41.6%, respectively, of the initial concentration of chloramine-T. Kinetics plots for chloramine-T degradation under UV irradiation in the presence of the nanocomposites fit well to the pseudo-second-order model, indicating a tendency toward chemisorption. By analyzing the degradation efficiency, the photodegradation rate was found to be enhanced by increasing the photocatalyst dosage, which is attributable to the increment of potential active sites and the ease of free-radical generation. When 50 mg/L of chloramine-T was used as an initial concentration, the removal efficiency was 70% by the CNFST/C-dots 10% after 70 min. Removal efficiency for 75 and 100 $mg \cdot L^{-1}$ concentrations was 65% and 45%, respectively, under the same conditions. Additionally, the degradation efficiency decreased from 65% to 35% as the solution pH rose from 3 to 10. Under acidic conditions, degradation of chloramine-T was faster than that under neutral or alkali conditions, an effect attributed to the electrostatic interaction that occurred between the negatively-charged chloramine-T and the positively-charged CNFST/C-dots 10%, which led to an increment in the activated sites. Finally, chloramine-T photodegradation efficiency decreased from 47% to about 43%, 41%, and 40% in the presence of methyl viologen, benzoquinone, and isopropanol, respectively. This result confirmed that the OH. radical was the principal species responsible for chloramine-T degradation. Our work informs the formulation of new nanocomposites for effective water treatment.

While for the Cu-loaded composites, the photodegradation of three types of pollutants under UV light was investigated. DFT analysis was carried out to investigate the adsorption and electronic properties of the prepared CNFST/Cu sample. Moreover, the antimicrobial performance against many pathogens was studied using various assays, such as well diffusion, UV-light activation assessment, and protein leakage. The results in this study show that FCC Cu NPs are formed and uniformly distributed on the surface of the prepared nanocomposite matrix as, revealed from XRD, SEM, and STEM mapping results. Upon Cu loading, the crystalline size, diameter of the particles, and the bandgap of the CNFST matrix slightly increase. However, the BET surface area is largely improved due to more mesopores being formed with respect to macropores, as shown in the BJH pore size distribution curves. The FTIR analysis shows no Cu–O stretching, suggesting that the Cu NPs loading occurs via van der Waals forces. The prepared nanocomposite exhibits strong absorption in the UV region at around 350 nm. Finally, XPS analysis shows the atomic ratios of the main elements that constitute the composite and confirms the existence of oxygen vacancies over the Cu-loaded composite. The photocatalytic properties of the prepared nanocomposite were tested and compared with those of bare Cu and CNFST samples, with the prepared Cu-loaded nanocomposite showing outstanding photocatalytic properties toward all tested pollutants. This efficiency can be attributed to the improved surface area, porosity, and the constructed heterojunction separating photogenerated charge carriers and elongating the reaction time. In addition, the effect of the pH on the photocatalytic properties of the prepared nanocomposite varied from one type of pollutant to another. Similarly, Cu-loaded nanocomposite shows significant antimicrobial properties toward almost all pathogenic microbes. This performance can be ascribed to the synergetic effect between the composite matrix and the loaded Cu NPs.

While for water splitting / H_2 evolution, molten flux method was used for the preparation of highly crystalline Al-doped $SrTiO_3$ photocatalyst with an average particle size of 150 nm. The prepared particles were highly crystalline and possessed cubic morphology of the perovskite materials. The most outstanding overall water splitting performance was exhibited under UV-rays due to the large bandgap of Al-$SrTiO_3$ particles (3.1 eV). In addition, our results showed that, by changing the photodeposition order of the cocatalysts and metal NPs, the photocatalytic H_2 production efficiencies changed. Moreover, loaded samples with Au NPs exhibited the highest photocatalytic water splitting performance compared with Cu and Pt loaded samples under UV and UV-Vis. light, which could be ascribed to their higher chemical stability, efficient light absorption, and good charge separation. Also, Au NPs concentration is significant due to the possible agglomeration and overlap with $RhCr_2O_3$ cocatalyst responsible for efficient HE. Finally, developed Al-$SrTiO_3$ loaded with $RhCr_2O_3$ (Rh = 0.1 wt%, Cr = 0.05 wt%) and Au NPs (4 wt.%) showed the highest H_2 evolution under visible light. This was attributed to the efficient hot electron transfer from Au NPs to Al-$SrTiO_3$ photocatalyst then to $RhCr_2O_3$. In addition, many Z-Scheme samples were prepared by a modified method known as post annealing of mixed powders, where Al-$SrTiO_3$ was combined with CdS and Au NPs for the photocatalytic H_2 evolution under visible light (λ > 400 nm). The phase, purity, and crystallinity of the prepared samples were confirmed along with the efficient conjugation of the constituting elements to build the proposed structure. While, Our H_2 evolution results confirmed that changing either the wt. % of Au NPs, or the wt. % ratio of Al-$SrTiO_3$ to CdS, possesses a significant effect on the H_2 evolution efficiency. The best sample was found to be Al-$SrTiO_3$/ 4 wt.% Au / CdS (1:1) which gave the maximum amount of evolved H_2 656.7

μ mole) after 3 h of visible light irradiation. This relatively higher activity is ascribed to an efficient light absorption, prolonged lifetime of the photogenerated charge carriers, and charge separation. Our study opens the way toward carbon neutrality and the efficient production of sustainable solar fuels. Moreover, ($Co_xNi_{1-x}Fe_2O_4$, x = 0.5/SiO_2/TiO_2) nanocomposite enhanced with CDs synthesized using a one-pot hydrothermal method, loaded on NF substrate, was investigated as a potential electrode material for hybrid SCs. The calculated specific capacitance value of the CDs-nanocomposite was 913.7 F/g at a scan rate of 5 mV/s, and it demonstrated good cyclic stability over 3000 cycles with capacitance retention of 72% and a superior energy density value of 130.7 Wh/kg. In conclusion, we suggest that the CDs-nanocomposite developed in this study has the potential to enhance the electrochemical performance of hybrid SCs and that the simple synthesis method can be applied to similar TiO_2 nanocomposites to create favorable electrode materials for advanced energy storage systems.

Generally, this PhD thesis has explored the applications of photocatalysis in water treatment, water splitting, and hydrogen (H_2) production, as well as the potential of supercapacitors in energy storage. The research conducted has shed light on the significant role that these technologies play in addressing critical challenges related to water scarcity, environmental pollution, and energy sustainability. In the realm of water treatment, photocatalysis has proven to be a powerful and promising approach. By utilizing semiconductor-based photocatalysts, such as metal oxides, organic pollutants and contaminants present in water can be effectively degraded through the process of photocatalytic oxidation. The research presented in this thesis has highlighted the key factors influencing the photocatalytic efficiency, such as catalyst synthesis, optimization of reaction conditions, and the role of co-catalysts. The findings contribute to the understanding of photocatalytic mechanisms and provide valuable insights for the development of efficient and scalable water treatment systems. Furthermore, the thesis has explored the utilization of photocatalysis for water splitting and hydrogen production, which are crucial for the advancement of sustainable energy systems. By harnessing solar energy, photocatalysts can drive the splitting of water into hydrogen and oxygen through the process of photocatalytic water splitting. The research presented has focused on enhancing the efficiency and stability of photocatalytic systems, investigating novel catalyst materials, and exploring strategies for improving hydrogen production rates. The findings contribute to the development of clean and renewable energy technologies, paving the way for a hydrogen-based economy. In addition to water treatment and hydrogen production, this thesis has also examined the potential of supercapacitors in energy storage applications. Supercapacitors offer high power density, rapid charge/discharge rates, and long cycle life, making them well-suited for various energy storage needs. The research conducted has investigated the design and fabrication of supercapacitor electrodes, optimization of electrolyte systems, and the exploration of new materials and architectures. The findings contribute to the advancement of supercapacitor technology, enhancing their performance and expanding their applications in energy storage systems, portable electronics, and electric vehicles. Overall, this PhD thesis has provided comprehensive insights into the applications of photocatalysis in water treatment and hydrogen production, as well as the potential of supercapacitors in energy storage. The research conducted contributes to the knowledge and understanding of these technologies, their underlying principles, and their practical implementation. The findings presented in this thesis hold great promise for addressing pressing global challenges related to water scarcity, environmental pollution, and the transition to sustainable energy systems. By harnessing the power of photocatalysis and supercapacitors, we can move towards a cleaner, more efficient, and more sustainable future.

References:

1. Kummu, M., et al., *Is physical water scarcity a new phenomenon? Global assessment of water shortage over the last two millennia.* Environmental Research Letters, 2010. **5**(3): pp. 034006.
2. Oki, T. and S. Kanae, *Global hydrological cycles and world water resources.* science, 2006. **313**(5790): pp. 1068-1072.
3. Bruun, C., *Water shortage and surplus in the ancient world.* Cura aquarum in Sicilia, Jansen CM [ed.], Leuven: Peeters Publishers, 2000: pp. 215-224.
4. Schwarzenbach, R.P., et al., *Global water pollution and human health.* Annual Review of Environment and Resources, 2010. **35**: pp. 109-136.
5. Amin, M., A. Alazba, and U. Manzoor, *A review of removal of pollutants from water/wastewater using different types of nanomaterials.* Advances in Materials Science and Engineering, 2014. **2014**.
6. Jeevanantham, S., et al., *Removal of toxic pollutants from water environment by phytoremediation: A survey on application and future prospects.* Environmental technology & innovation, 2019. **13**: pp. 264-276.
7. Lu, F. and D. Astruc, *Nanocatalysts and other nanomaterials for water remediation from organic pollutants.* Coordination Chemistry Reviews, 2020. **408**: pp. 213180.
8. Dachir, S., et al., *Decontaminant Against Toxic Agents.* Skin Decontamination: A Comprehensive Clinical Research Guide, 2019: pp. 101.
9. Powell, M. and J. Harris, *Influence of oxygen on the toxicity of chloramine-T to Atlantic salmon smolts in freshwater and seawater.* Journal of Aquatic Animal Health, 2004. **16**(2): pp. 83-92.
10. Olmstead, M.M. and P.P. Power, *Crystal and molecular structure of chloramine-T trihydrate. Absence of a sodium-nitrogen interaction in the oxidant.*

N-chloro-N-sodiotoluene-p-sulfonamide. Inorganic Chemistry, 1986. **25**(22): pp. 4057-4058.

11. Beljaars, P.R. and T.M. Rondags, *High Pressure Liquid Chromatographic Determination of Chloramine-T in Food.* Journal of the Association of Official Analytical Chemists, 1979. **62**(5): pp. 1087-1091.
12. Wang, J., Z. Li, and Y. Yang, *Vortex-Assisted Liquid–Liquid Microextraction for the Determination of Chloramine-T in Cosmetics Coupled with High-Performance Liquid Chromatography.* Analytical Letters, 2016. **49**(12): pp. 1795-1803.
13. Kujala, V., et al., *Occupational asthma due to chloramine-T solution.* Respiratory medicine, 1995. **89**(10): pp. 693-695.
14. Dijkman, J.H., P.H. Vooren, and J.A. Kramps, *Occupational asthma due to inhalation of chloramine-T.* International Archives of Allergy and Immunology, 1981. **64**(4): pp. 422-427.
15. Powell, M.D. and S.F. Perry, *Cardio-respiratory effects of chloramine-T exposure in rainbow trout.* Experimental Biology Online, 1999. **4**(5): pp. 1-59.
16. Masten, S., *Chloramine-T [127-65-1] and Metabolite p-Toluenesulfonamide [70-55-3]: Review of Toxicological Literature.* Toxicological Literature, Feb, 2002.
17. Etani, K., *Methods for water treatment*. 1989, Google Patents.
18. Kasprzyk-Hordern, B., M. Ziółek, and J. Nawrocki, *Catalytic ozonation and methods of enhancing molecular ozone reactions in water treatment.* Applied Catalysis B: Environmental, 2003. **46**(4): pp. 639-669.
19. Adams, C., et al., *Removal of antibiotics from surface and distilled water in conventional water treatment processes.* Journal of environmental engineering, 2002. **128**(3): pp. 253-260.
20. Abd Elkodous, M., et al., *Fabrication of Ultra-Pure Anisotropic Zinc Oxide Nanoparticles via Simple and Cost-Effective Route: Implications for UTI and EAC Medications.* Biological Trace Element Research, 2019.
21. Wong, C.W., et al., *Response Surface Methodology Optimization of Mono-dispersed MgO Nanoparticles Fabricated by Ultrasonic-Assisted Sol–Gel Method for Outstanding*

Antimicrobial and Antibiofilm Activities. Journal of Cluster Science, 2020. **31**(2): pp. 367-389.

22. Elkhenany, H., et al., *Comparison of different uncoated and starch-coated superparamagnetic iron oxide nanoparticles: Implications for stem cell tracking.* International Journal of Biological Macromolecules, 2020. **143**: pp. 763-774.
23. El-Batal, A.I., et al., *Factorial design-optimized and gamma irradiation-assisted fabrication of selenium nanoparticles by chitosan and Pleurotus ostreatus fermented fenugreek for a vigorous in vitro effect against carcinoma cells.* International Journal of Biological Macromolecules, 2019.
24. Samuel, M.S., et al., *Biosynthesized silver nanoparticles using Bacillus amyloliquefaciens; Application for cytotoxicity effect on A549 cell line and photocatalytic degradation of p-nitrophenol.* Journal of Photochemistry and Photobiology B: Biology, 2020. **202**: pp. 111642.
25. Samuel, M.S., et al., *Synthesized β-cyclodextrin modified graphene oxide (β-CD-GO) composite for adsorption of cadmium and their toxicity profile in cervical cancer (HeLa) cell lines.* Process Biochemistry, 2020. **93**: pp. 28-35.
26. Samuel, M.S., et al., *Preparation of graphene oxide/chitosan/ferrite nanocomposite for Chromium(VI) removal from aqueous solution.* International Journal of Biological Macromolecules, 2018. **119**: pp. 540-547.
27. Samuel, M.S., et al., *Ultrasonic-assisted synthesis of graphene oxide – fungal hyphae: An efficient and reclaimable adsorbent for chromium(VI) removal from aqueous solution.* Ultrasonics Sonochemistry, 2018. **48**: pp. 412-417.
28. Samuel, M.S., et al., *Ultrasound-assisted synthesis of metal organic framework for the photocatalytic reduction of 4-nitrophenol under direct sunlight.* Ultrasonics Sonochemistry, 2018. **49**: pp. 215-221.
29. Elkodous, M.A., et al., *C-dots dispersed macro-mesoporous TiO_2 phtocatalyst for effective waste water treatment.* Characterization and Application of Nanomaterials, 2018. **1**(2).

30. Huang, F., A. Yan, and H. Zhao, *Influences of doping on photocatalytic properties of TiO_2 photocatalyst.* Semiconductor Photocatalysis—Materials, Mechanisms and Applications; Cao, W., Ed, 2016: pp. 31-80.

31. Choudhury, B. and A. Choudhury, *Oxygen defect dependent variation of band gap, Urbach energy and luminescence property of anatase, anatase–rutile mixed phase and of rutile phases of TiO_2 nanoparticles.* Physica E: Low-Dimensional Systems and Nanostructures, 2014. **56**: pp. 364-371.

32. Bosc, F., et al., *Mesoporous TiO_2-based photocatalysts for UV and visible light gas-phase toluene degradation.* Thin Solid Films, 2006. **495**(1-2): pp. 272-279.

33. Ozawa, K., et al., *Electron–hole recombination time at TiO_2 single-crystal surfaces: influence of surface band bending.* The journal of physical chemistry letters, 2014. **5**(11): pp. 1953-1957.

34. Katoh, R., M. Murai, and A. Furube, *Electron–hole recombination in the bulk of a rutile TiO2 single crystal studied by sub-nanosecond transient absorption spectroscopy.* Chemical Physics Letters, 2008. **461**(4-6): pp. 238-241.

35. Yaghoubi, H., et al., *Toward a visible light-driven photocatalyst: the effect of midgap-states-induced energy gap of undoped TiO_2 nanoparticles.* Acs Catalysis, 2015. **5**(1): pp. 327-335.

36. Neville, E.M., et al., *Carbon-doped TiO_2 and carbon, tungsten-codoped TiO_2 through sol–gel processes in the presence of melamine borate: reflections through photocatalysis.* The journal of physical chemistry C, 2012. **116**(31): pp. 16511-16521.

37. Han, C., et al., *Innovative visible light-activated sulfur doped TiO_2 films for water treatment.* Applied Catalysis B: Environmental, 2011. **107**(1-2): pp. 77-87.

38. Parastar, S., et al., *Application of Ag-doped TiO_2 nanoparticle prepared by photodeposition method for nitrate photocatalytic removal from aqueous solutions.* Desalination and Water Treatment, 2013. **51**(37-39): pp. 7137-7144.

39. Zhang, N., et al., *Synthesis of M@ TiO_2 (M= Au, Pd, Pt) core–shell nanocomposites with tunable photoreactivity.* The Journal of Physical Chemistry C, 2011. **115**(18): pp. 9136-9145.

40. Torimoto, T., et al., *Effect of activated carbon content in TiO_2-loaded activated carbon on photodegradation behaviors of dichloromethane.* Journal of Photochemistry and Photobiology A: Chemistry, 1997. **103**(1-2): pp. 153-157.

41. Tettey, K.E., M.Q. Yee, and D. Lee, *Photocatalytic and conductive MWCNT/TiO_2 nanocomposite thin films.* ACS applied materials & interfaces, 2010. **2**(9): p. 2646-2652.

42. Xiang, Q., J. Yu, and M. Jaroniec, *Graphene-based semiconductor photocatalysts.* Chemical Society Reviews, 2012. **41**(2): pp. 782-796.

43. Yu, H., et al., *Smart utilization of carbon dots in semiconductor photocatalysis.* Advanced materials, 2016. **28**(43): pp. 9454-9477.

44. Chen, P., et al., *Study on the photocatalytic mechanism and detoxicity of gemfibrozil by a sunlight-driven TiO_2/carbon dots photocatalyst: The significant roles of reactive oxygen species.* Applied Catalysis B: Environmental, 2017. **204**: pp. 250-259.

45. Zhang, Y., et al., *The enhanced photoreduction of Cr (VI) to Cr (III) using carbon dots coupled TiO_2 mesocrystals.* Applied Catalysis B: Environmental, 2018. **226**: pp. 213-219.

46. Li, Y., et al., *Carbon dots-TiO_2 nanosheets composites for photoreduction of Cr (VI) under sunlight illumination: favorable role of carbon dots.* Applied Catalysis B: Environmental, 2018. **224**: pp. 508-517.

47. El-Sayyad, G.S., et al., *Merits of photocatalytic and antimicrobial applications of gamma-irradiated $Co_xNi_{1-x}Fe_2O_4/SiO_2/TiO_2$; $x = 0.9$ nanocomposite for pyridine removal and pathogenic bacteria/fungi disinfection: implication for wastewater treatment.* RSC Advances, 2020. **10**(9): pp. 5241-5259.

48. Elkodous, M.A., et al., *Layer-by-layer preparation and characterization of recyclable nanocomposite ($Co_xNi_{1-x}Fe_2O_4$; $X = 0.9/SiO_2/TiO_2$).* Journal of Materials Science: Materials in Electronics, 2019. **30**(9): pp. 8312-8328.

49. Jia, X., J. Li, and E. Wang, *One-pot green synthesis of optically pH-sensitive carbon dots with upconversion luminescence.* Nanoscale, 2012. **4**(18): pp. 5572-5575.

50. Boyanova, L., et al., *Activity of Bulgarian propolis against 94 Helicobacter pylori strains in vitro by agar-well diffusion, agar dilution and disc diffusion methods.* Journal of medical microbiology, 2005. **54**(5): pp. 481-483.

51. Rothenburger, S., et al., *In vitro antimicrobial evaluation of Coated VICRYL* Plus Antibacterial Suture (coated polyglactin 910 with triclosan) using zone of inhibition assays.* Surgical Infections, 2002. **3**(S1): pp. s79-s87.

52. El-Batal, A., et al., *Synthesis of silver nanoparticles and incorporation with certain antibiotic using gamma irradiation.* British Journal of Pharmaceutical Research, 2014. **4**(11): pp. 1341.

53. El-Batal, A.I., et al., *Biogenic synthesis of copper nanoparticles by natural polysaccharides and Pleurotus ostreatus fermented fenugreek using gamma rays with antioxidant and antimicrobial potential towards some wound pathogens.* Microbial pathogenesis, 2018. **118**: pp. 159-169.

54. El-Batal, A.I., et al., *Response surface methodology optimization of melanin production by Streptomyces cyaneus and synthesis of copper oxide nanoparticles using gamma radiation.* Journal of Cluster Science, 2017. **28**(3): pp. 1083-1112.

55. El-Sayyad, G.S., F.M. Mosallam, and A.I. El-Batal, *One-pot green synthesis of magnesium oxide nanoparticles using Penicillium chrysogenum melanin pigment and gamma rays with antimicrobial activity against multidrug-resistant microbes.* Advanced Powder Technology, 2018. **29**(11): pp. 2616-2625.

56. El-Batal, A.I., et al., *Penicillium chrysogenum-Mediated Mycogenic Synthesis of Copper Oxide Nanoparticles Using Gamma Rays for In Vitro Antimicrobial Activity Against Some Plant Pathogens.* Journal of Cluster Science, 2019.

57. Baraka, A., et al., *Synthesis of silver nanoparticles using natural pigments extracted from Alfalfa leaves and its use for antimicrobial activity.* Chemical Papers, 2017. **71**(11): pp. 2271-2281.

58. Christensen, G.D., et al., *Adherence of slime-producing strains of Staphylococcus epidermidis to smooth surfaces.* Infection and immunity, 1982. **37**(1): pp. 318-326.

59. Ansari, M.A., et al., *Antibiofilm efficacy of silver nanoparticles against biofilm of extended spectrum β-lactamase isolates of Escherichia coli and Klebsiella pneumoniae.* Applied Nanoscience, 2014. **4**(7): pp. 859-868.

60. El-Sayyad, G.S., et al., *Gentamicin-Assisted Mycogenic Selenium Nanoparticles Synthesized Under Gamma Irradiation for Robust Reluctance of Resistant Urinary Tract Infection-Causing Pathogens.* Biological Trace Element Research, 2019.
61. Abidi, S.H., et al., *Drug resistance profile and biofilm forming potential of Pseudomonas aeruginosa isolated from contact lenses in Karachi-Pakistan.* BMC ophthalmology, 2013. **13**(1): pp. 57.
62. Mathur, T., et al., *Detection of biofilm formation among the clinical isolates of staphylococci: an evaluation of three different screening methods.* Indian journal of medical microbiology, 2006. **24**(1): pp. 25.
63. El-Nemr, K.F., et al., *Polyvinyl alcohol/gelatin irradiated blends filled by lignin as green filler for antimicrobial packaging materials.* International Journal of Environmental Analytical Chemistry, 2019: pp. 1-25.
64. Brownlee, K., *Probit Analysis: A Statistical Treatment of the Sigmoid Response Curve*. 1952, JSTOR.
65. Mewada, A., et al., *Green synthesis of biocompatible carbon dots using aqueous extract of Trapa bispinosa peel.* Materials Science and Engineering: C, 2013. **33**(5): pp. 2914-2917.
66. Maier, J.P., *Electronic spectroscopy of carbon chains.* The Journal of Physical Chemistry A, 1998. **102**(20): pp. 3462-3469.
67. Zhang, J., et al., *Reduction of graphene oxide via L-ascorbic acid.* Chemical Communications, 2010. **46**(7): pp. 1112-1114.
68. Luo, D., et al., *Evaluation criteria for reduced graphene oxide.* The Journal of Physical Chemistry C, 2011. **115**(23): pp. 11327-11335.
69. Schneider, P., *Adsorption isotherms of microporous-mesoporous solids revisited.* Applied Catalysis A: General, 1995. **129**(2): pp. 157-165.
70. Terzyk, A.P., et al., *Fractal dimension of microporous carbon on the basis of Polanyi–Dubinin theory of adsorption. Part IV. The comparative analysis of two alternative solutions of the overall adsorption isotherm equation for microporous fractal*

solids. Colloids and Surfaces A: Physicochemical and Engineering Aspects, 1999. **152**(3): pp. 293-313.

71. Abidin, S.Z., et al., *Characterization of nanocarbon particles using nitrogen adsorption analysis: isotherm, pore type, pore size and BET surface area.* Proceedings of Mechanical Engineering Research Day, 2016. **2016**: pp. 127-128.

72. Sotomayor, F.J., K.A. Cychosz, and M. Thommes, *Characterization of micro/mesoporous materials by physisorption: Concepts and case studies.* Acc. Mater. Surf. Res, 2018. **3**(2): pp. 34-50.

73. Keerthana, B.G.T., et al., *Hydrothermal synthesis and characterization of* TiO_2 *nanostructures prepared using different solvents.* Materials Letters, 2018. **220**: pp. 20-23.

74. Chang, Q., et al., *Synthesis and properties of magnetic and luminescent* $Fe_3O_4/SiO_2/Dye/SiO_2$ *nanoparticles.* Journal of Luminescence, 2008. **128**(12): pp. 1890-1895.

75. Donia, A.M., et al., *Effect of structural properties of acid dyes on their adsorption behaviour from aqueous solutions by amine modified silica.* Journal of hazardous materials, 2009. **161**(2-3): pp. 1544-1550.

76. Arévalo-Cid, P., J. Isasi, and F. Martín-Hernández, *Comparative study of core-shell nanostructures based on amino-functionalized* Fe_3O_4*@* SiO_2 *and* $CoFe_2O_4$*@* SiO_2 *nanocomposites.* Journal of Alloys and Compounds, 2018.

77. Ditta, A., et al., *Structural, magnetic and spectral properties of Gd and Dy co-doped dielectrically modified Co-Ni (*$Ni_{0.4}Co_{0.6}Fe_2O_4$*) ferrites.* Physica B: Condensed Matter, 2017. **507**: pp. 27-34.

78. Amer, M., et al., *Characterization and structural and magnetic studies of as-synthesized* $Fe^{2+}Cr_xFe_{(2-x)}O_4$ *nanoparticles.* Journal of Magnetism and Magnetic Materials, 2017. **439**: pp. 373-383.

79. Amer, M., et al., *Structural and physical properties of the nano-crystalline Al-substituted Cr–Cu ferrite.* Journal of Magnetism and Magnetic Materials, 2013. **343**: pp. 286-292.

80. Kadam, R., et al., *Phase evaluation of Li^+ substituted $CoFe_2O_4$ nanoparticles, their characterizations and magnetic properties.* Journal of Magnetism and Magnetic Materials, 2014. **355**: pp. 70-75.

81. Ghasemi, A., *Compositional dependence of magnetization reversal mechanism, magnetic interaction and Curie temperature of $Co_{1-x}Sr_xFe_2O_4$ spinel thin film.* Journal of Alloys and Compounds, 2015. **645**: pp. 467-477.

82. Zhu, C., J. Zhai, and S. Dong, *Bifunctional fluorescent carbon nanodots: green synthesis via soy milk and application as metal-free electrocatalysts for oxygen reduction.* Chemical communications, 2012. **48**(75): pp. 9367-9369.

83. Roy, P., et al., *Photoluminescent carbon nanodots: synthesis, physicochemical properties and analytical applications.* Materials Today, 2015. **18**(8): pp. 447-458.

84. Zhou, W., et al., *Towards efficient dual-emissive carbon dots through sulfur and nitrogen co-doped.* Journal of Materials Chemistry C, 2017. **5**(32): pp. 8014-8021.

85. Juang, R.-S., et al., *Synthesis of Carbon Dots on Fe_3O_4 Nanoparticles as Recyclable Visible-Light Photocatalysts.* IEEE Transactions on Magnetics, 2017. **53**(11): pp. 1-4.

86. Kurdekar, A., et al., *Comparative performance evaluation of carbon dot-based paper immunoassay on Whatman filter paper and nitrocellulose paper in the detection of HIV infection.* Microfluidics and Nanofluidics, 2016. **20**(7): pp. 99.

87. Gonsalves, L., S. Mojumdar, and V. Verenkar, *Synthesis of cobalt nickel ferrite nanoparticles via autocatalytic decomposition of the precursor.* Journal of thermal analysis and calorimetry, 2010. **100**(3): pp. 789-792.

88. Tan, M., et al., *Enhanced photoluminescence and characterization of multicolor carbon dots using plant soot as a carbon source.* Talanta, 2013. **115**: pp. 950-956.

89. Cheng, S., et al., *Electrostatically assembled carbon dots/boron nitride nanosheet hybrid nanostructures for thermal quenching-resistant white phosphors.* Nanoscale, 2020.

90. Mahmoodi, N.M., *Photocatalytic ozonation of dyes using copper ferrite nanoparticle prepared by co-precipitation method.* Desalination, 2011. **279**(1): pp. 332-337.

91. Albroomi, H., et al., *FACTORS AFFECTING THE REMOVAL OF A BASIC AND AN AZO DYE FROM ARTIFICIAL SOLUTIONS BY ADSORPTION USING ACTIVATED CARBON.* Journal of the Turkish Chemical Society, Section A: Chemistry, 2015. **2**(1): pp. 17-33.

92. Elsayed, M., M. Gobara, and S. Elbasuney, *Instant synthesis of bespoke nanoscopic photocatalysts with enhanced surface area and photocatalytic activity for wastewater treatment.* Journal of Photochemistry and Photobiology A: Chemistry, 2017. **344**: pp. 121-133.

93. Mahmoodi, N.M., *Zinc ferrite nanoparticle as a magnetic catalyst: synthesis and dye degradation.* Materials Research Bulletin, 2013. **48**(10): pp. 4255-4260.

94. Elsayed, M., *Application of ultraviolet and ultrasound irradiation for the degradation of pyridine in wastewater: a comparative study.* Orbital-The Electronic Journal of Chemistry, 2014. **6**(4): pp. 195-204.

95. Casbeer, E., V.K. Sharma, and X.-Z. Li, *Synthesis and photocatalytic activity of ferrites under visible light: a review.* Separation and Purification Technology, 2012. **87**: pp. 1-14.

96. Elsayed, M. and M. Gobara, *Enhancement removal of tartrazine dye using? HCl-doped polyaniline and* TiO_2*-decorated PANI particles.* Materials Research Express, 2016. **3**(8): pp. 085301.

97. Tang, Z.-X. and B.-F. Lv, *MgO nanoparticles as antibacterial agent: preparation and activity.* Brazilian Journal of Chemical Engineering, 2014. **31**(3): pp. 591-601.

98. Wang, W., et al., *Enhanced photocatalytic activity of hierarchical macro/mesoporous* TiO_2*–graphene composites for photodegradation of acetone in air.* Applied Catalysis B: Environmental, 2012. **119-120**: pp. 109-116.

99. Zhang, G., et al., *Study on the Photocatalytic and Antibacterial Properties of* TiO_2 *Nanoparticles-Coated Cotton Fabrics.* Materials, 2019. **12**(12): pp. 2010.

100. Haghi, M., et al., *Antibacterial effect of* TiO_2 *nanoparticles on pathogenic strain of E. coli.* International Journal of Advanced Biotechnology and Research, 2012. **3**(3): pp. 621-624.

101. Abdel-Rahman, H.A., E.H. Awad, and R.M. Fathy, *Effect of modified nano zinc oxide on physico-chemical and antimicrobial properties of gamma-irradiated sawdust/epoxy composites.* Journal of Composite Materials, 2019: pp. 0021998319863835.

102. Maksoud, M.A., et al., *Antibacterial, antibiofilm, and photocatalytic activities of metals-substituted spinel cobalt ferrite nanoparticles.* Microbial pathogenesis, 2019. **127**: pp. 144-158.

103. El-Batal, A.I., et al., *Antibacterial and Antibiofilm Potential of Mono-dispersed Stable Copper Oxide Nanoparticles-Streptomycin Nano-drug: Implications for Some Potato Plant Bacterial Pathogen Treatment.* Journal of Cluster Science, 2019.

104. Ashajyothi, C., et al., *Antibiofilm activity of biogenic copper and zinc oxide nanoparticles-antimicrobials collegiate against multiple drug resistant bacteria: a nanoscale approach.* Journal of Nanostructure in Chemistry, 2016. **6**(4): pp. 329-341.

105. Park, H.-J., et al., *Removal characteristics of engineered nanoparticles by activated sludge.* Chemosphere, 2013. **92**(5): pp. 524-528.

106. Priyadarshini, S., et al., *Biosynthesis of TiO_2 nanoparticles and their superior antibacterial effect against human nosocomial bacterial pathogens.* Research on Chemical Intermediates, 2019: pp. 1-13.

107. El-Batal, A.I., et al., *Antimicrobial, antioxidant and anticancer activities of zinc nanoparticles prepared by natural polysaccharides and gamma radiation.* International journal of biological macromolecules, 2018. **107**: pp. 2298-2311.

108. El-Batal, A., et al., *Gamma irradiation induces silver nanoparticles synthesis by Monascus purpureus.* J Chem Pharm Res, 2013. **5**(8): pp. 1-15.

109. Stoimenov, P.K., et al., *Metal oxide nanoparticles as bactericidal agents.* Langmuir, 2002. **18**(17): pp. 6679-6686.

110. El-Batal, A.I., F.M. Mosallam, and G.S. El-Sayyad, *Synthesis of Metallic Silver Nanoparticles by Fluconazole Drug and Gamma Rays to Inhibit the Growth of Multidrug-Resistant Microbes.* Journal of Cluster Science: pp. 1-13.

111. Khan, M.F., et al., *Sol-gel synthesis of thorn-like ZnO nanoparticles endorsing mechanical stirring effect and their antimicrobial activities: Potential role as nano-antibiotics.* Scientific reports, 2016. **6**: pp. 27689.

112. Abd Elkodous, M., et al., *Carbon-dot-loaded* $Co_xNi_{1-x}Fe_2O_4$*; x = 0.9/*SiO_2*/*TiO_2 *nanocomposite with enhanced photocatalytic and antimicrobial potential: An engineered nanocomposite for wastewater treatment.* Scientific Reports, 2020. **10**(1): pp. 11534.

113. Marsooli, M.A., et al., *Preparation of Fe(*$_3$*)O(*$_4$*)/SiO(*$_2$*)/TiO(*$_2$*)/CeVO(*$_4$*) Nanocomposites: Investigation of Photocatalytic Effects on Organic Pollutants, Bacterial Environments, and New Potential Therapeutic Candidate Against Cancer Cells.* Frontiers in pharmacology, 2020. **11**: pp. 192-192.

114. Vakili Tajareh, A., H. Ganjidoust, and B. Ayati, *Synthesis of* TiO_2/Fe_3O_4*/MWCNT Magnetic and Reusable Nanocomposite with High Photocatalytic Performance in the Removal of Colored Combinations from Water.* Journal of Water and Environmental Nanotechnology, 2019. **4**(3): pp. 198-212.

115. Abd Elkodous, M., et al., *Layer-by-layer preparation and characterization of recyclable nanocomposite (*$Co_xNi_{1-x}Fe_2O_4$*; X= 0.9/*SiO_2/TiO_2*).* Journal of Materials Science: Materials in Electronics, 2019. **30**(9): pp. 8312-8328.

116. Fu, C., et al., *Preparation and characterization of* $Fe_3O_4@SiO_2@TiO_2$*–Co/rGO magnetic visible light photocatalyst for water treatment.* RSC Advances, 2019. **9**(35): pp. 20256-20265.

117. Abdel Maksoud, M.I.A., et al., *Nanostructured Mg substituted Mn-Zn ferrites: A magnetic recyclable catalyst for outstanding photocatalytic and antimicrobial potentials.* Journal of Hazardous Materials, 2020. **399**: pp. 123000.

118. Staudenmaier, L., *Verfahren zur Darstellung der Graphitsäure.* Berichte der deutschen chemischen Gesellschaft, 1898. **31**(2): pp. 1481-1487.

119. Poh, H.L., et al., *Graphenes prepared by Staudenmaier, Hofmann and Hummers methods with consequent thermal exfoliation exhibit very different electrochemical properties.* Nanoscale, 2012. **4**(11): pp. 3515-3522.

120. Kumar, R., et al., *Self-assembled nanostructures of 3D hierarchical faceted-iron oxide containing vertical carbon nanotubes on reduced graphene oxide hybrids for enhanced electromagnetic interface shielding.* Composites Part B: Engineering, 2019. **168**: pp. 66-76.

121. Kumar, R., et al., *Microwave-assisted synthesis of Mn_3O_4-Fe_2O_3/Fe_3O_4@rGO ternary hybrids and electrochemical performance for supercapacitor electrode.* Diamond and Related Materials, 2020. **101**: pp. 107622.

122. Kumar, R., et al., *Nitrogen–Sulfur Co-Doped Reduced Graphene Oxide-Nickel Oxide Nanoparticle Composites for Electromagnetic Interference Shielding.* ACS Applied Nano Materials, 2019. **2**(7): pp. 4626-4636.

123. Švarcová, S., et al., *Non-destructive micro-analytical differentiation of copper pigments in paint layers of works of art using laboratory-based techniques.* Spectrochimica Acta Part A: Molecular and Biomolecular Spectroscopy, 2014. **132**: pp. 514-525.

124. Al-Taweel, S.S. and H.R. Saud, *New route for synthesis of pure anatase TiO_2 nanoparticles via utrasound-assisted sol-gel method.* Journal of Chemical and Pharmaceutical Research, 2016. **8**(2): pp. 620-626.

125. Yusmaman, W. and J. Gunlazuardi. *The role of citric acid modifiers addition in the preparation of TiO_2 nanoparticles with the solvothermal method*. in *AIP Conference Proceedings*. 2020. AIP Publishing LLC.

126. Si, Z., et al., *Revisiting the preparation of titanium dioxide: aerosol-assisted production of photocatalyst with higher catalytic activity than P25.* Journal of Materials Science, 2020. **55**(2): pp. 565-576.

127. Hou, J., et al., *A mild and simple method to fabricate commercial TiO_2 (P25) and C_{60} composite for highly enhancing H_2 generation.* International Journal of Hydrogen Energy, 2020. **45**(4): pp. 2852-2861.

128. Zielińska, B., et al., *Photocatalytic degradation of Reactive Black 5: a comparison between TiO_2-Tytanpol A11 and TiO_2-Degussa P25 photocatalysts.* Applied Catalysis B: Environmental, 2001. **35**(1): pp. L1-L7.

129. Sa, K., et al., *Effect of reduced graphene oxide-carbon nanotubes hybrid nanofillers in mechanical properties of polymer nanocomposites.* IOP Conference Series: Materials Science and Engineering, 2018. **338**: pp. 012055.

130. Honarasa, F., F. Peyravi, and H. Amirian, *C-dots/Mn_3O_4 nanocomposite as an oxidase nanozyme for colorimetric determination of ferrous ion.* Journal of the Iranian Chemical Society, 2020. **17**(3): pp. 507-512.

131. Rasheed, A., et al., *A Flexible Supercapacitor Type Rectifier-free Self-charging Power Unit Based on a Multifunctional PVDF-ZnO-RGO Piezoelectric Matrix.* ACS Applied Materials & Interfaces, 2020.

132. Chegeni, M., et al., *Synthesis and application of the calcium alginate/SWCNT-Gl as a bio-nanocomposite for the curcumin delivery.* International Journal of Biological Macromolecules, 2020.

133. Abd Elkodous, M., et al., *Therapeutic and diagnostic potential of nanomaterials for enhanced biomedical applications.* Colloids and Surfaces B: Biointerfaces, 2019. **180**: pp. 411-428.

134. Sotomayor, F.J., K.A. Cychosz, and M. Thommes, *Characterization of micro/mesoporous materials by physisorption: concepts and case studies.* Acc. Mater. Surf. Res, 2018. **3**(2): pp. 36-37.

135. Liu, K., et al., *Fabrication of amino-modified electrospun nanofibrous cellulose membrane and adsorption for typical organoarsenic contaminants: Behavior and mechanism.* Chemical Engineering Journal, 2020. **382**: pp. 122775.

136. Fleyfel, F. and J.P. Devlin, *FT-IR spectra of carbon dioxide clusters.* The Journal of Physical Chemistry, 1989. **93**(21): pp. 7292-7294.

137. Abd, E.M., et al., *Carbon-dot-loaded $Co_xNi_{1-x}Fe_2O_4$; x= 0.9/SiO_2/TiO_2 nanocomposite with enhanced photocatalytic and antimicrobial potential: An engineered nanocomposite for wastewater treatment.* Scientific Reports (Nature Publisher Group), 2020. **10**(1).

138. Bourlinos, A.B., et al., *Luminescent surface quaternized carbon dots.* Chemistry of Materials, 2012. **24**(1): pp. 6-8.

139. Panwar, K., M. Jassal, and A.K. Agrawal, *TiO_2–SiO_2 Janus particles with highly enhanced photocatalytic activity.* RSC Advances, 2016. **6**(95): pp. 92754-92764.

140. Do, Y., et al., Bulletin of the Korean Chemical Society, 2013. **34**(12): pp. 3635-3640.

141. Nowacka, M., D. Ambrożewicz, and T. Jesionowski, *TiO_{2}-SiO_{2}/Ph-POSS Functional Hybrids: Preparation and Characterisation.* Journal of Nanomaterials, 2013. **2013**: pp. 680821.

142. Ibáñez, J., et al., *Hydration and carbonation of monoclinic* C_2S *and* C_3S *studied by Raman spectroscopy.* Journal of Raman Spectroscopy: An International Journal for Original Work in all Aspects of Raman Spectroscopy, Including Higher Order Processes, and also Brillouin and Rayleigh Scattering, 2007. **38**(1): pp. 61-67.

143. Ashour, A., et al., *Antimicrobial activity of metal-substituted cobalt ferrite nanoparticles synthesized by sol–gel technique.* Particuology, 2018. **40**: pp. 141-151.

144. Mahalingam, T., et al., *Structural, optical, morphological and thermal properties of* TiO_2*–Al and* TiO_2*–*Al_2O_3 *composite powders by ball milling.* Physics Letters A, 2017. **381**(21): pp. 1815-1819.

145. El-Sayyad, G.S., et al., *Merits of photocatalytic and antimicrobial applications of gamma-irradiated* $Co_xNi_{1-x}Fe_2O_4/SiO_2/TiO_2$*; x= 0.9 nanocomposite for pyridine removal and pathogenic bacteria/fungi disinfection: implication for wastewater treatment.* RSC Advances, 2020. **10**(9): pp. 5241-5259.

146. Kong, X., et al., *Synthesis of graphene-like carbon from biomass pyrolysis and its applications.* Chemical Engineering Journal, 2020. **399**: pp. 125808.

147. Tamayo, A., et al., *Further characterization of the surface properties of the SiC particles through complementarity of XPS and IGC-ID techniques.* Boletín de la Sociedad Española de Cerámica y Vidrio, 2018. **57**(6): pp. 231-239.

148. Dhar, S., et al., *Silicon-graphene composite synthesis: Microstructural, spectroscopic and electrical conductivity characterizations.* Materials Today: Proceedings, 2020.

149. Bashouti, M.Y., et al., *Silicon nanowires terminated with methyl functionalities exhibit stronger Si–C bonds than equivalent 2D surfaces.* Physical Chemistry Chemical Physics, 2009. **11**(20): pp. 3845-3848.

150. Chi, M., et al., *A quantitative XPS examination of UV induced surface modification of* TiO_2 *sorbents for the increased saturation capacity of sulfur heterocycles.* Fuel, 2019. **238**: pp. 454-461.

151. Abdullah, S.A., et al., *Neutron beam interaction with rutile TiO_2 single crystal (1 1 1): Raman and XPS study on Ti3+-oxygen vacancy formation.* Materials Letters, 2020. **263**: pp. 127143.

152. Naumenko, D., et al., *Graphene-enhanced Raman imaging of TiO_2 nanoparticles.* Nanotechnology, 2012. **23**(46): pp. 465703.

153. Zheng, Q., et al., *Highly transparent and conducting ultralarge graphene oxide/single-walled carbon nanotube hybrid films produced by Langmuir–Blodgett assembly.* Journal of Materials Chemistry, 2012. **22**(48): pp. 25072-25082.

154. How, G.T.S., et al., *Highly exposed {001} facets of titanium dioxide modified with reduced graphene oxide for dopamine sensing.* Scientific Reports, 2014. **4**(1): pp. 5044.

155. Zhang, H., et al., *A facile one-step synthesis of TiO_2/graphene composites for photodegradation of methyl orange.* Nano Research, 2011. **4**(3): pp. 274-283.

156. Gao, Y., et al., *Reduced graphene oxide as a catalyst for hydrogenation of nitrobenzene at room temperature.* Chemical Communications, 2011. **47**(8): pp. 2432-2434.

157. Kuzmany, H., et al., *Determination of SWCNT diameters from the Raman response of the radial breathing mode.* The European Physical Journal B-Condensed Matter and Complex Systems, 2001. **22**(3): pp. 307-320.

158. Wang, S., et al., *A novel and highly efficient photocatalyst based on P25–graphdiyne nanocomposite.* Small, 2012. **8**(2): pp. 265-271.

159. Apopei, P., et al., *Mixed-phase TiO_2 photocatalysts: Crystalline phase isolation and reconstruction, characterization and photocatalytic activity in the oxidation of 4-chlorophenol from aqueous effluents.* Applied Catalysis B: Environmental, 2014. **160-161**: pp. 374-382.

160. Zhang, Y., et al., *C-doped hollow TiO_2 spheres: in situ synthesis, controlled shell thickness, and superior visible-light photocatalytic activity.* Applied Catalysis B: Environmental, 2015. **165**: pp. 715-722.

161. Shao, J., et al., *In situ synthesis of carbon-doped TiO_2 single-crystal nanorods with a remarkably photocatalytic efficiency.* Applied Catalysis B: Environmental, 2017. **209**: pp. 311-319.

162. Zhang, Y., et al., *High photocatalytic activity of hierarchical SiO_2@C-doped TiO_2 hollow spheres in UV and visible light towards degradation of rhodamine B.* Journal of Hazardous Materials, 2017. **340**: pp. 309-318.

163. Kumar, A., A.S. Patel, and T. Mohanty, *Correlation of Photodegradation Efficiency with Surface Potential of Silver-TiO_2 Nanocomposite Thin Films.* The Journal of Physical Chemistry C, 2012. **116**(38): pp. 20404-20408.

164. Pugazhenthiran, N., S. Murugesan, and S. Anandan, *High surface area Ag-TiO_2 nanotubes for solar/visible-light photocatalytic degradation of ceftiofur sodium.* Journal of hazardous materials, 2013. **263**: pp. 541-549.

165. Lu, M., et al., *The synthesis of $Co_xNi_{1-x}Fe_2O_4$/multi-walled carbon nanotube nanocomposites and their photocatalytic performance.* RSC Advances, 2019. **9**(58): pp. 33806-33813.

166. Gammoudi, H., et al., *Influence of single-walled carbon nanotubes functionalization in photocatalytic performance of pyramidal porous silicon: Experimental evidence.* Materials Letters, 2020. **266**: pp. 127473.

167. Isari, A.A., et al., *N, Cu co-doped TiO_2@ functionalized SWCNT photocatalyst coupled with ultrasound and visible-light: An effective sono-photocatalysis process for pharmaceutical wastewaters treatment.* Chemical Engineering Journal, 2020. **392**: pp. 123685.

168. Zhou, Y., et al., *Flower-like $Bi_4Ti_3O_{12}$/Carbon nanotubes as reservoir and promoter of polysulfide for lithium sulfur battery.* Journal of Power Sources, 2020. **453**: pp. 227896.

169. Khamizov, R.K., et al., *Kinetic Models of Batch Sorption in a Limited Volume.* Russian Journal of Physical Chemistry A, 2018. **92**(9): pp. 1782-1789.

170. Khamizov, R.K., et al., *Kinetic model of batch sorption processes: Comparing calculated and experimental data.* Russian Journal of Physical Chemistry A, 2018. **92**(10): pp. 2032-2038.

171. Jun, B.-M., et al., *Accelerated photocatalytic degradation of organic pollutants over carbonate-rich lanthanum-substituted zinc spinel ferrite assembled reduced graphene*

oxide by ultraviolet (UV)-activated persulfate. Chemical Engineering Journal, 2020. **393**: pp. 124733.

172. Mady, A.H., et al., *Heterogeneous activation of peroxymonosulfate by a novel magnetic 3D γ-*MnO_2*@*$ZnFe_2O_4$*/rGO nanohybrid as a robust catalyst for phenol degradation.* Applied Catalysis B: Environmental, 2019. **244**: pp. 946-956.

173. Liu, Y., et al., *Enhanced catalytic degradation of methylene blue by α-*Fe_2O_3*/graphene oxide via heterogeneous photo-Fenton reactions.* Applied Catalysis B: Environmental, 2017. **206**: pp. 642-652.

174. Su, S., et al., *Efficient transformation and elimination of roxarsone and its metabolites by a new α-FeOOH@GCA activating persulfate system under UV irradiation with subsequent As(V) recovery.* Applied Catalysis B: Environmental, 2019. **245**: pp. 207-219.

175. Hammouda, S.B., et al., *Sulfate radical-mediated degradation and mineralization of bisphenol F in neutral medium by the novel magnetic* Sr_2CoFeO_6 *double perovskite oxide catalyzed peroxymonosulfate: Influence of co-existing chemicals and UV irradiation.* Applied Catalysis B: Environmental, 2018. **233**: pp. 99-111.

176. Tang, J., Z. Zou, and J. Ye, *Kinetics of MB degradation and effect of pH on the photocatalytic activity of* MIn_2O_4 *(M = Ca, Sr, Ba) under visible light irradiation.* Research on Chemical Intermediates, 2005. **31**(4): pp. 513-519.

177. Khan, M. and I.M.C. Lo, *A holistic review of hydrogel applications in the adsorptive removal of aqueous pollutants: Recent progress, challenges, and perspectives.* Water Research, 2016. **106**: pp. 259-271.

178. Chumha, N., et al., *Photocatalytic activity of* $CuInS_2$ *nanoparticles synthesized via a simple and rapid microwave heating process.* Materials Research Express, 2020. **7**(1): pp. 015074.

179. Khan, M., et al., *Elucidating the predominant role of crystal disorders in hierarchical photocatalysts governing their charge carrier separation and associated activity in photocatalytic water treatment.* Journal of Colloid and Interface Science, 2020. **573**: pp. 336-347.

180. Ahmed, M.A., et al., *Effect of porphyrin on photocatalytic activity of* TiO_2 *nanoparticles toward Rhodamine B photodegradation.* Journal of Photochemistry and Photobiology B: Biology, 2017. **176**: pp. 25-35.

181. Verma, S., et al., *Studies on growth of Au cube-ZnO core-shell nanoparticles for photocatalytic degradation of methylene blue and methyl orange dyes in aqueous media and in presence of different scavengers.* Journal of Environmental Chemical Engineering, 2019. **7**(4): pp. 103209.

182. Alshakhanbeh, M.A., et al., *Influence of dispersion of various proportions of metallic gold nanoparticles on the optical and photocatalytic properties of titania.* Materials Science for Energy Technologies, 2020. **3**: pp. 429-439.

183. Yousefi-Mohammadi, S., M. Movahedi, and H. Salavati, *MnCo–Ferrite/*TiO_2 *composite as an efficient magnetically separable photocatalyst for decolorization of dye pollutants in aqueous solution.* Surfaces and Interfaces, 2018. **11**: pp. 91-97.

184. Chen, C.-C., et al., *Magnetic recyclable photocatalysts of Ni-Cu-Zn ferrite@SiO2@TiO2@Ag and their photocatalytic activities.* Journal of Photochemistry and Photobiology A: Chemistry, 2017. **334**: pp. 74-85.

185. Li, D., et al., *Influence of morphology and interfacial interaction of* TiO_2*-Graphene nanocomposites on the visible light photocatalytic performance.* Journal of Solid State Chemistry, 2020. **286**: pp. 121301.

186. Nuengmatcha, P., et al., *Visible light-driven photocatalytic degradation of rhodamine B and industrial dyes (texbrite BAC-L and texbrite NFW-L) by ZnO-graphene-*TiO_2 *composite.* Journal of Environmental Chemical Engineering, 2016. **4**(2): pp. 2170-2177.

187. Xu, S., et al., *Preparations and photocatalytic properties of magnetically separable nitrogen-doped* TiO_2 *supported on nickel ferrite.* Applied Catalysis B: Environmental, 2007. **71**(3): pp. 177-184.

188. Liu, C., et al., *Fabrication of multilayer porous structured* TiO_2–$ZrTiO_4$–SiO_2 *heterostructure towards enhanced photo-degradation activities.* Ceramics International, 2020. **46**(1): pp. 476-486.

189. Zolnikov, T.R., et al., *A systematic review on informal waste picking: Occupational hazards and health outcomes.* Waste Management, 2021. **126**: pp. 291-308.

190. Laszakovits, J.R. and A.A. MacKay, *Removal of cyanotoxins by potassium permanganate: Incorporating competition from natural water constituents.* Water research, 2019. **155**: pp. 86-95.

191. Agrawal, V.K., et al., *Potassium permanganate toxicity: A rare case with difficult airway management and hepatic damage.* Indian journal of critical care medicine: peer-reviewed, official publication of Indian Society of Critical Care Medicine, 2014. **18**(12): pp. 819.

192. Pavesi, T. and J.C. Moreira, *Mechanisms and individuality in chromium toxicity in humans.* Journal of Applied Toxicology, 2020. **40**(9): pp. 1183-1197.

193. Miskam, M., N.K. Abu Bakar, and S. Mohamad, *Determination of polar aromatic amines using newly synthesized sol–gel titanium (IV) butoxide cyanopropyltriethoxysilane as solid phase extraction sorbent.* Talanta, 2014. **120**: pp. 450-455.

194. Abd Elkodous, M., et al., *Fabrication of Ultra-Pure Anisotropic Zinc Oxide Nanoparticles via Simple and Cost-Effective Route: Implications for UTI and EAC Medications.* Biological trace element research, 2020. **196**(1): pp. 297-317.

195. Atacan, K., et al., *Efficiency of glucose oxidase immobilized on tannin modified* $NiFe_2O_4$ *nanoparticles on decolorization of dye in the Fenton and photo-biocatalytic processes.* Journal of Photochemistry and Photobiology A: Chemistry, 2019. **382**: pp. 111935.

196. He, X., et al., *Photocatalytic degradation of microcystin-LR by modified* TiO_2 *photocatalysis: A review.* Science of The Total Environment, 2020: pp. 140694.

197. Xiao, F.-X., et al., *Spatially branched hierarchical ZnO nanorod-*TiO_2 *nanotube array heterostructures for versatile photocatalytic and photoelectrocatalytic applications: towards intimate integration of 1D–1D hybrid nanostructures.* Nanoscale, 2014. **6**(24): pp. 14950-14961.

198. Wang, H., et al., *Semiconductor heterojunction photocatalysts: design, construction, and photocatalytic performances.* Chemical Society Reviews, 2014. **43**(15): pp. 5234-5244.

199. Scarisoreanu, M., et al., *Ag, Au and Pt decorated TiO_2 biocompatible nanospheres for UV & vis photocatalytic water treatment.* Applied Surface Science, 2020. **509**: pp. 145217.

200. Afsari, M., et al., *Remarkable improvement of visible light photocatalytic activity of TiO_2 nanotubes doped sequentially with noble metals for removing of organic and microbial pollutants.* Materials Research Bulletin, 2017. **94**: pp. 15-21.

201. Reddy, N.R., et al., *Highly efficient solar light-driven photocatalytic hydrogen production over Cu/FCNTs-titania quantum dots-based heterostructures.* Journal of Environmental Management, 2020. **254**: pp. 109747.

202. Kibombo, H.S., et al., *Versatility of heterogeneous photocatalysis: synthetic methodologies epitomizing the role of silica support in TiO_2 based mixed oxides.* Catalysis Science & Technology, 2012. **2**(9): pp. 1737-1766.

203. Chen, J., et al., *Recent progress in enhancing photocatalytic efficiency of TiO_2-based materials.* Applied Catalysis A: General, 2015. **495**: pp. 131-140.

204. Bellardita, M., et al., *Photocatalytic activity of TiO_2/SiO_2 systems.* Journal of Hazardous Materials, 2010. **174**(1-3): pp. 707-713.

205. Abdel Maksoud, M.I.A., et al., *Advanced materials and technologies for supercapacitors used in energy conversion and storage: a review.* Environmental Chemistry Letters, 2021. **19**(1): pp. 375-439.

206. Zhang, W., et al., *Structural, morphological and magnetic properties of Ni–Co ferrites by the Mn^{2+} ions substitution.* Journal of Materials Science: Materials in Electronics, 2019. **30**(20): pp. 18729-18743.

207. Lassoued, A. and J.F. Li, *Magnetic and photocatalytic properties of Ni–Co ferrites.* Solid State Sciences, 2020. **104**: pp. 106199.

208. Sinha, T. and M. Ahmaruzzaman, *Photocatalytic decomposition behavior and reaction pathways of organic compounds using Cu nanoparticles synthesized via a green route.* Photochemical & Photobiological Sciences, 2016. **15**(10): pp. 1272-1281.

209. Long, J., et al., *Photochemical synthesis of submicron-and nano-scale Cu_2O particles.* Journal of colloid and interface science, 2009. **333**(2): pp. 791-799.

210. Arulprakasajothi, M., et al., *Performance study of conical strip inserts in tube heat exchanger using water based titanium oxide nanofluid.* Thermal Science, 2018. **22**(1 Part B): pp. 477-485.

211. Chawla, S., N. Sankarraman, and J. Payer, *Diagnostic spectra for XPS analysis of Cu O S H compounds.* Journal of electron spectroscopy and related phenomena, 1992. **61**(1): pp. 1-18.

212. Peng, Y., et al., *Oxygen vacancy enhanced photoreduction Cr (VI) on few-layers BiOBr nanosheets.* Catalysts, 2019. **9**(6): pp. 558.

213. Tu, Y., et al., *Control of oxygen vacancies in ZnO nanorods by annealing and their influence on ZnO/PEDOT: PSS diode behaviour.* Journal of Materials Chemistry C, 2018. **6**(7): pp. 1815-1821.

214. Nawaz, H., et al., *Photodegradation of textile pollutants by nanocomposite membranes of polyvinylidene fluoride integrated with polyaniline–titanium dioxide nanotubes.* Chemical Engineering Journal, 2021. **419**: pp. 129542.

215. Banerjee, S. and M.C. Chattopadhyaya, *Adsorption characteristics for the removal of a toxic dye, tartrazine from aqueous solutions by a low cost agricultural by-product.* Arabian Journal of Chemistry, 2017. **10**: pp. S1629-S1638.

216. Miyah, Y., et al., *Assessment of adsorption kinetics for removal potential of Crystal Violet dye from aqueous solutions using Moroccan pyrophyllite.* Journal of the Association of Arab Universities for Basic and Applied Sciences, 2017. **23**: pp. 20-28.

217. Zhang, H., et al., *Kinetic studies of direct blue photodegradation over flower-like* TiO_2*.* Research on Chemical Intermediates, 2017. **43**(3): pp. 1529-1542.

218. El-Khawaga, A.M., et al., *Antimicrobial and Photocatalytic Degradation Activities of Chitosan-coated Magnetite Nanocomposite.* Journal of Cluster Science, 2020.

219. Hohenberg, P. and W. Kohn, *Density functional theory (DFT).* Phys. Rev, 1964. **136**: pp. B864.

220. Frisch, M., et al., *Gaussian 16*. 2016, Gaussian, Inc. Wallingford, CT.

221. Assadi, M.H.N. and D.A. Hanaor, *The effects of copper doping on photocatalytic activity at (101) planes of anatase* TiO_2*: A theoretical study.* Applied Surface Science, 2016. **387**: pp. 682-689.

222. Dorraj, M., et al., *Improved visible-light photocatalytic activity of* TiO_2 *co-doped with copper and iodine.* Applied Surface Science, 2018. **439**: pp. 999-1009.

223. Sharmila, G., M. Thirumarimurugan, and C. Muthukumaran, *Green synthesis of ZnO nanoparticles using Tecoma castanifolia leaf extract: characterization and evaluation of its antioxidant, bactericidal and anticancer activities.* Microchemical Journal, 2019. **145**: pp. 578-587.

224. Naik, M.M., et al., *Green synthesis of zinc ferrite nanoparticles in Limonia acidissima juice: characterization and their application as photocatalytic and antibacterial activities.* Microchemical Journal, 2019. **146**: pp. 1227-1235.

225. Qing, W., et al., Cu^{2+}*-doped carbon dots as fluorescence probe for specific recognition of Cr (VI) and its antimicrobial activity.* Microchemical Journal, 2020. **152**: pp. 104262.

226. Rani, H., et al., *In-vitro catalytic, antimicrobial and antioxidant activities of bioengineered copper quantum dots using Mangifera indica (L.) leaf extract.* Materials Chemistry and Physics, 2020. **239**: pp. 122052.

227. Samavati, A., et al., *Copper-substituted cobalt ferrite nanoparticles: structural, optical and antibacterial properties.* Materials Express, 2016. **6**(6): pp. 473-482.

228. Gaunt, L.F., C.B. Beggs, and G.E. Georghiou, *Bactericidal action of the reactive species produced by gas-discharge nonthermal plasma at atmospheric pressure: a review.* IEEE Transactions on Plasma Science, 2006. **34**(4): pp. 1257-1269.

229. Fathy, R.M. and A.Y. Mahfouz, *Eco-friendly graphene oxide-based magnesium oxide nanocomposite synthesis using fungal fermented by-products and gamma rays for outstanding antimicrobial, antioxidant, and anticancer activities.* Journal of Nanostructure in Chemistry: pp. 1-21.

230. Joe, A., et al., *Antimicrobial activity of ZnO nanoplates and its Ag nanocomposites: Insight into an ROS-mediated antibacterial mechanism under UV light.* Journal of Solid State Chemistry, 2018. **267**: pp. 124-133.

231. Bradford, N., *A rapid and sensitive method for the quantitation microgram quantities of a protein isolated from red cell membranes.* Anal. Biochem, 1976. **72**(248): pp. e254.

232. Rajesh, S., V. Dharanishanthi, and A.V. Kanna, *Antibacterial mechanism of biogenic silver nanoparticles of Lactobacillus acidophilus.* Journal of Experimental Nanoscience, 2015. **10**(15): pp. 1143-1152.

233. El-Batal, A.I., F.M. Mosallam, and G.S. El-Sayyad, *Synthesis of metallic silver nanoparticles by fluconazole drug and gamma rays to inhibit the growth of multidrug-resistant microbes.* Journal of Cluster Science, 2018. **29**(6): pp. 1003-1015.

234. Abd Elkodous, M., et al., *Therapeutic and diagnostic potential of nanomaterials for enhanced biomedical applications.* Colloids and Surfaces B: Biointerfaces, 2019. **180**: pp. 411-428.

235. Maksoud, M.A., et al., *Nanostructured Mg substituted Mn-Zn ferrites: A magnetic recyclable catalyst for outstanding photocatalytic and antimicrobial potentials.* Journal of Hazardous Materials, 2020. **399**: pp. 123000.

236. Ham, Y., et al., *Flux-mediated doping of* $SrTiO_3$ *photocatalysts for efficient overall water splitting.* Journal of Materials Chemistry A, 2016. **4**(8): pp. 3027-3033.

237. Pan, R., et al., *Two-Dimensional All-in-One Sulfide Monolayers Driving Photocatalytic Overall Water Splitting.* Nano Letters, 2021. **21**(14): pp. 6228-6236.

238. Guerrero, A. and J. Bisquert, *Perovskite semiconductors for photoelectrochemical water splitting applications.* Current Opinion in Electrochemistry, 2017. **2**(1): pp. 144-147.

239. Chiang, T.H., et al., *Efficient Photocatalytic Water Splitting Using Al-Doped* $SrTiO_3$ *Coloaded with Molybdenum Oxide and Rhodium–Chromium Oxide.* ACS Catalysis, 2018. **8**(4): pp. 2782-2788.

240. Canu, G. and V. Buscaglia, *Hydrothermal synthesis of strontium titanate: thermodynamic considerations, morphology control and crystallisation mechanisms.* CrystEngComm, 2017. **19**(28): pp. 3867-3891.

241. Wang, J., et al., *Few-layer* $BiVO_4$ *nanosheets decorated with* $SrTiO_3$*: Rh nanoparticles for highly efficient visible-light-driven overall water splitting.* Applied Catalysis B: Environmental, 2020. **279**: pp. 119377.

242. Goto, Y., et al., *A Particulate Photocatalyst Water-Splitting Panel for Large-Scale Solar Hydrogen Generation.* Joule, 2018. **2**(3): pp. 509-520.

243. Sanwald, K.E., et al., *Kinetic coupling of water splitting and photoreforming on $SrTiO_3$-based photocatalysts.* ACS Catalysis, 2018. **8**(4): pp. 2902-2913.

244. Goto, Y., et al., *A particulate photocatalyst water-splitting panel for large-scale solar hydrogen generation.* Joule, 2018. **2**(3): pp. 509-520.

245. Liu, Y., et al., *Ni single atoms anchored on nitrogen-doped graphene as H_2-Evolution cocatalyst of $SrTiO_3(Al)/CoO_x$ for photocatalytic overall water splitting.* Carbon, 2021. **183**: pp. 763-773.

246. Zong, S., et al., *Photocatalytic overall water splitting without noble-metal: Decorating CoP on Al-doped $SrTiO_3$.* Journal of Colloid and Interface Science, 2022. **606**: pp. 491-499.

247. Takata, T., et al., *Photocatalytic water splitting with a quantum efficiency of almost unity.* Nature, 2020. **581**(7809): pp. 411-414.

248. Abouelela, M.M., G. Kawamura, and A. Matsuda, *A review on plasmonic nanoparticle-semiconductor photocatalysts for water splitting.* Journal of Cleaner Production, 2021. **294**: pp. 126200.

249. Kawamura, G. and A. Matsuda, *Synthesis of Plasmonic Photocatalysts for Water Splitting.* Catalysts, 2019. **9**(12): pp. 982.

250. Saadetnejad, D. and R. Yıldırım, *Photocatalytic hydrogen production by water splitting over Au/Al-$SrTiO_3$.* International Journal of Hydrogen Energy, 2018. **43**(2): pp. 1116-1122.

251. Zwara, J., et al., *The effect of imidazolium ionic liquid on the morphology of Pt nanoparticles deposited on the surface of $SrTiO_3$ and photoactivity of Pt–$SrTiO_3$ composite in the H_2 generation reaction.* International Journal of Hydrogen Energy, 2019. **44**(48): pp. 26308-26321.

252. Chen, S., T. Takata, and K. Domen, *Particulate photocatalysts for overall water splitting.* Nature Reviews Materials, 2017. **2**(10): pp. 1-17.

253. Rayalu, S.S., et al., *Photocatalytic water splitting on Au/TiO_2 nanocomposites synthesized through various routes: Enhancement in photocatalytic activity due to SPR effect.* Applied Catalysis B: Environmental, 2013. **142-143**: pp. 684-693.

254. Seh, Z.W., et al., *Janus Au-TiO_2 photocatalysts with strong localization of plasmonic near-fields for efficient visible-light hydrogen generation.* Advanced Materials, 2012. **24**(17): pp. 2310-2314.

255. Devi, N.Y., et al., *Effect of Gd and Nb co-substitution on enhancing the thermoelectric power factor of nanostructured $SrTiO_3$.* Ceramics International, 2021. **47**(3): pp. 3201-3208.

256. Krishnamurthy, S., et al., *Yucca-derived synthesis of gold nanomaterial and their catalytic potential.* Nanoscale Research Letters, 2014. **9**(1): pp. 627.

257. Zhao, Z., et al., *Electronic structure basis for enhanced overall water splitting photocatalysis with aluminum doped $SrTiO_3$ in natural sunlight.* Energy & Environmental Science, 2019. **12**(4): pp. 1385-1395.

258. Kawamura, G., et al., *Charge behavior in a plasmonic photocatalyst composed of Au and TiO_2.* Catalysis Science & Technology, 2018. **8**(7): pp. 1813-1818.

259. Schultz, A.M., P.A. Salvador, and G.S. Rohrer, *Enhanced photochemical activity of α-Fe_2O_3 films supported on $SrTiO_3$ substrates under visible light illumination.* Chemical Communications, 2012. **48**(14): pp. 2012-2014.

260. Zhang, M., et al., *Semiconductor/covalent-organic-framework Z-scheme heterojunctions for artificial photosynthesis.* Angewandte Chemie, 2020. **132**(16): pp. 6562-6568.

261. Jiang, C., et al., *Photoelectrochemical devices for solar water splitting–materials and challenges.* Chemical Society Reviews, 2017. **46**(15): pp. 4645-4660.

262. Chang, X., et al., *The development of cocatalysts for photoelectrochemical CO_2 reduction.* Advanced Materials, 2019. **31**(31): pp. 1804710.

263. Zhang, G., et al., *Rationally design and in-situ fabrication of ultrasmall pomegranate-like $CdIn_2S_4$/$ZnIn_2S_4$ Z-scheme heterojunction with abundant vacancies for improving CO_2 reduction and water splitting.* Chemical Engineering Journal, 2022. **442**: pp. 136309.

264. Jiang, M., et al., *Photocatalytic CO_2 reduction promoted by a $CuCo_2O_4$ cocatalyst with homogeneous and heterogeneous light harvesters.* Applied Catalysis B: Environmental, 2016. **198**: pp. 180-188.

265. Bi, W., et al., *Construction of $CuInS_2$/C/TiO_2 hierarchical tandem heterostructures with optimized CO_2 photoreduction under visible light.* Chemical Engineering Journal, 2022. **433**: pp. 133679.

266. Xiao, N., et al., *The roles and mechanism of cocatalysts in photocatalytic water splitting to produce hydrogen.* Chinese Journal of Catalysis, 2020. **41**(4): pp. 642-671.

267. He, Y., et al., *3D hierarchical $ZnIn_2S_4$ nanosheets with rich Zn vacancies boosting photocatalytic CO_2 reduction.* Advanced Functional Materials, 2019. **29**(45): pp. 1905153.

268. Zhang, G., Z. Wang, and J. Wu, *Construction of a Z-scheme heterojunction for high-efficiency visible-light-driven photocatalytic CO_2 reduction.* Nanoscale, 2021. **13**(8): pp. 4359-4389.

269. Grabowska, E., *Selected perovskite oxides: Characterization, preparation and photocatalytic properties—A review.* Applied Catalysis B: Environmental, 2016. **186**: pp. 97-126.

270. Sulaeman, U., S. Yin, and T. Sato, *Solvothermal synthesis and photocatalytic properties of chromium-doped $SrTiO_3$ nanoparticles.* Applied Catalysis B: Environmental, 2011. **105**(1): pp. 206-210.

271. Wang, B., S. Shen, and L. Guo, *$SrTiO_3$ single crystals enclosed with high-indexed {023} facets and {001} facets for photocatalytic hydrogen and oxygen evolution.* Applied Catalysis B: Environmental, 2015. **166-167**: pp. 320-326.

272. Chen, W., et al., *Polymerizable complex synthesis of $SrTiO_3$:(Cr/Ta) photocatalysts to improve photocatalytic water splitting activity under visible light.* Applied Catalysis B: Environmental, 2016. **192**: pp. 145-151.

273. Chang, Y., et al., *Z-Scheme Pt@ CdS/3DOM-$SrTiO_3$ composite with enhanced photocatalytic hydrogen evolution from water splitting.* Catalysis Today, 2019. **327**: pp. 315-322.

274. Qiu, B., et al., *Efficient solar light harvesting CdS/Co_9S_8 hollow cubes for Z-scheme photocatalytic water splitting.* Angewandte Chemie International Edition, 2017. **56**(10): pp. 2684-2688.

275. Pan, J., et al., *The overall water splitting of CdS/Ti^{3+}-$SrTiO_3$ core–shell heterojunction via OER enhancement of MnO_x nanoparticles.* Chemical Engineering Journal, 2021. **424**: pp. 130357.

276. Chang, Y., et al., *Ternary CdS/Au/3DOM-$SrTiO_3$ composites with synergistic enhancement for hydrogen production from visible-light photocatalytic water splitting.* Applied Catalysis B: Environmental, 2017. **215**: pp. 74-84.

277. Li, Z., et al., *Porous direct Z-scheme heterostructures of S-deficient CoS/CdS hexagonal nanoplates for robust photocatalytic H_2 generation.* CrystEngComm, 2022. **24**(2): pp. 404-416.

278. Abd Elkodous, M., et al., *Metallic nanoparticles loaded Al–$SrTiO_3$ supported with $RhCr_2O_3$ and CoOOH cocatalysts for overall water splitting.* International Journal of Hydrogen Energy, 2022. **47**(85): pp. 36139-36148.

279. Cheng, T., et al., *Preparation of core-shell heterojunction photocatalysts by coating CdS nanoparticles onto $Bi_4Ti_3O_{12}$ hierarchical microspheres and their photocatalytic removal of organic pollutants and Cr (VI) ions.* Colloids and Surfaces A: Physicochemical and Engineering Aspects, 2022. **633**: pp. 127918.

280. Wang, S., et al., *Achieving overall water splitting on plasmon-based solid Z-scheme photocatalysts free of redox mediators.* Journal of catalysis, 2017. **354**: pp. 250-257.

281. Sasaki, Y., et al., *Solar water splitting using powdered photocatalysts driven by Z-schematic interparticle electron transfer without an electron mediator.* The Journal of Physical Chemistry C, 2009. **113**(40): pp. 17536-17542.

282. Britto Hurtado, R., et al., *One-step synthesis of reduced graphene oxide/gold nanoparticles under ambient conditions.* Arabian Journal of Chemistry, 2020. **13**(1): pp. 1633-1640.

283. Venkatareddy, C., et al., *UV–Visible light driven photocatalytic activities of CdS nanoparticles supported ZnO layers.* Materials Science and Engineering: B, 2018. **232**: pp. 68-75.

284. Chang, B.Y.S., et al., *Hydrothermally prepared graphene-titania nanocomposite for the solar photocatalytic degradation of methylene blue.* Desalination and Water Treatment, 2016. **57**(1): pp. 238-245.

285. Abd Elkodous, M., et al., *Enhanced photocatalytic and antimicrobial performance of a multifunctional Cu-loaded nanocomposite under UV light: theoretical and experimental study.* Nanoscale, 2022. **14**(23): pp. 8306-8317.

286. Dhage, S.R., H.A. Colorado, and T. Hahn, *Morphological variations in cadmium sulfide nanocrystals without phase transformation.* Nanoscale Research Letters, 2011. **6**(1): pp. 420.

287. Gu, L., et al., *Defects enhanced photocatalytic performances in* $SrTiO_3$ *using laser-melting treatment.* Journal of Materials Research, 2017. **32**(4): pp. 748-756.

288. Kumar, P., et al., *Nanotwinning and structural phase transition in CdS quantum dots.* Nanoscale Research Letters, 2012. **7**(1): pp. 584.

289. Ling, Y., et al., *New two-layer Ruddlesden—Popper cathode materials for protonic ceramics fuel cells.* Journal of Advanced Ceramics, 2021. **10**(5): pp. 1052-1060.

290. Pramanik, G., et al., *Gold nanoclusters with bright near-infrared photoluminescence.* Nanoscale, 2018. **10**(8): pp. 3792-3798.

291. Chen, K.-Q., et al., *Thermodynamic and Economic Assessment on the Supercritical Compressed Carbon Dioxide Energy Storage System coupled with Solar Thermal Storage.* Journal of Energy Storage, 2021. **41**: pp. 102959.

292. Li, M.-J., C.-X. Song, and W.-Q. Tao, *A hybrid model for explaining the short-term dynamics of energy efficiency of China's thermal power plants.* Applied Energy, 2016. **169**: pp. 738-747.

293. Li, M.-J. and W.-Q. Tao, *Review of methodologies and polices for evaluation of energy efficiency in high energy-consuming industry.* Applied Energy, 2017. **187**: pp. 203-215.

294. Cosic, A., et al., *Mixed-integer linear programming based optimization strategies for renewable energy communities.* Energy, 2021: pp. 121559.

295. Wang, K.-B., Q. Xun, and Q. Zhang, *Recent progress in metal-organic frameworks as active materials for supercapacitors.* EnergyChem, 2020. **2**(1): pp. 100025.

296. Abdalla, A.N., et al., *Integration of energy storage system and renewable energy sources based on artificial intelligence: An overview.* Journal of Energy Storage, 2021. **40**: pp. 102811.

297. Gasanzade, F., et al., *Subsurface renewable energy storage capacity for hydrogen, methane and compressed air – A performance assessment study from the North German Basin.* Renewable and Sustainable Energy Reviews, 2021. **149**: pp. 111422.

298. Weitemeyer, S., et al., *Integration of Renewable Energy Sources in future power systems: The role of storage.* Renewable Energy, 2015. **75**: pp. 14-20.

299. Wråke, M., M. Liljeberg, and F. Martinsson, *Nordic Energy Technology Perspectives 2016*. 2016, IVL Svenska Miljöinstitutet.

300. Zheng, S., et al., *Dual-ligand and hard-soft-acid-base strategies to optimize metal-organic framework nanocrystals for stable electrochemical cycling performance.* National Science Review, 2021.

301. Zhou, Y., et al., *Two-birds-one-stone: multifunctional supercapacitors beyond traditional energy storage.* Energy & Environmental Science, 2021. **14**(4): pp. 1854-1896.

302. Fic, K., et al., *Sustainable materials for electrochemical capacitors.* Materials Today, 2018. **21**(4): pp. 437-454.

303. dos Reis, G.S., et al., *Flexible supercapacitors of biomass-based activated carbon-polypyrrole on eggshell membranes.* Journal of Environmental Chemical Engineering, 2021: pp. 106155.

304. Mo, Y., et al., *N-doped mesoporous carbon nanosheets for supercapacitors with high performance.* Diamond and Related Materials, 2021. **111**: pp. 108206.

305. Bai, Y., et al., *MXene-Copper/Cobalt Hybrids via Lewis Acidic Molten Salts Etching for High Performance Symmetric Supercapacitors.* Angewandte Chemie, 2021. **133**(48): pp. 25522-25526.

306. Jorn-am, T., et al., *Quasi-solid, bio-renewable supercapacitor with high specific capacitance and energy density based on rice electrolytes and rice straw-derived carbon dots as novel electrolyte additives.* Colloids and Surfaces A: Physicochemical and Engineering Aspects, 2021: pp. 127239.

307. Zhang, S., et al., *Large-Scale and Low-Cost Motivation of Nitrogen-Doped Commercial Activated Carbon for High-Energy-Density Supercapacitor.* ACS Applied Energy Materials, 2019. **2**(6): pp. 4234-4243.

308. Hussain, N., et al., *Green Synthesis of S- and N-Codoped Carbon Nanospheres and Application as Adsorbent of Pb (II) from Aqueous Solution.* International Journal of Chemical Engineering, 2020. **2020**: pp. 9068358.

309. Unnikrishnan, B., et al., *Carbon Dot-Mediated Synthesis of Manganese Oxide Decorated Graphene Nanosheets for Supercapacitor Application.* ACS Sustainable Chemistry & Engineering, 2016. **4**(6): pp. 3008-3016.

310. Rahman, M.M., et al., *Improvement of capacitive performance of polyaniline based hybrid supercapacitor.* Heliyon, 2021. **7**(7): pp. e07407.

311. Youssry, S.M., et al., *Superior performance of* $Ni(OH)_2$*-ErGO@ NF electrode materials as pseudocapacitance using electrochemical deposition via two simple successive steps.* Journal of Energy Storage, 2020. **30**: pp. 101485.

312. Pholauyphon, W., et al., *Ultrahigh-performance titanium dioxide-based supercapacitors using sodium polyacrylate-derived carbon dots as simultaneous and synergistic electrode/electrolyte additives.* Electrochimica Acta, 2021. **390**: pp. 138805.

313. Elmouwahidi, A., et al., *Carbon–*TiO_2 *composites as high-performance supercapacitor electrodes: synergistic effect between carbon and metal oxide phases.* Journal of Materials Chemistry A, 2018. **6**(2): pp. 633-644.

314. Sharavath, V., S. Sarkar, and S. Ghosh, *One-pot hydrothermal synthesis of* TiO_2*/graphene nanocomposite with simultaneous nitrogen-doping for energy storage application.* Journal of Electroanalytical Chemistry, 2018. **829**: pp. 208-216.

315. Xiao, K., et al., *Amorphous MnO2 supported on 3D-Ni nanodendrites for large areal capacitance supercapacitors.* Electrochimica Acta, 2014. **149**: pp. 341-348.

316. Gao, P., et al., *Understanding the Synergistic Effects and Structural Evolution of Co* $(OH)_2$ *and* Co_3O_4 *toward Boosting Electrochemical Charge Storage.* Advanced Functional Materials, 2021: pp. 2108644.

317. Tang, P., et al., *Covalency competition induced active octahedral sites in spinel cobaltites for enhanced pseudocapacitive charge storage.* Advanced Energy Materials, 2021.

318. Ghosh, D., et al., *Synthesis and characterisations of TiO_2 coated multiwalled carbon nanotubes/graphene/polyaniline nanocomposite for supercapacitor applications.* Open Journal of Applied Sciences, 2012. **2**(02): pp. 70.

319. Hu, C., et al., *Design and fabrication of carbon dots for energy conversion and storage.* Chemical Society Reviews, 2019. **48**(8): pp. 2315-2337.

320. Zhang, E., et al., *Carbon dots@ rGO paper as freestanding and flexible potassium-ion batteries anode.* Advanced Science, 2020. **7**(15): pp. 2000470.

321. Seetharaman, A., et al., *TiO_2/Carbon allotrope nanohybrids for supercapacitor application with theoretical insights from density functional theory.* Applied Surface Science, 2021. **563**: pp. 150259.

322. Subramani, K., et al., *Orange peel derived activated carbon for fabrication of high-energy and high-rate supercapacitors.* ChemistrySelect, 2017. **2**(35): pp. 11384-11392.

323. Karnan, M., et al., *Aloe vera derived activated high-surface-area carbon for flexible and high-energy supercapacitors.* ACS applied materials & interfaces, 2016. **8**(51): pp. 35191-35202.

324. Abd Elkodous, M., et al., *Nanocomposite matrix conjugated with carbon nanomaterials for photocatalytic wastewater treatment.* Journal of Hazardous Materials, 2021. **410**: pp. 124657.

325. Rajan, A.S., S. Sampath, and A.K. Shukla, *An in situ carbon-grafted alkaline iron electrode for iron-based accumulators.* Energy & Environmental Science, 2014. **7**(3): pp. 1110-1116.

326. Wang, T., et al., *Boosting the cycling stability of transition metal compounds-based supercapacitors.* Energy Storage Materials, 2019. **16**: pp. 545-573.

327. Ji, Z., et al., *High-performance hybrid supercapacitor realized by nitrogen-doped carbon dots modified cobalt sulfide and reduced graphene oxide.* Electrochimica Acta, 2020. **334**: pp. 135632.

328. Hoang, V.C. and V.G. Gomes, *High performance hybrid supercapacitor based on doped zucchini-derived carbon dots and graphene.* Materials Today Energy, 2019. **12**: pp. 198-207.

329. El-Hallag, I.S., et al., *Facile in-situ simultaneous electrochemical reduction and deposition of reduced graphene oxide embedded palladium nanoparticles as high performance electrode materials for supercapacitor with excellent rate capability.* Electrochimica Acta, 2019. **314**: pp. 124-134.

330. Pholauyphon, W., et al., *Ultrahigh-performance titanium dioxide-based supercapacitors using sodium polyacrylate-derived carbon dots as simultaneous and synergistic electrode/electrolyte additives.* Electrochimica Acta, 2021: pp. 138805.

331. Zhou, Y., et al., *CoO/rGO composite prepared by a facile direct-flame approach for high-power supercapacitors.* Ceramics International, 2018. **44**(14): pp. 16900-16907.

332. Kumar, D. and S. Hiranwal. *Descriptive Study and Analysis of Forest Change detection techniques using Satellite Images*. in *2019 International Conference on Smart Systems and Inventive Technology (ICSSIT)*. 2019.

333. Zhu, S., et al., *Hydrothermal synthesis of graphene-encapsulated 2D circular nanoplates of* α-Fe_2O_3 *towards enhanced electrochemical performance for supercapacitor.* Journal of Alloys and Compounds, 2019. **775**: pp. 63-71.

334. Ashourdan, M., et al., *Synthesis of* $CuMnO_2$*/graphene quantum dot nanocomposites as novel electrode materials for high performance supercapacitors.* Journal of Energy Storage, 2021. **36**: pp. 102449.

335. Abbasi, L., M. Arvand, and S.E. Moosavifard, *Facile template-free synthesis of 3D hierarchical ravine-like interconnected* $MnCo_2S_4$ *nanosheet arrays for hybrid energy storage device.* Carbon, 2020. **161**: pp. 299-308.

336. Leitner, K.W., et al., *Combination of redox capacity and double layer capacitance in composite electrodes through immobilization of an organic redox couple on carbon black.* Electrochimica Acta, 2004. **50**(1): pp. 199-204.

337. Navalpotro, P., et al., *Insights into the energy storage mechanism of hybrid supercapacitors with redox electrolytes by Electrochemical Impedance Spectroscopy.* Electrochimica Acta, 2018. **263**: pp. 110-117.

338. Ghenaatian, H.R., M.F. Mousavi, and M.S. Rahmanifar, *High performance hybrid supercapacitor based on two nanostructured conducting polymers: Self-doped polyaniline and polypyrrole nanofibers.* Electrochimica Acta, 2012. **78**: pp. 212-222.

339. Li, Q., et al., *Carbon/MnO_2 Double-Walled Nanotube Arrays with Fast Ion and Electron Transmission for High-Performance Supercapacitors.* ACS Applied Materials & Interfaces, 2014. **6**(4): pp. 2726-2733.

340. Zhu, G., et al., *Highly conductive three-dimensional MnO_2–carbon nanotube–graphene–Ni hybrid foam as a binder-free supercapacitor electrode.* Nanoscale, 2014. **6**(2): pp. 1079-1085.

341. Xu, X., et al., *Highly crumpled graphene-like material as compression-resistant electrode material for high energy-power density supercapacitor.* Chemical Engineering Journal, 2020. **397**: pp. 125525.

342. Kumar, R., et al., *Graphene-wrapped and cobalt oxide-intercalated hybrid for extremely durable super-capacitor with ultrahigh energy and power densities.* Carbon, 2014. **79**: pp. 192-202.

343. Li, J., et al., *Three-dimensional nanobranched TiO_2-carbon nanotube for high performance supercapacitors.* Applied Surface Science, 2021. **563**: pp. 150301.

344. Mendoza, R., et al., *Improving the electrochemical performance of flexible carbon nanotubes based supercapacitors by depositing Ni@TiO_2:W nanoparticles on their anodes.* Journal of Physics and Chemistry of Solids, 2021. **155**: pp. 110128.

345. Sirengo, K., et al., *Fish bladder-based activated carbon/Co_3O_4/TiO_2 composite electrodes for supercapacitors.* Materials Chemistry and Physics, 2019. **232**: pp. 49-56.

346. Lal, M.S., et al., *Hydrothermal synthesis of single-walled carbon nanotubes/TiO_2 for quasi-solid-state composite-type symmetric hybrid supercapacitors.* Journal of Energy Storage, 2021. **40**: pp. 102794.

347. Xie, Y. and H. Du, *Electrochemical capacitance of a carbon quantum dots–polypyrrole/titania nanotube hybrid.* RSC Advances, 2015. **5**(109): pp. 89689-89697.

List of publications

1. M. Abd Elkodous, Go Kawamura, and Atsunori Matsuda*, Al-$SrTiO_3$/Au/CdS Z-Schemes for the efficient photocatalytic H_2 production under visible light, ***International Journal of Hydrogen Energy***, 30 May 2023.
2. M. Abd Elkodous, Aziz Aatiqah, Go Kawamura*, Wai Kian Tan, and Atsunori Matsuda*, Metallic nanoparticles loaded Al-$SrTiO_3$ supported with $RhCr_2O_3$ and CoOOH cocatalysts for overall water splitting, ***International Journal of Hydrogen Energy***, Volume 47, Issue 85, Pages 36139-36148, 15 October 2022. DOI: 10.1016/j.ijhydene.2022.08.199
3. M. Abd Elkodous, Go Kawamura, Wai Kian Tan, and Atsunori Matsuda*, Facile one-pot preparation of Cu/CuO/Cu_2O heterojunction for photocatalytic applications, ***Materials Letters***, Volume 323, 132606, 15 September 2022. DOI: 10.1016/j.matlet.2022.132606
4. M. Abd Elkodous, Ahmed M. El-Khawaga, M. I. A. Abdel Maksoud, Gharieb S. El-Sayyad*, Nurhaswani Alias, Hazem Abdelsalam, Medhat A. Ibrahim, Mohamed A. Elsayed, Go Kawamura, Zainovia Lockman, Wai Kian Tan, and Atsunori Matsuda*, Enhanced photocatalytic and antimicrobial performance of a multifunctional Cu-loaded nanocomposite under UV light: theoretical and experimental study, ***Nanoscale***, Volume 14, Issue 23, Pages 8306-8317, 18 May 2022 2022. DOI: 10.1039/D2NR01710E
5. Sally M. Youssry†, M. Abd Elkodous†, Go Kawamura, and Atsunori Matsuda*, Carbon dots conjugated nanocomposite for the enhanced electrochemical performance of

supercapacitor electrodes, ***RSC Advances***, Volume 11, Issue 63, Pages 39636-39645, 13 Dec 2021. DOI: 10.1039/D1RA08045H

6. M. Abd Elkodous, Gharieb S. El-Sayyad, M. I. A. Abdel Maksoud, Rajesh Kumar, Keiichiro Maegawa, Go Kawamura*, Tan Wai Kian and Atsunori Matsuda*, Nanocomposite matrix conjugated with carbon nanomaterials for photocatalytic wastewater treatment, ***Journal of Hazardous Materials***, Volume 410, 124657, 15 May 2021. DOI: 10.1016/j.jhazmat.2020.124657
7. M. Abd Elkodous†, Gharieb S. El-Sayyad†, Sally M. Youssry, Hanady G. Nada, Mohamed Gobara, Mohamed A. Elsayed, Ahmed M. El-Khawaga, Go Kawamura*, Tan Wai Kian, Ahmed I. El-Batal and Atsunori Matsuda*, Carbon-dot-loaded $Co_xNi_{1-x}Fe_2O_4$; x=0.9 / SiO_2 / TiO_2 nanocomposite with enhanced photocatalytic and antimicrobial potential: An engineered nanocomposite for wastewater treatment, ***Scientific Reports***, Volume 10, 11534, 13 July 2020. DOI: 10.1038/s41598-020-68173-1

Supplementary materials

Chapter 2:

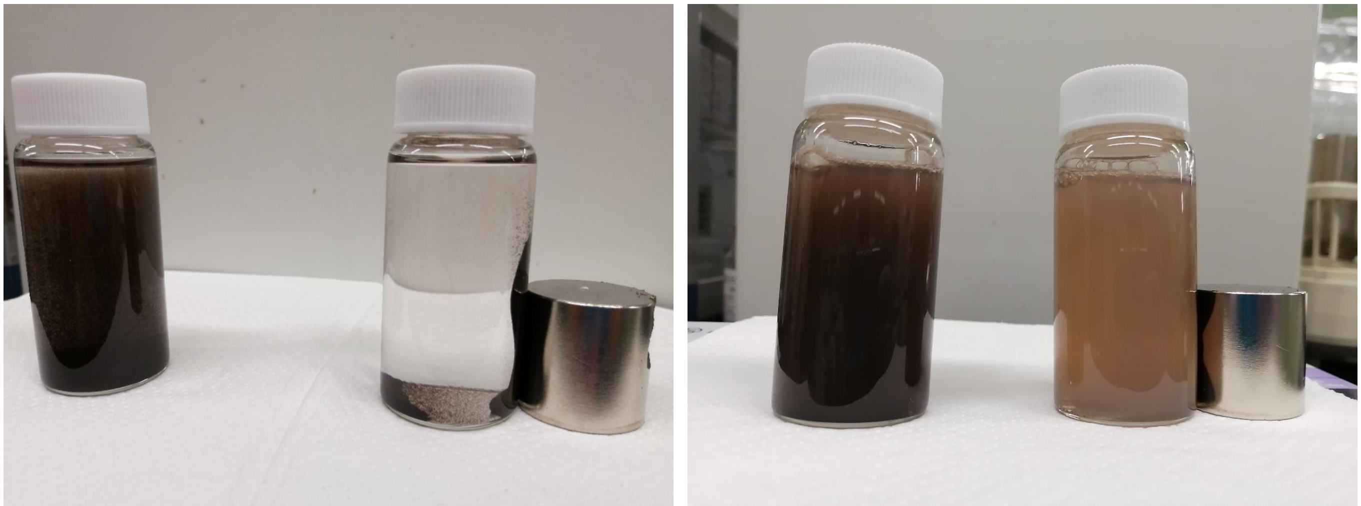

Fig. S. 2.1: Magnetic separation of a) $Co_{0.9}Ni_{0.1}Fe_2O_4/SiO_2$ core shell structure and b) $Co_{0.9}Ni_{0.1}Fe_2O_4/SiO_2/TiO_2$ nanocomposite using 550 mT Nd magnet.

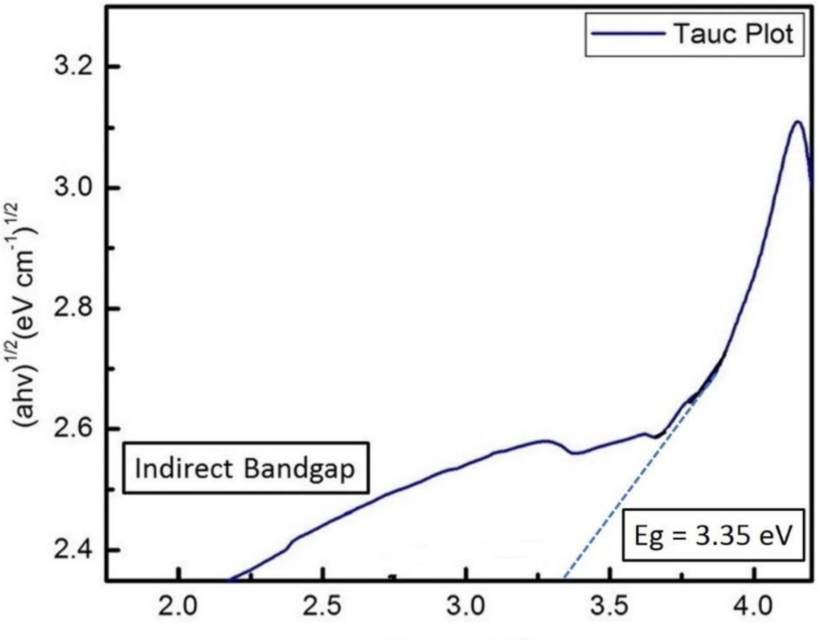

Fig. S. 2.2: Band gap calculation of the prepared nanocomposite using Tauc plot.

Chapter 3:

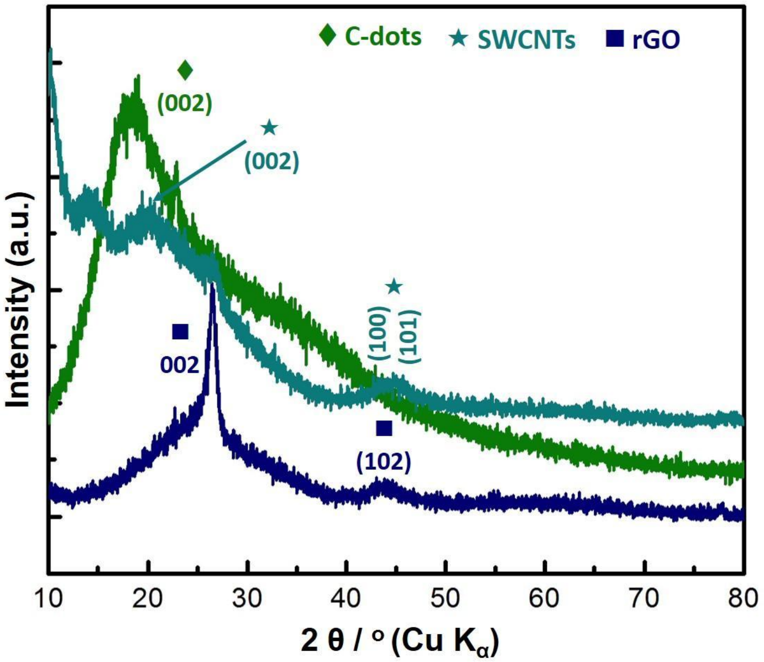

Fig. S.3.1: XRD patterns of separate samples of carbon nanomaterials (C-dots, rGO and SWCNTs).

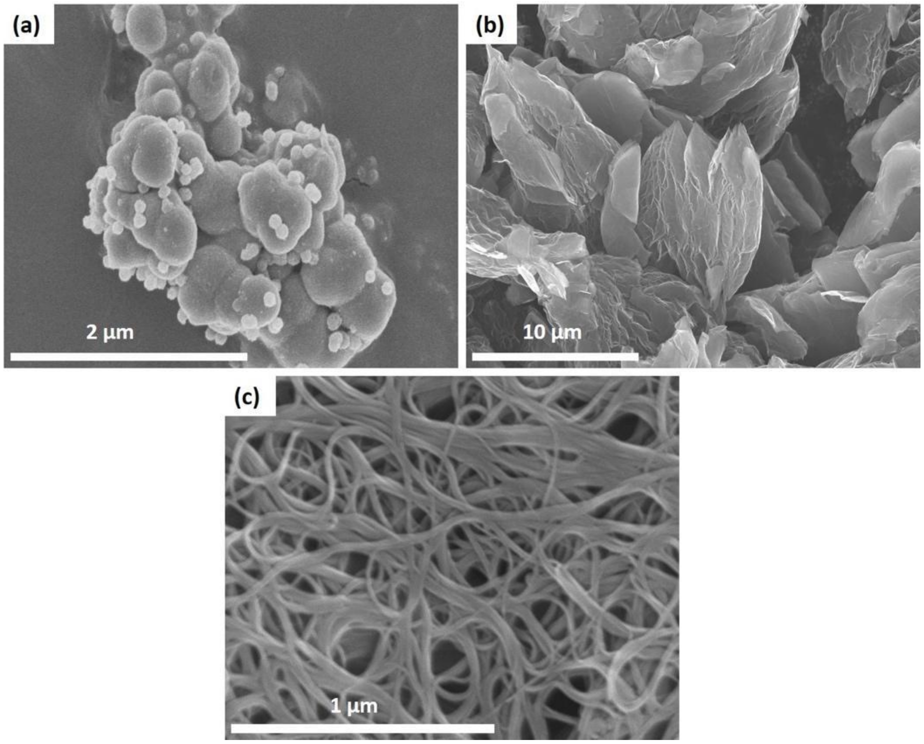

Fig. S.3.2 SEM images of the employed carbon nanomaterials a) C-dots, b) rGO and C) SWCNTs.

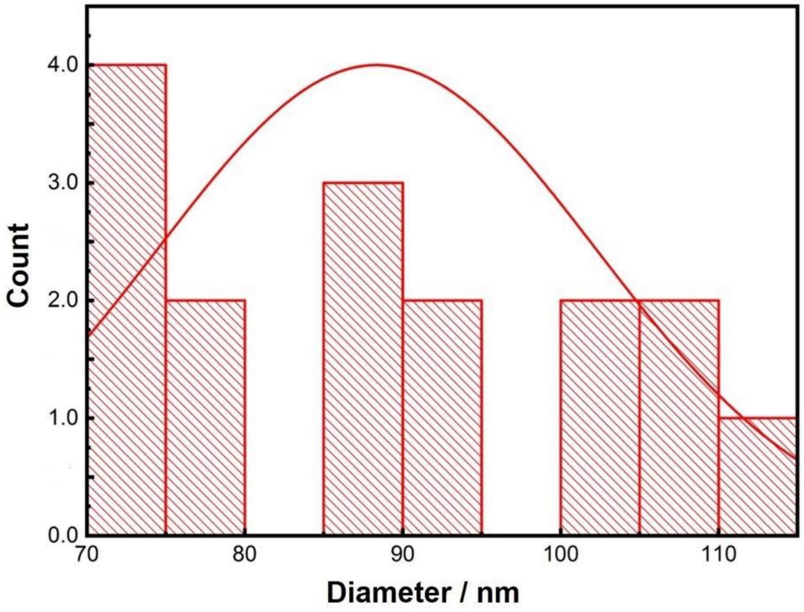

Fig. S.3.3 Particle size distribution of the prepared composite matrix (CNFST).

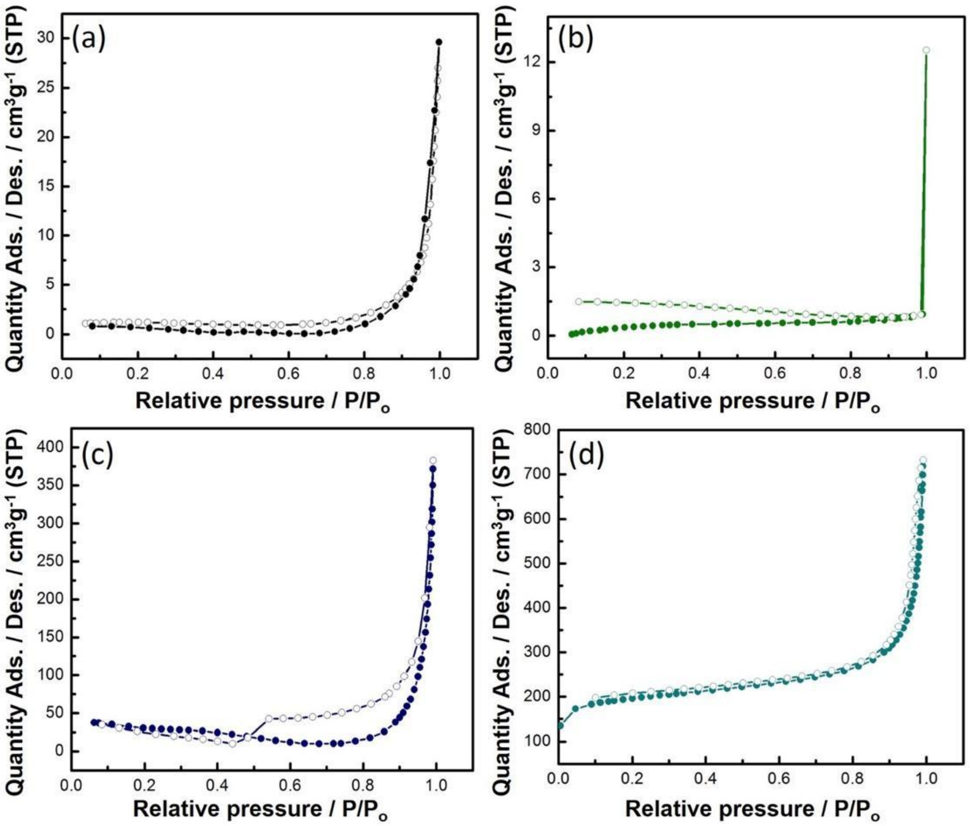

Fig. S.3.4 N_2 adsorption-desorption isotherms of the prepared nanomaterials a) CNFST matrix, b) C-dots, c) rGO and d) SWCNTs.

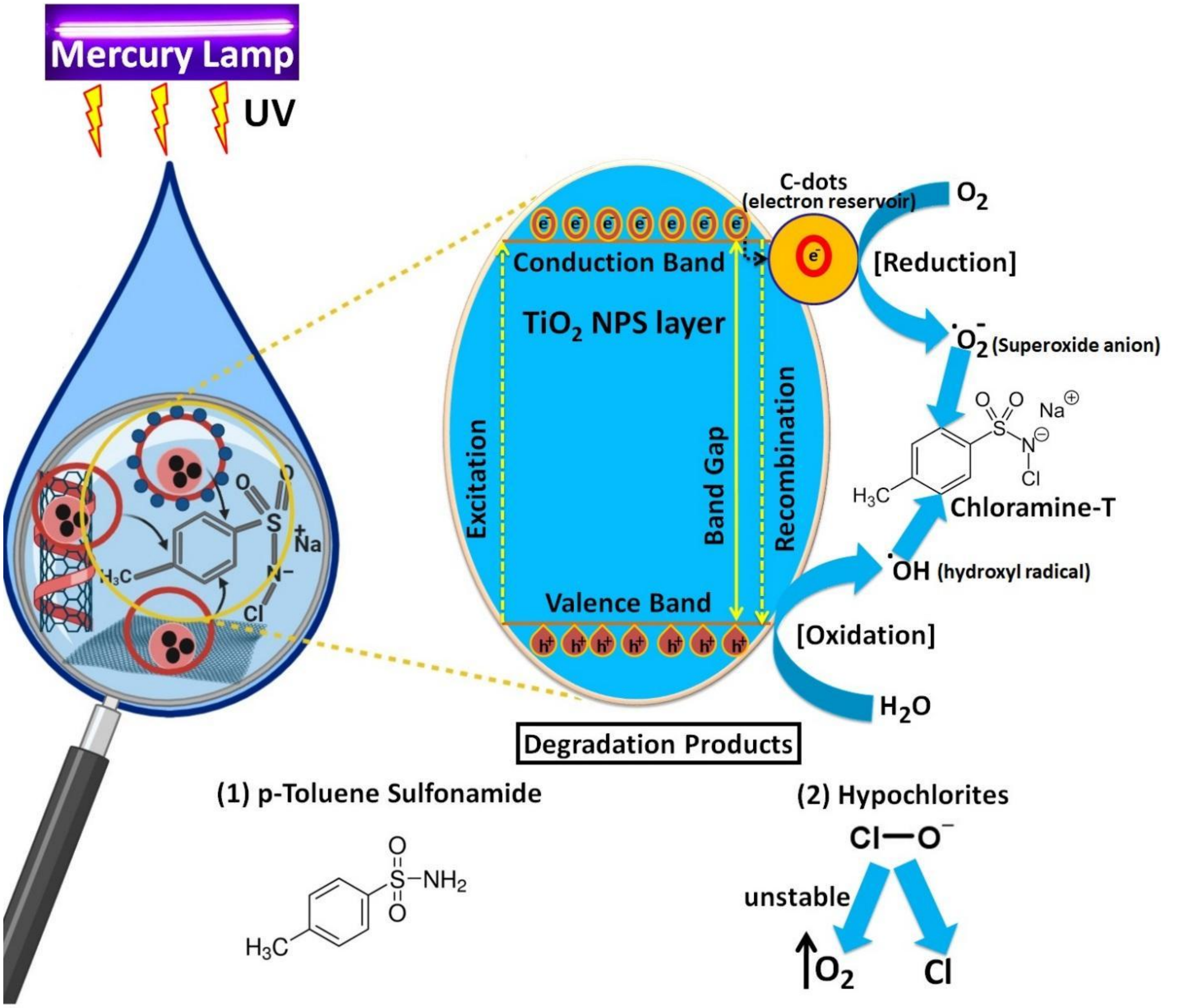

Fig. S.3.5 Proposed reaction mechanism of Chloramine-T degradation by the prepared nanocomposites.

Chapter 3:

1. Preparation of the composite matrix ($Co_{0.5}Ni_{0.5}Fe_2O_4/SiO_2/TiO_2$A layer-by-layer method was used in the preparation of the composite matrix employed in this study, the detailed steps of which are mentioned in previously published articles [1, 2] and are presented in **Fig. S. 4.1**, where the composite matrix is denoted as (CNFST).

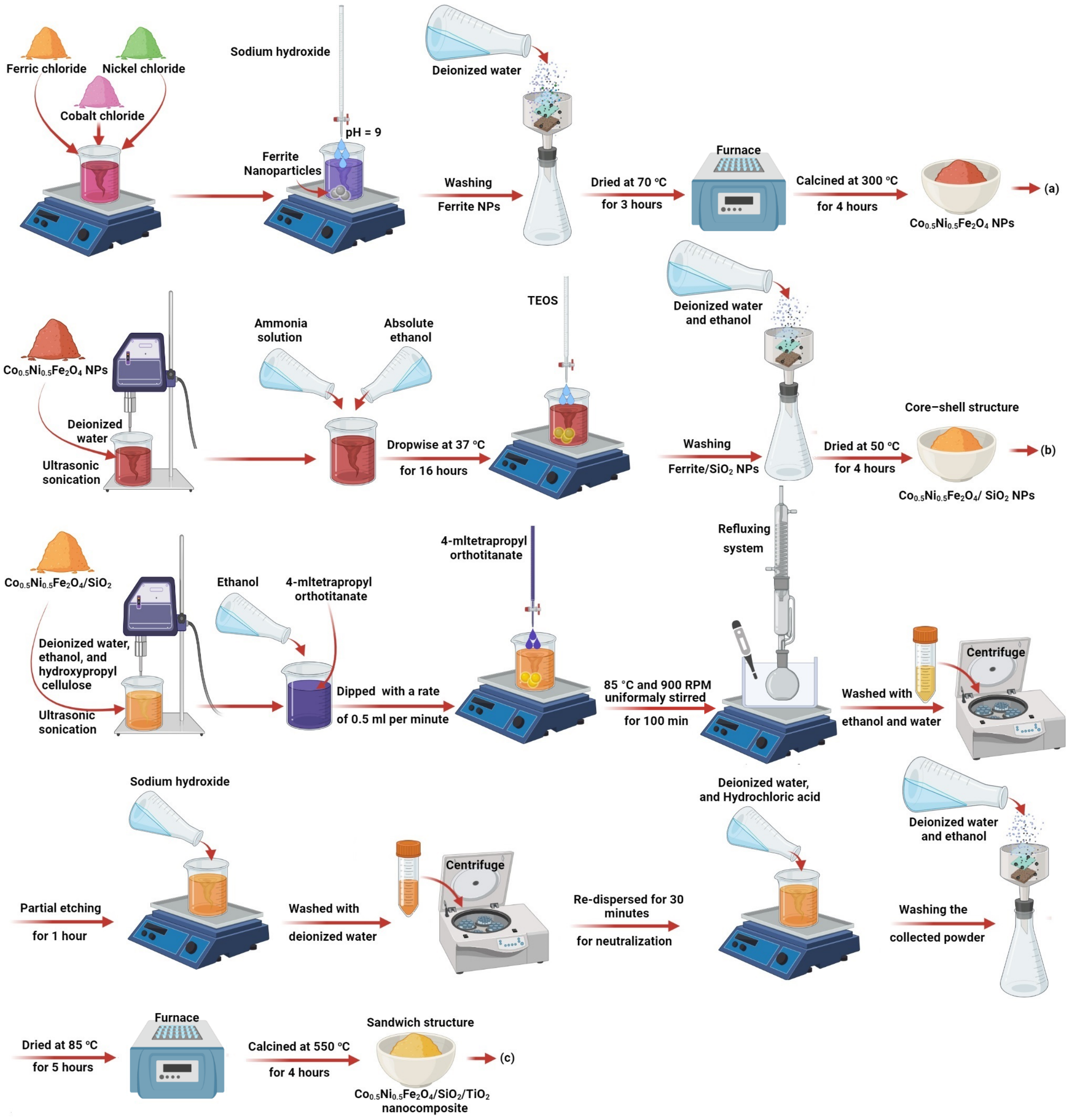

Fig. S. 4.1: Step-by-step preparation steps of CNFST nanocomposite.

2. Preparation of copper nanoparticles (Cu NPs)

Cu NPs were prepared using a modified hydrothermal method developed by Jia *et al.* [3] Briefly, ascorbic acid (6.8 g) was dissolved in deionized (DI) water (400 mL) under magnetic stirring for 10 min. Then, copper acetate monohydrate (0.8 g) was added to the above solution under constant stirring for a further 10 min at room temperature. After that, the reaction vessel was moved into a water bath and the temperature was increased to 90°C, after which the reaction was continued for 5 h. After this time, the carbon dot (C-dot)-containing supernatant was discarded, and the formed Cu precipitate was collected via centrifugation at 7000 rpm for 12 min. After that, the collected particles were washed several times using DI water. Finally, the washed particles were dried at 80°C for 2 h in air, as shown in **Fig. S.4.2**.

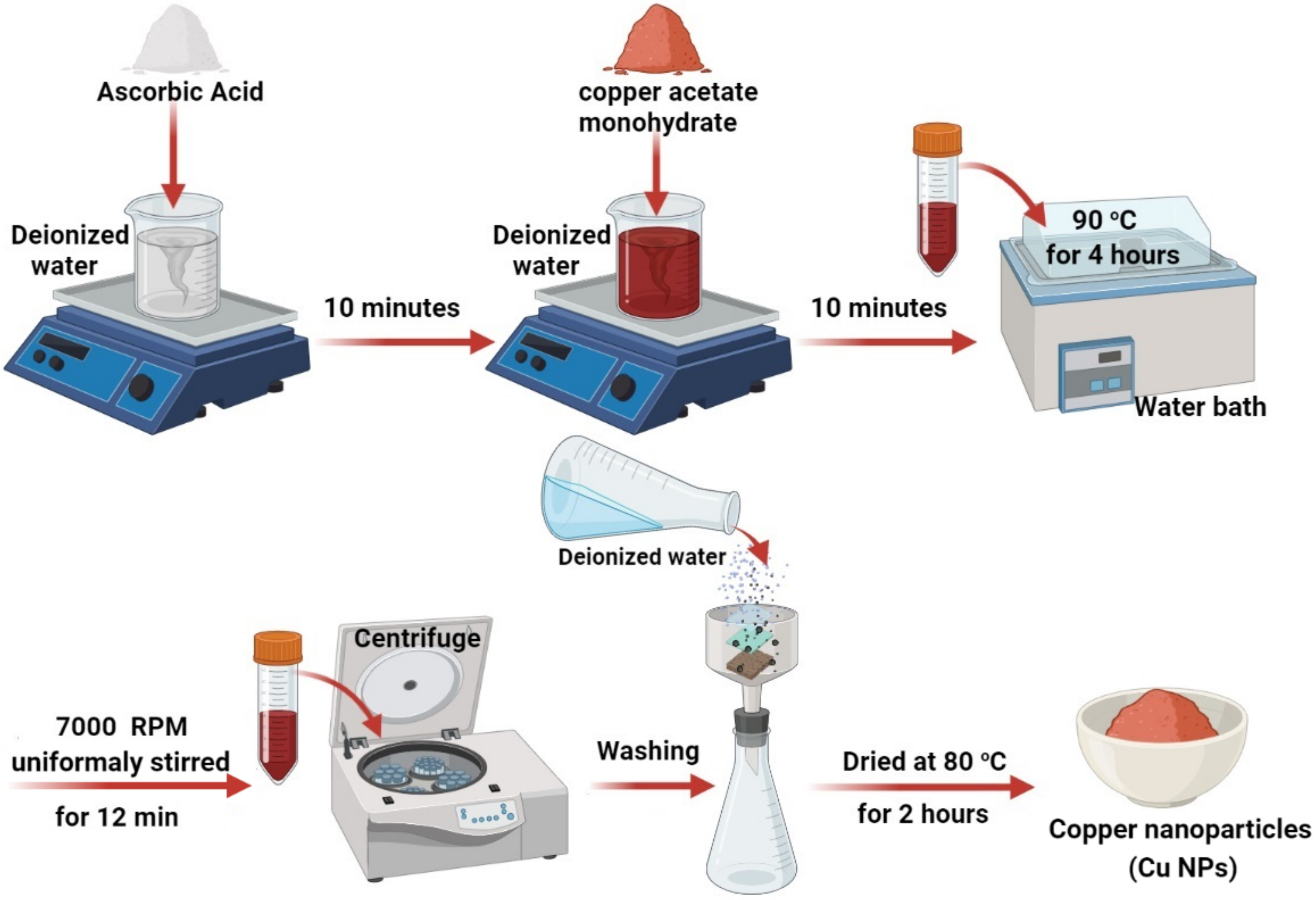

Fig. S. 4.2: Step-by-step preparation of Cu NPs.

3. Preparation of the Cu-loaded nanocomposite ($Co_{0.5}Ni_{0.5}Fe_2O_4/SiO_2/TiO_2/Cu$)

The Cu NPs obtained from the method described in the previous section were uniformly distributed over the external surface of the prepared composite matrix (section 2.2.1) using a simple impregnation method. Firstly, the CNFST composite matrix (250 mg) was dispersed in super dehydrated ethanol (50 mL) via water bath sonication for 45 min. Next, the prepared Cu NPs (27.77 mg) were added into the dispersion, which was then vigorously stirred overnight. Finally, the resultant powder was collected via centrifugation, washed many times using DI water, and dried at 60°C for 2 h. **Fig. S.4.3** shows a schematic presentation of the preparation steps used to prepare the CNFST/Cu nanocomposite.

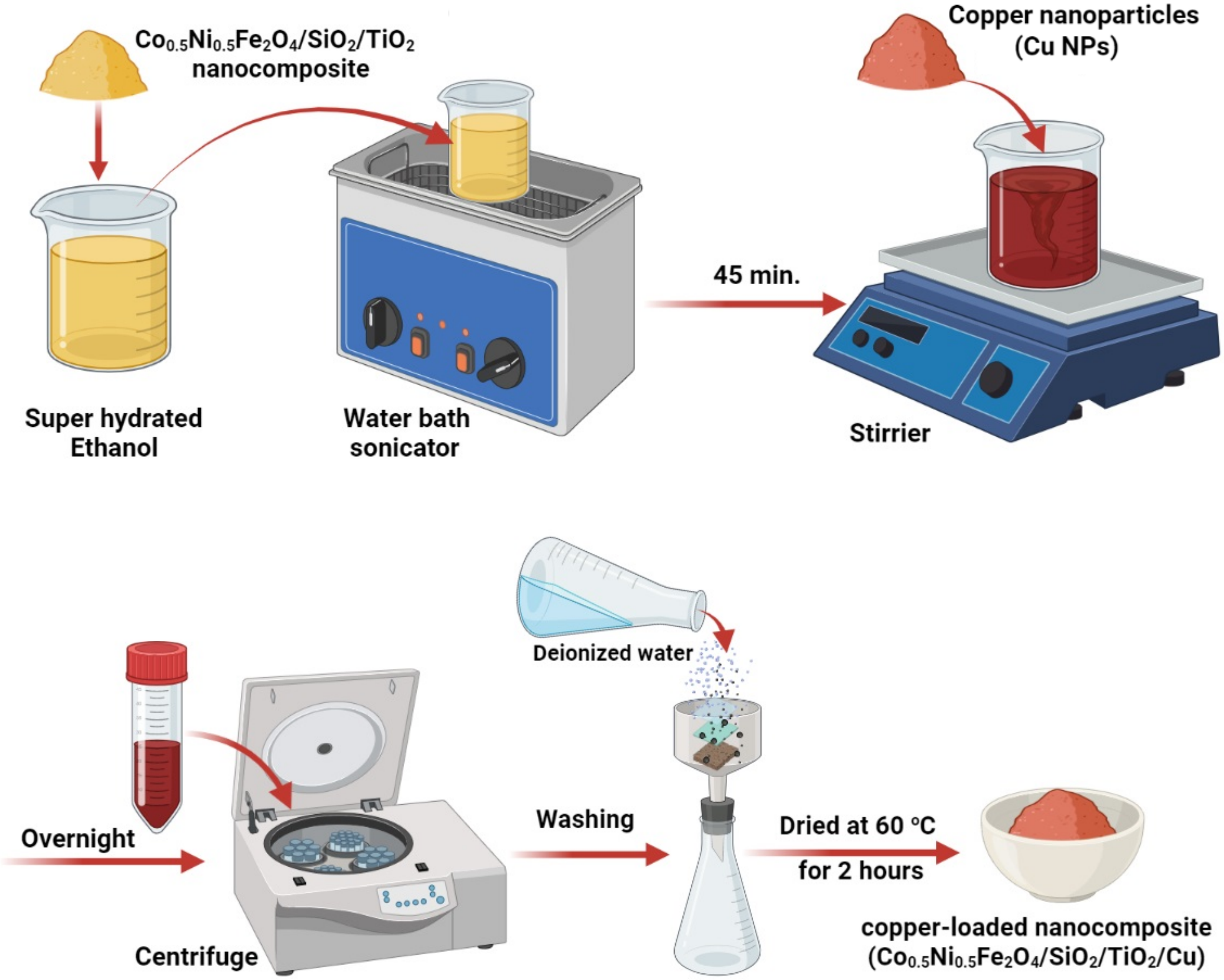

Fig. S. 4.3: Step-by-step preparation steps of CNFST/Cu nanocomposite.

4. Photocatalytic degradation assessment

Photocatalytic removal of aqueous solutions of potassium permanganate and pNA was carried out at ambient temperature (25°C ± 2°C). Initially, a fixed quantity of each sample was mixed with known volume and fixed initial concentration of dyes at a determined pH value. For Photolysis evaluation, tested pollutants were irradiated with UV light over time without photocatalysts. While for removal efficiencies due to adsorption, no UV light was used. Finally, for the photocatalysis experiments of potassium permanganate and pNA, suspensions were stirred for 2 h in the dark until adsorption–desorption equilibrium was reached. Then, suspensions were irradiated under a 10 W high pressure mercury lamp with a mean wavelength of 254 nm. After that, at fixed time intervals (10 min), the supernatant (2 mL) was sampled using a filter-supported syringe (2.5 μm filter pore size). Then, the filtered supernatant was further purified via centrifugation at 7000 rpm for 12 min to eliminate any remaining photocatalyst particles. Eventually, the change in the concentration of the dyes during photodegradation was determined via liquid cuvette configuration spectroscopic UV–vis analysis from absorbance calculations at λ_{max}, in which DI water was employed as a reference for the UV–vis calculations. While for the chromium reduction experiments, 100 ppm of a stock solution of Cr (VI) was prepared by dissolving 0.0283 g of $K_2Cr_2O_7$ in 100 mL DI water. The samples (0.01 g) were dispersed in a beaker filled with Cr (VI) (20 ppm, 20 mL). The effects of pH and EDTA were studied using 1 mM of EDTA as a hole scavenger in solution at pH 2 and 5. The 1 mM of EDTA was prepared by dissolving 0.003 g of EDTA in 100 mL of Cr (IV) solution, and the pH was adjusted using H_2SO_4. The prepared samples were continuously stirred in the dark for 60 min to reach adsorption–desorption equilibrium before UV irradiation. After this, the samples were then irradiated under a TUV 54-W UVC germicidal light (Philips, illumination at 254 nm) for 2 h. Then, 1.5 mL aliquots of the sample solutions were withdrawn at different time intervals during the exposure, and the remaining concentration of Cr (VI) in the solutions was calculated using **Eq. S.4 (1)** and via UV–vis spectroscopic analysis at a wavelength of 350 nm.

$$\mathbf{Cr(VI)\ degradation} = C_t / C_o \text{-----------------} \mathbf{Eq\ S.4(1)}$$

where C_t is the concentration at each time interval and C_o is the initial concentration after adsorption–desorption equilibrium was reached.

5. Antimicrobial activity of the prepared samples

5.1 Well diffusion assay

The pathogenic microbial strains (bacteria and unicellular fungi) were obtained from culture collection by the Drug Microbiology Lab., NCRRT, Cairo, Egypt. The tested microbes were *Staphylococcus aureus* (*S. aureus*), *Escherichia coli* (*E. coli*), *Pseudomonas aeruginosa* (*P. aeruginosa*), *Klebsiella pneumoniae* (*K. pneumoniae*), *Salmonella typhi* (*S. typhi*), *Proteus vulgaris* (*P. vulgaris*), *Proteus mirabilis* (*P. mirabilis*), *Candida albicans* (*C. albicans*), *and Candida tropicalis* (*C. tropicalis*). In these experiments, all of the isolated and examined microbial strains were maintained over nutrient agar slants at 4°C [4]. The well diffusion method was used to assess the antimicrobial impacts of the prepared nanocomposites according to the zone of inhibition (ZOI) against the examined bacteria and unicellular fungi, by employing the method reported by Chavez-Esquivel *et al.*, [5]. Firstly, samples suspended in dimethyl sulfoxide (DMSO, 10 µg/mL) were prepared. Then, the microbial suspension was fixed and set to a standard 0.5 McFarland's concentration equal to 1–2 × 10^8 CFU/mL. After that, the tested bacteria and unicellular fungi were inoculated in a nutrient agar medium, and the 6 mm wells on the surface of the nutrient agar plate were packed with 100 µL of the prepared nanocomposites, in which DMSO was used as a negative control and amoxicillin (antibacterial standard) and Nystatin (antifungal standard) were used as positive controls. All tests were conducted in triplicate and the plates were incubated overnight at 37°C. A microbial spot with no growth was defined as a ZOI, measured in mm.

In addition, minimum inhibitory concentration (MIC) values of the samples against the employed bacterial and yeast strains were also measured using the well diffusion method according to the procedure reported by Kowalska-Krochmal *et al.* [6] The overnight incubated cultures were kept at 37°C for 2 h. Following that, the inoculum of the examined bacteria and yeast was set to a concentration of 0.5 McFarland. Then, a volume of 100 µL of McFarland's bacterial suspension was injected into the nutrient agar medium plates. The prepared nanocomposites were serially diluted two-fold using DMSO to various concentrations (µg/mL) and were then separately added to the 6 mm wells on the surface of the inoculated agar plates, which were then incubated overnight at 37°C. The MIC values were determined as the minimum concentration of the nanocomposites that hinder the growth of bacteria and yeast after overnight incubation.

5.2 Growth curve assay

The influence that the prepared nanocomposites has on the growth of *S. aureus* (the most sensitive microbe) was investigated using the growth curve assay method developed by Huang *et al.* [7] In this method, the bacterial suspension was adjusted to 0.5 McFarland (1×10^8 CFU/ml) in 5 mL nutrient broth tubes. Equal volumes of the nanocomposites were then separately added to each of the test tubes. The absorbance at 600 nm of the bacterial growth after treatment was evaluated every 2 h up to 24 h. The average of duplicate readings was calculated with respect to time to obtain a regular growth curve.

5.3 Potential effect of UV activation on the antimicrobial activity of the synthesized nanocomposites

The antimicrobial potential of the prepared samples in the presence and absence of UV light was investigated against the tested pathogenic microbes (*S. aureus)* using optical density design [8]. Bacterial cultures that had been incubated for 2 h were set to a standard 0.5 McFarland (1×10^8 CFU/ml). 100 μL nanocomposite samples were mixed with the tested microbial tubes. The tubes were then divided into two groups, tubes with non-UV irradiated nanocomposites and tubes containing nanocomposites that had been UV irradiated for 15, 30, 45, 60, and 75 min with 6.9 mW cm^{-2} intensity light. Then, the turbidity of the samples was measured at 600 nm [9]. The inhibition percentage (%) of the examined bacterial pathogens was determined using **Equ. S.4(2)**, according to the method reported by Abd Elkodous *et al.* [10]

$$Inhibition\,\% = \frac{ODc - ODt}{ODc} \times 100 \qquad Equ.\ \boldsymbol{S.4\ (2)}$$

where ODc is the absorbance of a control sample that had not been subjected to any treatment and ODt is the absorbance of the treated samples.

5.4 Effect of the synthesized nanocomposites on protein leakage from bacterial cell membranes

Pure bacterial cells (100 μL) that had been cultured for 18 h and set at 0.5 McFarland (1×10^8 CFU/ml) were injected into nutrient broth (10 mL) containing well-sonicated and dispersed composite samples of various concentrations (0.125, 0.25, 0.5, and 1 mg/mL). Nanocomposite-free broth injected with cultured cells was used as a control. All samples were incubated at 37°C for 5 h before being centrifuged for 15 min at 5500 rpm [11]. For all of the samples, supernatant (100 μL) combined with Bradford reagent (1 mL) was analyzed. The optical densities of the samples were measured at 595 nm after 10 min of incubation in the dark [11].

5.5 Reaction mechanism estimation by SEM analysis of bacterial cells

Bacterial cells (*S. aureus*) were rinsed with phosphate buffered saline (PBS) and fixed with 3.5% glutaraldehyde. After that, the fixed cells were washed repeatedly with PBS and rinsed with ethanol for 20 min at 27°C before being dried. Finally, the *S. aureus* cells were attached to aluminum stumps to carry out SEM observations [8]. Morphological and surface characteristics of the composite-treated and control (untreated) *S. aureus* cells were analyzed [10, 12].

6. Statistical analysis

Statistical examination of the obtained data was conducted using one-way analysis of variance (ANOVA) (at $P < 0.05$) with Duncan's multiple series and least significant difference analyses [13]. In addition, the data were examined using the SPSS software, version 15.

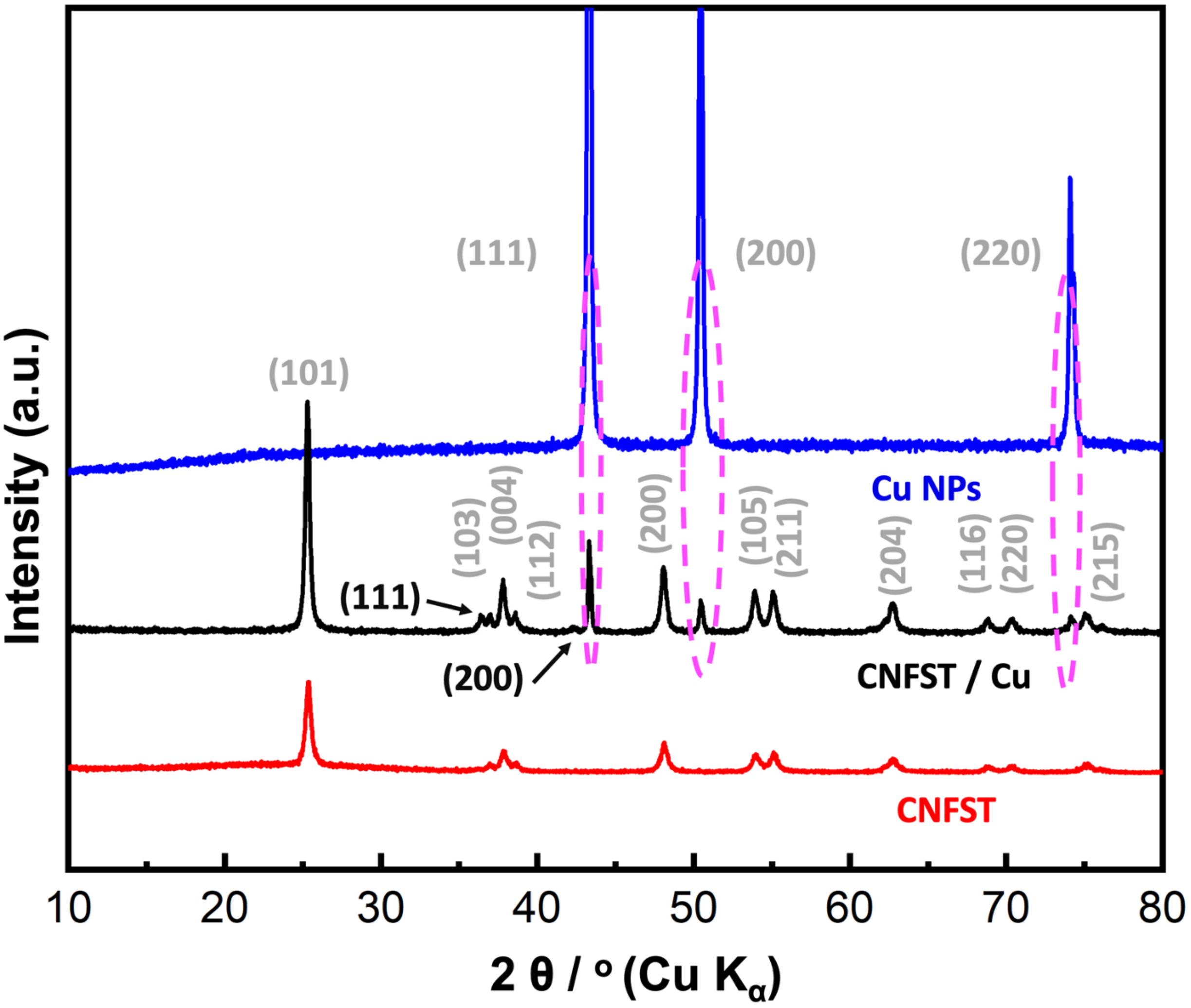

Fig. S. 4.4: XRD θ-2θ patterns of the prepared samples.

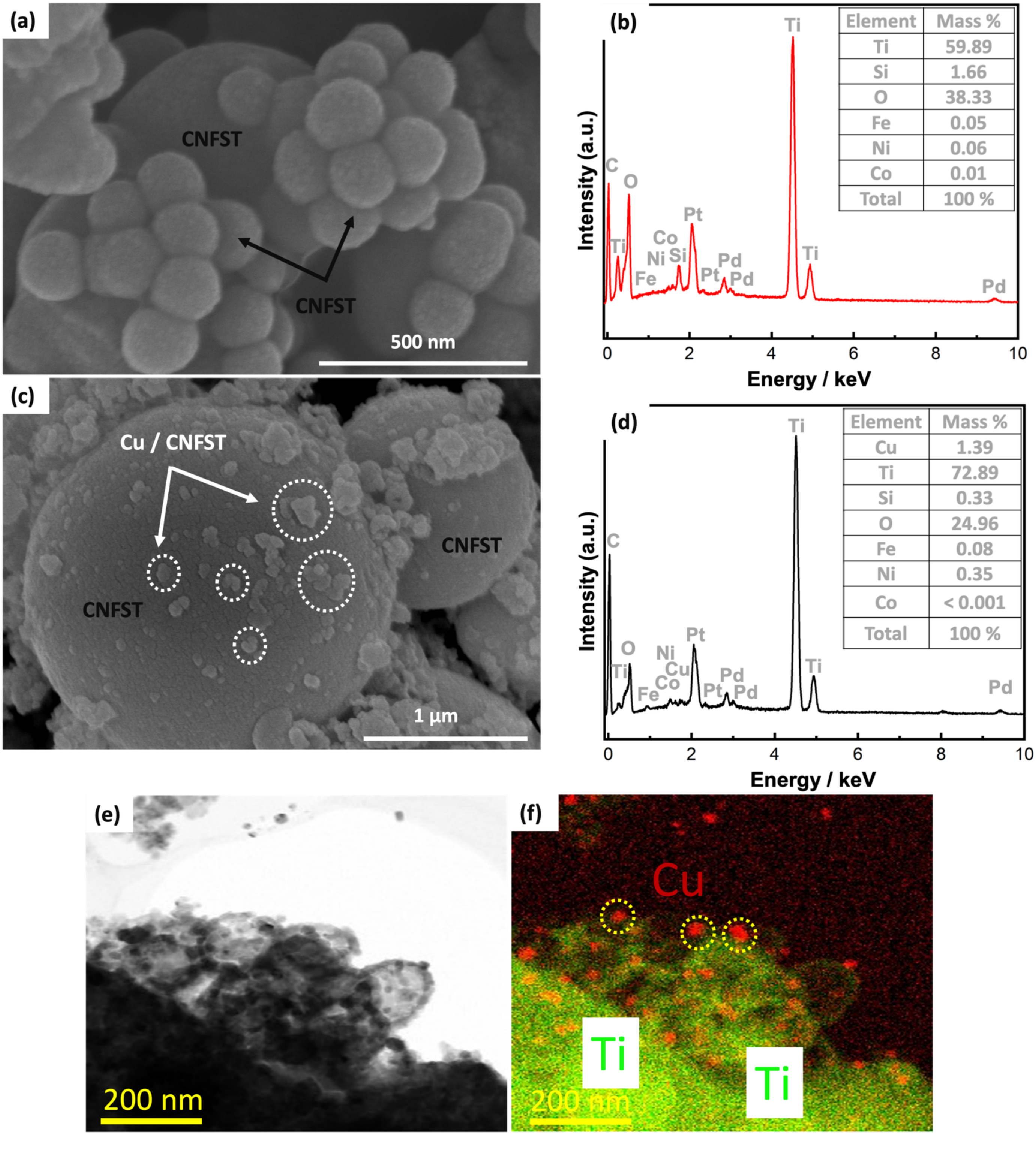

Element	Mass %
Ti	59.89
Si	1.66
O	38.33
Fe	0.05
Ni	0.06
Co	0.01
Total	100 %

Element	Mass %
Cu	1.39
Ti	72.89
Si	0.33
O	24.96
Fe	0.08
Ni	0.35
Co	< 0.001
Total	100 %

Fig. S. 4.5: SEM, EDX, and STEM mapping analyses of the prepared CNFST composite matrix, and CNFST / Cu nanocomposite.

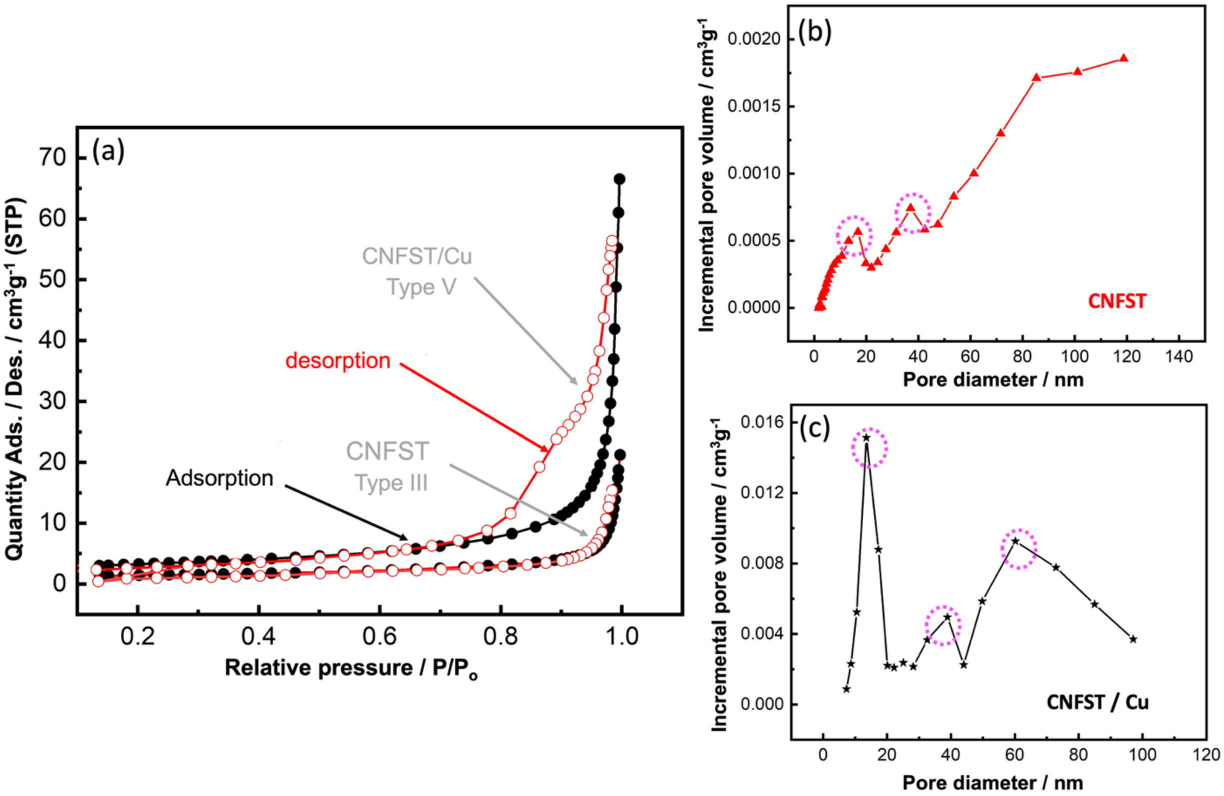

Fig. S.4. 6: a) N_2 adsorption-desorption isotherms, b) CNFST BJH pore size distribution, and c) CNFST/ Cu BJH pore size distribution.

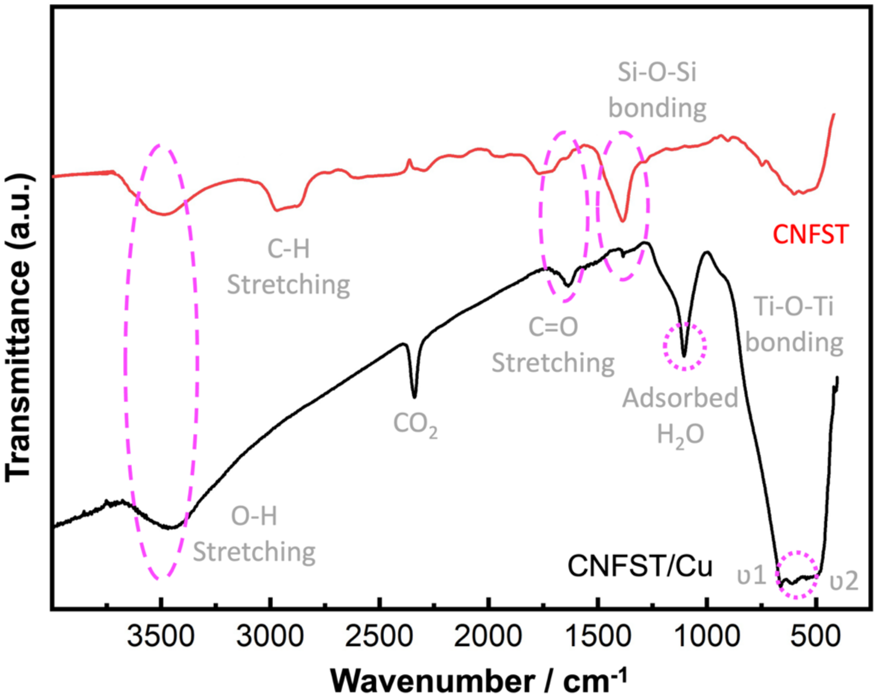

Fig. S. 4.7: FTIR spectra of bare CNFST matrix and CNFST/Cu 10% nanocomposite.

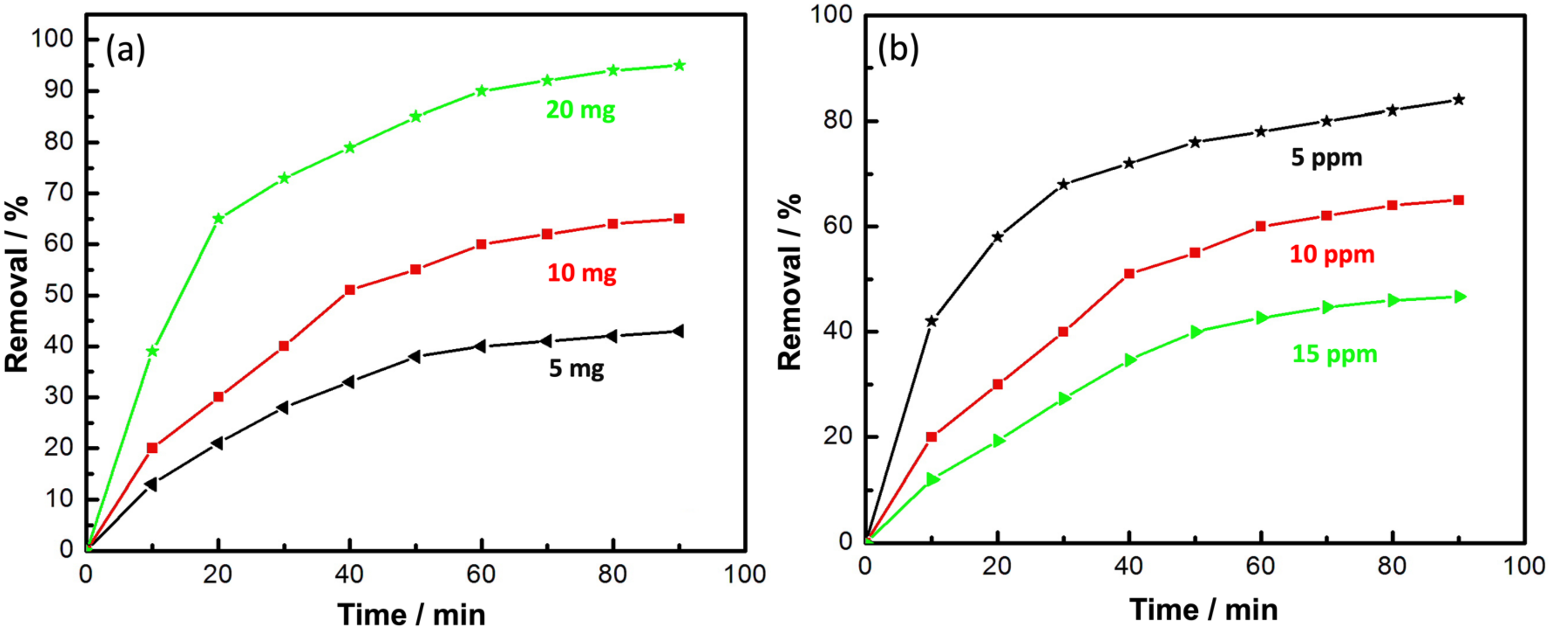

Fig. S. 4.8: a) Photocatalyst dose effect and b) initial pNA concentration impact on the photocatalytic performance of CNFST/ Cu photocatalyst.

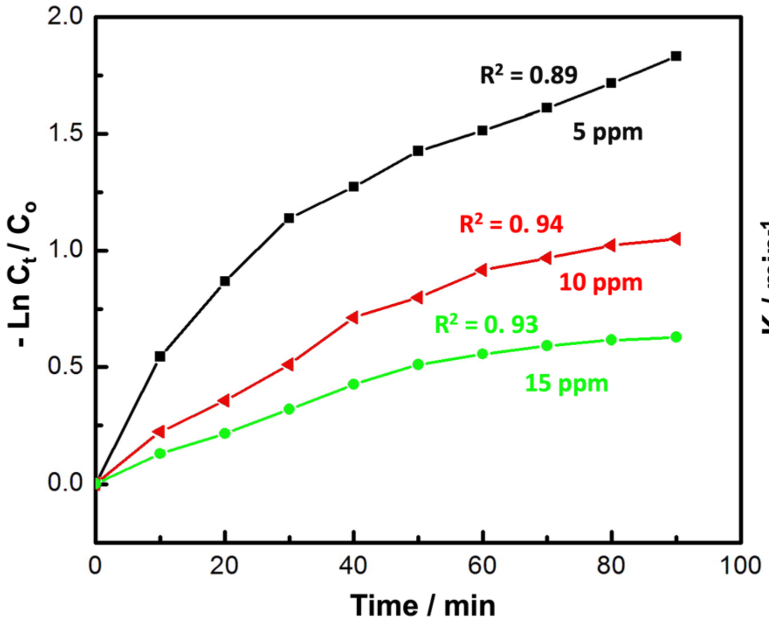

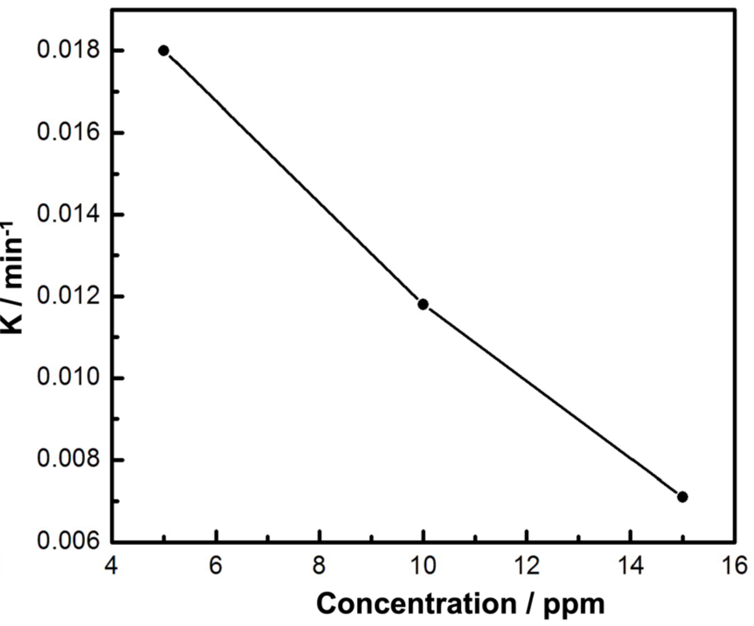

Fig. S. 4.9: a) Pseudo first-order kinetics plots and b) variation of apparent rate constant (k) with pNA concentration.

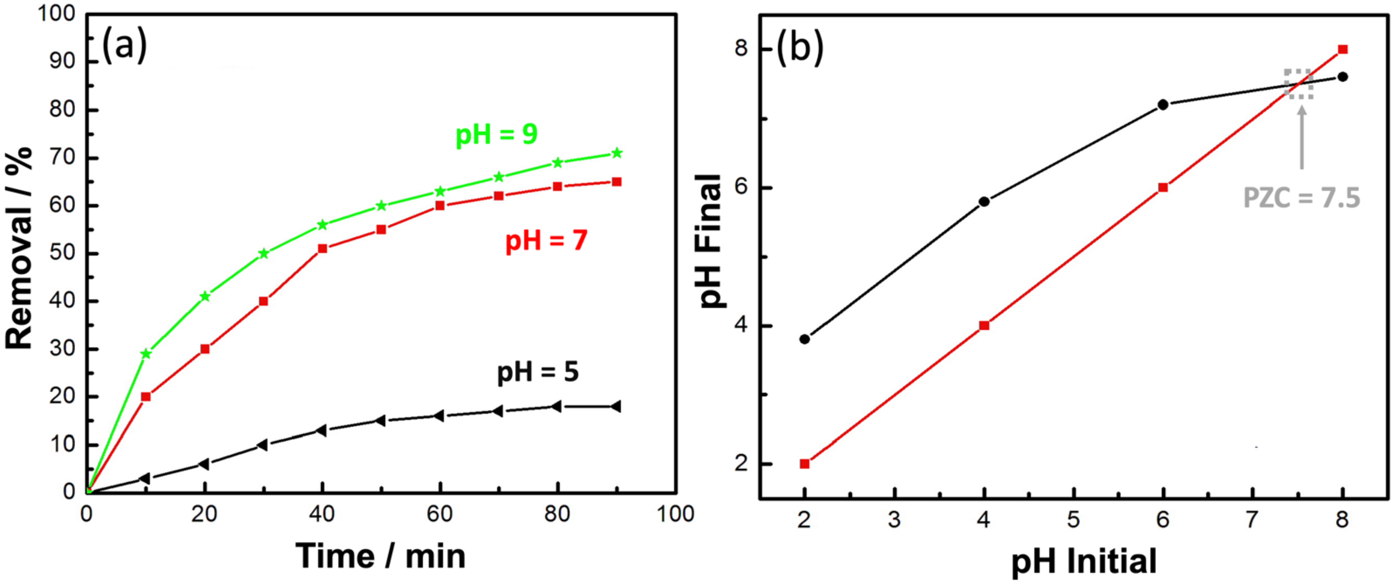

Fig. S. 4.10: a) Effect of pH on the removal percentage of pNA and b) PZC calculation.

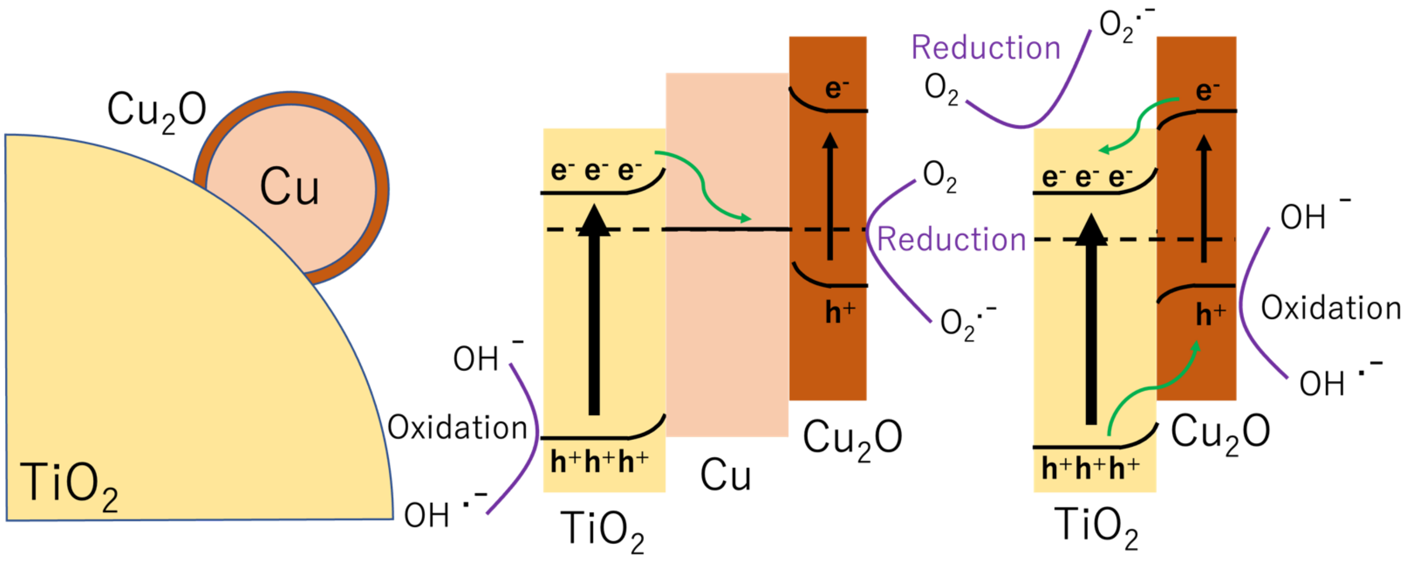

Fig. S. 4.11: Proposed photocatalytic reaction mechanism over the surface of CNFST/Cu photocatalyst.

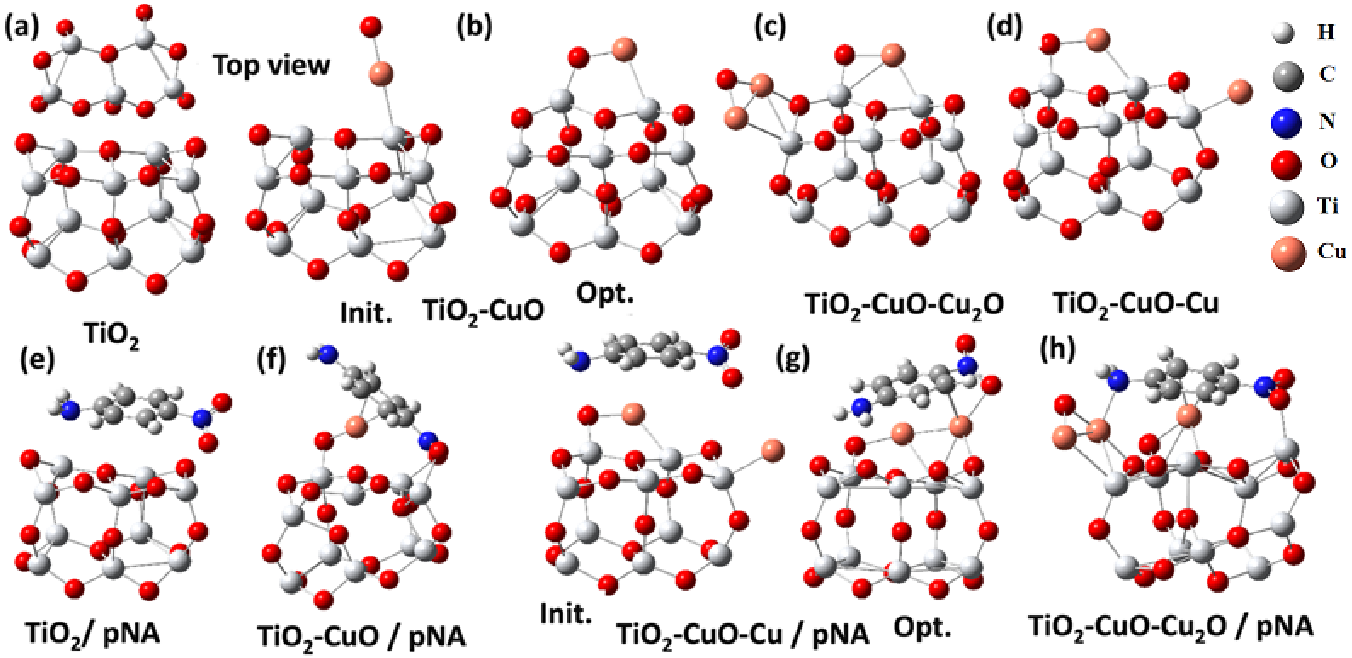

Fig. S. 4.12: (a) The optimized structure of TiO$_2$ nanoflake, (b-d) the optimized structure of TiO$_2$ after adding CuO, Cu$_2$O, and Cu. (e-h) adsorption of pNA on the previous structures. (b) and (g) shows the difference between the Initial structure (init.) and the optimized structutre (opt.).

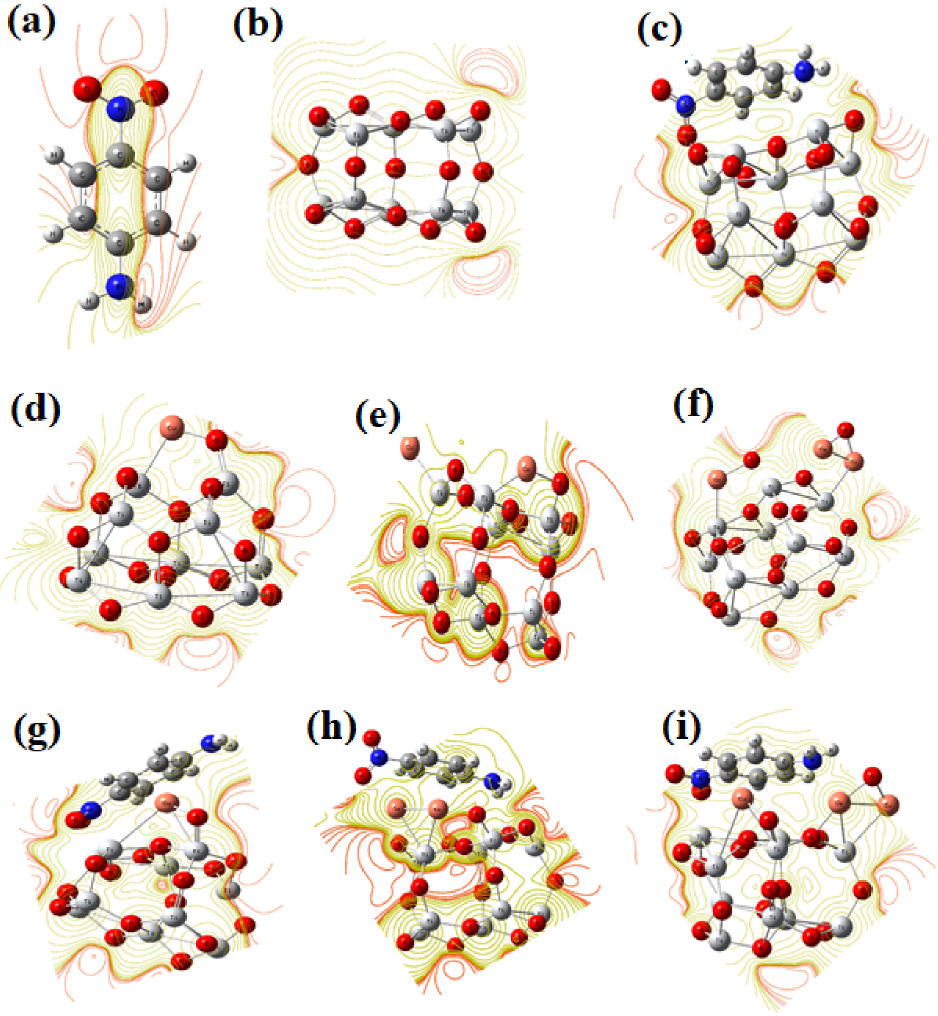

Fig. S. 4.13: DFT: M062X/6-31g (d, p) MESP mapping as contour for a) pNA, b)TiO_2, c) TiO_2/pNA, d) TiO_2-CuO, e) TiO_2-CuO-Cu, f) TiO_2-CuO-CuO_2, g) TiO_2-CuO/pNA, h) TiO_2-CuO-Cu/pNA, and i) TiO_2-CuO-CuO_2/pNA.

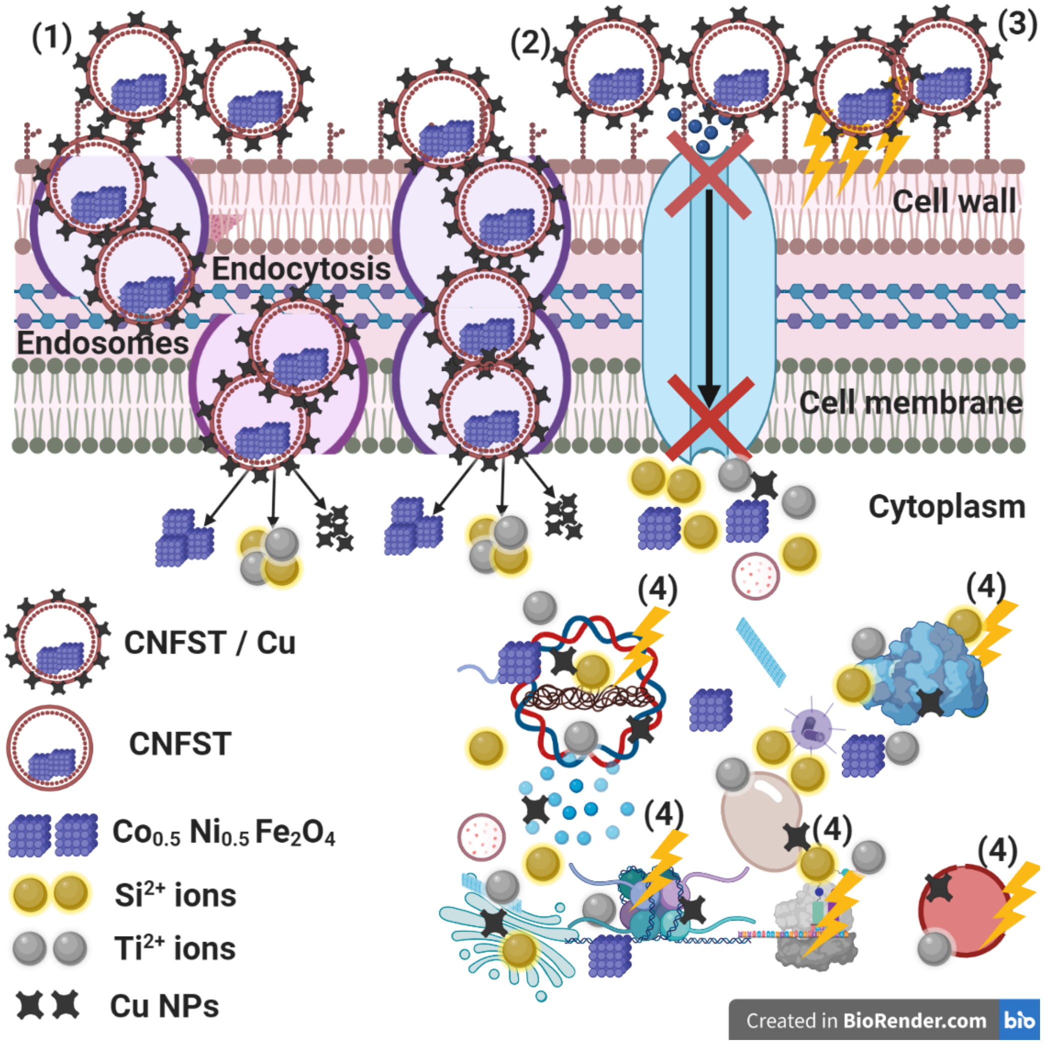

Fig. S. 4.14: Schematic representation of the four prominent routes of the antibacterial activity of CNFST/Cu nanocomposite, 1) nanocomposite adherence to the bacterial cell surface leading to membrane damage and switching off its transport activity, 2) nanocomposite blocking the ions transport from and to the bacterial cell, 3) ROS creation leading to bacterial cell wall damage, and 4) nanocomposite penetrates the bacterial cells and interact with their cellular organelles and biomolecules, affecting their cellular machinery, and modulating the cellular signaling system causing cell death. The prepared nanocomposite may serve as a vehicle to effectively-deliver Ti^{2+}, and Si^{2+} ions (from its outer shells) to the bacterial cytoplasm and membrane, where proton motive force would decrease the pH to be less than 3 facilitating the antimicrobial activity of Cu NPs and ferrites.

Chapter 5:

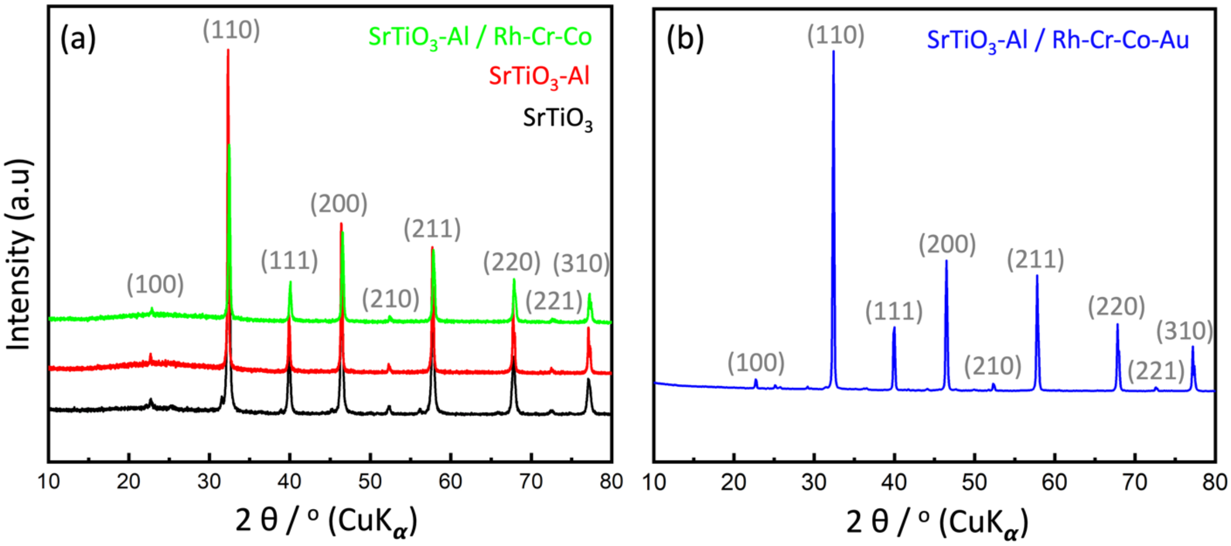

Fig. S. 5.1: a) XRD pattern of as received SrTiO$_3$, prepared Al-SrTiO$_3$, and prepared Al-SrTiO$_3$ loaded with RhCr$_2$O$_3$ (Rh = 0.1 wt. % - Cr = 0.05 wt. %) and CoOOH (Co = 0.05 wt. %.) cocatalysts and b) Al-SrTiO$_3$ loaded with RhCr$_2$O$_3$ (Rh = 0.1 wt. % - Cr = 0.05 wt. %), CoOOH (Co = 0.05 wt. %.), and Au NPs (Au = 0.3 wt.%).

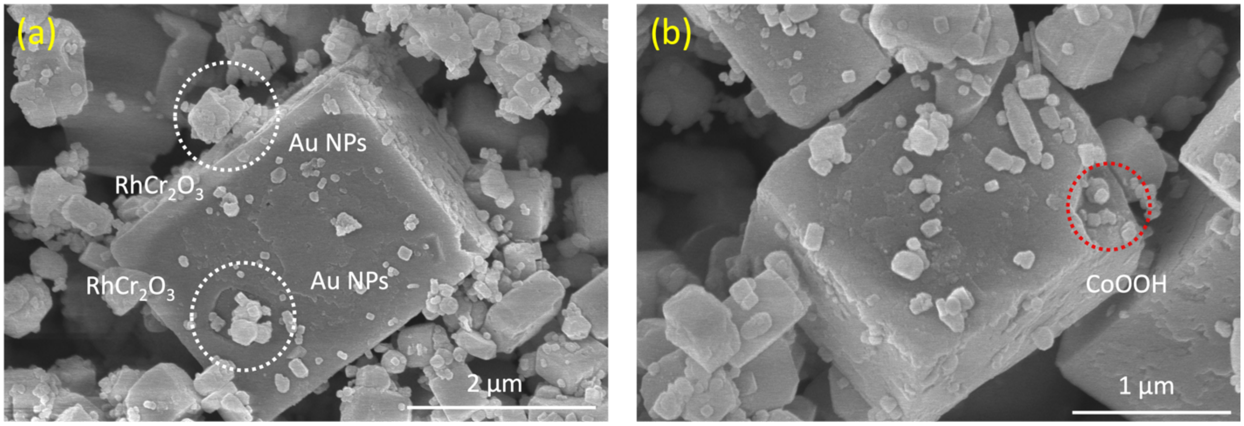

Fig. S. 5.2: SEM images of a) RhCr$_2$O$_3$ cocatalyst and P. Au NPs loaded Al-SrTiO$_3$ microspheres and b) CoOOH cocatalyst loaded Al-SrTiO$_3$ sample.

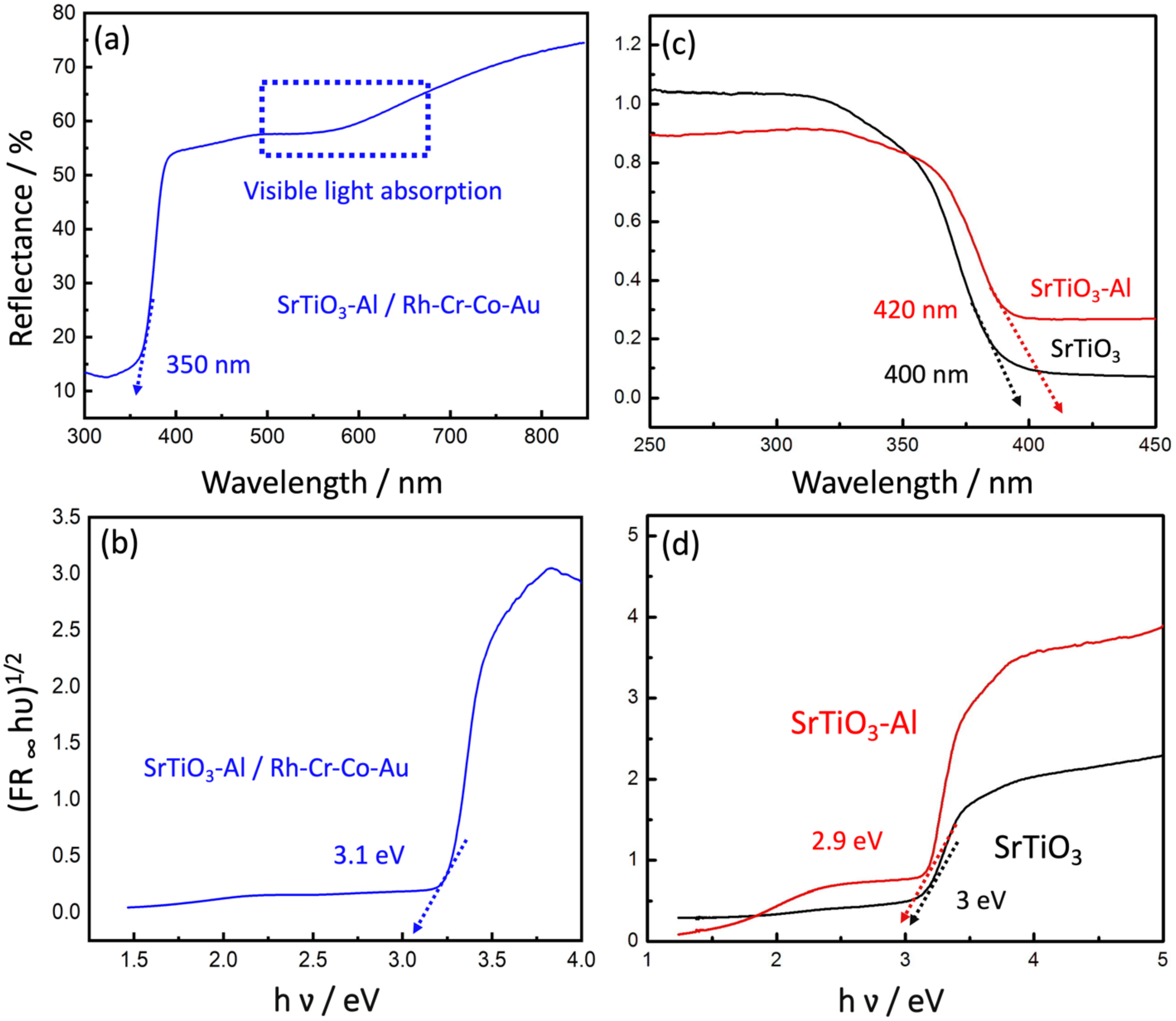
(a)
Reflectance / %
Wavelength / nm
Visible light absorption
SrTiO$_3$-Al / Rh-Cr-Co-Au
350 nm
(b)
$(FR_\infty h\upsilon)^{1/2}$
h ν / eV
SrTiO$_3$-Al / Rh-Cr-Co-Au
3.1 eV
(c)
Wavelength / nm
SrTiO$_3$-Al
420 nm
SrTiO$_3$
400 nm
(d)
h ν / eV
SrTiO$_3$-Al
2.9 eV
SrTiO$_3$
3 eV

Fig. S. 5.3: a) UV-Vis. diffuse reflectance spectrum of Al-$SrTiO_3$ loaded with $RhCr_2O_3$ (Rh = 0.1 wt. % - Cr = 0.05 wt. %), CoOOH (Co = 0.05 wt. %.), and Au NPs (Au = 0.3 wt.%), b) its calculated bandgap energy, c) diffuse reflectance spectrum of the as received $SrTiO_3$ and the prepared Al-$SrTiO_3$ samples, and d) their calculated bandgap energy.

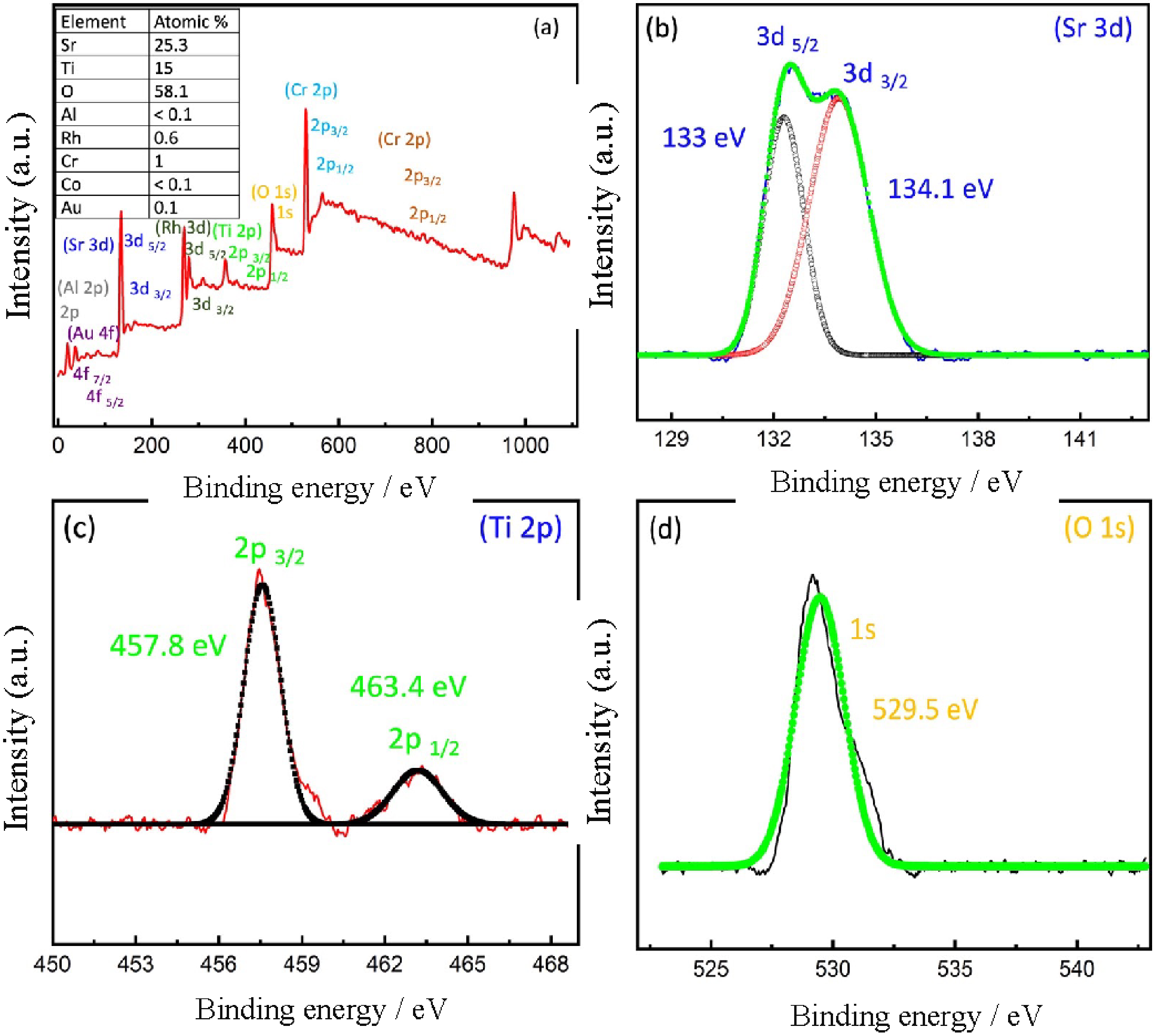

Element	Atomic %
Sr	25.3
Ti	15
O	58.1
Al	< 0.1
Rh	0.6
Cr	1
Co	< 0.1
Au	0.1

Fig. S. 5.4: a) Survey analysis showing the atomic % of the main elements, b) deconvoluted Sr 3d, c) Ti 2p, and d) O 1s spectra.